



Cardiff University
School of Engineering

Personalised Advanced 3D Dosimetry in Peptide Receptor Radionuclide Therapy

Salvatore Berenato

Thesis submitted in candidature for the degree of Doctor of
Philosophy (PhD) at Cardiff University

June 2020

TABLE OF CONTENTS

CONTRIBUTIONS TO PUBLICATIONS.....	I
ACKNOWLEDGEMENTS.....	IV
LIST OF FIGURES.....	V
LIST OF TABLES	XIV
LIST OF ACRONYMS.....	XVI
ABSTRACT.....	1
1. INTRODUCTION	3
1.1. Development of Molecular Radiotherapy	4
1.2. MRT treatments and incidence of tumours.....	8
1.3. Neuro Endocrine Tumours.....	11
1.3.1. Peptide Receptor Radionuclide Therapy	16
1.3.1.1. Yttrium-90.....	18
1.3.1.2. Lutetium-177	21
1.4. Dosimetry calculation in MRT.....	24
1.4.1. Fundamental concepts and units.....	24
1.4.2. MIRD schema.....	28
1.4.2.1. OLINDA/EXM.....	31
1.4.3. Image-based dosimetry	35
1.4.3.1. Voxel dosimetry.....	36
1.4.3.2. CT and SPECT.....	37
1.4.3.3. Image registration	44
1.4.3.4. Image segmentation	56
1.5. Objectives.....	60
1.6. Thesis outline	61

2. MONTE CARLO DOSE CALCULATION.....	63
2.1. The Monte Carlo method.....	63
2.1.1. Monte Carlo for particle transport.....	65
2.1.2. Geant4.....	72
2.2. Raydose Monte Carlo code	76
2.2.1. Calibration of Raydose	82
3. DOTATER CLINICAL TRIAL.....	86
3.1. Aims of the trial	86
3.2. Cohort and therapy description	87
4. WORKFLOW DEVELOPMENT	95
4.1. Impact of registration: rigid vs non-rigid algorithm	99
4.2. Impact of rigid and non-rigid registration algorithms on dose calculation	112
4.3. Impact of the non-rigid algorithm: activity vs dose registration.....	120
5. PERSONALISED ADVANCED 3D DOSIMETRY.....	128
5.1. Raydose vs MIRD schema	128
5.2. Lesion segmentation: dose peak threshold.....	139
6. CONCLUSIONS.....	160
6.1. Final remarks	160
6.2. Future work	167
APPENDIX A: PUBLICATIONS AND PRESENTATIONS	170
APPENDIX B: RAYDOSE MANUAL	174
APPENDIX C: MATLAB CODING	208
REFERENCES	210

Contributions to publications

This thesis contains work that has been published and prepared for publication, where I was the first author or one of the authors. My contributions to such publications are outlined below. A full list of publications and presentations related to the work reported in this thesis can be found in Appendix A.

Part of the work included in Chapter 4 (sections 4.1 and 4.2) was published in:

- Grassi E, Fioroni F, Berenato S, et al. *Effect of image registration on 3D absorbed dose calculations in ^{177}Lu -DOTATOC peptide receptor radionuclide therapy*. Phys Medica. 2018 Jan 1; 45:177–85.

My contribution to this paper as co-author was to participate to the design of the experiments, to perform data analysis, to write the relevant sections and review the final version of the paper.

The work described in section 4.3 is being prepared as a manuscript and will be submitted for publication as:

- Berenato S, Grassi E, Fioroni F, et al. *Development and impact of two non-rigid registration workflows for a clinical trial in Peptide Receptor Radionuclide Therapy using Monte Carlo code Simulation.*

My contribution is lead author of the manuscript, review of referenced literature, designer of the experiment and collection and analysis of the data and write initial draft.

The work described in section 5.2 is being prepared as a manuscript and will be submitted for publication as:

- Berenato S, Grassi E, Fioroni F, et al. *A novel segmentation method of neuroendocrine tumours for image-based dosimetry.*

My contribution to this work was lead author for the manuscript, design the methodology, perform all the experimental work, collect and analyse the data and write initial draft.

Part of the work described in Chapters 4 and 5 is being used to write a book chapter titled “The Raydose software for image-based dosimetry in molecular radiotherapy” with co-authors Dr. Emiliano Spezi and Dr. Nick Patterson. The chapter will be features in the book “Therapeutic applications

of Monte Carlo calculations in Nuclear Medicine” Second Edition (IoP Publishing) edited by Zaidi H.

During my PhD work I contributed to the development and enhancements of the Raydose Monte Carlo code, originally established with funding by the National Institute for Social Care and Health Research (NISCHR) Project grant no HA09-003 and EURAMET MetroMRT project (European Commission, Belgium Seventh Framework Programme, Belgium, Grant agreement no.217257 HTL11-REG1 (Spezi et al).

I contributed to general testing and quality assurance of the code, find bugs and suggest fix to the code and suggest, design and test the following new features that were implemented by the code developers:

- Implementation and evaluation of the percentage error on the Monte Carlo simulation;
- Calculation of total absorbed dose using an effective decay constant.

Since the Raydose code is not publicly available, in agreement with the Raydose project PI, a copy of the Raydose manual is included in appendix B to help the reader of this thesis to understand the functionalities of the code and the used that I made of it.

Acknowledgements

A special thanks goes to Cancer Research Wales for providing the funding for the project. This PhD would not have been possible without it.

I would like to thank my two supervisors Dr. Emiliano Spezi and Dr. Geraint Lewis for the continuous support and motivation during these three years. It has been a pleasure to work with them.

I would also like to extend my thanks to the staff of Arcispedale Santa Maria Nuova in Reggio Emilia, for their help during the experiments with the phantoms. A special thanks goes to Dr. Elisa Grassi and Dr. Federica Fioroni for transferring the huge amount of data used for this project.

A sincere thanks also goes to Dr. Concetta Piazzese who supported and put up with me for the last two years.

I am forever thankful to Joshua for his help in proof-reading this thesis. Your feedback surely improved the value of this thesis.

Finally, I would like to thank and dedicate this thesis to my family. I would not be here without them, their love and optimism.

Grazie, vi voglio bene.

List of Figures

Figure 1: Scheme of the typical steps during a treatment in MRT (3).....	3
Figure 2: Decay of the radionuclide $^{139}\text{Cesium}$ by electron capture resulting in (A) X-ray emission or (B) Auger electron emission. An electron vacancy in a shell is illustrated as an empty circle and an electron as a filled circle (5).	7
Figure 3: Annual incidence of NETs by year (1973 to 2004). This data is from the US Surveillance, Epidemiology, and End Results Program (SSER), but this pattern has also been observed in different corners of the world (18).....	11
Figure 4: Cumulative survival of patients with foregut NETs according to the grading system proposed (29).....	15
Figure 5: Radionuclide-labelled peptide binds to a receptor on cancer cell surface and enters into the cell, followed by emission of radiation that destroys DNA and cancer cell (33).....	17
Figure 6: Decay schema of ^{90}Y (45).....	19
Figure 7: Decay scheme of ^{177}Lu (49).....	21
Figure 8: Family of anthropomorphic phantoms from Oak Ridge National Laboratory (55).	30
Figure 9: Main window of OLINDA/EXM version 1 running on a Windows based virtual machine.	32
Figure 10: List of the anthropomorphic phantoms included in OLINDA/EXM version 1.....	33

Figure 11: Exponential model for organ dose calculation in OLINDA/EXM version 1.....	34
Figure 12: On the left a schematic diagram of a spiral CT scanner. On the right, a detailed scheme of a fourth-generation CT-scanner geometry (67).....	38
Figure 13: On the left a schematic diagram of detector arrays of a SPECT scanner surrounding the patient area. On the right a detailed schema of a γ -camera (67,68).....	39
Figure 14: Example of the first page of the "change" program, where it is possible to change all the components materials.....	41
Figure 15: A SPECT/CT system using a shared bed for the patient (76). ...	43
Figure 16: Basic workflow of image registration algorithms (79).	44
Figure 17: Example of a) temporal sequence, b) rigid registration and c) deformable registration for a multiple image-based clinical trial. Scans acquired at the same time point are represented by the double line connector (=). Identical registrations are represented by a double line connector, while rigid and deformable registrations are represented by the straight- and curved-line connectors respectively. NM stands for nuclear medicine image, CT for computer tomography image (106)...	56
Figure 18: Illustration of thesis structure.	62
Figure 19: Example of a particle-history: it starts with a primary photon p (straight line) via Compton interactions and pair production events leading to secondary photons p (straight lines) and secondary electrons e^- (dashed lines) and positrons e^+ (dashed-dotted line) (134).....	66

Figure 20: Example of a particle history starting with an electron (dashed line) via multiple interactions such as Møller scatter and Bremsstrahlung (134).	68
Figure 21: Example of a simulated electron path using the CH technique (134).	69
Figure 22: Same as the previous figure, but this time the random hinge method was used (134).	70
Figure 23: Electron path simulated in a non-homogeneous medium (134).	71
Figure 24: The diagram shows the class categories used by Geant4 during the simulation. Diagram was adapted from the Geant User manual.	75
Figure 25: The two Dell machines where Raydose has been developed and tested.	76
Figure 26: The scheme shows briefly how Raydose use the CT and the activity images to produce the 3D dose rate.	78
Figure 27: Overview of a 5 scans simulation showing how the individual voxel activities are used to determine the total number of decays for a given voxel (x,y,z). This figure is adapted from the Raydose manual (Appendix B).	80
Figure 28: Graphical User Interface of Raydose with the input data for the simulation of the uniform phantom.	84
Figure 29: User interface of Velocity. After the CT scans are chosen, it is possible to select the registration algorithm from a drop list. The picture shows in greyscale the CT1 taken as reference and in green-scale the CT3 ready to be co-registered.	96

Figure 30: Example of the registration process created with the MICE toolkit. Parameters of the elastix module can be modified in the settings panel aside. This also shows the node approach used in MICE.	97
Figure 31: Example of a Bland-Altman analysis is plotted.....	98
Figure 32: Example of a CT overlapping after a) rigid registration and b) non-rigid registration in axial, sagittal and coronal visualization. The CT of reference is on gray scale, the overlapped CT is on green scale.	100
Figure 33: Scheme which summarises a) the rigid registration workflow and b) the non-rigid registration workflow. The non-rigid algorithm is applied after a preliminary rigid registration.....	102
Figure 34: SSIM calculated for the six registration algorithms in four different plots for every subsequent CT acquired (CT2, CT3, CT4 and CT5). The black line indicates what is generally considered very good overlap between reference and evaluated image.	104
Figure 35: Comparison between CT1 and CT2 for case 13 using the Velocity algorithm (a and b) and the MICE toolkit (c and d) on axial and sagittal view.	105
Figure 36: Comparison between CT1 and CT3 for case 17 using the Velocity algorithm (a and b) and the MICE toolkit (c and d) on axial and sagittal view.	106
Figure 37: Sagittal view of patient 2 during CT1 (on the left) and CT5 (on the right). The lumbar support required by the patient changed the shape of the spine, causing the registration mismatch. Window level settings for CT5 were manually modified in order to show the lumbar support..	107

Figure 38: Sagittal view of the co-registration between CT1 (in greyscale) and CT5 (in green scale) for the algorithms: a) Velocity B-spline; b) Velocity rigid; c) manual; d) MICE B-spline; e) MICE rigid; f) MICE thin plate-spline.....	108
Figure 39: Difference in scan length for patient 3 during a) CT1 and b) CT5.	109
Figure 40: The boxplot reports the distribution of the percentage differences between the two registration methods for the OARs and the lesions. The y-axis has been cut off at -175% for a better legibility, for the lesions four whiskers are missing (-218.75, -233.16, -402.13, -622.78)	115
Figure 41: Bland-Altman plot for OARs and lesions. At the top of the plot are reported the reproducibility coefficient (RPC) and the coefficient of variation (CV). The dotted lines are the limits of agreement ($\pm 1.96SD$) and the solid line is the mean difference between the two approaches. All data are in Gy units.	116
Figure 42: The picture shows the example of a SPECT number 3 (in colour scale) rigidly registered (a) and non-rigidly registered (b) to the CT1 (in greyscale). The contour of the right kidney is in light green. It can be noted that in the rigid registration case, some radioactivity from the liver overlapped the kidney anatomy, which does not happen if a non-rigid registration is used.	117
Figure 43: The picture shows a) NM1 over CT1 identically registered and b) NM3 over CT1 non-rigidly registered. This mis-registration caused the outlier in the Bland-Altman plot for the dose analysis between the rigid and the non-rigid registration algorithm. Liver outline is in cyan, while stomach is outlined in red.	118

Figure 44: Details of AD workflow (left) and DD workflow (right) implemented in this study for 3D dosimetry assessment.	121
Figure 45: Time Activity Curve calculated for AD workflow (solid line) and DD workflow (dotted line).....	122
Figure 46: Boxplot with the distribution of percentage differences between AD and DD workflow for OARs and lesions.	123
Figure 47: Bland-Altman plot for OARs and lesions. At the top of the plot are reported the reproducibility coefficient (RPC) and the coefficient of variation (CV). The dotted lines are the limits of agreement ($\pm 1.96SD$) and the solid line is the mean difference between the two approaches. All data are in Gy units.	125
Figure 48: The boxplot reports the mean percentage errors for the MC calculation of each VOI.....	130
Figure 49: The boxplot reports the distribution of the differences between the two calculation methods for OARs and lesions. The plot is limited between -100% and 100% because of some whiskers $\gg 500\%$	132
Figure 50: Bland-Altman plot for OARs and lesions. At the top of the plot are reported the reproducibility coefficient (RPC) and the coefficient of variation (CV). The dotted lines are the limits of agreement ($\pm 1.96SD$) and the solid line is the mean difference between the two approaches. All data are in Gy units.	134
Figure 51: Example of how the background was outlined and analysed. The ruler tool shows the average distance between the sphere and the lesion uptake of 4.5mm.	141

Figure 52: The picture shows the Jaszack phantom simulated for the experiment with the average (on the left) and the maximum (on the right) volume of the lesions chosen for the inserts.....	142
Figure 53: Fitting plot of the experimental data using the functions: a) power with 1 term; b) power with 2 terms; c) exponential with 1 term; d) exponential with 2 terms; e)linear.....	145
Figure 54: Threshold distribution of the lesions outlined for the purpose of this work. Orange line represents the cumulative percentage distribution to the left of the point of interest.....	147
Figure 55: Histogram for the JACCARD analysis performed in this study. Orange line represents the cumulative percentage distribution to the left of the point of interest.....	148
Figure 56: Histogram of the distance in cm between the two COM in the three-dimensional space. Orange line represents the cumulative percentage distribution to the left of the point of interest.....	149
Figure 57: Collection of images showing the lesion outlined with the standard method (in red) and with the DS method (in yellow). In particular the following images are reported: a) Dose map in axial plane; b) Dose map in coronal plane; c) Dose map in sagittal plane; d) NM1 over CT1 identically registered; e) NM2 over CT1 non-rigidly registered; f) NM2 over CT1 rigidly registered; g) NM3 over CT1 non-rigidly registered; h) NM3 over CT1 rigidly registered; i) NM4 over CT1 non-rigidly registered; j) NM4 over CT1 rigidly registered; k) NM5 over CT1 non-rigidly registered; l) NM5 over CT1 rigidly registered; *)image chosen by the physician to outline the lesion.	151

Figure 58: Collection of images showing the lesion outlined with the standard method (in red) and with the DS method (in yellow). In particular the following images are reported: a) Dose map in axial plane; b) Dose map in coronal plane; c) Dose map in sagittal plane; d) NM1 over CT1 identically registered; e) NM2 over CT1 non-rigidly registered; f) NM2 over CT1 rigidly registered; g) NM3 over CT1 non-rigidly registered; h) NM3 over CT1 rigidly registered; i) NM4 over CT1 non-rigidly registered; j) NM4 over CT1 rigidly registered; k) NM5 over CT1 non-rigidly registered; l) NM5 over CT1 rigidly registered; *)image chosen by the physician to outline the lesion. 152

Figure 59: Collection of images showing the lesion outlined with the standard method (in red) and with the DS method (in yellow). In particular the following images are reported: a) Dose map in axial plane; b) Dose map in coronal plane; c) Dose map in sagittal plane; d) NM1 over CT1 identically registered; e) NM2 over CT1 non-rigidly registered; f) NM2 over CT1 rigidly registered; g) NM3 over CT1 non-rigidly registered; h) NM3 over CT1 rigidly registered; i) NM4 over CT1 non-rigidly registered; j) NM4 over CT1 rigidly registered; k) NM5 over CT1 non-rigidly registered; l) NM5 over CT1 rigidly registered; *)image chosen by the physician to outline the lesion. 153

Figure 60: The histogram reports the percentage differences of the volumes of the lesions obtained with the two methods..... 154

Figure 61: Bland-Altman plot for the volume analysis. It shows an average overestimation of 3.7 cc for the volumes obtained with the manual segmentation method..... 155

Figure 62: Histogram for the percentage differences on dose calculation.	
.....	156

Figure 63: Bland-Altman plot for the dose analysis. Plot axes are cut to improve the readability of the graph.....	157
---	-----

List of Tables

Table 1: Properties of some radionuclides of current interest in MRT.....	7
Table 2: MRT treatments currently in clinical use.	10
Table 3: Grading system suggested by the ENETS and the WHO for the classification of NETs.....	14
Table 4: Radiation weighting factors recommended by the ICRP.....	27
Table 5: Summary of the transformation models most commonly used in clinical practice. In the table, N is the number of voxels in the image...	45
Table 6: Treatment schemes suggested by the guidelines.	91
Table 7: The table reports if the differences between all the algorithms calculated using a Wilcoxon test are statistically significant (or not).	109
Table 8: The table reports the mean computational time in seconds required by each registration algorithm and its standard deviation.....	110
Table 9: The table reports the mean absorbed dose in Gy/GBq calculated with Raydose and OLINDA/EXM with its standard deviation error...	131
Table 10: The table reports the mean dose in Gy/MBq \pm the standard deviation error for some works available in literature for the absorbed dose to the kidneys. For Marin et al. the mean does is reported as [Q1;median;Q3].....	135
Table 11: Experimental data obtained from the Jaszack phantoms simulations to obtain the relationship between threshold function and Dose Peak-Background Ratio.....	143

Table 12: List of the fitting type used reporting the equation the R-squared value and the sum of squared errors (SSE).	144
---	-----

List of Acronyms

3D – Three-Dimensional

AD – Activity Deformation

AUSL-IRCSS - Azienda Unità Sanitaria Locale - Arcispedale Santa Maria

Nuova – Istituto di Ricerca e Cura a Carattere Scientifico

BED – Biological Effective Dose

Bq - Becquerel

CF – Calibration Factor

CH – Condensed History technique

COM – Centre Of Mass

CS – Clinical Standard

CT – Computed Tomography

CV – Coefficient of Variation

DD – Dose Deformation

DICOM – Digital Imaging and COmmunications in Medicine

DIR – Deformable Image Registration

DM – Dose Maps

DP:B – Dose Peak to Background ratio

DS – Dose Segmentation

EBRT – External Beam RadioTherapy

EW – Energy Window

FOV – Field-Of-View

Gy - Gray

HU – Hounsfield Unit

ICRP – International Commission on Radiological Protection

LoA – Limit of Agreement

MC – Monte Carlo

MI – Mutual Information

MIRD – Medical Internal Radiation Dose

MRT – Molecular RadioTherapy

NET – NeuroEndocrine Tumours

NM – Nuclear Medicine image

OAR – Organs At Risk

OLINDA/EXM – Organ Level INternal Dose Assessment/EXponential
Modelling

OS – Overall Survival

p.i. – post injection

PRRT – Peptide Receptor Radionuclide Therapy

Q1 – first quartile

Q3 – third quartile

RPC – ReProducibility Coefficient

SD – Standard Deviation

SPECT – Single Photon Emission Computed Tomography

SSIM – Structural SIMilarity index

SUV – Standardised Uptake Value

TAC – Time Activity Curve

T:B – Tumour-to-Background ratio

T:NT – Tumour-to-Non-Tumour ratio

VOI – Volume Of Interest

W/L – Window Level

Abstract

Peptide Receptor Radionuclide Therapy is one of the most efficient therapies against Neuroendocrine tumours. In clinical practice, absorbed dose calculations are computed based on the Medical Internal Radiation Dose (MIRD) schema which is not planned or optimised for patient-specific characteristics. This PhD project has aimed to assess the impact that advanced personalised 3D dosimetry can have within a Molecular Radiotherapy (MRT) treatment with an image-based dosimetry component. For this purpose, the impact of image registration algorithms has been studied, comparing rigid and non-rigid schemes. Results showed that non-rigid algorithms performed better than rigid equivalents in aligning images to the same frame of reference. The non-rigid algorithm was then used to investigate a workflow which involved dose maps instead of SPECT images, because such analysis has not previously been reported in the literature. Raydose, a Monte Carlo-based software package, was used to perform 3D personalised dosimetry; the results were compared against the calculations carried out with OLINDA/EXM, a MIRD-based software system. Differences were statistically significant only for kidneys and lesions ($p\text{-value} < 0.005$). Finally, a new segmentation method for tumour delineation is described and its performance compared with a manual segmentation performed by expert

physicians. JACCARD analysis showed that the two methods do not have a good overlap (mean JACCARD coefficient = 0.29). From visual assessment, the proposed approach obtained better results than the manual segmentation according to the target tissue characteristics. Furthermore, quantitative analysis showed that the manual segmentation significantly overestimates the volume by 3.7 ± 13.3 cc (p-value<0.05), while it significantly underestimates the dose by -2.67 ± 6.8 Gy (p-value< 0.05) compared to the proposed method.

This study has demonstrated the importance of assessing accurate personalised 3D absorbed dose distribution to lesions and organs at risk. It also has the potential to be extended to other MRT treatments and other tumour sites.

1. Introduction

Molecular Radiotherapy (MRT) is a modality of treatment for cancer using radiopharmaceuticals and it is defined as the delivery of radiation to malignant tissues through the interaction of the radiopharmaceutical with molecular sites and receptors. MRT has the potential to deliver larger amounts of radiation more selectively to target tissues than external-beam radiotherapy, and it is also relatively easy to use with a minimally invasive procedure and few side-effects (1,2) (Figure 1, (3)).

Molecular imaging & therapy

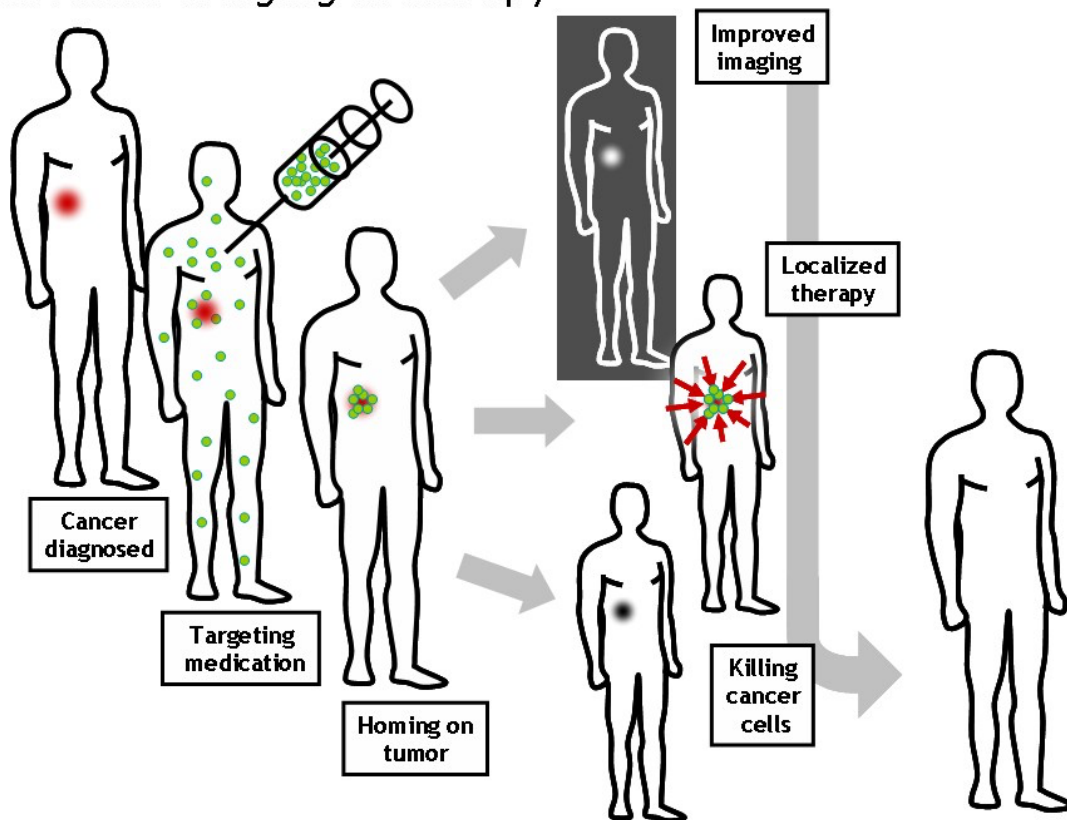


Figure 1: Scheme of the typical steps during a treatment in MRT (3).

The amount of radiation is measured by a physical quantity called “absorbed dose”, or more often just “dose”. A more detailed description of the absorbed dose is provided in Chapter 1.4.

1.1. Development of Molecular Radiotherapy

When Wilhelm Conrad Roentgen discovered X-radiation in 1895, the idea of seeing the internal structures of the human body without the use of a scalpel was revolutionary for that period. For this reason, the first application of nuclear medicine was in the field of diagnostics, analyzing structure and procedures in order to detect new diseases and potential human health issues. With day-by-day practice, the radiopharmaceuticals employed in diagnostic procedures also started being used in therapeutic applications, with the aim to destroy malignant tissues through nuclear radiation.

The majority of early treatments involved intravenous or oral administrations of the radioactive agent and consequently were referred to as systemic radionuclide therapies. These were based on the preferential uptake and protracted withholding of the radiolabelled agent by the tumour, resulting in a high tumour-to-healthy tissue dose ratio. Radioactive materials were used as biological tracers for the first time in 1924 by Georg

de Hevesy and colleagues, performing radiotracer studies of the kinetics of lead-210 (^{210}Pb) and bismuth-210 (^{210}Bi) in animals. In 1925, ^{214}Bi was used to evaluate blood flow rate in humans by Hermann Blumgart and Otto Yens. The most currently used radionuclides in MRT studies in therapeutic and diagnostic procedures, iodine-131 (^{131}I) and technetium-99m ($^{99\text{m}}\text{Tc}$) respectively, were discovered in 1938 by Emilio Segre and Glenn Seaborg (4).

After the first use of ^{131}I to treat thyroid cancer, in the early 1940s, MRT has established a small but important role in the treatment of other types of cancer. With a more and more advanced knowledge of the molecular biology of cancer, new molecular sites, receptors, and biological processes have been identified as trademarks of cancer and later as targets for MRT.

The development of new radiopharmaceuticals has increased the number of therapy options to treat cancers in curative, adjuvant, and palliative settings. Unlike the radionuclides used in the diagnostic field, which are mainly gamma ray (γ) emitters, therapeutic radionuclides emanate radiations with a high linear energy transfer to destroy tumour cells. A low emission of γ radiation is useful in order to confirm the target and to perform the calculation of the dose during the therapy. If the γ emitted are higher than 10% of the total emission, they may contribute to the whole-body dose,

bringing serious problems for the radioprotection of the patient, relatives, and staff.

Depending on the radiation they emit, radionuclides can be divided into three main categories:

- Beta emitters (β) have been and are the most commonly used type of radionuclide in clinical trials. The dose deposition has a minimum range of 200 μm up to a few millimetres.
- Alpha emitters (α) have the potential to deliver a high dose in a short range (50-90 μm). Compared to the beta-emitting radionuclides, alpha emitters have a complex decay scheme, for this reason, accurate targeting is important to avoid damage to healthy organs from a dissociated radionuclide.
- In electron capture or inner conversion radionuclides, an inner shell electron vacancy is created and subsequently filled from an outer shell electron, with the emission of an Auger electron (Figure 2.B), or low energy X-rays (Figure 2.A) (5). The range of these emissions is less than 1 μm so it is essential that the radionuclide is localised within the cell.

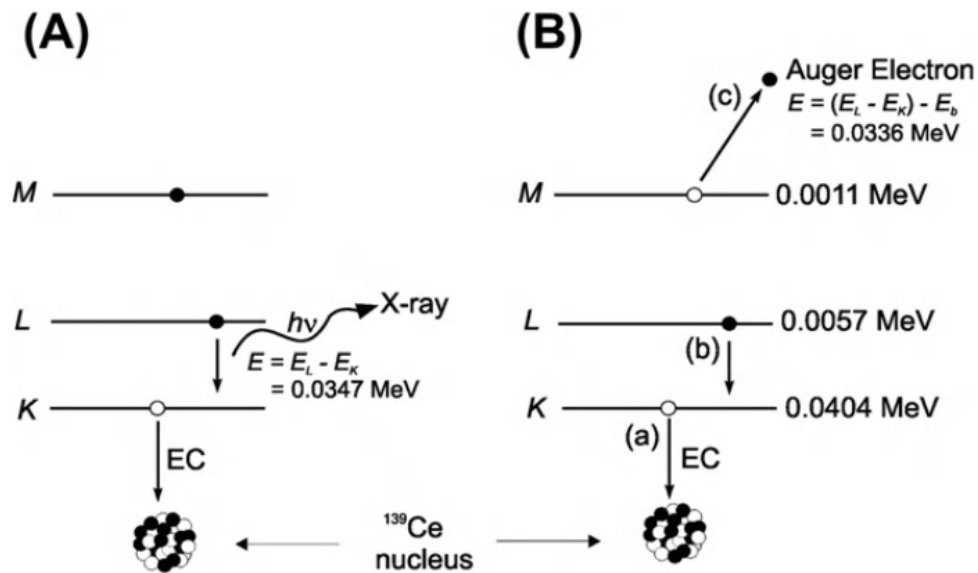


Figure 2: Decay of the radionuclide ^{139}Cs by electron capture resulting in (A) X-ray emission or (B) Auger electron emission. An electron vacancy in a shell is illustrated as an empty circle and an electron as a filled circle (5).

Properties of some radionuclides of current interest in MRT are listed in Table 1 (2).

Radionuclide	Half-life	Emission	Mean particle range
^{90}Y	2.7 d	β	5 mm
^{131}I	8 d	β	0.8 mm
^{67}Cu	2.5 d	β	0.6 mm
^{199}Au	3.1 d	β	0.3 mm
^{211}At	7 h	α	0.05 mm
^{212}Bi	1 h	α	0.05 mm
^{125}I	60 d	Auger	$\sim 1 \mu\text{m}$
^{77}Br	2.4 d	Auger	$\sim 1 \mu\text{m}$

Table 1: Properties of some radionuclides of current interest in MRT.

1.2. MRT treatments and incidence of tumours

The main application of MRT has been the treatment of thyroid cancer with ^{131}I since the 1940s and it is used worldwide (6). In 2015, it was the 20th most common cancer in the UK, with 3528 cases documented and 382 deaths registered in 2016 (7). A small amount of the radiopharmaceutical is administered orally to the patient and it passes into the bloodstream via the gastrointestinal tract and then preferentially absorbed from the blood by the thyroid gland. Radioactive Iodine therapy is also a treatment for an overactive thyroid (hyperthyroidism).

Breast cancer is the most common cancer in the UK, accounting for 15% of all new cancer cases. There are 55000 cases every year, with a 10-year survival rate of 78% (11563 deaths registered in 2016) (7). Nowadays (in certain instances) breast cancer may be treated using agents involving indium-111 (^{111}In) (8).

Tumours from haematological tissues are a heterogeneous group that include different disorders: lymphomas, leukaemias and myelomas. Radioisotopes such as phosphorus-32 (^{32}P) and iron-57 (^{57}Fe) were first used in the 1940s to treat leukaemia. Since then, many new agents for haematological proliferations have been introduced successfully but currently ^{32}P remains the preferred treatment option for these disorders (9).

In 2015, 9900 cases of leukaemia were registered in UK and 4712 cases of death in 2016. For this type of tumour there is no licensed MRT agent, but the antibody anti-CD25 labelled with ^{131}I or yttrium-90 (^{90}Y) is the most currently used (1,10). There are different types of lymphoma, but the most common are the non-Hodgkin's lymphomas (NHL) and the Hodgkin's lymphomas (HD). There were 13682 new cases of NHL and 2110 of HD in the UK in 2015, with 4920 and 304 deaths respectively registered in 2016 for these categories. Myelomas are relatively uncommon with around 5700 new cases registered every year and 3000 deaths (7).

Lung cancer is the 3rd most common cancer and it accounts for the 13% of all the cancers diagnosed in the UK. There are around 46,700 new lung cancer cases in the country every year with a survivability of 5% (35620 deaths registered in 2016) (7). MRT treatments for this tumour may use somatostatin analogues traced with rhenium-88 (^{88}Rh) (11).

Bone metastases are experienced by up to 90% of the patients with castration-resistant prostate cancer. Patients are commonly treated with radium-223 (^{223}Ra) radiopharmaceuticals (12,13); however, in the UK, two different commercial products are also in relatively common use: strontium-89 (^{89}Sr) chloride (14) and samarium-153 (^{153}Sm) lexidronam (15).

A schema of all MRT treatments currently in clinical use is provided in Table 2 (16).

Nuclide	Chemical	Indication
¹⁹⁸ Au	colloid	Malignant disease
¹³¹ I	Iodide	Thyroid
³² P	PO4---	Polycythaemia vera
⁸⁹ Sr	chloride	Bone metastases
¹³¹ I	mIBG	Neuroendocrine disease
³² P	colloidal chromic phosphate	Cystic intracranial lesions
³² P	PO4---	Leukaemia
¹³¹ I	lipiodol	Hepatic malignancy
⁹⁰ Y	microspheres	Hepatic malignancy
¹⁵³ Sm	EDTMP	Bone metastases
¹⁸⁶ Re	HEDP	Bone metastases
⁹⁰ Y	DOTATOC	Malignant diseases
⁹⁰ Y	ibritumomab tiuxetan (Zevalin) ®	Non-Hodgkin's lymphoma
²²³ Ra	dichloride	Bone metastases in castration-resistant prostate cancer
¹⁷⁷ Lu	DOTATATE	Neuroendocrine tumours
⁹⁰ Y	DOTATATE	Neuroendocrine tumours
⁹⁰ Y	DOTANOC	Somatostatin expressing tumours
¹¹¹ In	DTPA-hEGF	Breast Cancer
¹⁷⁷ Lu	DOTATOC	Neuroendocrine tumours
¹⁷⁷ Lu	DOTANOC	Somatostatin expressing tumours
¹⁷⁷ Lu	DOTA-HH1	Non-Hodgkin's B-cell lymphoma

Table 2: MRT treatments currently in clinical use.

1.3. Neuro Endocrine Tumours

Neuroendocrine tumours (NETs) are rare tumours responsible for approximately 0.5% of all cancers (17). The incidence is continuously on the rise (Figure 3, (18)) due in part by the improvement in the imaging modalities and a better understanding of this tumour; it is approximately 5.86/100,000 per year in the US with 2.5 female patients for every 1 male (19,20).

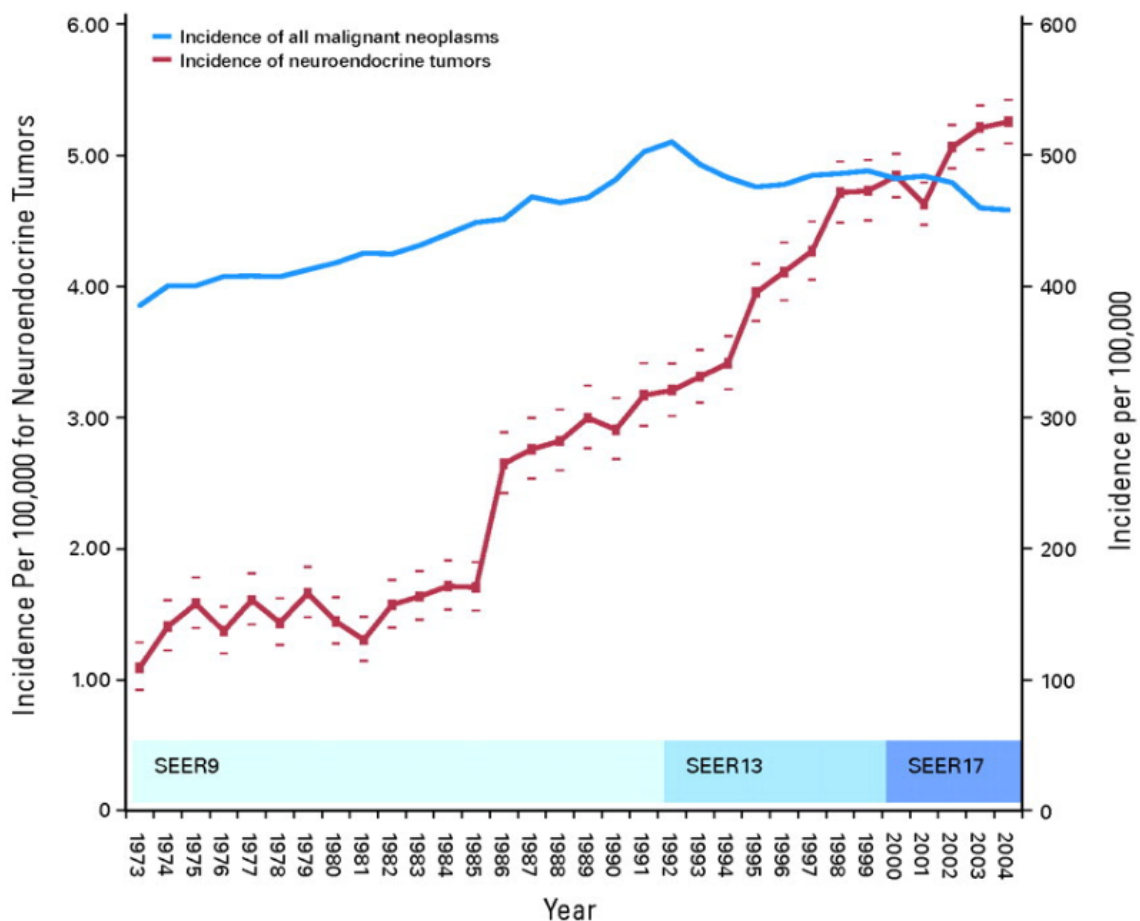


Figure 3: Annual incidence of NETs by year (1973 to 2004). This data is from the US Surveillance, Epidemiology, and End Results Program (SSER), but this pattern has also been observed in different corners of the world (18).

Around 3,000 cases are diagnosed every year in the UK and around 100,000 cases in the United States (21). The 5-year overall survival (OS) for all NETs is 67.2% (22), while the 10-year OS rate is 46.5% (23), a low OS when compared with the most common cancer in the UK (breast cancer, 10-year OS: 78%).

NETs are an epithelial heterogeneous group of neoplasms with predominant neuroendocrine differentiation. The system affected by the NETs is the neuroendocrine system, that is mainly composed of the hypothalamus and pituitary gland and it has the role to regulate the production of hormones in the bloodstream. In particular, this system maintains an optimal level of hormone secretion for normal body functions, such as blood pressure, reproduction, metabolism, energy utilization and eating and drinking behaviour. The neuroendocrine system also regulates the production of the growth hormone (GH). This hormone is necessary for cells to grow in size, increasing protein synthesis, reduction of liver uptake of glucose, stimulation of the immune system, and more. Release of GH is determined by the balance of two peptides: growth hormone-releasing hormone (GHRH) and somatostatin (growth hormone release inhibiting factor), which is controlled by stimulators (slow-wave sleep, exercise, nutrition) and inhibitors (hyperglycaemia and free fatty acids). Somatostatin also inhibits

a variety of physiological functions in the gastrointestinal tract, such as gastrointestinal motility, gastric acid production, pancreatic enzyme secretion, bile secretion and colonic fluid secretion. It also inhibits the secretion of pancreatic and intestinal hormones. More generally, the neuroendocrine system controls the entire spectrum of human behaviour including the fine and gross motor movements, language, affective (relating to the emotions) and cognitive behaviour (relating to thinking), and sociosexual function & behaviour. (24)

This type of tumour can arise in most organs, but largely in the gastrointestinal tract (gut, 62-67%) and lungs (22-27%) (19). NETs that develop in the gut and pancreas are usually grouped together and called gastroenteropancreatic neuroendocrine tumours or simply GEP-NETs.

NETs are variable in their presentation and may be divided into two subgroups based on their symptoms (25):

- Functioning tumours release a large number of peptide hormones and bioactive substances into the bloodstream that can lead to clinical symptoms such as flushing, diarrhoea or hypoglycaemia;
- Non-functioning tumours are more common, and they have no specific clinical symptoms.

These tumours develop slowly over the years and in earlier stages of the disease, patients present non-functioning tumours with no signs or vague symptoms (26). For this reason, it is difficult to early diagnose NETs and they are often misdiagnosed as other gastrointestinal disorders. The correct diagnosis is then delayed by several years by which time the primary tumour has already metastasized.

NETs were traditionally classified according to their embryonic origin:

- Foregut NET: lung and respiratory tract, stomach, duodenum;
- Midgut NET: small bowel, appendix, proximal colon;
- Hindgut NET: transverse colon, descending colon and rectum.

In 2007, the European Neuroendocrine Tumour Society (ENETS) proposed a grading system for all the NETs based on mitotic count and Ki-67 labelling index (27). In 2010, this system was modified and incorporated into the one proposed by the World Health Organization (WHO) (28). The new scheme is summarised in Table 3.

Grade	Mitotic count (for 10 High-Power Field)	Ki-67 index
GX	Grade cannot be assessed	
G1	<2	<3%
G2	2-20	3%-20%
G3	>20	>20%

Table 3: Grading system suggested by the ENETS and the WHO for the classification of NETs.

These two parameters are not always concordant. For this reason, it is recommended that the higher of the two should be used to assign the grade. The survival and the prognosis have been demonstrated to be mainly dependent on the grade of the tumour (29) as shown in Figure 4.

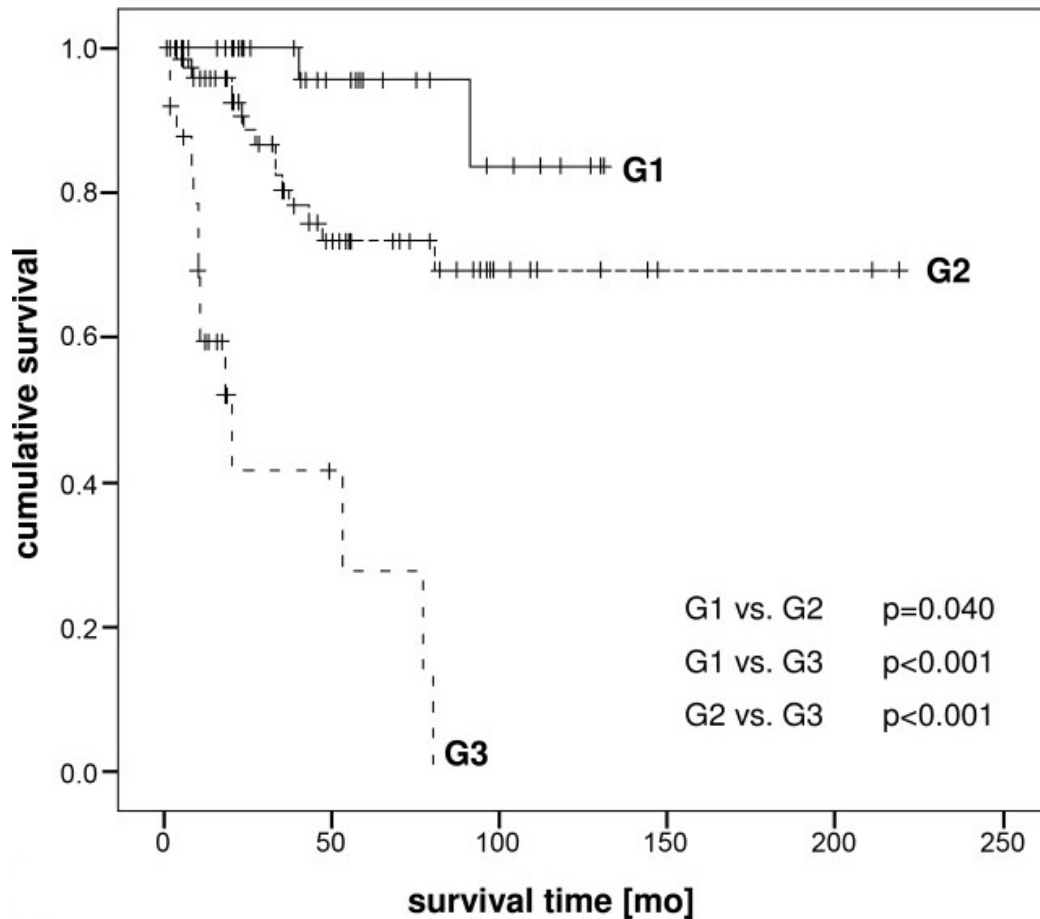


Figure 4: Cumulative survival of patients with foregut NETs according to the grading system proposed (29).

1.3.1. Peptide Receptor Radionuclide Therapy

Peptide Receptor Radionuclide Therapy (PRRT) is currently the most effective MRT treatment against NETs. It is presently also used for prostate and pancreatic tumours. (30–32) PRRT is the systemic administration of a targeted radionuclide in order to achieve important clinical outcomes such as improved quality of life, disease stabilization and improved OS.

As Figure 5 (33) shows, in this therapy, a cell-targeting protein (or peptide) called octreotide is combined with a radioactive material, or radionuclide, creating a type of radiopharmaceutical called a radiopeptide (Figure 5.A). When injected into the patient's bloodstream, this radiopeptide travels to (Figure 5.B) and binds to neuroendocrine tumour cells (Figure 5.C), delivering a high dose of radiation to the cancer cell (Figure 5.D), destroying it (Figure 5.E).

The cell-targeting protein is a laboratory-made version of the somatostatin hormone that binds receptors onto the surface of NETs.

In fact, NET cells express a high density of somatostatin receptors on their surface.

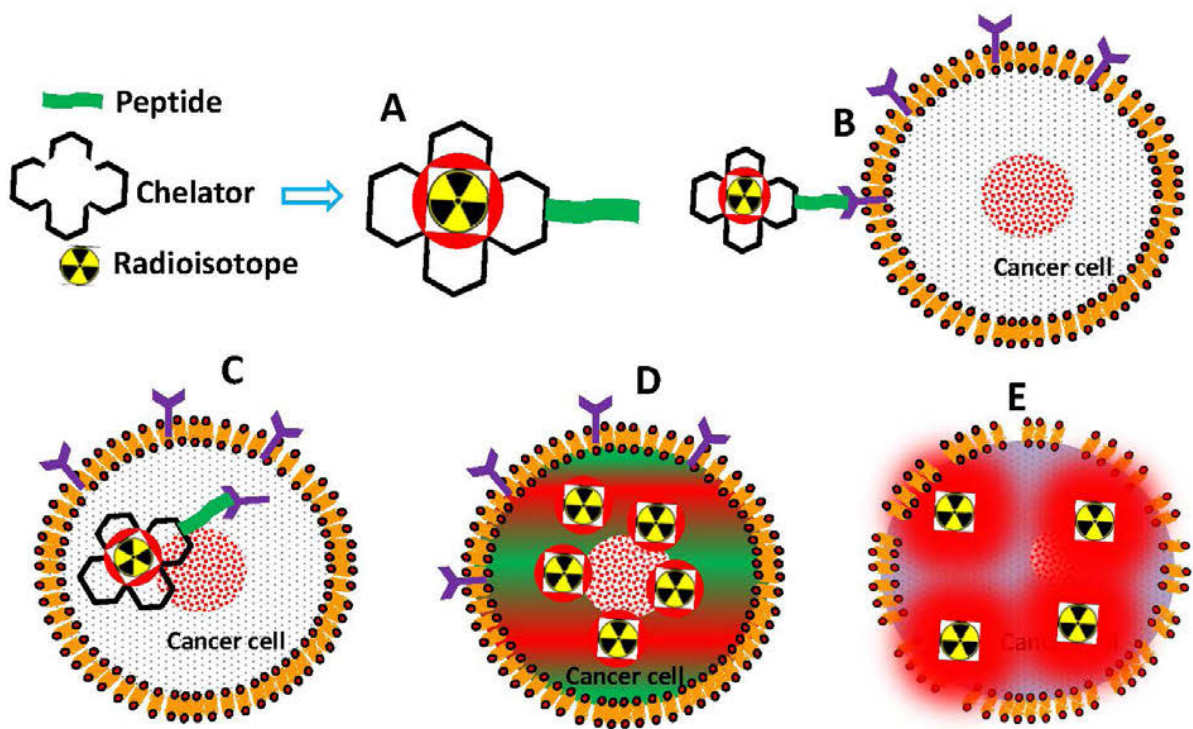


Figure 5: Radionuclide-labelled peptide binds to a receptor on cancer cell surface and enters into the cell, followed by emission of radiation that destroys DNA and cancer cell (33).

Five somatostatin receptors (sst) subtypes have been cloned and characterised (sst₁, sst₂, sst₃, sst₄ and sst₅), but sst₂ predominance is generally found on NET surfaces. The sst₁ and sst₄ receptors do not bind to somatostatin analogues, whereas sst₂, sst₃ and sst₅ receptors display a high, low, and moderate affinity respectively. The predominant expression of sst₂ receptors on NETs forms the basis for the successful clinical application of somatostatin analogues in MRT (34).

In PRRT, there are two widely used somatostatin analogues: [DOTA⁰-Tyr³]octreotide (DOTATOC) and [DOTA⁰-Tyr³]octreotate (DOTATATE). There are several studies in the literature which analyse the efficacy and the

safety of these peptides (35–40). In general, the affinity of the DOTATATE for the sst₂ receptors was found to be higher than the DOTATOC, but this has the lowest kidney uptake compared to the other peptide (41), as also reported in several works (42–44). The most commonly used radionuclides to be combined with the somatostatin analogues are ⁹⁰Y and lutetium-177 (¹⁷⁷Lu). This thesis work is based on the DOTATER clinical trial (cf. Chapter 3) and the somatostatin analogue used was the DOTA⁰-Tyr³-OCtreotide (DOTATOC).

1.3.1.1. Yttrium-90

Yttrium-90 (⁹⁰Y) is a radioisotope of the 39th element of the periodic table with a half-life of 2.6 days. It emits only beta particles with a maximum energy of 2278 keV (99.98%), decaying into Zirconium-90 (⁹⁰Zr) (Figure 6) (45). Its half-life is comparable with the pharmacokinetics of many tumour targeting molecules (46).

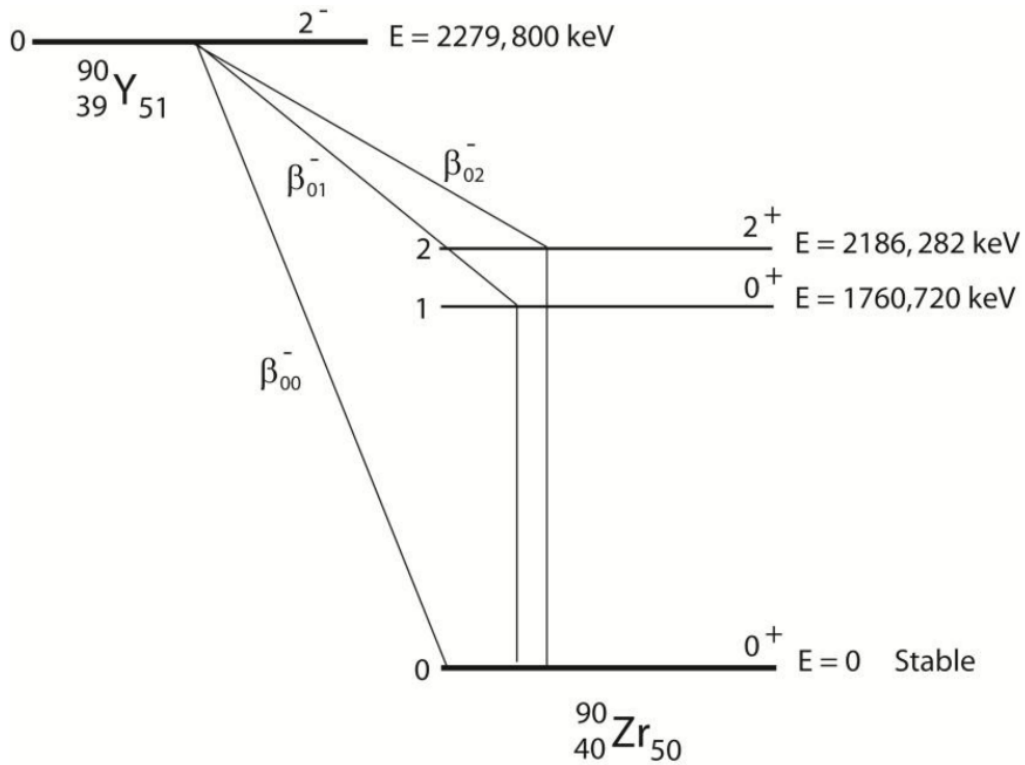
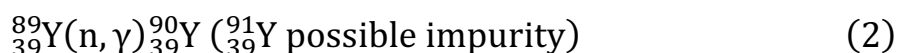
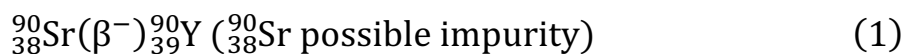


Figure 6: Decay schema of ^{90}Y (45).

Along with the PRRT, ^{90}Y can be used in radioimmunotherapy to treat the Non-Hodgkin's lymphoma and in trans-arterial radioembolization therapy to treat hepatocellular carcinoma and metastatic colorectal cancer. In radioimmunotherapy, monoclonal antibodies marked with ^{90}Y are used as targeting vehicles to selectively deliver radionuclides to cancer cells (47). In radioembolization therapy, instead, microspheres ($25 \mu\text{m}$ to $35 \mu\text{m}$ of diameter) loaded with ^{90}Y are delivered to the capillary bed of the tumour via injection into the hepatic artery.

Yttrium-90 can be produced in different ways, but mainly with the following nuclear reactions:



Usually, a radionuclide generator consists of a chromatographic column into which the parent radionuclide is loaded (${}^{90}_{38}\text{Sr}$ in this case), with the daughter radionuclide being eluted using either aqueous or organic eluents. ${}^{90}\text{Y}$ produced in nuclear reactors contains more impurities (in particular ${}^{88}\text{Y}$ and ${}^{91}\text{Y}$), while ${}^{90}\text{Y}$ produced with ${}^{90}\text{Sr}/{}^{90}\text{Y}$ commercial generators may contain measurable traces of ${}^{90}\text{Sr}$ (48). ${}^{90}\text{Y}$ used in this study is produced by PerkinElmer, with a patented process exclusively licensed to them to extract the radionuclide from ${}^{90}\text{Sr}$. It is a proprietary process in compliance with the Good Manufacturing Practice Guidance for Active Pharmaceutical Ingredients (August 2001) and it is stated to have a high purity with a low level of contaminants. This radionuclide is provided to the hospital on a fortnight basis and it is certified to have a radio-nuclidic purity >95%; chemical impurities including Zn, Fe, Cu and Pb are < $0.5\mu\text{g}/\text{GBq}$ and the detected ${}^{90}\text{Sr}$ impurities are < $10^{-5}\%$.

1.3.1.2. Lutetium-177

Lutetium-177 (^{177}Lu) is a non-stable radioisotope of the 71st element in the periodic table. Its half-life of 6.7 days for decay to ^{90}Y (2.7 days) has different radiobiological implications for both tolerability and tumour response (30). It emits beta particles of 490 keV with a probability of 78.6%, decaying to stable Hafnium-177 (^{177}Hf) in the ground state.

In the remaining 21.4% of cases, the de-excitation of ^{177}Hf emits gamma rays of 113 keV (6%) and 208 keV (11%) that are intensive enough to be detected by a gamma-camera and used also for diagnostic imaging. This decay process is shown in Figure 7 (49).

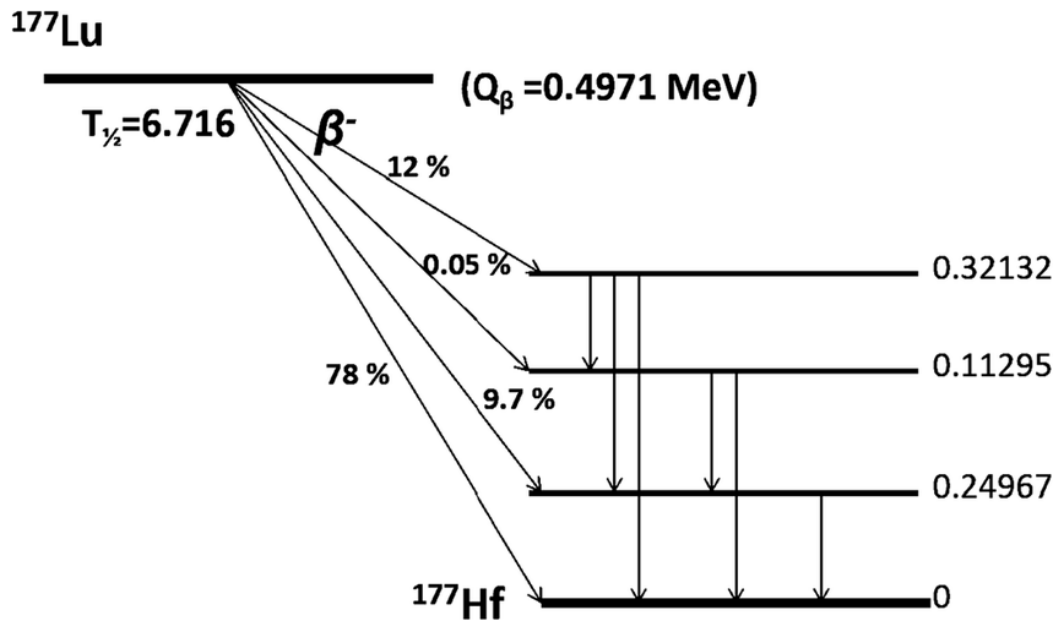
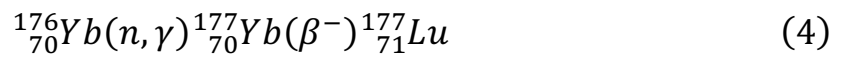


Figure 7: Decay scheme of ^{177}Lu (49).

This radionuclide can be also used for the treatment of the metastatic castration resistant prostate cancer (Prostate Specific Membrane Antigen

therapy). Analogously to PRRT, ^{177}Lu is bonded to a molecule which travels to and binds with the receptors overexpressed by the prostate cancer cells.

It may be produced from the irradiation of ^{176}Lu or ytterbium-176 (^{176}Yb) with neutrons:



The direct process arising from reaction (3) is less expensive and technically less demanding than that from reaction (4), but only 25% of the atoms produced are ^{177}Lu , the other 75% consists of a product mixture of nonradioactive contaminating $^{175/176}\text{Lu}$ atoms. The indirect process from reaction (4) is more expensive and produces more radioactive waste, but it offers the potential to provide ^{177}Lu of the highest possible radionuclide purity. From this process, the presence of long-lived radioactive impurities ($^{177\text{m}}\text{Lu}$) is precluded and below the detection limit ($<10^{-5}\%$) (49).

The ^{177}Lu used in this work is produced by Isotopen Technologien Munich AG using reaction (4), while the DOTA⁰-Tyr³-OCtreotide (DOTATOC) peptide is marked by chemists in Azienda Unità Sanitaria Locale - Arcispedale Santa Maria Nuova – Istituto di Ricerca e Cura a Carattere Scientifico di Reggio Emilia, Italy (AUSL-IRCCS). It arrives fresh at the hospital on a fortnightly basis and the certificate of analysis which comes

with the vial states a radio-nuclidic purity of 99.99%. Sum of chemical impurities (including Fe, Cu, Zn, Pb and ^{176}Yb) is certified to be $\leq 0.5 \mu\text{g}/\text{GBq}$. The vial also contains traces of radioactive impurity of $^{175}\text{Yb} \leq 0.01\%$. Sum of other radio-nuclidic impurities is also certified to be $\leq 0.01\%$. No traces of $^{177\text{m}}\text{Lu}$ were found.

1.4. Dosimetry calculation in MRT

In MRT, the aim of dosimetry is to assess the radiation dose absorbed by organs and tissues of patients undergoing treatment with an internal administration of radiopharmaceutical in order to evaluate the benefits of the therapy against the risk of possible complications (50).

1.4.1. Fundamental concepts and units

In nature, radioactive materials decay according to a first-order kinetic:

$$dN = -\lambda N \cdot dt \quad (5)$$

where N is the number of radioactive nuclei, dN is the change of this number per unit of time dt and λ is the probability of decay per nucleus per unit of time. This decay constant λ is specific for each decay mode of each nuclide. The radioactivity (or decay rate) A is defined as the number of disintegrations per unit time:

$$A = -\frac{dN}{dt} = \lambda N \quad (6)$$

By the integration of this relation and applying the initial boundary condition that at $t = 0$ follows that $A = A_0$, the equation of an exponential decay is obtained:

$$A(t) = A_0 e^{-\lambda t} \quad (7)$$

Therefore, if we consider a radioactive material in a human body, it is necessary to consider different first-order processes: the radioactive decay and the biological 'wash-out'.

For this reason, the effective decay constant (λ_e) may be used, described as the sum of the physical decay constant (λ_p) plus the biological decay constant (λ_b):

$$\lambda_e = \lambda_b + \lambda_p \quad (8)$$

The amount of radiation emitted by the radionuclide and absorbed by the patient is identified by the absorbed dose.

In physical terms, dose is defined as the energy absorbed per unit mass of any material as follows:

$$D = \frac{d\varepsilon}{dm} \quad (9)$$

where $d\varepsilon$ is the incremental energy of the radiation imparted to the matter in a volume of mass dm . The unit of absorbed dose is J/kg, or in medical

applications Gray (Gy). The dose absorbed by a volume of mass m may depend upon different factors, such as the amount of activity present, the particles emitted and their energy.

For this reason, it is possible to develop a formula for the dose rate:

$$\dot{D} = \frac{kA \sum_i y_i E_i \phi_i}{m} \quad (10)$$

where \dot{D} is the absorbed dose rate, A is the activity, y is the number of radiations i with energy E , ϕ is the fraction of energy emitted and absorbed by the volume of mass m and k is a proportionality constant. To obtain the cumulative dose absorbed by the patient, it is necessary to integrate the quantities that have a time-dependence, in this case the activity A .

Therefore, the equation for the dose is as follows:

$$D = \frac{k\tilde{A} \sum_i y_i E_i \phi_i}{m} \quad (11)$$

where D is the absorbed dose and \tilde{A} is the number of nuclear decays or cumulated activity. The residence time τ , instead, is defined as the cumulated activity divided by the administered activity A_0 :

$$\tau = \frac{\tilde{A}}{A_0} \quad (12)$$

On the other hand, the equivalent dose H is defined to take account of the effect or the damage that a particular radiation can produce in a tissue:

$$H_{T,R} = w_R D_{T,R} \quad (13)$$

where $D_{T,R}$ is the dose delivered by the radiation R to a tissue or an organ T and w_R is the weighting factor of the radiation R . The values for w_R recommended by the International Commission on Radiological Protection (ICRP) are showed in Table 4.

Type of radiation	w_R
Photons, electrons and muons	1
Neutrons ($E < 10 \text{ keV} \vee E > 20 \text{ MeV}$) Protons ($E > 2 \text{ MeV}$)	5
Neutrons ($10 \text{ keV} < E < 100 \text{ keV} \vee 2 \text{ MeV} < E < 20 \text{ MeV}$)	10
Alpha particles, heavy nuclei, fission fragments Neutrons ($100 \text{ keV} < E < 2 \text{ MeV}$)	20

Table 4: Radiation weighting factors recommended by the ICRP.

When β^- particles are considered, the equivalent dose H is identical to the absorbed dose D .

The ICRP has also developed two different dosimetry systems to protect radiation workers, but also applicable to nuclear medicine workers.

In the ICRP II system (51), the following equation for equivalent dose rate is found:

$$H = \frac{51.2 * A * \sum_i y_i \phi_i w_{Ri}}{m} \quad (14)$$

The constant 51.2 is k from the Eq. (11). In the ICRP 30 system (52), the equivalent cumulative dose is given:

$$H = \frac{1.6 * 10^{-6} * \sum_S U_S \sum_i y_i \phi_i (T \leftarrow S) w_{Ri}}{m_T} \quad (15)$$

where T is the target, S is the source of the radiation U_S is another term for cumulated activity and the factor $1.6*10^{-6}$ is again k .

1.4.2. MIRD schema

The Medical Internal Radiation Dose schema (MIRD) was originally developed by the Society of Nuclear Medicine and provides data and algorithms to calculate the average absorbed dose by tumours and healthy organs and tissues (53).

According to the MIRD schema, the absorbed dose is calculated as the product of two factors: a biological and a physical component. The first one includes the distribution and the kinetic parameters of the radiopharmaceutical (cumulated activity \tilde{A}), while the physical component

includes the properties of the radionuclide and the geometries of the target r_T and the source r_S (S-value):

$$D(r_T \leftarrow r_S) = \sum_S \tilde{A}_S S(r_T \leftarrow r_S) \quad (16)$$

$S(r_T \leftarrow r_S)$ is called S-value and represents the time independent physical component, expressed as follows:

$$S(r_T \leftarrow r_S) = \frac{k \sum \Delta_i \phi_i(r_T \leftarrow r_S)}{m} \quad (17)$$

where Δ_i is the mean energy emitted from the i radiation, ϕ_i is the energy absorbed by the target r_T and emitted by the source r_S and m is the mass of the target. The absorbed fraction ϕ_i depends on the type and energy of the emitted radiation and on the size and relative positions on the sources and targets. S-values have been evaluated for several radionuclides and different configurations of sources and targets (54), but they can also be calculated using the MIRDose software package or with analytical methods.

In the S-value definition, there is the assumption that the volume of the object remains constant; however, following the treatment, the tumour volume generally decreases, so the S-value should increase.

Furthermore, the mass of the subject is typically unknown; for organs and tissues it is usually estimated from anthropomorphic phantoms (Figure 8) (55) while tumours are usually evaluated from different imaging modalities (SPECT, PET or CT).

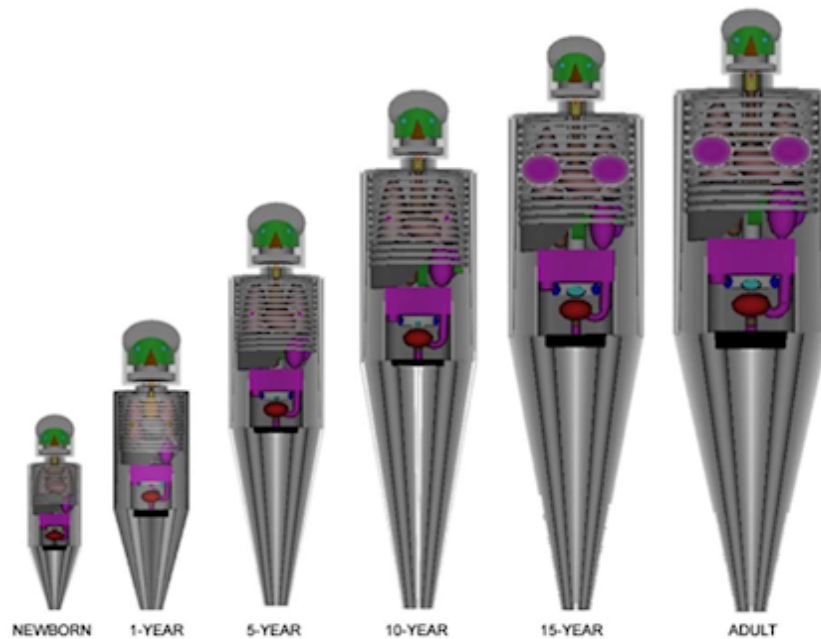


Figure 8: Family of anthropomorphic phantoms from Oak Ridge National Laboratory (55).

Traditionally, the MIRD schema have been applied to each organ or major component of an organ assuming an uniform radioactivity distribution (56). In reality, radiopharmaceuticals have an inhomogeneous distribution, especially in tumours which often have necrotic zones, calcification or fibrosis where the radiation cannot penetrate (57). However, there is nothing intrinsic in the MIRD schema that precludes extension to smaller regions (i.e. voxels) (56). Patient-specific sub-organ dosimetry has become more feasible after the development of accurate, three-dimensional

anatomic (MRI and CT) and physiologic (PET and SPECT) imaging devices, and more accurate methods of dose calculation (e.g. Monte Carlo radiation transport) (56).

In the following section, a code developed for dose calculation at the organ level commonly used in clinical practice is described. The application of the MIRD formalism at the voxel level is described in section 1.4.3, along with the description of the elements to perform an image-based dosimetry.

1.4.2.1. OLINDA/EXM

Organ Level Internal Dose Assessment/EXponential Modelling (OLINDA/EXM) version 1 is a code developed by Michael Stabin in 2004 for calculating organ and effective doses in nuclear medicine studies (58).

OLINDA is based on the MIRDOSE personal computer software (59) developed in the early 1990s which was able to automate and standardize internal dose calculations for nuclear medicine studies. OLINDA (Figure 9) uses the RADAR method of dose calculation (60) and the dose conversion factors are available on the RADAR website¹.

¹ <http://www.doseinfo-radar.com/OLINDA.html>

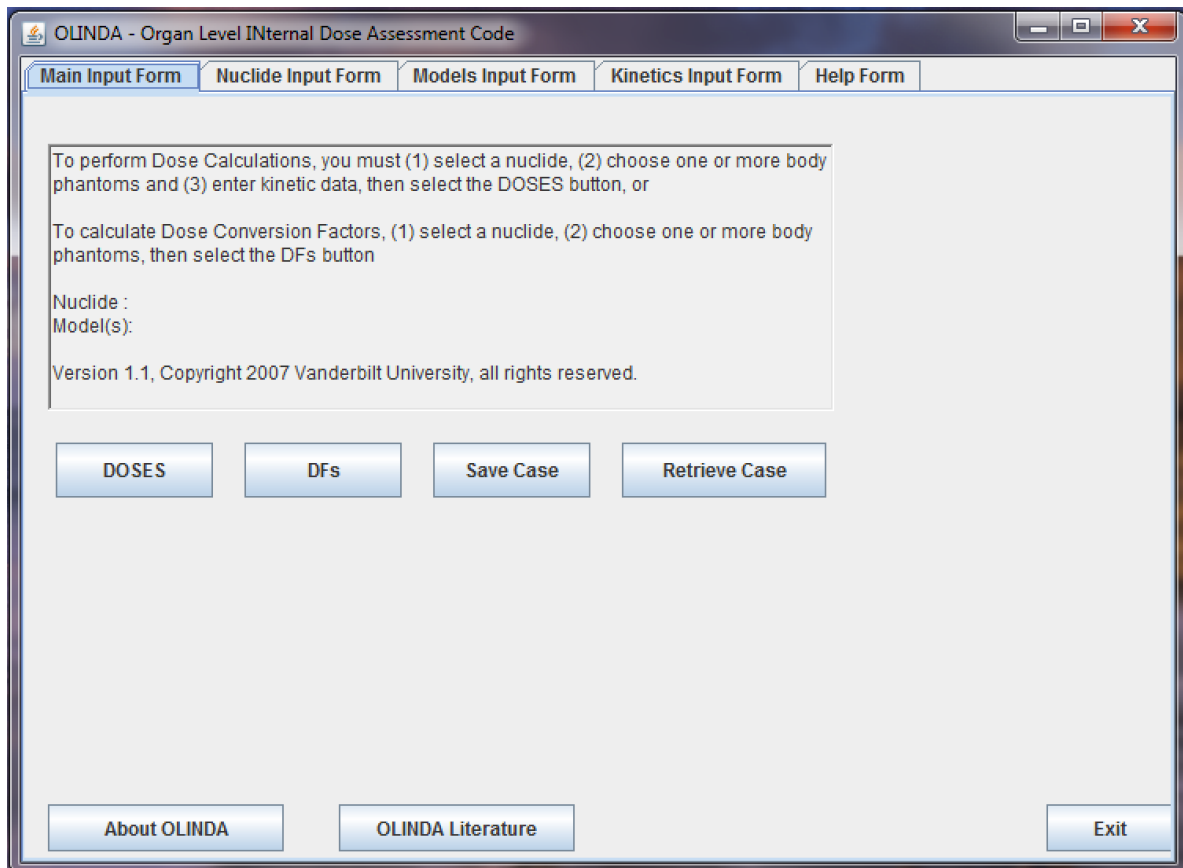


Figure 9: Main window of OLINDA/EXM version 1 running on a Windows based virtual machine.

Compared to the MIRDose software, OLINDA uses the same calculating system, but it has been updated with new anthropomorphic phantoms (Figure 10), new radionuclides, an improved bone model, the possibility to modify the organ masses to patient-specific values and a code for analysis of biokinetic data.

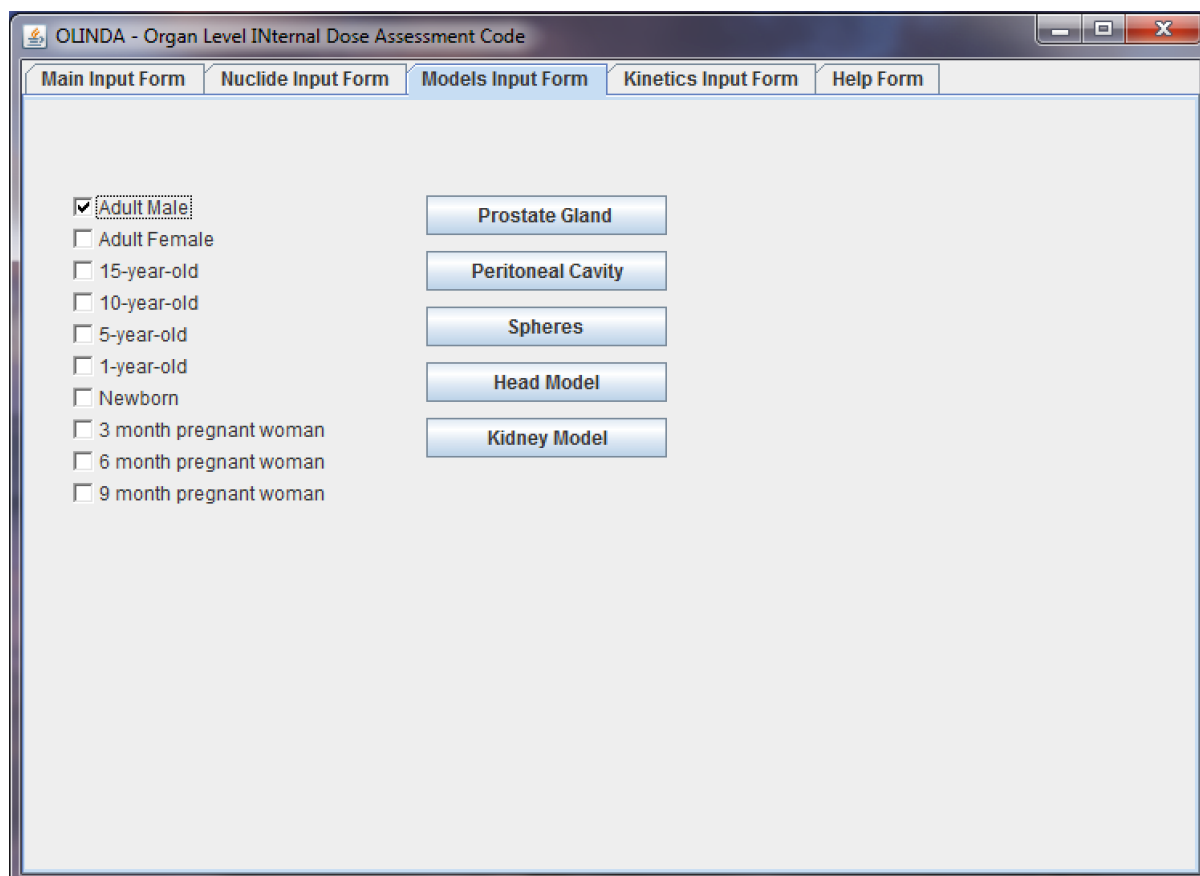


Figure 10: List of the anthropomorphic phantoms included in OLINDA/EXM version 1.

This code was developed by Drs Sparks and Crowe of CDE, Inc. and it allows one to calculate the dose from activity data with a mono-, bi-, or tri-exponential fit model. As shown in Figure 11, users may enter up to 10 sampling times and measured activity values (in %) at the top right of the window. The exponential model is chosen by ticking one to three exponential terms, each of them with two parameters: the coefficient (A, B and C) and the rate constant (a, b and c). In the code, a non-linear regression is used to converge to a minimum in the error function, based on the initial estimate of the parameters supplied by the user. On the left part of the

window, the result of the fit in decimal (top left) and logarithmic (bottom left) scale is shown.

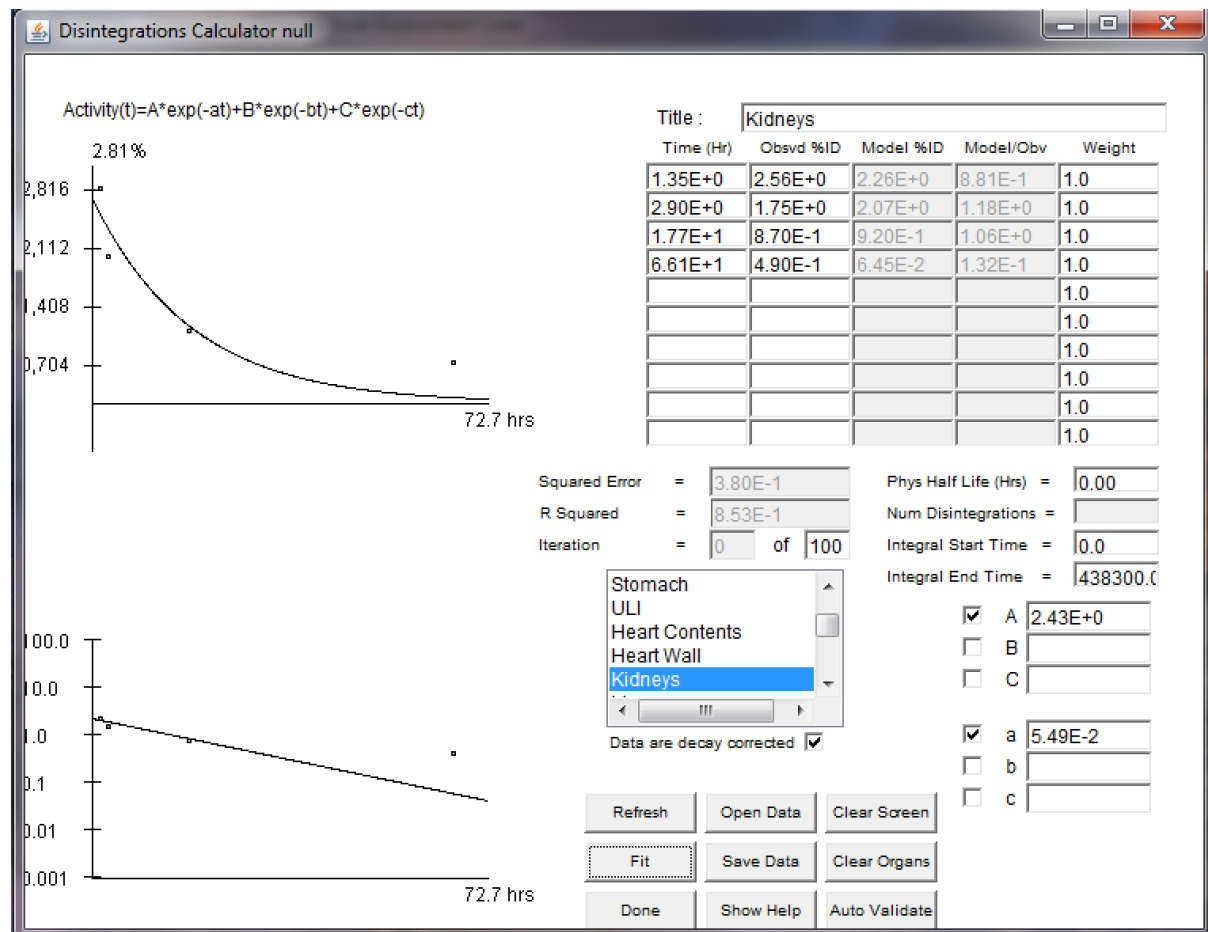


Figure 11: Exponential model for organ dose calculation in OLINDA/EXM version 1.

For tumour dosimetry, the approach is based on a spherical model that assumes that tumours are isolated unit density spheres in an infinite unit density medium (61). The S-values for this simplistic spherical model have been pre-calculated based on an evaluation of electron- and photon-absorbed fractions in spheres of various sizes from Stabin *et al.* (62). These S-values cannot be evaluated for each tumour, because the organ-to-tumour

dose (cross-dose) depends almost exclusively on the proximity of tumour relative to the organ and because the locations of the tumours are arbitrary. For this reason, doses estimated from this approach account only for the self-dose² and not for any cross-dose from any extra-tumour activity (61).

1.4.3. Image-based dosimetry

The last decades have seen a great increase in imaging of patients in order to obtain anatomic and physiologic information. This information is obtained from magnetic resonance imaging (MRI) or computed tomography (CT) and is expressed in three-dimensions with a typical resolution of 1 mm. Information about physiology is obtained from positron emission tomography (PET) or single photon emission tomography (SPECT), also displayed a 3D distribution with a resolution between 5 and 10 mm. Nowadays, new systems with CT or MRI combined with SPECT or PET are used in order to obtain both anatomic and radiopharmaceutical information with a single imaging session without moving the patient.

² Self-dose is the dose deposited in a source tissue by the radioactive decays occurring within it.

1.4.3.1. Voxel dosimetry

MIRD pamphlet no. 17 (56) describes a voxel (volumetric picture element) based method where the absorbed dose is calculated from a matrix of small volumes, taking into account the non-homogeneous activity distribution in the tissues. Voxel-dosimetry calculates the absorbed dose distribution from a tomographic imaging procedure such as SPECT or PET; the dimension of the voxels depends on the resolution of the scanner and on the field-of-view (FOV) of the gamma-camera used to acquire the images.

Following the MIRD schema, the mean dose in the voxel target is calculated analogously as (16):

$$D(T \leftarrow S) = \sum_S \tilde{A}_S S(T \leftarrow S) \quad (18)$$

where T and S are respectively the target and the source voxel.

$S(T \leftarrow S)$ is the S-value at the voxel level, defined analogously as (17):

$$S(T \leftarrow S) = \frac{k \sum \Delta_i \phi_i(T \leftarrow S)}{m} \quad (19)$$

where Δ_i is the mean energy emitted from the i radiation, ϕ_i is the energy absorbed by the voxel target T and emitted by the voxel source S and m is the mass of the voxel. Nowadays, voxel-dosimetry is not largely used in clinical practice, but some research groups are developing their own

software or code for this dosimetric calculation (STRATOS (63), Jada (64), Raydose (65), Mr. Voxel (66)).

S-values at the voxel level are listed in (56), but only for 5 radionuclides (^{32}P , ^{89}Sr , ^{90}Y , $^{99\text{m}}\text{Tc}$, ^{131}I) and for 2 cubic voxel dimensions (3 and 6 mm).

1.4.3.2. CT and SPECT

Computed tomography (CT) is a computerized x-ray imaging procedure in which a fan beam of x-rays is aimed at a patient and quickly rotated around the body, producing signals that are processed by the machine's computer to generate slices of the body. In certain applications, high-resolution imaging is required (e.g. brain imaging). For the other body parts, a faster scan at lower radiation dose can be obtained by spiral CT, slightly sacrificing image resolution and sharpness (Figure 12 (67)).

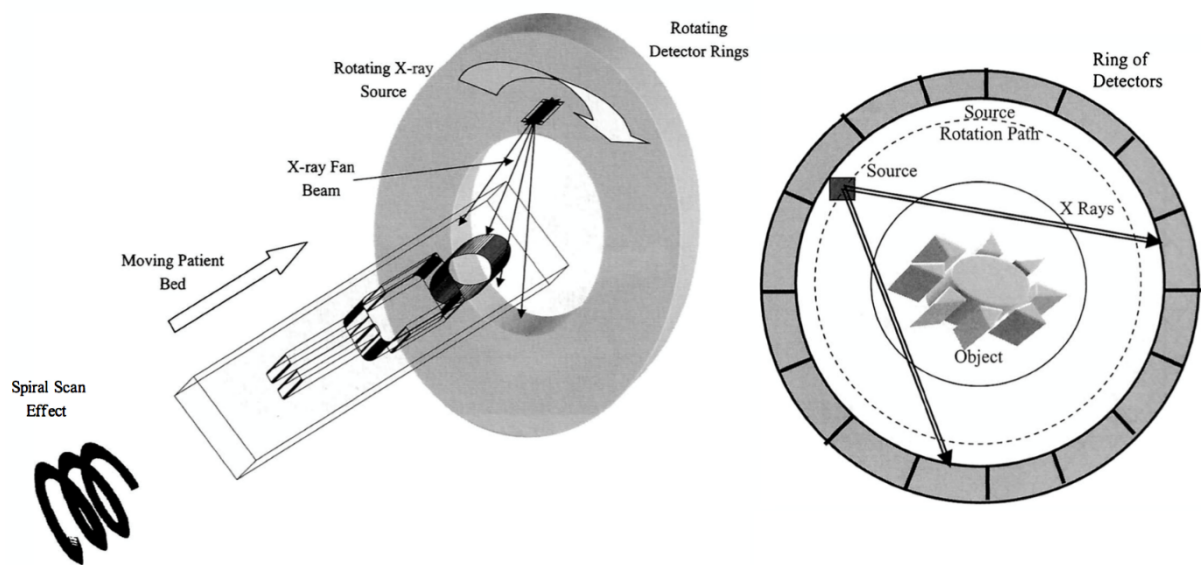


Figure 12: On the left a schematic diagram of a spiral CT scanner. On the right, a detailed scheme of a fourth-generation CT-scanner geometry (67).

Then, the slices are digitally assembled together to form a 3D image of the patient that allows for easier identification and location of basic structures and eventually tumours.

Single-photon emission computed tomography (SPECT) is a nuclear medicine tomographic imaging technique using γ rays. It shares same technology with conventional nuclear medicine planar imaging using a gamma camera, but is able to provide true 3D information. To perform SPECT imaging, a gamma-emitting radioisotope is typically injected into the bloodstream or administered orally, and then the gamma rays are detected by a gamma-camera schematically shown in Figure 13 (67,68).

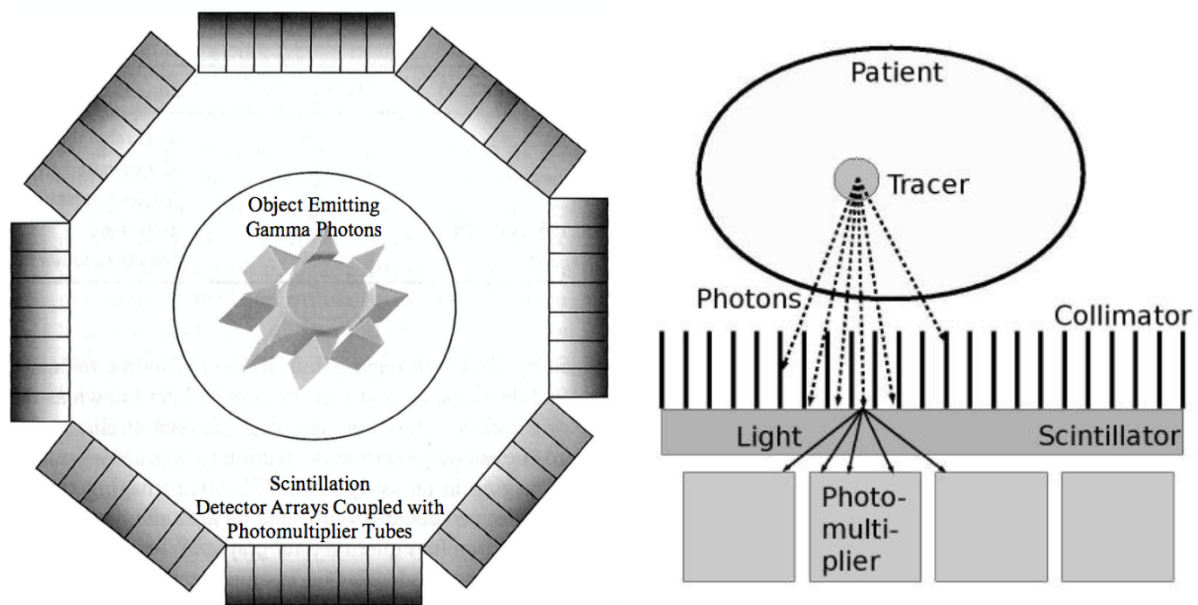


Figure 13: On the left a schematic diagram of detector arrays of a SPECT scanner surrounding the patient area. On the right a detailed schema of a γ -camera (67,68).

The rays are "focused" by the septa of the collimator, which block incoming radiation with an oblique angle of incidence. The photons that pass the collimator hit the scintillator, where the photon produces a scintillation consisting of an avalanche of low-energy photons. Several photomultipliers are hit by the photons; the centroid of the signal intensities from the photomultipliers allows for a localization of the original scintillation event with an accuracy in the range of 2–3 mm.

A conventional gamma-camera is composed of sodium-iodine scintillation detectors (NaI camera). In the first decade of the 21st century, a new technology using cadmium-zinc-telluride (CZT) detectors has been introduced. This crystal is able to transform directly the signal induced by gamma rays into electric impulses without the need for photo-detectors

(69). The intrinsic detection efficiency of CZT detectors is similar to that of conventional NaI cameras, but the pixelated nature of the CZT crystals improves the spatial resolution (2 mm against 4 mm) (70). There is also an improvement of energy resolution which gives a better scatter correction and the possibility to implement multiple isotope scanning protocols. SPECT scanners using CZT technology have also been demonstrated to reduce the acquisition time and the radiopharmaceutical dose (71). Although the advantages that this new detector technology can bring in the nuclear medicine imaging, the use of CZT-based digital cameras has so far been limited to cardiac imaging. To the best of my knowledge, the use of CZT detectors on non-cardiac applications is very limited (70,72), but as it could be expected, same advantages were found.

The SPECT scanner acquires bi-dimensional images and then a tomographic algorithm is applied to yield a 3D dataset. Since this modality is not a quantitative imaging technique, the implementation of a calibration protocol is required. So, a calibration factor (CF) has to be derived in order to convert the SPECT count data in absolute activity per voxel.

Performance of SPECT scanners may be optimised using Monte Carlo simulation software, such as the SIMIND Monte Carlo program (73), which is a reliable code for modelling scintillation camera imaging and has been

widely used for the last 30 years (74). It describes a standard clinical SPECT camera and can easily be modified for almost any type of calculation or measurement encountered in SPECT imaging. The SIMIND system has two main programs, namely “change” and “simind”. The “change” program (Figure 14) provides a way of defining the system to be simulated and writing data to external data files.

```

-----
C H A N G E: Main page for SIMIND version V6.2
-----
1 - .....:
2 - Change some general data .....:
3 - Change simulation flags.....:
4 - Export to a SMC file.....: simind.smc
5 - Import from a SMC file.....:
6 - Clear all SMC data.....:
7 - Comment sentence.....:
8 - Transfer changes to other files:
9 - Phantom soft tissue.....file: h2o
10 - Phantom bone tissue.....file: h2o
11 - Cover material.....file: al
12 - Crystal material.....file: nai
13 - Density map.....file: alders
14 - Source map.....file: none
15 - Backscatter material.....file: lucite

Option number....: █

```

Figure 14: Example of the first page of the “change” program, where it is possible to change all the components materials.

Option number 2 (see Figure 14) includes 99 indices which allow the user to modify individual values of the simulation. It is possible to perform simulations with a variety of radioactive sources and phantoms including

standard phantoms (rectangular, cylindrical, Jaszczak) and non-homogeneous phantoms (Zubal distribution, NCAT/XCAT).

The actual Monte Carlo simulation is performed by the “simind” program, which reads input files created by “change” and outputs results to the screen or to different data files. A thorough and complete description of the characteristics of this software is available in the SIMIND manual (75). This software was used for the work described in section 5.2 to simulate a standard Jaszczak phantom with several spherical inserts filled with water.

Since 2005 there has been an increasing trend to combine SPECT with CT in a combined scanner. This system acquires data from the two image modalities with a single integrated patient bed and gantry, with the patient remaining on the table, which is moved from the CT scanner to the SPECT system (Figure 15) (76).

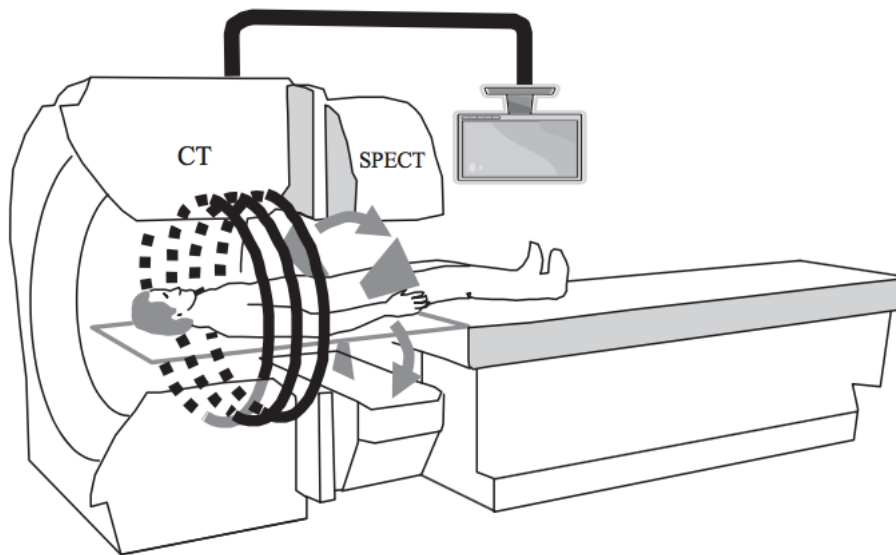


Figure 15: A SPECT/CT system using a shared bed for the patient (76).

The primary advantages of a combined SPECT/CT over a stand-alone SPECT system are an improved attenuation correction for SPECT reconstruction using the high-resolution anatomical information from the CT, and the possibility of the anatomical location of radioactive 'hot' or 'cold' spots with reduced partial volume effects compared to SPECT alone.

The only disadvantage is that the scans are acquired serially rather than simultaneously, which can potentially lead to misregistrations between SPECT data and the CT-derived attenuation maps if the patient moves position.

1.4.3.3. Image registration

In PRRT with ^{177}Lu , it is possible to evaluate how the distribution of the radiopharmaceutical varies with time by performing multiple SPECT/CT scans. This is important because, through multiple imaging, it is possible to derive the time-activity curve (TAC) to be used in absorbed dose calculation. A common issue, related to the use of sequential images, is the need to co-register the tomographic sequential scans prior to calculating the absorbed doses to the tissues. Image registration is the process of spatially aligning two or more image datasets taken at different times (77), establishing a transformation between the coordinates of a fixed image taken as reference and a moving image (78).

Registration algorithms require three main components: a geometric transformation, a similarity metric and an optimizer (Figure 16) (79).

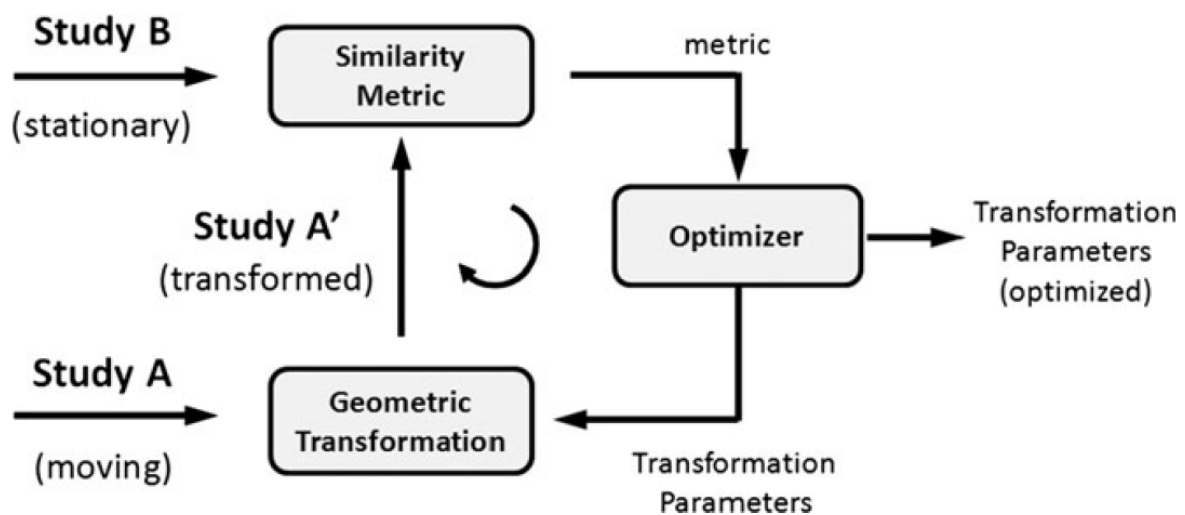


Figure 16: Basic workflow of image registration algorithms (79).

In this section, the most common transformation models used in clinical practice are described. A summary can be found in Table 5.

Transformation	Max dimensionality of transformation
Rigid	6
Affine	12
Spline-based methods	3N

Table 5: Summary of the transformation models most commonly used in clinical practice. In the table, N is the number of voxels in the image.

The transformation can simply consist of three translations and three rotation parameters (6 degrees of freedom) but can be affine (see below) if other parameters are considered such as scaling, shearing or reflection (up to 12 degrees of freedom). This kind of transformation is referred to as rigid registration.

A rigid registration can be defined as follows:

$$T_{\mu}(x) = R(x - c) + t + c \quad (20)$$

where x is all the voxels from the domain of the fixed image, R is the rotation matrix, c is the centre of rotation and t is the translation vector. μ is the parameter vector and it consists of the Euler angles (3 in a 3D space) and the translation vector (3 directions in a 3D space).

So, the μ vector has a length of 6. This gives the 6 degrees of freedom of this transformation. The rotation matrix R will have the following structure:

$$R = \begin{bmatrix} 1 & 0 & 0 & 0 \\ 0 & \cos(\theta) & \sin(\theta) & 0 \\ 0 & -\sin(\theta) & \cos(\theta) & 0 \\ 0 & 0 & 0 & 1 \end{bmatrix} \begin{bmatrix} \cos(\phi) & 0 & \sin(\phi) & 0 \\ 0 & 1 & 0 & 0 \\ -\sin(\phi) & 0 & \cos(\phi) & 0 \\ 0 & 0 & 0 & 1 \end{bmatrix} \begin{bmatrix} \cos(\psi) & \sin(\psi) & 0 & 0 \\ -\sin(\psi) & \cos(\psi) & 0 & 0 \\ 0 & 0 & 1 & 0 \\ 0 & 0 & 0 & 1 \end{bmatrix} \quad (21)$$

The first matrix refers to a rotation around the axis x of an angle θ , the second matrix refers to a rotation around the axis y of an angle ϕ and the third matrix refers to a rotation around the axis z of an angle ψ .

An affine transformation, instead, is defined as follows:

$$T_{\mu}(x) = A(x - c) + t + c \quad (22)$$

In this case, the image can be translated, rotated, scaled and sheared. A is the affine matrix and it is composed by the rotation matrix R (Eq. 21), a scaling matrix S (Eq. 23) and a shear matrix G (Eq. 24).

$$S = \begin{bmatrix} s_x & 0 & 0 & 0 \\ 0 & s_y & 0 & 0 \\ 0 & 0 & s_z & 0 \\ 0 & 0 & 0 & 1 \end{bmatrix} \quad (23)$$

$$G = \begin{bmatrix} 1 & 0 & 0 & 0 \\ a & 1 & 0 & 0 \\ b & 0 & 1 & 0 \\ 0 & 0 & 0 & 1 \end{bmatrix} \begin{bmatrix} 1 & c & 0 & 0 \\ 0 & 1 & 0 & 0 \\ 0 & d & 1 & 0 \\ 0 & 0 & 0 & 1 \end{bmatrix} \begin{bmatrix} 1 & 0 & e & 0 \\ 0 & 1 & f & 0 \\ 0 & 0 & 1 & 0 \\ 0 & 0 & 0 & 1 \end{bmatrix} \quad (24)$$

In the S matrix, s_x , s_y and s_z are the parameters needed to scale in the x, y and z axis (3 degrees of freedom). In the G matrix, instead, in the first matrix the shear is proportional to the x axis, in the second matrix the shear is proportional to the y axis and in the third matrix the shear is proportional to the z axis (3 degrees of freedom in total). The parameter vector μ consists of the elements of the matrix A (R , S and G matrices) and the translation vector; in a 3D space, the vector μ has a length of 12.

The registration can also consider a number of parameters as extensive as three times the number of voxels of the image. In this case, the transformation is referred to as deformable or non-rigid.

Thin plate spline method (80–84) is a well-known representation for non-rigid registrations. It uses a parametric grid of function control points (or landmarks) from the fixed and the moving image to parametrize the deformation. Each control point will cause a global influence on the image, so when the position of a point is perturbed, all the other positions will be perturbed accordingly. This means that the transformation is global. This

can be a disadvantage because it limits the capability of localized deformations (85).

Thin plate spline method can be expressed as a combination of an affine registration and a non-rigid component:

$$T_{\mu}(x) = x + Ax + t + \sum_{k^{fix}} c_i G(x - k_i^{fix}) \quad (25)$$

where $G(r)$ is a basis function and c_i are the coefficients corresponding to each control point. The affine components A and t are computed from the displacements of the landmarks between the moving and the fixed image. The parameter vector μ is given by the moving image landmarks k_i^{mov} .

In contrast, the B-spline method (86–90), use a weighted grid of parametric function control points; in this case, the transformation is limited to the region of each control point, so the perturbation of a single point will not influence the other points (85). This also makes this method more computationally efficient (91). Furthermore, B-spline methods have recently become very popular because of their flexibility and robustness and because they are able to perform both mono-modality and multi-modality image registration (92).

B-spline methods often use the following parameterisation:

$$T_{\mu}(x) = x + \sum_{k \in \mathcal{N}} p_k \beta^3 \left(\frac{x - k}{\sigma} \right) \quad (26)$$

where k are the control points, β^3 is the cubic multidimensional B-spline polynomial, p_k the coefficient vectors, σ the control point spacing and \mathcal{N} is the set of control points. In this case, the parameter vector μ consist of the coefficient vectors p_k . The number of parameters μ_i is determined by the number of the control points:

$$\mu_i = (k_1 \times \dots \times k_d) \times d \quad (27)$$

where d is the image dimension (e.g. 3 in a 3D space). The control points k_i are defined as:

$$k_i \approx \frac{s_i}{\sigma_i} \quad (28)$$

where s_i is the image size and σ_i is the uniform spacing between control points.

To better find the best alignment between the two images, it is possible to reformulate this as a mathematical problem. In this case, a cost function which quantifies dissimilarities between the two images is built and then the transformation T^* which minimises its cost is found:

$$T^* = \arg \min_{T \in S_T} C(X, T(Y)) \quad (29)$$

where S_T is the space of allowable transformations, C is the cost function, X and Y are the reference and the moving images respectively and $T(Y)$ represents the moving image after the transformation (93).

For image registration, several cost functions have been proposed. They can quantify the similarity and the dissimilarity between the two images taken into account based on geometrically defined features, which are found within the image, or they can work directly with the intensity values in the images (94).

The most common geometry-based cost functions (or metrics) are based on point or surface matching. In point matching, the coordinates of pairs of corresponding points from two different images A and B are used to define the following registration metric:

$$C = \frac{\sum (P_A - P_B)^2}{N} \quad (30)$$

where P_A and P_B are the coordinates of the two points and N is the total number of points. In surface matching, the overlap between surfaces from the two images is maximized; the stationary image is represented as a surface while the other one is represented as a set of sample points from the surface. So, the registration metric is the following:

$$C = \frac{\sum \text{dist}(P_A, S_B)^2}{N} \quad (31)$$

where $dist(P_A, S_B)$ is the minimum distance between the point P_A and the surface S_B and N is the number of points in image A .

Intensity-based metrics use numerical grayscale information to measure how the images are registered. The most widely used one is the mutual information (MI) technique, which aligns voxels whose values have common probabilities of being present in their respective image sets. The registration metric is defined thus:

$$R = \sum_B \sum_A p(I_A, I_B) \log_2 \left[\frac{p(I_A, I_B)}{p(I_A)p(I_B)} \right] \quad (32)$$

where $p(I_A)$ and $p(I_B)$ are the probability distribution functions of the intensities I of the images A and B respectively, while $p(I_A, I_B)$ is the joint probability distribution function.

MI was first implemented as similarity measure for CT and MRI by Studholme (95) and with time it became the classical similarity metric for medical applications, since it provides a robust evaluation of intensity variations and it can be also considered as a good alignment metric for image tracking (96,97). Mathematical descriptions of other cost functions can be found in the literature (94).

Intensity-based cost functions were found to be more accurate and reliable compared to the geometry-based ones (98). For this reason, the majority of

registration algorithms implement an intensity-based cost function. As an example, the algorithms used for this research work with the MI technique. The last component of the registration algorithms is the optimizer. The optimization process aims to find the best set of parameters to obtain the best alignment between the two images. A large number of optimization methods are used in both rigid and deformable registrations, but for similarity metrics, the optimizers are usually iterative; this means that they try different transformation parameters until the metric converges to an optimal value. In summary:

$$\mu_{k+1} = \mu_k + a_k j_k \quad (33)$$

where μ is the parameter vector described above, j is the “search direction”, k is the iteration number and a is a scalar gain factor which controls the step size along the search direction.

The Gradient Descent method (99) take the search direction as the negative gradient of the cost function:

$$\mu_{k+1} = \mu_k - a_k * g(\mu_k) \quad (34)$$

where $g(\mu_k)$ is the derivative of the cost function C evaluated at the position μ_k . In the majority of cases, a_k is a predefined function of k . It can perform

fast registration using a random subset of voxels newly selected at the beginning of every iteration.

A more robust version of the Gradient Descent method is the Adaptive Stochastic Gradient Descent method, described by Klein et al. (100) which requires less parameters to be set compared to the original version. In summary, the derivative $g(\mu_k)$ is not evaluated at the position μ_k but at the time t_k , which is the inner product of $g(\mu_k)$ and the previous $g(\mu_{k-1})$. If the derivatives point in the same direction, the inner product is positive, and therefore the time is reduced, which leads to a larger step size. In this way, an adaptive step size mechanism is introduced. All the assumptions are well described in the original article by Klein et al. (100).

In case of very large images, cost functions can be very difficult to solve; for this reason, instead of storing the total matrix $n \times n$ of the second derivatives (Hessian matrix), some methods store only a few vectors of length n that represent the approximations implicitly. A widely used optimizer belonging to this category is the limited-memory Broyden–Fletcher–Goldfarb–Shanno (L-BFGS) algorithm. The main idea of this iterative method is to use curvature information from only the most recent iterations to construct the approximation (101). The algorithm starts with an initial estimate of the optimal value x_0 , and proceeds iteratively to refine that estimate with a

sequence of better estimates x_1, x_2, \dots, x_n . The derivatives of the cost function $g(\mu_k)$ are used as key drivers of the algorithm to identify the direction of the steepest descent. Each step of the L-BFGS algorithm has the following form:

$$x_{k+1} = x_k - \alpha_k H_k g(\mu_k) \quad (35)$$

where α_k is the step size and H_k is the Hessian matrix. A detailed mathematical description of this optimizer and other widely used optimization algorithms can be found in this comprehensive book by Noceredan and Wright (101).

More details about the generic registration process can also be found in the Report 40 of the AAPM Radiation Therapy Committee (79).

In clinical practice, mis-registrations can derive from (a) incorrect patient repositioning, (b) internal organ deformation, (c) tumour variation or (d) respiratory motion, as reported in several works, mainly related to the use of PET/CT in the diagnosis of cancer and external beam radiotherapy (EBRT) (102–104). To minimize these sources of error in dosimetric calculation, registration algorithms are applied between images scanned at different time points, in order to align (or register) the different volumes of interest. CT and SPECT images acquired at the same time are linked with a so-called “identity” registration by default.

The registration algorithms which just use roto-translational movement to register the images cannot solve all the errors mentioned above. To better estimate the patient-specific dose delivered to the tissues, non-rigid registration algorithms can be used. As described previously, these algorithms have more degrees of freedom, so they can better solve the differences in local shape and improve the correspondence of the anatomical locations in the images. The superiority of non-rigid algorithms over rigid ones has been demonstrated recently in the literature (105,106). Figure 17 (106) shows schematically the application of a rigid and non-rigid algorithm to an image registration process.

The first line of the graph (Figure 17.a) reports the temporal sequence of the scans, with the identical registration represented by the double line.

Rigid registration is carried out between the nuclear medicine image (NM) and the CT, as shown in Figure 17.b, while the deformable image is carried out between the CT scans (Figure 17.c), and then the deformation map is applied to the corresponding NM image through the identical registration.

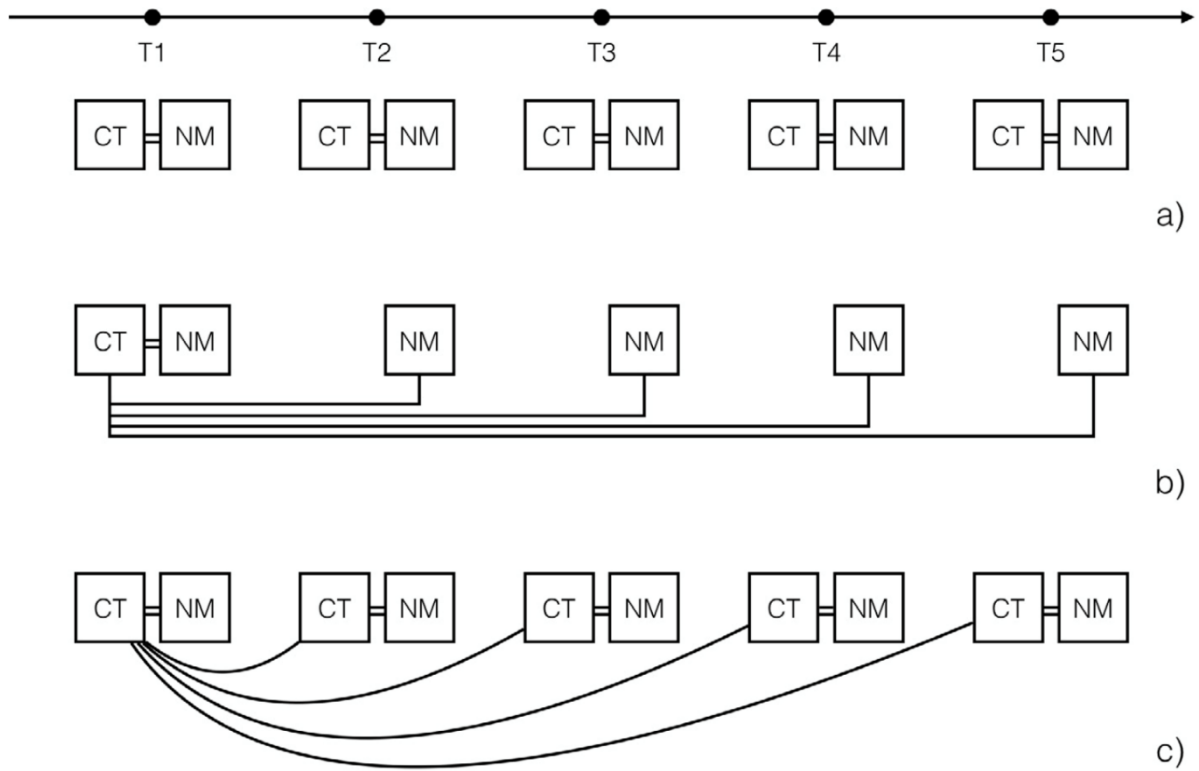


Figure 17: Example of a) temporal sequence, b) rigid registration and c) deformable registration for a multiple image-based clinical trial. Scans acquired at the same time point are represented by the double line connector (=). Identical registrations are represented by a double line connector, while rigid and deformable registrations are represented by the straight- and curved-line connectors respectively. NM stands for nuclear medicine image, CT for computer tomography image (106).

1.4.3.4. Image segmentation

Image segmentation is the process of defining regions in a 3D image set. It is used in radiotherapy to identify target volumes or other regions of interest for density specification or fiducial marking (107). With the increased interest in image-based dosimetry, the demand for image segmentation is magnified, where all the structures and volumes of interest need to be identified on the scans acquired for the therapy. This increased the need for more efficient manual segmentation tools as well as robust automatic

segmentation strategies for PET images (108–110), which share many of the sources of image degradation with SPECT images, even if the image characteristics are typically more favourable in the PET case (2 mm resolution against 4 mm resolution). The most common method for medical image segmentation is manual delineation, which suffers from being user-dependent and time consuming (111). The most basic approach is to point and click the mouse (or any alternative pointing device) on the location of the desired vertex and draw a line to the location of the new vertex. When completed, the last vertex is connected with the first one to close the contour. After the completion, every vertex can be moved to a new location to improve the contouring.

A more complex instrument is the pencil tool; in this case, every tracking update from the pointing device motion generates a new vertex, adding a line between the two generated vertices. Because tracking events are very frequent, this tool generates a huge number of vertices which makes a subsequent tuning more difficult.

The paintbrush tool is the primary manual tool which can be used for refining a contour. The shape and the size of the brush are defined by the user and it can be used to enlarge or contract the existing contour.

Because the region is being defined in a 3D image, contours must be drawn on each plane where the VOI exists. To accelerate this process, it is possible to copy the contour from one slice to another and then to apply minor modifications by the user.

Automatic segmentation uses an algorithm to detect features in an image that represent the boundaries of the structures and then to define the contours of the VOI (107).

There are many methods of automatic segmentation in medical imaging and it remains a large field of study; the simplest and most used is the threshold method. The user specifies a threshold value that represents the boundary of the structure. Then, the algorithm searches for the two pixels where the threshold value is crossed. It is possible to start this search from a seed point chosen by the user with the pointing device. In this case, method is called “region growing”. From that crossing point, the algorithm proceeds to ‘walk’ along the pixels which have neighbouring pixels that cross that value. The process is repeated for multiple 2D images to create a full 3D segmentation (107). Threshold based method is most effective on images with a high contrast, since the disruption on pixel value may indicate the edges of the region to contour.

There are no specific guidelines about lesion delineation on SPECT, so different methods are taken into account by different research groups. From a systematic review performed on the SCOPUS platform, using the keywords “Lu-177”, “dosimetry” and “NET”, 28 articles from 2003 to 2019 were found to be pertinent. In particular, planar images were widely used to perform the segmentation (112–119), along with a CT segmentation (120–125). In the majority of cases, the method to delineate the regions of interest was not stated, but manual delineation was preferred in three cases (112,119,124). When SPECT images were used, the small volume technique³ was used by three research groups (126–128), while another two used a manual method (129,130). Only one research group was found to use a semi-automated segmentation toolkit (131,132).

It is notable that the use of automatized SPECT image segmentation for MRT dosimetry has been relatively little investigated in the literature to date, particularly in relation to its potential benefits and consequences for absorbed-dose estimation (111). In section 5.2 of this work, a semi-automated segmentation method based on a threshold technique is investigated and compared with a method typically used in clinical practice.

³ In the small volume technique, a sphere with a volume of $\sim 4 \text{ cm}^3$ is drawn around the voxel with the maximum uptake.

Their performances are evaluated in terms of volume and absorbed dose estimation.

1.5. Objectives

This project has been funded by Cancer Research Wales (CRW) and carried out as a collaboration with AUSL-IRCCS.

The overall aim of this project is to incorporate advanced personalised 3D dosimetry into a clinical trial in PRRT and to assess the impact that this more accurate dosimetry can have within the context of a regulated study in MRT with a well-defined image-based dosimetry component.

The specific aims of the projects are:

- 1) To develop a workflow in which MRT treatments can be planned and optimised and in which the individual variations in the delivered therapeutic dose can be quantitatively evaluated;
- 2) To analyse the systematic imaging data available for each patient enrolled in the trial to refine the biokinetic model and to incorporate it in the calculation.

The thesis outline is described in the following section.

1.6. Thesis outline

This thesis is organised as follows and summarised pictorially in Figure 18.

Chapter 1 gives a historical background of the development of MRT and a description of the treatments currently available. This chapter also includes a description of neuroendocrine tumours and PRRT therapy. It also provides a description of the dosimetric calculation, with a detailed explanation of the MIRD schema and the image-based dosimetry calculation.

Chapter 2 discusses in greater depth the dosimetry based on Monte Carlo simulation. It also provides information for Raydose, the Monte Carlo based software used for this work.

Chapter 3 provides the details of the clinical trial on which this work is based.

Chapters 4 and 5 report the workflow developed for the data analysis performed as part of this work and provide a detailed analysis of the data obtained from the dosimetric analysis.

Chapter 6 summarizes the whole thesis and discusses the outcomes of the research. This chapter also identifies areas for future development.

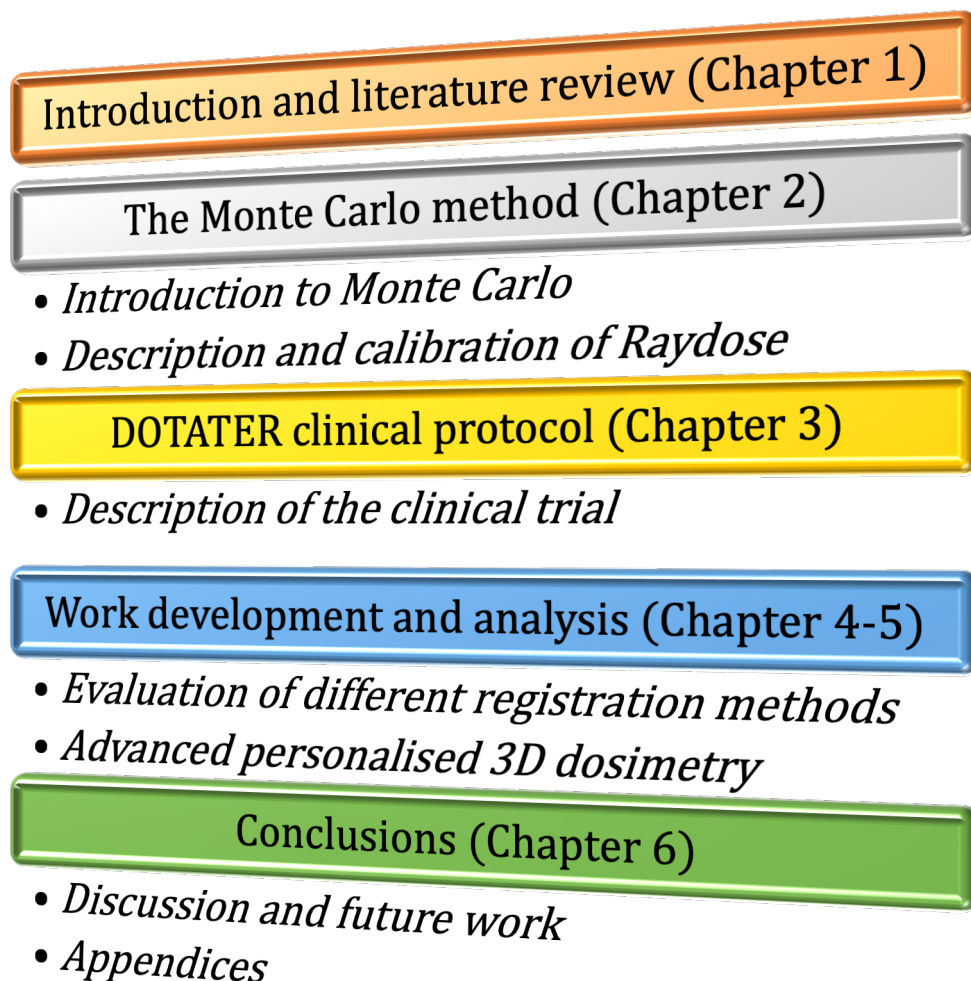


Figure 18: Illustration of thesis structure.

2. Monte Carlo dose calculation

The Monte Carlo (MC) method describes an extensive area of science, in which physical systems and phenomena are simulated by statistical methods employing random numbers (133).

In order to mimic a natural behaviour, the interactions are processed randomly and repetitively, until the results converge to estimated values. The conceptual idea is to create a model as similar as possible to the real system of interest and to create interactions within that system on known probabilities of occurrence with a random sampling of the distribution of events that occur on our system (called probability density function) (133). In this sense, MC proposes itself as a solution to a macroscopic system throughout the simulation of its microscopic interactions (134).

2.1. The Monte Carlo method

The major components of a MC method are the following:

- Probability density functions;
- Random number generator (RNG)
- Sampling rule

- Number integration
- Error estimation
- Variance reduction

The two most important aspects of the MC method in relation to this thesis are the RNG and the numerical integration.

The generation of the random numbers is based on predictable algorithms, so the numbers are not truly random. To be used in a MC method, the numbers need to possess these main characteristics (135):

- The sequences of numbers must be uncorrelated (in other words, n-tuples of numbers need to be independent of one another);
- The generator should not repeat (or only after a large set of numbers);
- The sequence of numbers should be repeatable in order to find errors if they occur;
- The algorithm has to generate numbers quickly.

Subsequently, the function shall be integrated between the x-axis and the interval where the function is evaluated, that is the area enclosed by the function. If the integral is impossible to solve analytically, different MC integrations are available, based on uniform distribution of random

numbers. A deep description of the MC method can be found in several publications (136–138).

2.1.1. Monte Carlo for particle transport

In MRT, multidimensional numerical integration is necessary to solve the system of coupled transport equations such as in the dose calculation. It is a system of equations because it includes the transport problem for photons and particles, and it is coupled because electrons influence the photon transport with the phenomenon of bremsstrahlung and vice versa with phenomena such as Compton scatter, photoelectric absorption and pair production.

Theoretically, the problem has an infinite parameter space because the number of secondary photons and electrons generated is physically unlimited when a primary particle of definite energy is involved; hence, the numerical integration has to be performed in a space with infinite dimensions. Practically, the dimensionality is limited because the region of interest is limited, and the simulation is stopped if the photon or electron energy falls below an established minimum energy.

For numerical integration using the MC method, a random point in a high-dimensional parameter space must be sampled. This point can be demonstrated by the “particle history,” a cascade of secondary particles generated by the primary particle (Figure 19, (134)).

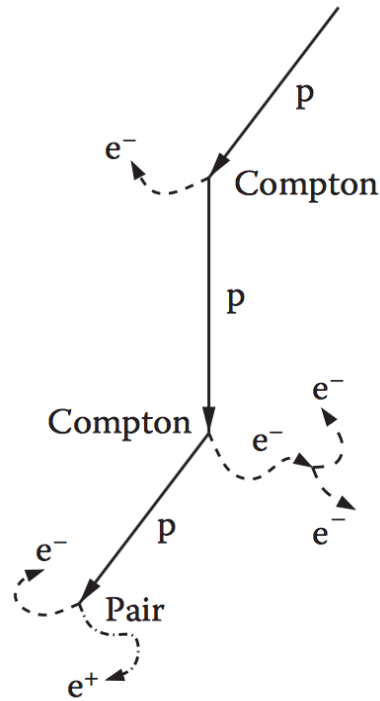


Figure 19: Example of a particle-history: it starts with a primary photon p (straight line) via Compton interactions and pair production events leading to secondary photons p (straight lines) and secondary electrons e^- (dashed lines) and positrons e^+ (dashed-dotted line) (134).

The probability $p(s)$ that a photon interacts after a path of length s is given by the attenuation law:

$$p(s)ds = \mu(E)e^{-\mu(E)s}ds \quad (36)$$

where $\mu(E)$ is the linear attenuation coefficient of the medium for a photon of energy E .

The mean free path $\langle s \rangle$ of the photon can be calculated from its distribution function if the medium is considered infinity extended below the surface:

$$\langle s \rangle = \int_0^\infty ds s p(s) = \mu(E) \int_0^\infty ds s e^{-\mu(E)s} = \frac{1}{\mu(E)} \quad (37)$$

The number of mean free path lengths is defined as:

$$\lambda = \frac{s}{\langle s \rangle} = \mu(E)s \quad (38)$$

Now it is possible to express the Eq. (36) in terms of the number of mean free path lengths:

$$p(\lambda)d\lambda = e^{-\lambda}d\lambda \quad (39)$$

Taking into account the geometric setup of the simulation, the photon is tracked λ_1 mean free path lengths to the first interaction point and then the type of the interaction is sampled. In the energy range of MRT, four types of interactions are the most common: photoelectric absorption (A), Raleigh scatter (R), Compton scatter (C) and pair production (P). They are represented by the corresponding interaction coefficients as material parameters at the interaction site:

$$\mu(E) \equiv \mu_{tot}(E) = \mu_A(E) + \mu_R(E) + \mu_C(E) + \mu_P(E) \quad (40)$$

This type of simulation is standard for uncharged particles because the free path between two interactions is in the same size order of the geometry

taken into account. When charged particles are considered (e.g. electrons) the type of interactions is different, giving back a complex particle history (Figure 20) (134).

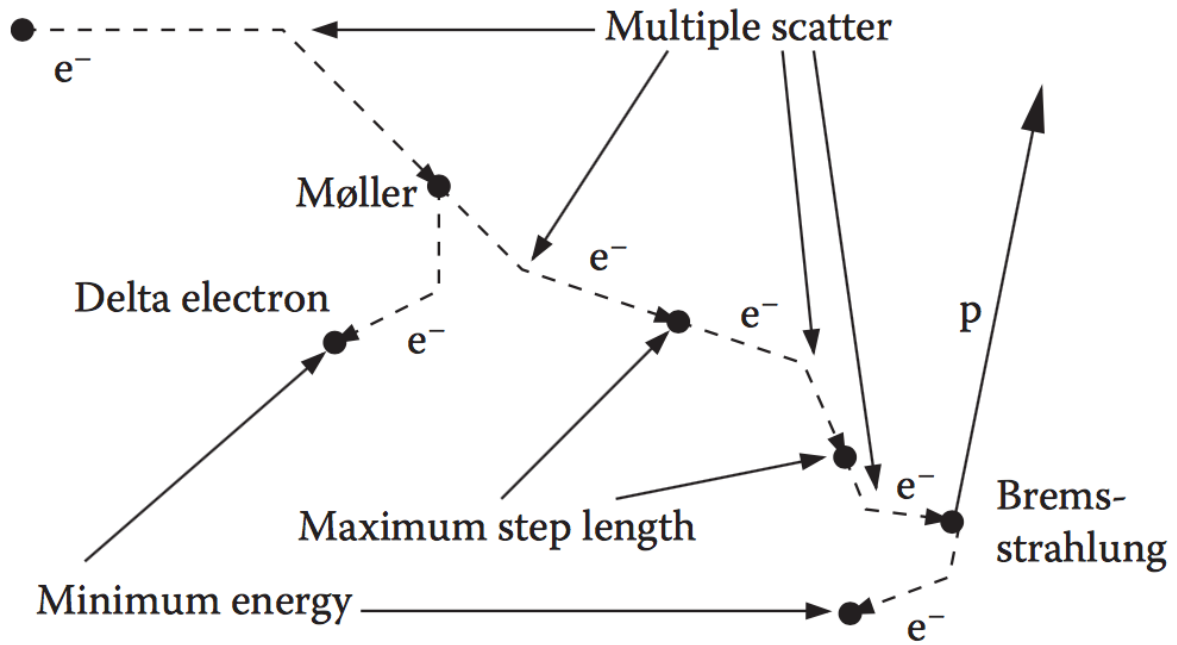


Figure 20: Example of a particle history starting with an electron (dashed line) via multiple interactions such as Møller scatter and Bremsstrahlung (134).

Hence these interactions are mainly elastic or semi-elastic, no energy or little quantities of energy are transferred to the surrounded material. This allows simulating the free paths of these particles using the Condensed History technique (CH) introduced by Berger in 1963 (134).

CH algorithm divides interactions into hard and soft collisions by an arbitrary kinetic energy E_C , and in hard and soft bremsstrahlung distinguished by the parameter k_C . It is also useful to introduce the maximum distance s_{max} that a simulated electron can reach in a CH step; this

distance is calculated from the percentage of energy loss between steps E_{step} .

Generally, electrons move on straight lines during CH steps, but the simulated path length needs to be corrected in order to take into account for a transversal displacement (Figure 21) (134).

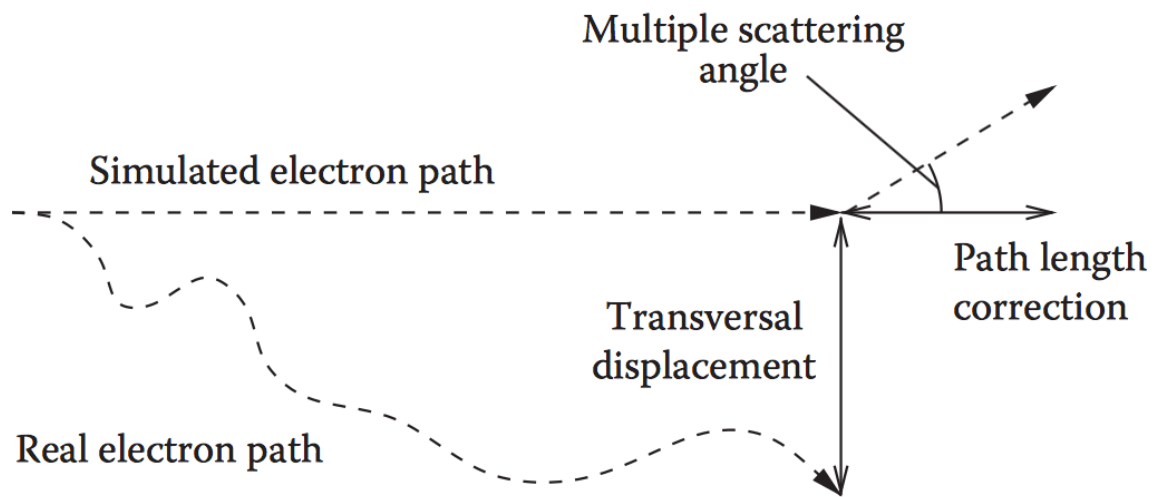


Figure 21: Example of a simulated electron path using the CH technique (134).

The position of the multiple scattering can be then determined randomly using the random hinge method (Figure 22, (139,140)).

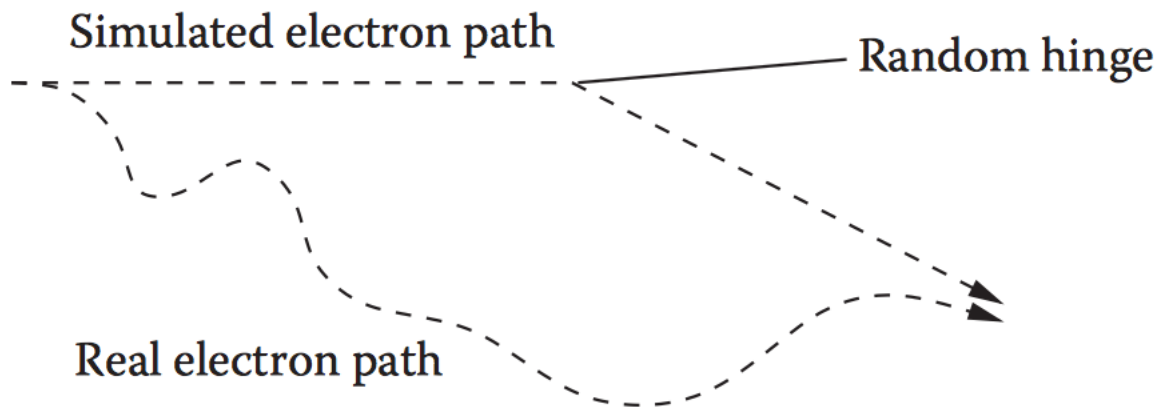


Figure 22: Same as the previous figure, but this time the random hinge method was used (134).

This method works only if a homogeneous medium is considered. When two or more materials are involved, the CH theory is not valid anymore for multiple scattering.

As Figure 23 shows, using the random hinge method, the simulated electron path is not influenced by the material that in reality has influenced the real electron path.

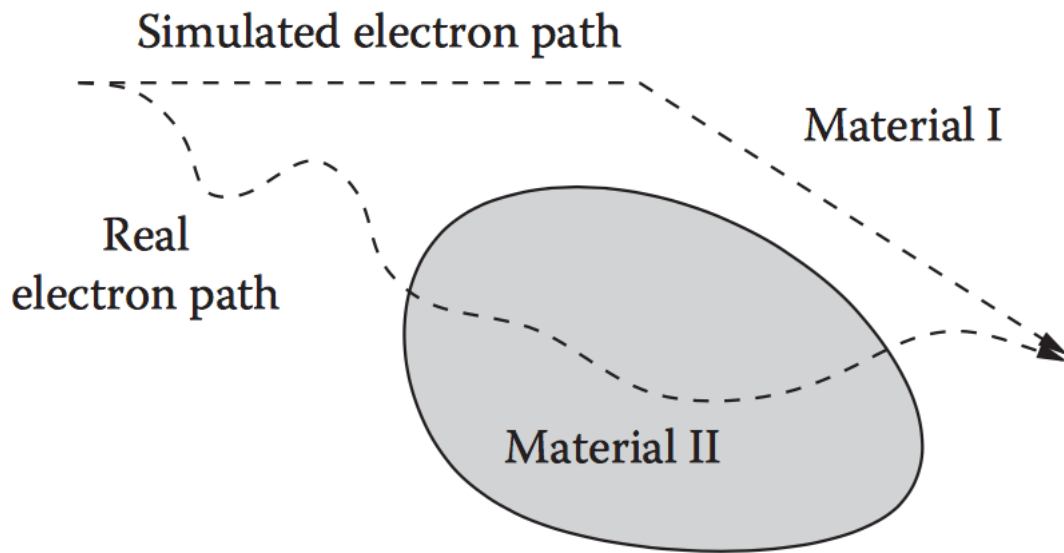


Figure 23: Electron path simulated in a non-homogeneous medium (134).

To avoid this artefact, s_{\max} must be decreased, resulting in smaller step sizes and longer calculation times. Reducing the size of the step can also become an obstacle on that, before an electron crosses the boundary, its CH step size becomes infinitesimally small. To permit boundary crossing anyway, the step size reduction must be switched off if a minimum step size is achieved. The software used for this work is based on GEANT4 MC toolkit (141), explained more accurately in the following paragraph.

More details about the transport of particles in MC calculation can be found in (141–147).

2.1.2. Geant4

Geant4 is a free open-source software package originally developed by CERN in 1993 to accurately simulate the passage of particles through matter (148). It includes a variety of physics models to process the interactions of particles with matter across a wide energy range. The simulation process includes different aspects, including:

- the geometry of the system,
- the materials involved,
- the fundamental particles of interest,
- the generation of primary events,
- the tracking of particles through materials and electromagnetic fields,
- the physics processes governing particle interactions,
- the response of sensitive detector components,
- the generation of event data,
- the storage of events and tracks,
- the visualization of the detector and particle trajectories,
- the capture and analysis of simulation data at different levels of detail and refinement.

Geant4 uses a combination of composition and rejection MC methods (143,149,150).

The diagram in Figure 24 shows the Geant4 class category, providing the foundation of the toolkit. Categories at the top of the diagram are used by virtually all lower categories.

The “global” category contains the system of units, constants, numerics and random number handling. The “materials” and “particles” categories describe the physical properties of particles and materials for the simulation of particle-matter interactions.

The “geometry” module defines the geometrical structure and propagates particles through it. All of these categories describe the tracking of particles and the physical processes they undergo.

Below these categories, the “track” category contains classes for tracks and steps, used by the “processes” category, which contains models of physical interactions (electromagnetic interactions of leptons, photons, hadrons and ions, and hadronic interactions).

All processes are invoked by the “tracking” category, which manages their contribution to the evolution of a track’s state and provides information in sensitive volumes for hits and digitization.

Then, the “event” category operates events in terms of their tracks and the “run” category manages collections of events that share a common beam and detector implementation. A “readout” category allows the handling of pile-up.

Finally, capabilities that use all of these categories and connect to facilities outside the toolkit through abstract interfaces, provide “visualization”, “persistency” and “user interface” capabilities.

Additional details about the transport of single particles can be found in the Geant Physics Reference Manual (151).

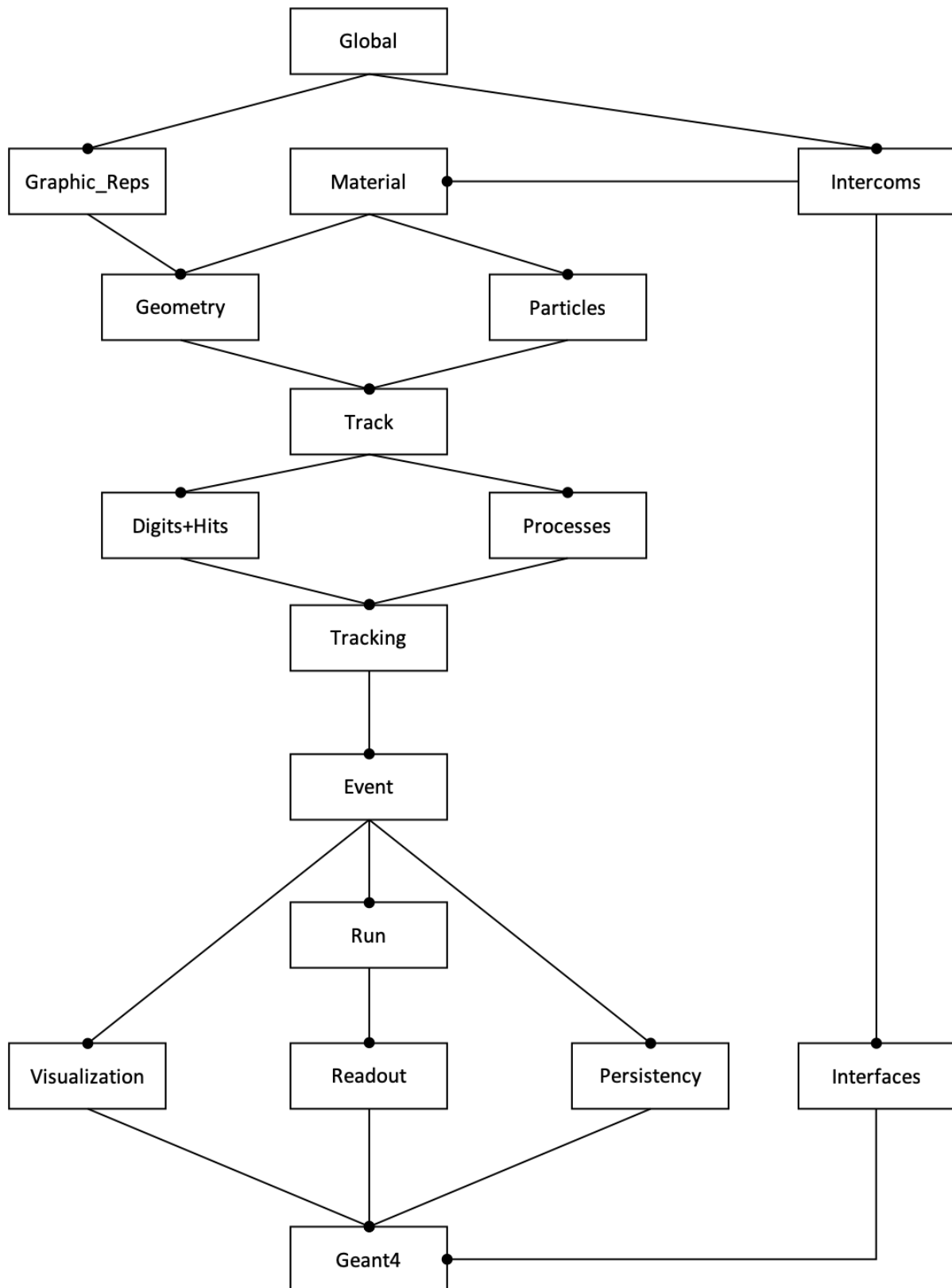


Figure 24: The diagram shows the class categories used by Geant4 during the simulation. Diagram was adapted from the Geant User manual.

2.2. Raydose Monte Carlo code

Raydose (65) is a MC-based application to perform three-dimensional (3D) patient-specific dosimetry in MRT. It is based on the open-source Geant4 MC toolkit (141), and it is able to bring a full 3D MC simulation of the source and patient's anatomy including the possibility of taking in account the spatial variations in the biodistribution of the radiopharmaceutical thanks to the simulation of multiple emission scans.

Raydose has been developed and tested on two 20 core (2 threads per core) Dell PowerEdge rack server (Intel Xeon E5-2670 v2 @ 2.50 GHz) running Ubuntu 14.04 LTS with each machine equipped with 64 GB RAM (Figure 25).



Figure 25: The two Dell machines where Raydose has been developed and tested.

Running simulation where the CT scan has, for example, dimensions of 512x512x100 slices will not run on a standard desktop with 8GB of RAM, because each voxel stores a float value of 4 bytes; therefore, this means that 4TB of RAM is needed. For this reason, more RAM is required, or it is possible

to sample the CT down (which can be done in Raydose) so that the simulation can be run in machines with less RAM.

In Raydose the following particles are simulated: pseudo-particles; gamma, optical photons, leptons, mesons, baryons and ions) and the following physics processes: pair production, bremsstrahlung, Compton scatter, Rayleigh scatter, multiple scatter, gamma conversion, photo-electric effect, ionization and annihilation.

In order to perform the dose calculation, Raydose requires data in DICOM format as input: one patient CT scan and a minimum of one activity image (e.g. SPECT or PET). The activity images provided need to be registered to the CT before being used with Raydose.

The CT image is then used by Raydose to create a virtual phantom of the patient where charged particles and photons can propagate, while the Hounsfield units (HU) are converted in materials with different density ranges as stated in ICRU report no. 46 (152). In the Raydose code these ten materials are defined: air, lung, adipose tissue, breast, water, muscle, liver, trabecular bone, dense bone and plexiglass. On the other hand, the activity image is used to sample random events from different positions which reflect the underlying activity intensity (Figure 26).

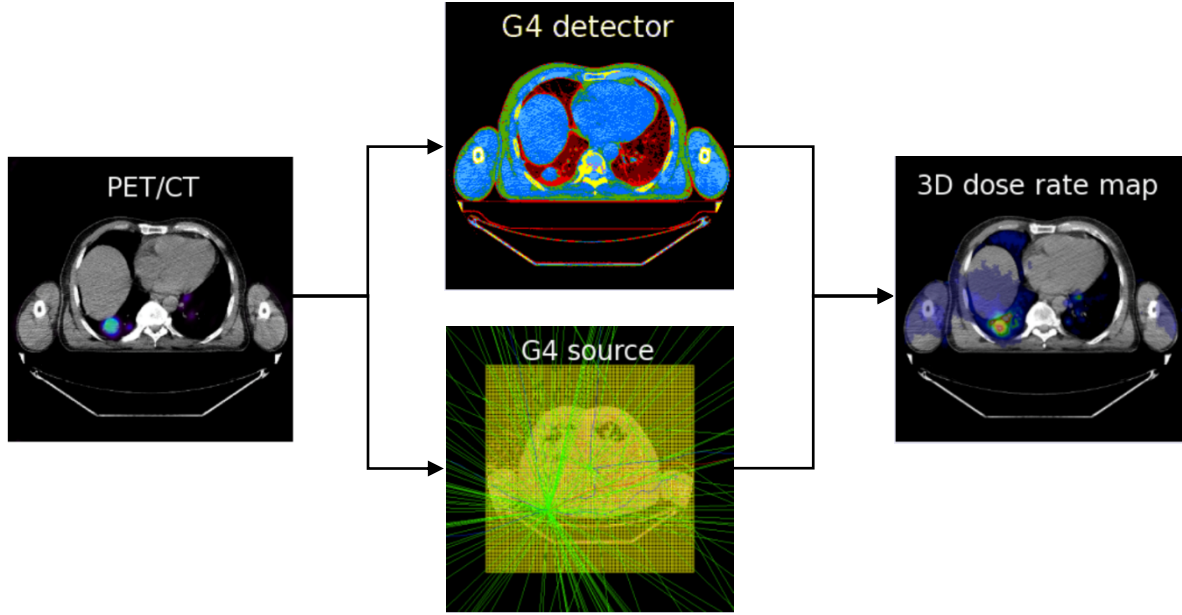


Figure 26: The scheme shows briefly how Raydose use the CT and the activity images to produce the 3D dose rate.

The activity data are used to generate a dose rate grid in Gy/events units with N number of events (also called histories). A random generator is created for each thread where the dose cumulated in each voxel is stored.

This map grows as voxels are hit, and after the last history has been simulated, all the maps from each thread are summed in a single map.

This 3D scored dose grid is then normalized by the number of events simulated:

$$\dot{D}^i = \frac{D^i}{N_{events}} \quad (41)$$

The total number of decays in the voxel (x, y, z) between two-time events (e.g. the first and the second activity image) is evaluated as follows:

$$\tilde{A}_{(x,y,z)}^{i \rightarrow j} = A_{(x,y,z)} \cdot [1 - e^{-\lambda \Delta T}] \quad (42)$$

where $A(x, y, z)$ is the total activity in the voxel (x, y, z) and ΔT is the time interval between the two events. The total number of events in the patient volume will be:

$$\tilde{A}_{total}^{i \rightarrow j} = \sum_{x=1}^{nx} \sum_{y=1}^{ny} \sum_{z=1}^{nz} \tilde{A}_{(x,y,z)}^{i \rightarrow j} \quad (43)$$

Successively, the total dose map between the two events is given by scaling the dose per simulated event grid by the total number of decays:

$$D^{i \rightarrow j} = \dot{D}^i \cdot \tilde{A}^{i \rightarrow j} \quad (44)$$

The total deposited dose between the first and the last scan inside the patient is:

$$D = \sum_i^{N-1} (\dot{D}^i \cdot \tilde{A}_{total}^{i \rightarrow i+1}) \quad (45)$$

where N is the number of activity scans.

After the last scan point, the potential dose is calculated with an exponential decay.

Assuming the N last scan, the total number of decays is:

$$\tilde{A}_{total}^{tail} = \sum_{x=1}^{nx} \sum_{y=1}^{ny} \sum_{z=1}^{nz} \frac{\tilde{A}_{(x,y,z)}^N}{\lambda} [1 - e^{-\lambda T}] \quad (46)$$

So, the total dose after the last scan point is:

$$D_{\text{tail}} = \dot{D}^N \cdot \tilde{A}_{\text{total}}^{\text{tail}} \quad (47)$$

The general equation of the Raydose MC simulation that takes into account for the 3D dose grid plus an exponential tail is given by the sum of the Eq. 45 plus the Eq. 47:

$$D = \left[\sum_i^{N-1} (\dot{D}^i \cdot \tilde{A}_{\text{total}}^{i \rightarrow i+1}) \right] + [\dot{D}^N \cdot \tilde{A}_{\text{total}}^{\text{tail}}] \quad (48)$$

Figure 27 shows the Time Activity Curve (TAC) used by Raydose for the simulation.

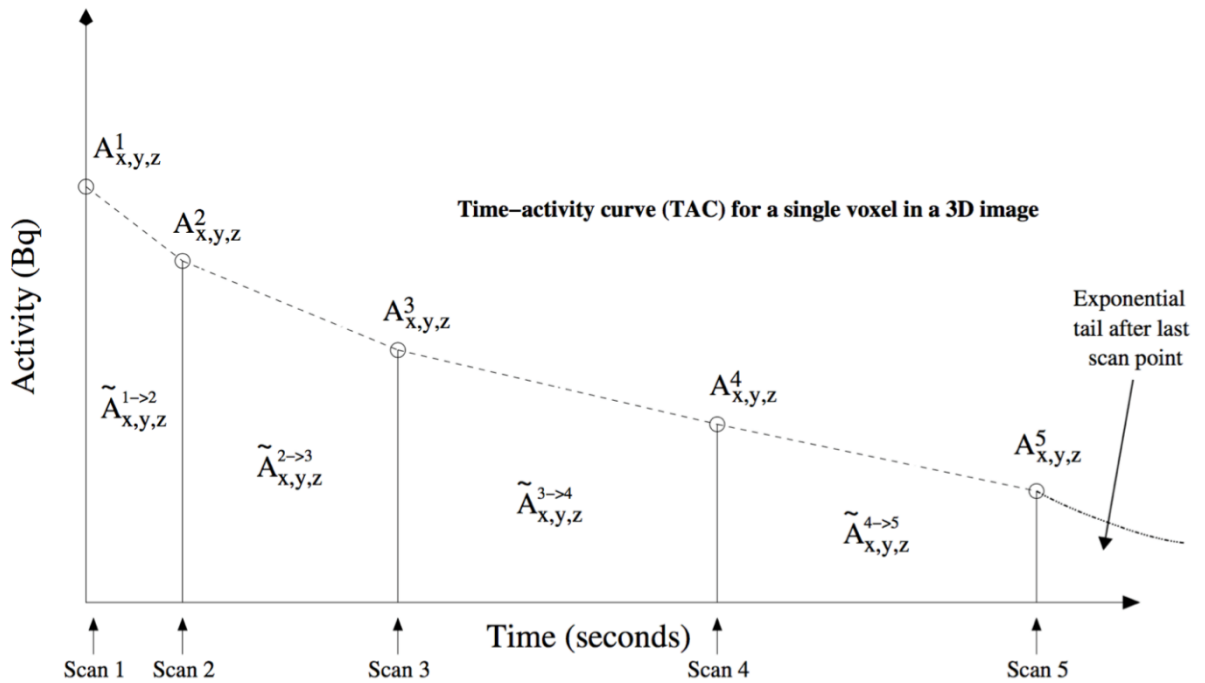


Figure 27: Overview of a 5 scans simulation showing how the individual voxel activities are used to determine the total number of decays for a given voxel (x,y,z) . This figure is adapted from the Raydose manual (Appendix B).

Uncertainties in Raydose are calculated using a history by history method from the BEAM code system (153). This method is well known and has been used in other codes since the 1986 (the MCNP code (154)).

The uncertainty in the average of the scored quantity X (the dose in this context) is:

$$s_{\bar{x}} = \sqrt{\frac{1}{N-1} \left(\frac{\sum_{i=1}^N X_i^2}{N} - \left(\frac{\sum_{i=1}^N X_i}{N} \right)^2 \right)} \quad (49)$$

where N is the number of independent events (i.e. histories), X_i is the value of X in the history i and \bar{X} is the mean value of X evaluated over all histories.

This is a slightly modified version of the original history by history method (attributed to *Salvat* from Barcelona University (155)) which allows to reduce the computation time required to update the scored quantities after each history.

More details about how Raydose works can be found in the manual in Appendix B.

2.2.1. Calibration of Raydose

The accuracy of cross-sections and particle transport was validated using a NEMA phantom with the inserts filled with ^{18}F and compared the results with the reference data by Stabin *et al.* (58). Dose distributions in a heterogeneous media were validated against experimental data using a phantom composed of several layers of different materials and filled with a 35 MBq of ^{131}I on the source cavity (65).

For this thesis, to evaluate the reliability of Raydose in simulating ^{177}Lu , the first simulations were made using a homogeneous phantom provided by ASMN-IRCSS with a nominal volume of 5640 ml. A solution of 1426 MBq of ^{177}Lu was injected and the phantom was scanned with a SPECT/CT scanner 3 times post-injection (3, 12 and 27 days after the administration). Chemical information about the ^{177}Lu used by ASMN-IRCSS can be found in section 1.3.1.2. Activity was directly measured from the syringe before the injection, then the residual activity in the syringe after the injection into the phantom was measured and subtracted from the initial value, obtaining an activity of 1426 MBq. Activity measurements were taken using an Aktivimeter isomed 1010 (Nuvia Instruments GmbH, Germany; accuracy $\pm 5\%$). The instrumentation was calibrated using vials of different sizes and filled with a different volume of ^{177}Lu solution (from 1 to 17 cc) and with a syringe of

1cc. For ^{177}Lu , the calibration factor was not influenced by the geometry or the material of the container used for the measurement. The CF for this study was equal to 28.5 Bq/counts. The calibration protocol is described in detail elsewhere (63).

To simplify the calculation, day 3 has been considered as the time of injection and the injected activity has been recalculated as 1054 MBq. The activity images were rigidly registered by expert physicians from ASMN. The analysis was computed on a volume of interest (VOI) countered by the physicians, taking into account only the water inside the phantom obtaining a volume of 5926.4 ml. The images were imported in Raydose and simulated with 10^8 histories and analysed with the conventional trapezoidal method plus an exponential tail cut at 1000 hours after the last scan point (Figure 28).

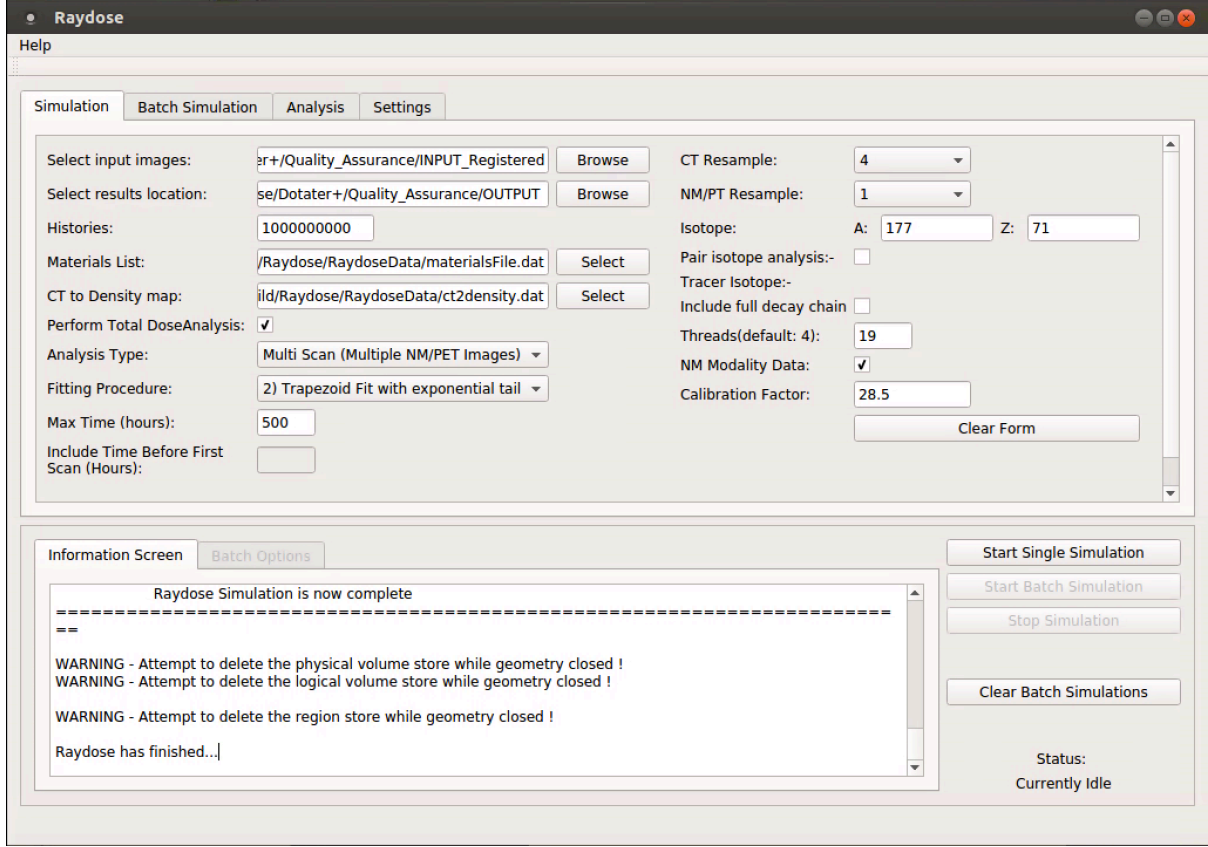


Figure 28: Graphical User Interface of Raydose with the input data for the simulation of the uniform phantom.

The mean dose obtained from the Raydose calculation was compared with analytical results obtained from Eq. (11). Using $\lambda = 1.22 * 10^{-6} s^{-1}$ and a mean energy of $2.15 * 10^{-14} J$, the mean dose from the analytical approach was 3.15 Gy, on the other hand, Raydose calculated a mean dose of 3.27 Gy for the VOI.

Percentage difference (PD) between the two methods has been calculated as follow:

$$PD = \frac{D_{Raydose} - D_{analytical}}{D_{analytical}} \cdot 100 \quad (50)$$

A very good agreement was found between the analytical method and the MC simulation of Raydose with a PD of 3.81%. This difference is mainly due to the following reasons: a) uncertainty of source activity equals to $\pm 5\%$, b) uncertainty of MC simulation equals to $\pm 0.62\%$.

3. DOTATER clinical trial

The data set for this thesis comes from an Italian clinical trial named DOTATER studying the effect of radioreceptor therapy with labelled somatostatin analogues in tumours with a high expression of somatostatin receptors. It is a non-randomized phase II clinical trial from ASMN-IRCSS (Dr Annibale Versari Chief Investigator) and is still ongoing. All the information about this clinical trial can be found in the EU clinical trial register⁴ with the EudraCT number 2013-002605-65.

3.1. Aims of the trial

The main aims of the trial are:

- To correlate the dosimetric results of each lesion with its response to PRRT in patients with cyto-histological diagnosis of NETs or other cancer SSTR₂-positive;
- To evaluate the toxicity on PRRT treated patients.

⁴ <https://www.clinicaltrialsregister.eu>

The secondary aims are:

- To evaluate the therapeutic response to PRRT with ^{68}Ga PET/CT and its correlation with the morphological evaluation (contrast-enhanced CT or MRI);
- To correlate the results of kidney and marrow Biological Effective Dose (BED) with nephrotoxicity and haematological toxicity determined by PRRT.

The endpoints of the protocol are:

- To assess patient survival at 3 and 6 months;
- To correlate the response to PRRT with the degree of histological differentiation at diagnosis and with the stage of the disease at enrolment.

3.2. Cohort and therapy description

One hundred patients were enrolled in this clinical trial between March 2014 to March 2016 with the following inclusion criteria:

- Patients > 18 years, and either gender or any ethnicity;

- Cyto-histological diagnosis of NET or other SSSTR-positive tumours (brain cancer, colorectal cancer, differentiated thyroid carcinoma, lymphoma, breast cancer, melanoma, lung cancer, renal cancer, sarcoma, prostate cancer, hepatocellular carcinoma, thymic neoplasms);
- Presence of at least one measurable lesion > 1 cm;
- High expression of somatostatin receptors in the ^{68}Ga PET/CT in target lesions. It is defined as "high expression of somatostatin receptors" the demonstration examination ^{68}Ga PET/CT (semi-quantitative analysis) of a ratio $\text{SUV}_{\text{max}} \text{ tumour} / \text{SUV}_{\text{mean}} \text{ muscle} > 4:1^5$;
- CT with contrast or MRI < 2 months of enrolment in this clinical study;
- Adequate blood chemistry: white blood cells $> 2500/\text{pL}$; platelets $> 90,000/\text{pL}$; Hemoglobin > 9 g/dL; creatinine < 2 mg/dL; bilirubin < 2.5 mg/dL;

⁵ SUV is the Standardized uptake Value corresponding to the ratio of the image derived radioactivity concentration and the whole body concentration of the injected radioactivity.

- ECOG performance status⁶ ≤ 2 ;
- Informed consent.

The following criteria were reasons for exclusion:

- Pregnant (women of childbearing age) occurred through pregnancy tests (dosage of beta-HCG urine) on the day of administration;
- If breastfeeding, refusal to terminate nursing;
- Surgery, chemotherapy, radiation therapy or biologics in the 4 weeks preceding the PRRT (except radiotherapy with palliative intent of lesions in symptomatic patients pluri-metastatic);
- Participation in another clinical protocol experimental therapy within 4 weeks before the PRRT;
- Invasion of the medullary disease ascertained $> 25\%$;
- Patients with other therapeutic option validated as effective;
- Life expectancy < 6 months;
- Not using adequate contraceptives (e.g. abstention from sexual relations within the 30 days prior to administration, oral

⁶ The Eastern Cooperative Oncology Group performance status describes a patient's level of functioning in terms of their ability to care for themselves, daily activity and physical ability.

contraceptives, barrier contraceptives, intrauterine devices, sterilization).

As mentioned before, the primary objectives of this study are the correlation of the dosimetric data of each target lesion with the response of the lesion to PRRT and the toxicity of PRRT with ^{90}Y and ^{177}Lu . Target lesions will be defined as follows:

- lesions (up to 5) with the highest degree of uptake for the ^{68}Ga PET/CT in any organ of origin (except bone) in the visual analysis;
- > 1 cm;
- preferentially localized in the abdomen.

For all target lesions (≤ 5) in which dosimetry has been calculated, a correlation study will be executed, aimed to identify the minimum dose to determine a response in tissue function of belonging. The therapeutic response will be evaluated by the RECIST 1.1 criteria (156) and by a ^{68}Ga PET/CT scan. The results of the PET/CT will be related to the RECIST evaluation. All patients will be followed for 6 months after the last administration of PRRT. In all patients, the survival at 3 and 6 months will be assessed.

The toxicity will be assessed according to the Common Terminology Criteria for Adverse Events v4 (CTCAE) (157). For each patient, the toxicity after each administration and overall toxicity of PRRT for the 6-month follow-up will be assessed.

In case of high values of BED to the kidney (> 46 Gy) or high dosimetry estimates to the spinal cord (> 2 Gy), the experimenter can decide to suspend the PRRT or reduce, in the event of risk factors, the injected activity for a single administration.

For the therapeutic scheme, a combination of ^{90}Y and ^{177}Lu was injected. This combination has been a subject of several experimental clinical trials and been demonstrated to increase the effectiveness of the treatment (112,158–161). Table 6 shows the possible scheme of treatments as suggested in the current guidelines (162).

Scheme PRRT		Number of administrations	weeks between doses	Maximum recommended cumulative activity (GBq)
^{90}Y	DOTATATE	2	6-12	18
	DOTATOC	2-4		
^{177}Lu		3-5	6-12	37
$^{90}\text{Y} + ^{177}\text{Lu}$		2-6	6-16	42

Table 6: Treatment schemes suggested by the guidelines.

In the DOTATER clinical trial, the maximum total activity was stated as follow:

- 33.3 GBq of maximum cumulative injected for $^{90}\text{Y}+^{177}\text{Lu}$;
- 1.85-2.59 GBq of injected activity for ^{90}Y ;
- 3.7-5.55 GBq of injected activity for ^{177}Lu (at least one administration within the first two cycles).

The injected activity and the type of isotope used in individual doses have been evaluated based on the availability of the radiopharmaceutical and the characteristics of the individual patient (e.g. weight, age, kidney and spinal dosimetry, risk factors, size injury). The standard interval between doses was 6-12 weeks. If haematological toxicity limited the following administration (inadequate blood chemistry levels specified by the criteria for inclusion), that range was expanded to a maximum of 16 weeks after which the investigator had the right to suspend permanently the PRRT.

Within the first two administrations of PRRT, in all patients the dosimetric evaluation was performed for the predictive estimate of the dose to the kidney (BED), to the spinal and to the target lesions (maximum 5). Each patient received the dosimetric evaluation only once during the treatment of PRRT. Currently the role of dosimetry in PRRT is to respect the safety of the

treatment, in particular to prevent possible kidney damage in the hope that the results of future studies may lead to the PRRT plan based on the dosimetric results (163).

Before intravenous injection of radiolabelled peptide, the patient was treated to reduce the absorption of renal radiolabelled peptide. This treatment involved the addition of an appropriate hydration (at least 1 L of water per day on the day of administration, and in the two days following the PRRT), the intravenous administration of Bio-arginine (L-arginine hydrochloride) and saline solution.

All patients gave written informed consent for the study; after the first injection of ^{177}Lu they were scanned 5 times with a SPECT/CT machine (Symbia T2, Siemens Medical, Germany, NaI:Tl detector thickness 3/8") for the dosimetric purpose at 1, 4, 24, 44 and 72 h post injection (p.i.). SPECT images were acquired with two Medium Energy High Resolution collimators; matrix=128 \times 128; zoom=1; views=32 \times 2; time/view=30s; step and shoot mode; degree of rotation=180°; non-circular orbit; detector configuration=180°.

The energy windows (EW) for ^{177}Lu were set at 113 keV \pm 7.5% (104.53 – 121.47 keV) and 208.4 keV \pm 7.5% (192.40 – 223.60 keV). Triple EW scatter correction (164) was employed for the lower photopeak with the lower

scatter window from 87.58 keV to 104.53 keV (using a default window weight of 0.5), and the upper scatter window from 121.47 keV to 130.51 keV (using a default window weight of 0.9375). Double EW scatter correction (165) was employed for the upper photopeak with the lower scatter window from 171.60 keV to 192.40 keV (using a default window weight of 0.75) (166,167). These parameters were recently included in the latest MIRD pamphlet 26 (168) which suggests that “if a medium energy collimator is used, the data should be collected in a 15%–20% energy window centred on the 208-keV photopeak. If the number of counts collected in the 208-keV window is considered insufficient, a second energy window centred on the 113-keV photopeak can be used”.

The estimation of dose to the lesions was performed using the sphere model from OLINDA/EXM (see section 1.4.2.1), which allows the estimation of the dose in spheres characterized by a material of uniform density, for spheres of mass of 0.01-6000 g. This calculation model is intended to provide a quick way for the calculation of the dose to spherical objects by combining data from the decay of the radionuclide with the data relative to the absorbed fraction from the balls, according to the calculation developed by Stabin and Konijnenberg (62). At the time of writing, the DOTATER clinical trial is still ongoing, and no data regarding the response to the therapy are available yet.

4. Workflow development

This chapter describes the workflow development undertaken in the first year of the project. The impact of different registration methods on the dosimetric calculation was evaluated, comparing non-rigid approaches with rigid ones. Subsequently, the impact that the registration method can have on the workflow was also investigated, i.e. if dose maps are involved in the workflow instead of activity maps.

Image registration studies on this section were carried out using the ‘Velocity’ advanced imaging workstation version 3.2 (Varian Medical Systems, Palo Alto, CA), and the MICE toolkit (NONPI Medical AB, Sweden). Velocity is a commercial stand-alone software product that provides the user with a means for comparison of medical imaging data from multiple DICOM compliant imaging modality sources. It implements a B-spline registration algorithm with mutual information metrics and a L-BFGS optimizer (169). Figure 29 shows the user interface of the Velocity workstation. After the CT images to register are chosen, it is possible to select the registration algorithm from a drop list. For this study the two Velocity algorithms used were the rigid one and the deformable multi-pass (a 3-pass (coarse-medium-fine resolution) deformable option that yields finer adjustment, particularly built for CT-CT registration).

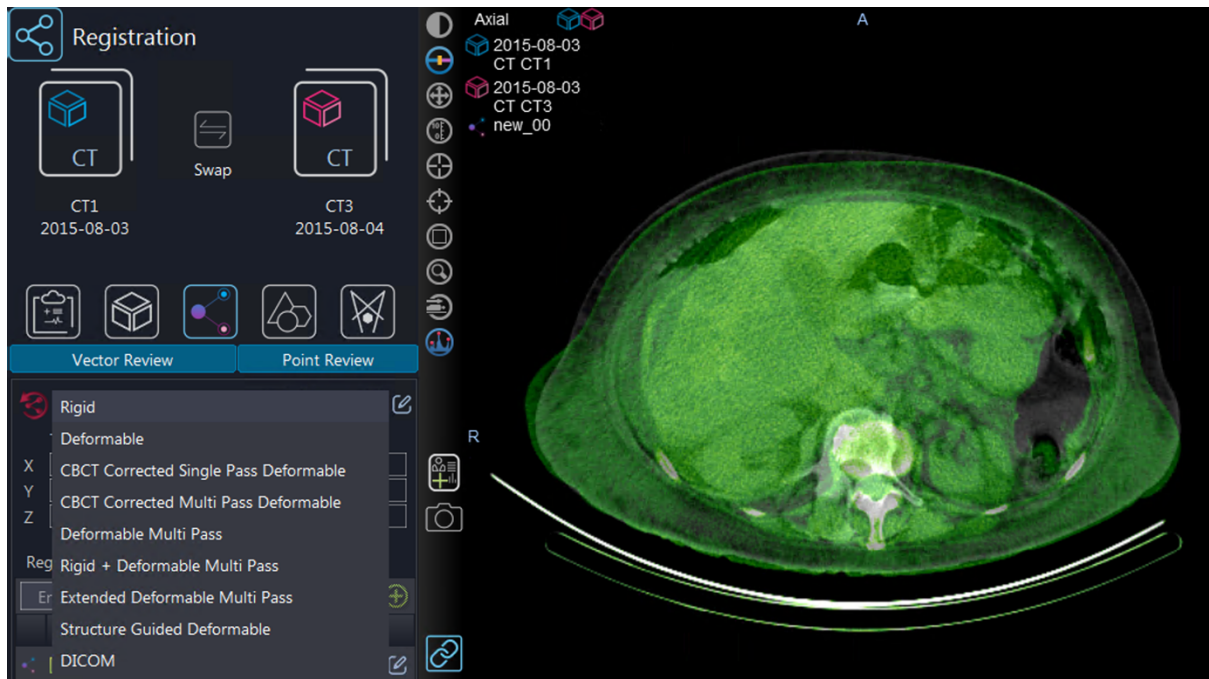


Figure 29: User interface of Velocity. After the CT scans are chosen, it is possible to select the registration algorithm from a drop list. The picture shows in greyscale the CT1 taken as reference and in green-scale the CT3 ready to be co-registered.

The MICE Toolkit (Medical Interactive Creative Environment) is a graphical programming user interface that is user-friendly and flexible. It has a lite version which includes some free functionalities, but a premium licence can be purchased to have access to full options. It is built mainly using the C# programming language using the .NET-framework, while some parts of the software are written in C++. Many of the filters and functions in MICE are from ITK (The Insight Segmentation and Registration Toolkit (170)), which is open-source and widely considered a benchmark implementation for image registration in many research and commercial applications (171). The registration functions in MICE are based on “elastix” (172,173), which is in turn based on ITK. For all the algorithms, the mutual information metric and

the Adaptive Stochastic Gradient Descent optimizer were used. Algorithms, metrics and optimizers used in this section have been explained in section 1.4.3.3.

MICE has a color-coded node interface where every module can be attached with the matching data type (or colour) to build a personalised medical image processing workflow. This system is very useful when advanced processes are created. Figure 30 shows the process built for the registration workflow. To change registration algorithm, it is possible to modify the parameters file included in the setting panel. The output can be visualised inside the software in another panel or exported in a particular format (DICOM in the example) to be used in other platforms.

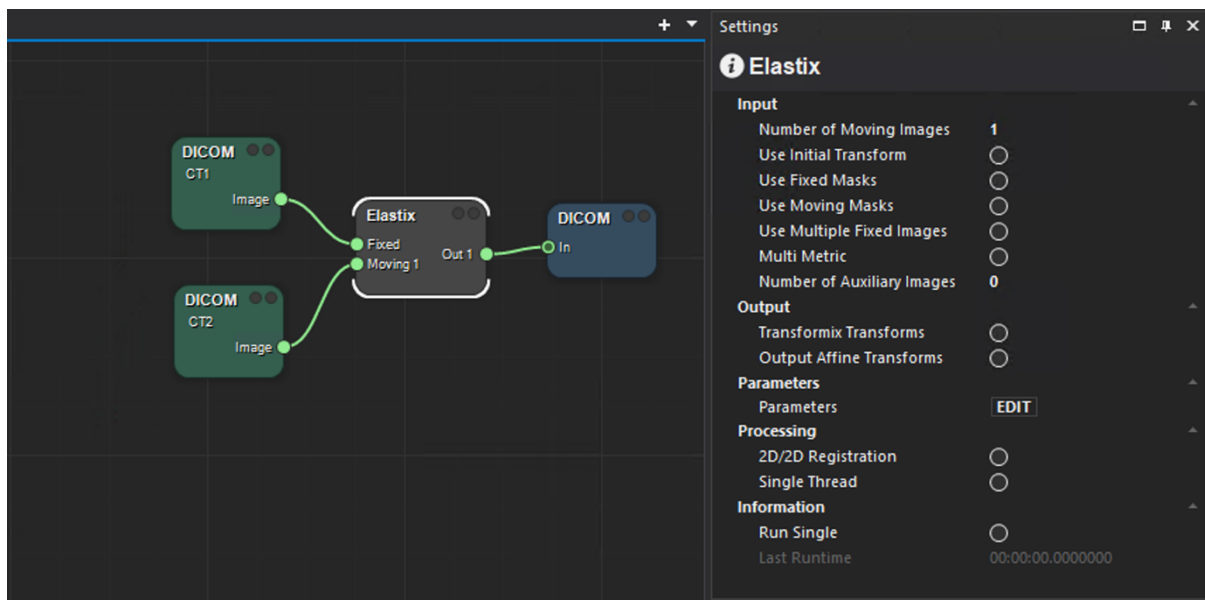


Figure 30: Example of the registration process created with the MICE toolkit. Parameters of the elastix module can be modified in the settings panel aside. This also shows the node approach used in MICE.

Dosimetric calculations were performed with the Raydose system described in section 2.2. The number of histories chosen for the MC simulation was 10^7 , with a typical associated calculation time of 2.5 hours per patient.

Differences in all comparison exercises were evaluated via a Bland-Altman analysis, a standard method used to analyse the agreement between two different datasets (174,175). The Bland-Altman plot (Figure 31) reports the average between the two measurements of the same quantity on the x-axis, while in the y-axis the difference is stated. The solid line indicates the mean difference and the dotted lines are the upper and lower limit of agreement (LoA), equivalent to the mean differences plus or minus 1.96

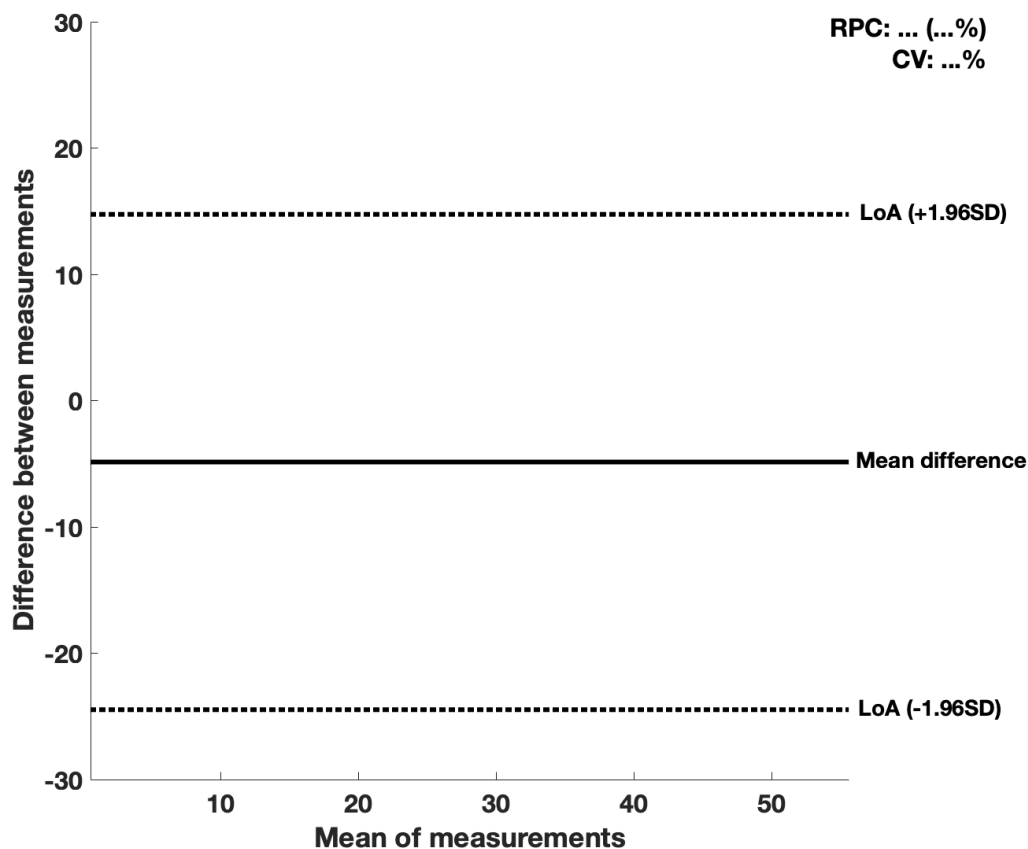


Figure 31: Example of a Bland-Altman analysis is plotted.

times the standard deviation (SD). The plot also reports the reproducibility coefficient (RPC), defined as the LoA, and its percentage value. Coefficient of variation (CV) is also reported, defined as the SD of the mean values in percentage terms.

4.1. Impact of registration: rigid vs non-rigid algorithm

As mentioned in section 1.4.3.3, a common issue related to the use of sequential images for dosimetry studies in MRT is the need to co-register the scans in a single frame of reference. This ensures that the cumulative activity in tumours and OARs is recorded accurately so that dose calculation can be carried out (167,176,177). When using a full 3D imaging protocol involving sequential scans, with intra-fraction as well as inter-fraction internal organ movements, variations in patient repositioning between fractions and respiratory motion can all lead to uncertainties in the calculation of absorbed doses in both tumours and OARs, as reported in work on PET/CT and external beam radiotherapy (102–104). With rigid registration the assumption is made that the anatomy is subject only to roto-translational movements. In most cases, rigid registration is unable to account for the

complex motion and deformation exhibited by internal organs. As an example, Figure 32 shows the application of a) a rigid registration algorithm

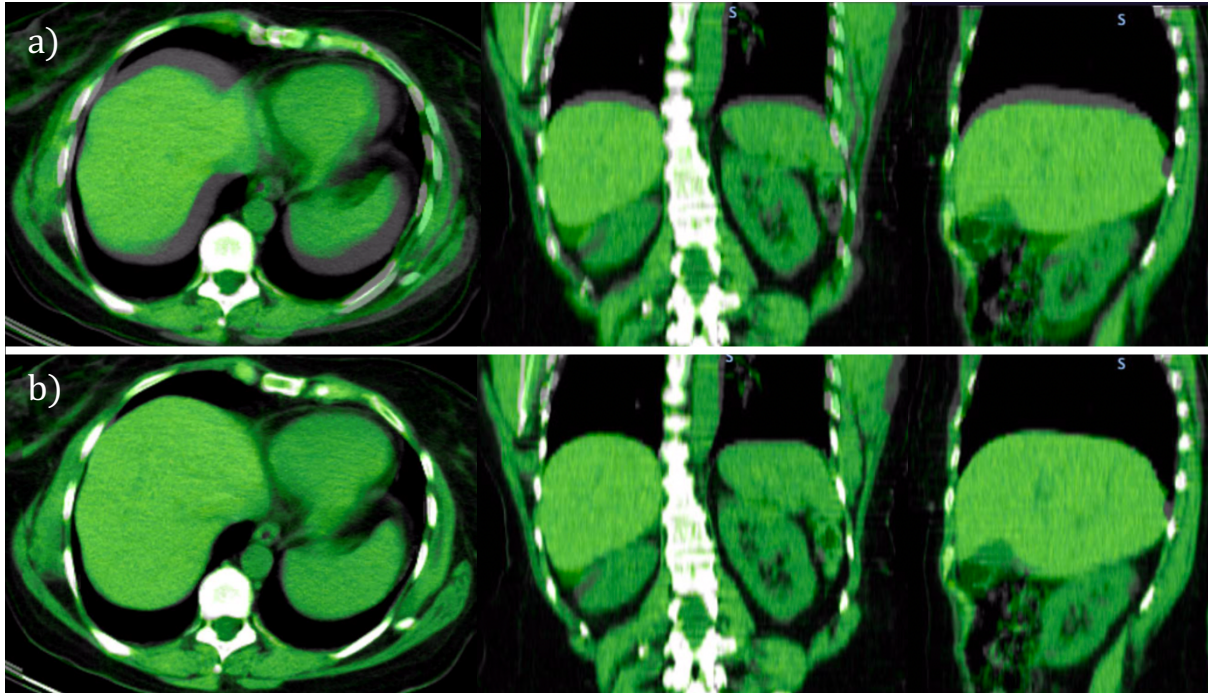


Figure 32: Example of a CT overlapping after a) rigid registration and b) non-rigid registration in axial, sagittal and coronal visualization. The CT of reference is on gray scale, the overlapped CT is on green scale.

and b) a non-rigid registration algorithm to the same set of images.

Non-rigid registration algorithms can help improve dosimetry in MRT as they can account for local non-rigid shape differences and can improve the correspondence of anatomical and functional locations in the relevant scans.

In the present section, the performance of different rigid and non-rigid registration methods applied on anatomical images were compared using a similarity metric. To this end, a subset of the first twenty patients from the clinical protocol described in Chapter 3 was used. For each patient, the sequential CT scans were registered onto the same frame of reference as the

initial CT scan using the rigid and non-rigid registration methods listed below.

For the rigid registration, the following algorithms were used:

- Manual registration focused on kidneys and bone matching;
- Automatic rigid registration from Velocity AI;
- Automatic rigid registration from MICE toolkit.

In addition, the following non-rigid registration algorithms were used:

- B-spline method from Velocity AI;
- B-spline method from MICE toolkit;
- Thin plate spline method from MICE toolkit.

In order to get close enough for a reasonable deformable registration, the rigid registration from the same software was first created. The process is schematically summarised in Figure 33.

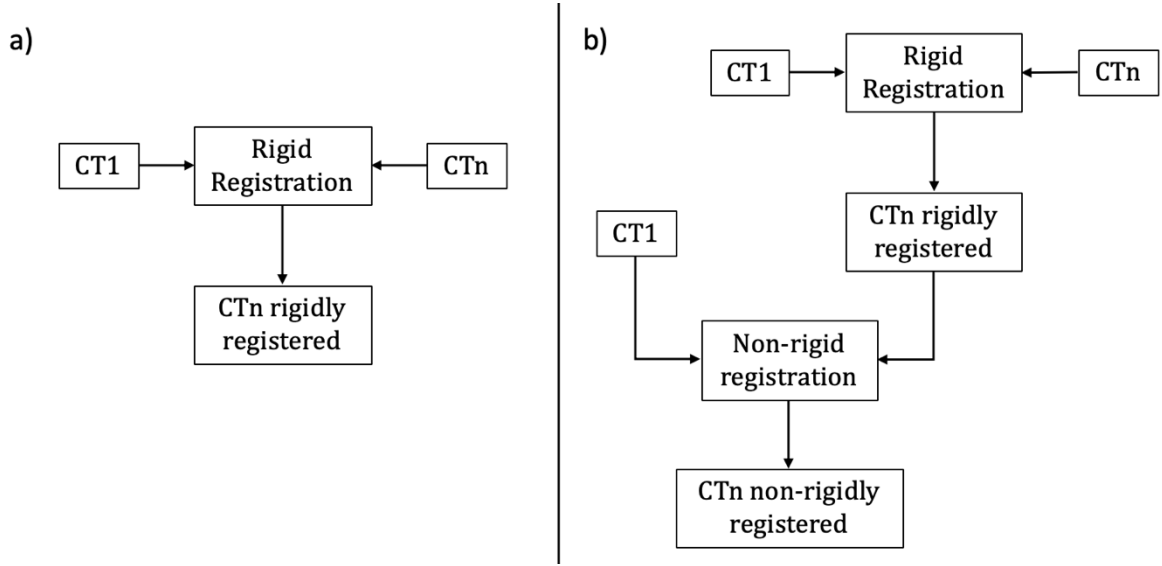


Figure 33: Scheme which summarises a) the rigid registration workflow and b) the non-rigid registration workflow. The non-rigid algorithm is applied after a preliminary rigid registration.

For each patient a total of 24 registration maps (4 CTs per each registration algorithm) were generated.

To evaluate the quality of the image registration numerically, the Structural Similarity Index (SSIM) was used (79). This metric is calculated as a combination of pixel intensity i , contrast c and structural information s between a distorted image (the registered CT) and a non-distorted image (the CT taken as reference) (178). The overall index is a multiplicative combination of the three terms:

$$SSIM(x, y) = i(x, y) \cdot c(x, y) \cdot s(x, y) \quad (51)$$

where

$$i(x, y) = \frac{2\mu_x\mu_y + C_1}{\mu_x^2 + \mu_y^2 + C_1} \quad (52)$$

$$c(x, y) = \frac{2\sigma_x\sigma_y + C_2}{\sigma_x^2 + \sigma_y^2 + C_2} \quad (53)$$

$$s(x, y) = \frac{\sigma_{xy} + C_3}{\sigma_x\sigma_y + C_3} \quad (54)$$

μ_x , μ_y , σ_x , σ_y , and σ_{xy} are the local means, standard deviations, and cross-covariance for images x and y . C_1 , C_2 and C_3 are regularization constants and they avoid instability where the local mean or standard deviation is close to zero. The SSIM is calculated between 0 and 1, where 1 represents a perfect match between the two images.

Figure 34 shows the SSIM values for the rigidly and non-rigidly registered images. According to a previous work (179), conformity indices higher than 0.70 show a very good overlap and this is reported as a solid black line in Figure 34. It can be seen that in general the non-rigid registration algorithms consistently performed better than the rigid ones in terms of SSIM value across the patient cohort in particular the two B-spline algorithms.

In most of the cases (81% of registrations), the B-spline algorithm from the MICE toolkit performed somewhat better than the one from the Velocity workstation. In general, the MICE b-spline algorithm was better able to register the spleen-stomach region than Velocity.

1

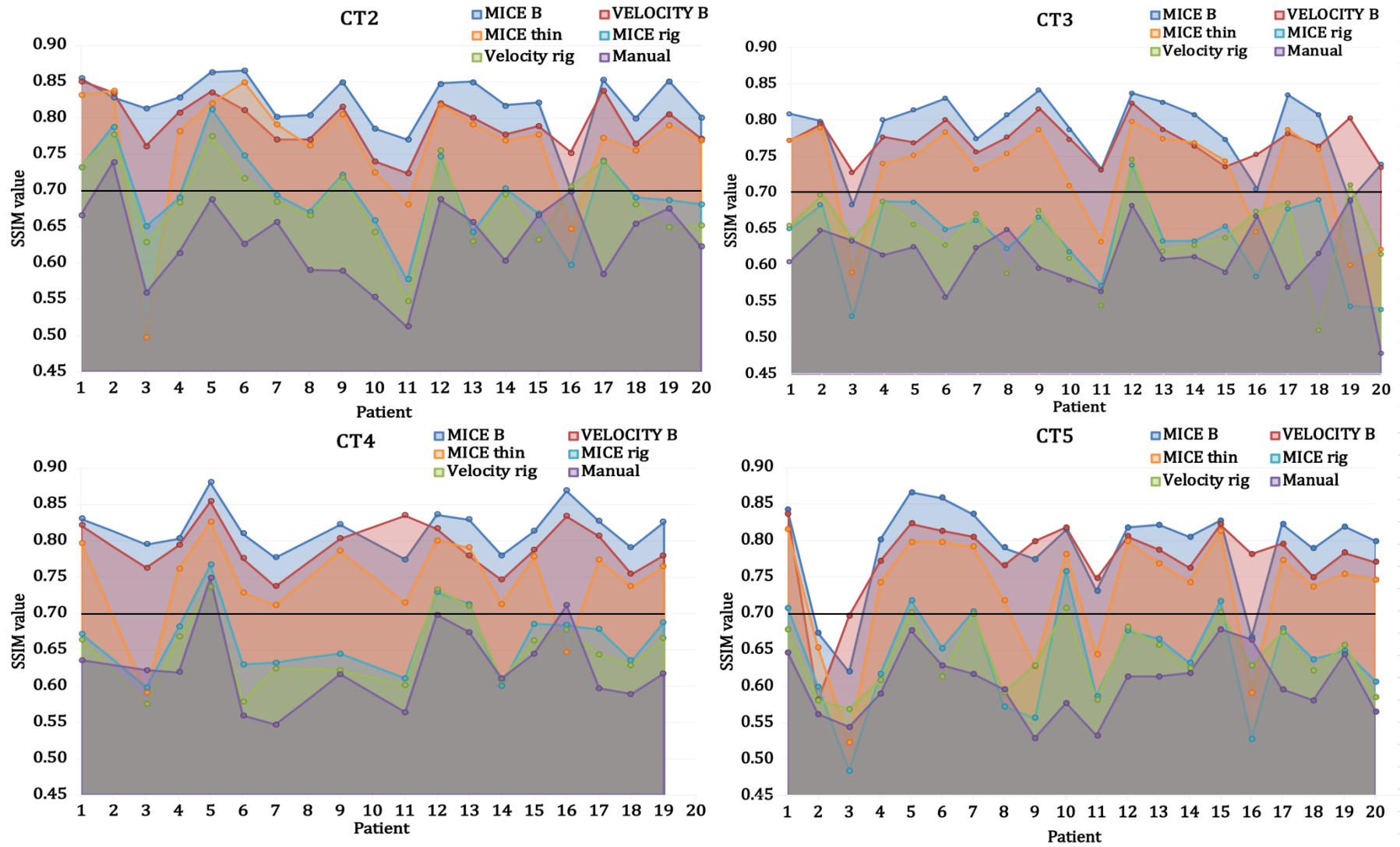


Figure 34: SSIM calculated for the six registration algorithms in four different plots for every subsequent CT acquired (CT2, CT3, CT4 and CT5). The black line indicates what is generally considered very good overlap between reference and evaluated image.

Figure 35 and Figure 36 show two visual examples (CT2 of case 13 and CT3 of case 17) of the differences between the two algorithms in the spleen region. In both cases spleen was better registered by MICE, giving a higher quality registration metric as output.

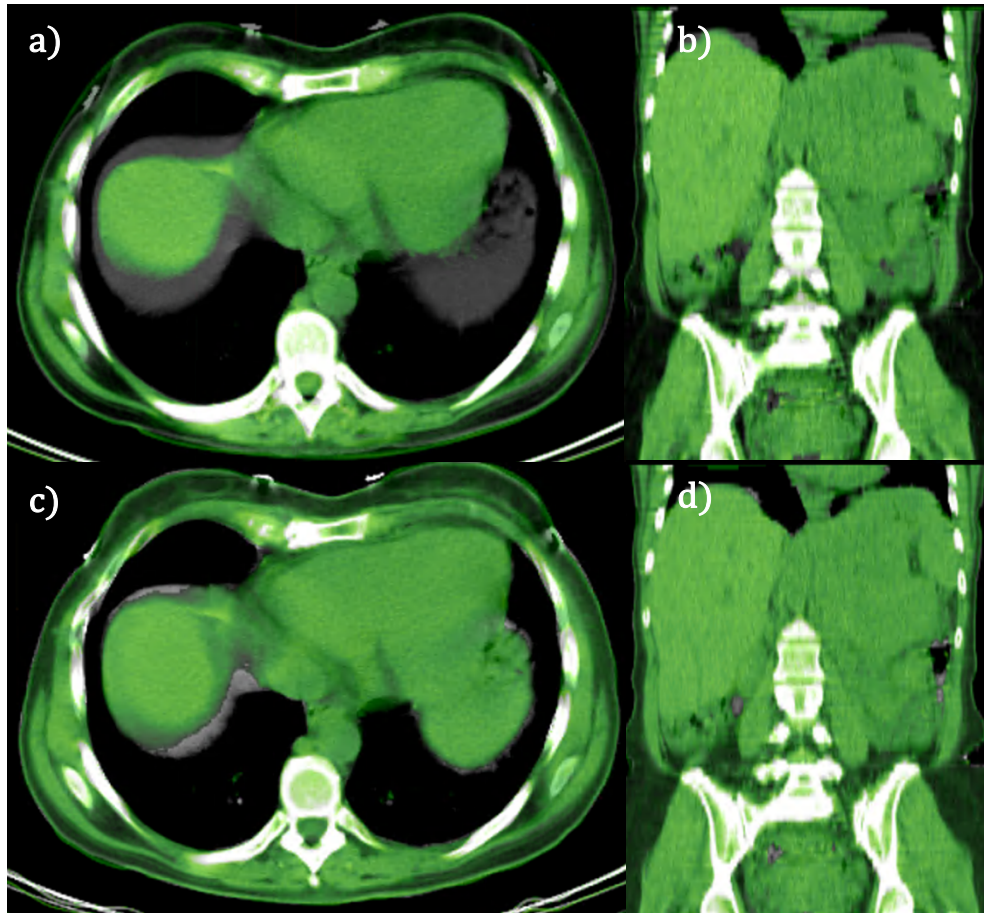


Figure 35: Comparison between CT1 and CT2 for case 13 using the Velocity algorithm (a and b) and the MICE toolkit (c and d) on axial and sagittal view.

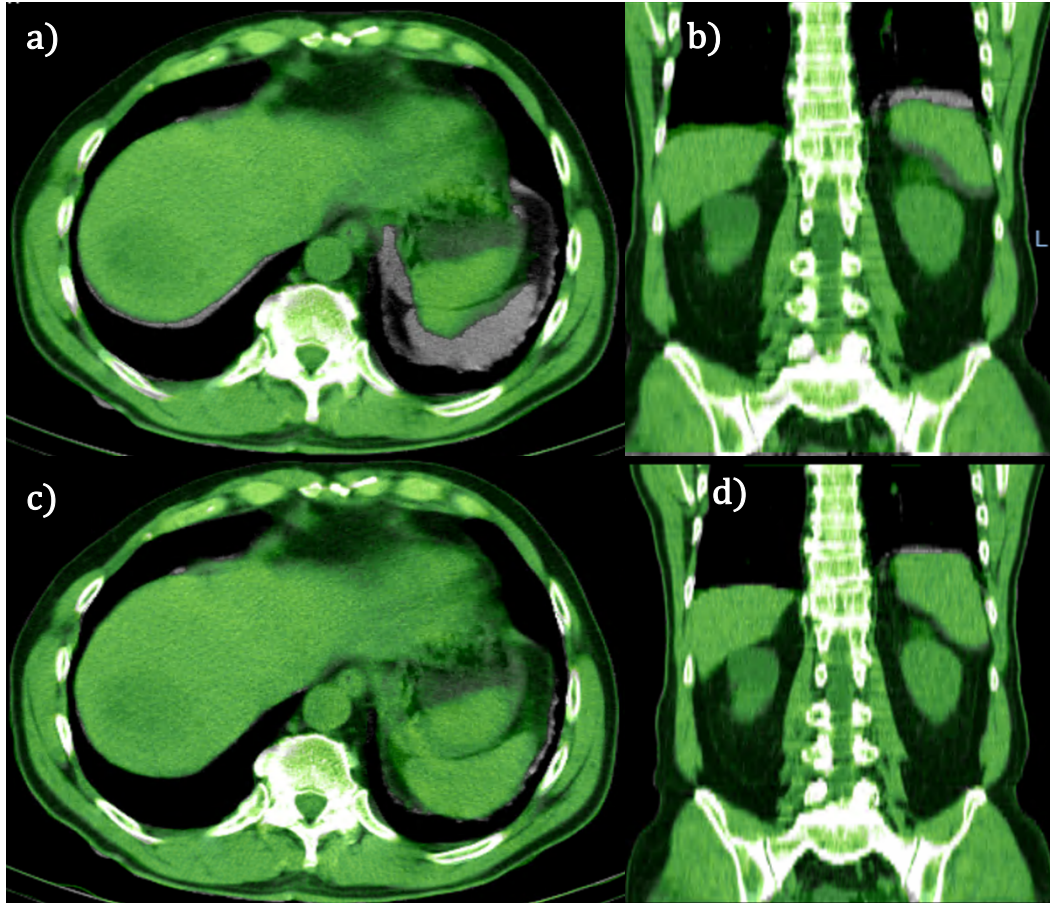


Figure 36: Comparison between CT1 and CT3 for case 17 using the Velocity algorithm (a and b) and the MICE toolkit (c and d) on axial and sagittal view.

From the SSIM analysis (Figure 34), it can also be noted a significant drop in the SSIM value for patient 2 and patient 3 on the co-registration of CT1 and CT5.

For patient 2 this is due to a different lie down position of the patient: during the last scan, the patient required a lumbar support to minimize the pain, which results in a different spinal curvature, as shown in Figure 37.



Figure 37: Sagittal view of patient 2 during CT1 (on the left) and CT5 (on the right). The lumbar support required by the patient changed the shape of the spine, causing the registration mismatch. Window level settings for CT5 were manually modified in order to show the lumbar support.

It is interesting to see how the algorithms performed against this issue; visual assessment is reported in Figure 38.

The Velocity B-spline algorithm (Figure 38.a) was able to better co-register the entire spine, ignoring the bed matching. On the other hand, MICE toolkit gave the priority to bed matching, as can be noted in Figure 38.d, Figure 38.e and Figure 38.f. During the manual registration (Figure 38.c), priority was given to the kidney region.

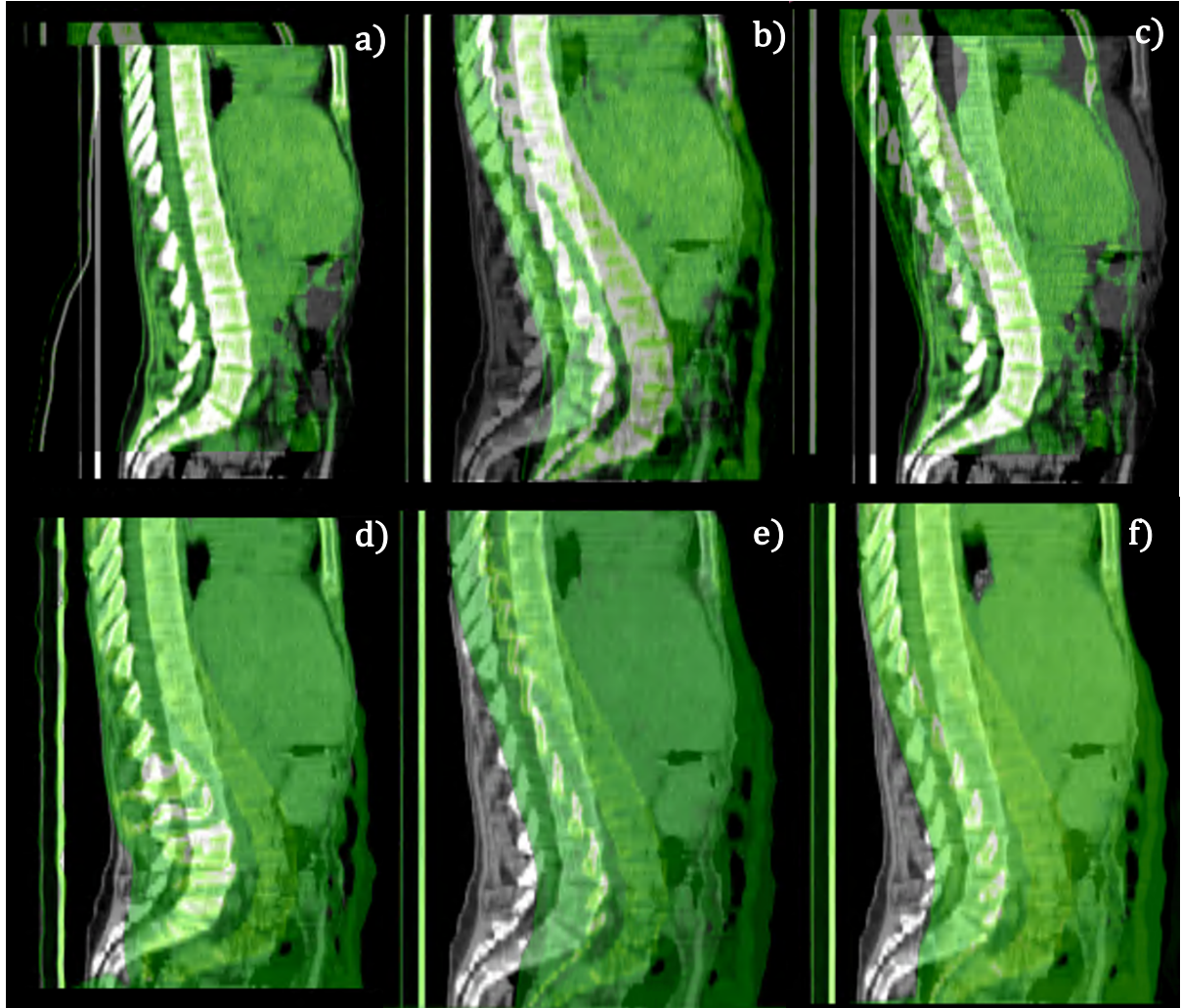


Figure 38: Sagittal view of the co-registration between CT1 (in greyscale) and CT5 (in green scale) for the algorithms: a) Velocity B-spline; b) Velocity rigid; c) manual; d) MICE B-spline; e) MICE rigid; f) MICE thin plate-spline.

For patient 3, the difference was due to the fact that CT1 and CT5 were acquired with a significantly different extension of the scan region in the superior-inferior direction as shown in Figure 39. This resulted in a detrimental impact in the SSIM similarity index value.

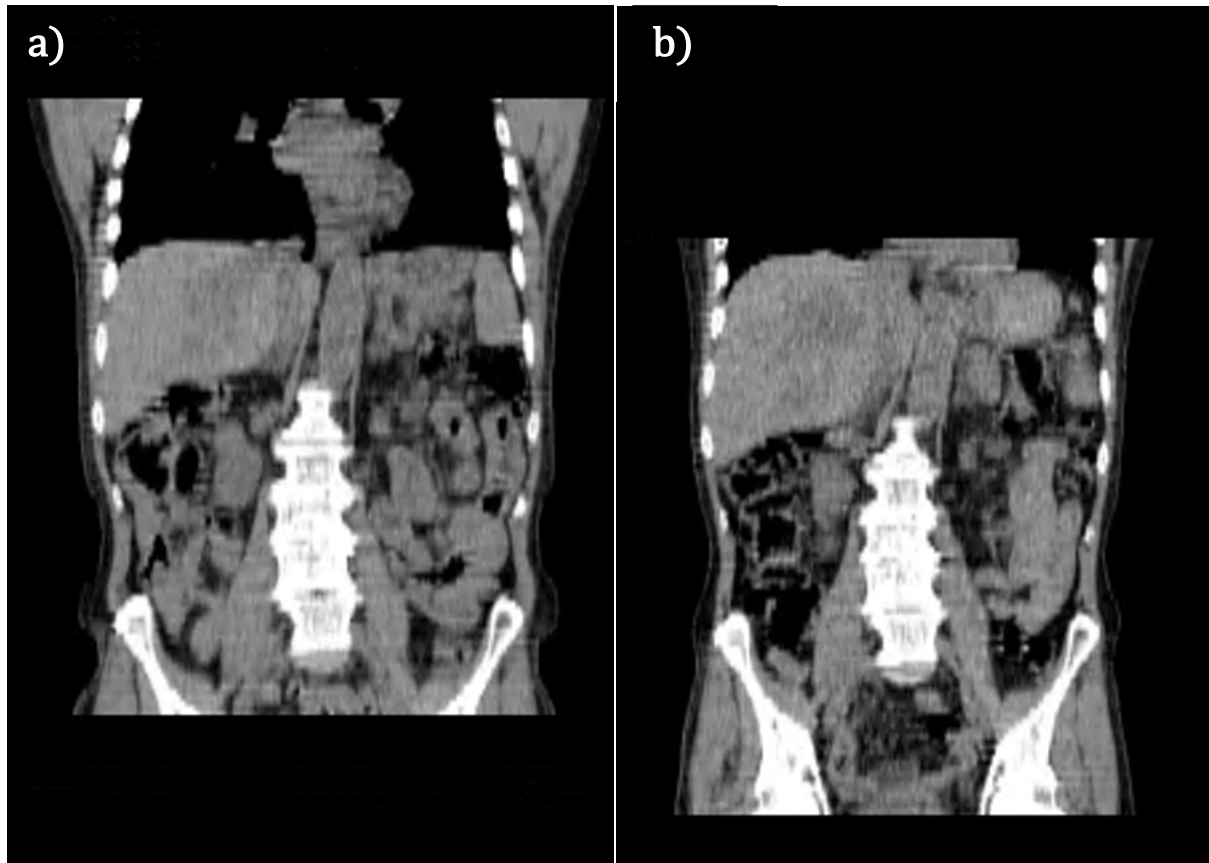


Figure 39: Difference in scan length for patient 3 during a) CT1 and b) CT5.

Differences between all the registration methods were quantitatively evaluated with a Wilcoxon test (two sides, significance level 0.05) and Table 7 reports the cases where differences were found to be statistically significant.

p-values	CT2	CT3	CT4	CT5
MICE B vs Velocity B	YES	NO	YES	NO
Velocity B vs MICE thin	YES	YES	YES	YES
MICE B vs MICE thin	YES	YES	YES	YES
MICE rigid vs Velocity rigid	YES	NO	YES	NO
Velocity rigid vs manual	YES	YES	YES	YES
MICE rigid vs manual	YES	YES	YES	YES

Table 7: The table reports if the differences between all the algorithms calculated using a Wilcoxon test are statistically significant (or not).

Differences were found highly statistically significant in particular between the B-spline algorithms and the thin plate spline algorithm. Differences between the two B-spline methods were found statistically significant only on CT1 and CT4. The same trend was found for the comparison between the two rigid registration methods.

The registration algorithms were also very different in terms of computational time. Average time in seconds and the linked standard deviation error is reported in Table 8.

Registration method	Mean time (s)
MICE B spline	346.8 ± 4.9
MICE thin plate spline	3177.7 ± 19.9
MICE rigid	34.7 ± 0.9
Velocity B spline	27.6 ± 0.4
Velocity rigid	4.6 ± 0.2
Manual	116.1 ± 46.2

Table 8: The table reports the mean computational time in seconds required by each registration algorithm and its standard deviation.

This time study showed that Velocity algorithm was much faster than the MICE toolkit. In particular, the B spline registration algorithm was approximately 15 times faster, while the rigid algorithm was 10 times faster. As expected, the manual method was the algorithm which required more time to perform. The high variation in the measurement reflects large

variations in patient initial position, which can vary considerably between each patient and scan.

The SSIM analysis showed that the non-rigidly registered CT scans conform more closely to the reference CT than the rigidly registered ones. This proves that non-rigid registration algorithms, in particular B-spline algorithms, are high quality methods and they have an appropriate nature of the image registration workflow used in this study.

The B-spline algorithm implemented in MICE performed better in 81% of the cases against the one implemented in Velocity, but differences were found to be statistically significant only on CT1 and CT4. For this reason, performances of the two B-spline algorithms can be considered comparable. The same considerations can be made for the two rigid registration algorithms; differences were statistically significant in half the cases, analogous to the B-spline algorithms. Despite the similar performances, the algorithms required a significantly different amount of computational time. The non-rigid registration method implemented in Velocity runs approximately 15 times faster than the algorithm implemented in the MICE toolkit, while the rigid registration algorithm runs 10 times faster. Performance of the thin-plate spline algorithm was acceptable in most of the cases, but it is a very time consuming algorithm, depending on the number

of landmarks chosen for the registration. A lower number of landmarks would have speeded up the algorithm, but reduced the performance of the registration algorithm.

Because of the large number of data elements available from the DOTATER protocol, the more efficient Velocity platform was preferred in order to speed up the analysis in the following sections, since its performance was in other respects comparable with the ITK toolkit.

4.2. Impact of rigid and non-rigid registration algorithms on dose calculation

In this section, the performances of the rigid and non-rigid registration algorithms from the Velocity platform are compared in terms of their impact on the dosimetric calculation. For this analysis, the same subset of patients from the previous section was chosen. For each one of the 5 sequential scans, the SPECT images were already co-registered with an identity registration with the corresponding CT scan (SPECT1 with CT1, SPECT2 with CT2, SPECT3 with CT3, SPECT4 with CT4 and SPECT5 with CT5) since anatomical and functional scan were acquired in the same frame of reference. For each patient, the sequential CT scans were registered onto the same frame of

reference as the initial CT scan. Using the Velocity software, it is possible to apply the registration maps to any secondary volume, or indeed radiotherapy object such as contours or dose maps, associated with the primary volume of each scan. Hence each sequential SPECT scan (SPECT2, SPECT3, SPECT4 and SPECT5) was also registered on the same frame of reference of the first CT scan (CT1) using the registration maps generated in the previous section.

Dosimetric calculations were performed with the Raydose system described in section 2.2. For each simulation, a number of histories of 10^7 was chosen, with a typical associated calculation time of 2.5 hours per patient.

Standard dose quantities such as mean and maximum doses were used to assess the dose distribution for the two registration methods chosen. Percentage differences (PD) between mean doses were evaluated analogously to equation (50):

$$PD = \frac{D_{rig} - D_{def}}{D_{rig}} \cdot 100 \quad (55)$$

D_{rig} is the dose calculated after the rigid registration and D_{def} calculated after the non-rigid registration. Rigid registration has been arbitrarily taken as reference.

The box plot in Figure 40 shows the percentage differences as defined in equation (55). It can be noted that the PD are negative for:

- left kidney (range: $[-20.24, 19.01]$; median = -0.85 ; first quartile (Q1) = -1.90 ; third quartile (Q3) = 3.11),
- right kidney (range: $[-20.15, 7.59]$; median = -6.17 ; Q1 = -14.09 ; Q3 = -3.89),
- spleen (range: $[-106.72, 2.34]$; median = -9.31 ; Q1 = -37.36 ; Q3 = -3.06)
- lesions (range: $[-622.78, 61.19]$; median = -16.99 ; Q1 = -63.08 ; Q3 = 1.06).

For the liver, PD is positive (range: $[-27.75, 14.71]$; median = 3.01 ; Q1 = -2.41 ; Q3 = 8.32); this may be related to the large mobility of the liver and the wide number of lesions usually present in the organ.

This trend indicates that the dose calculated using a rigid registration algorithm is generally lower than the dose calculated using a non-rigid registration algorithm.

The differences between the two registration methods were statistically significant for right kidney, spleen and lesions (p-values < 0.05).

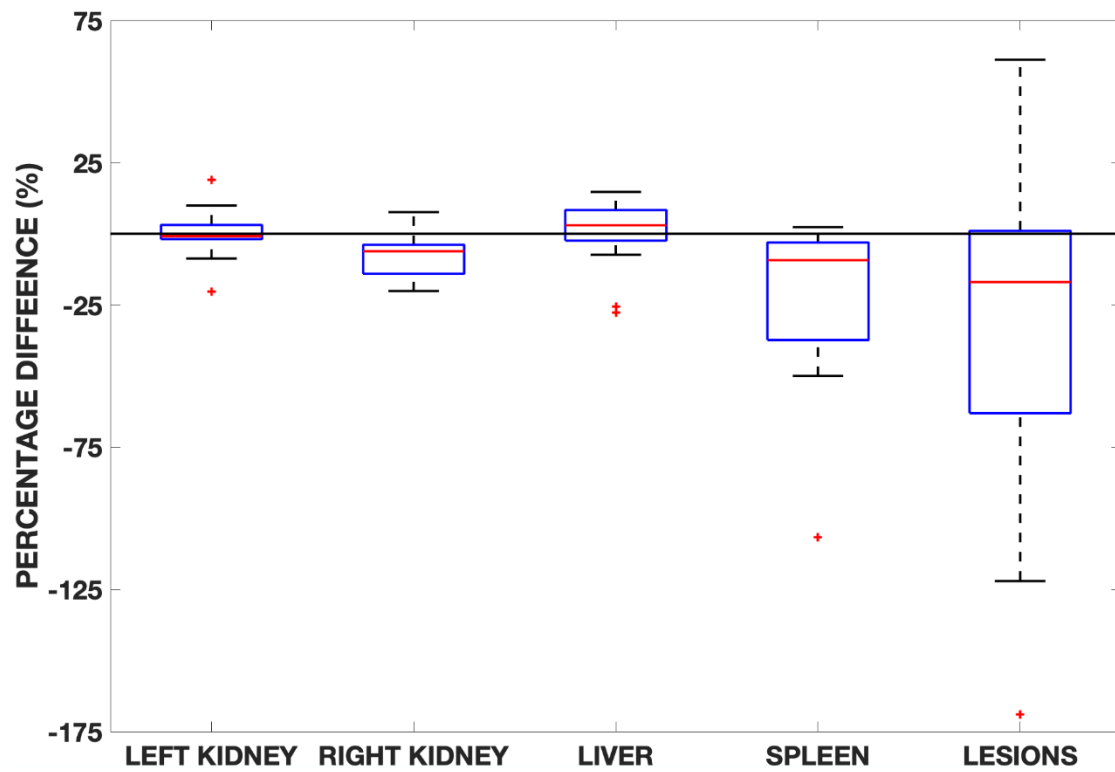


Figure 40: The boxplot reports the distribution of the percentage differences between the two registration methods for the OARs and the lesions. The y-axis has been cut off at -175% for a better legibility, for the lesions four whiskers are missing (-218.75, -233.16, -402.13, -622.78)

The opposite assumption can be made for left kidney and liver. Figure 41 reports graphically the Bland-Altman analysis for all OARs and lesions; the mean differences are:

- for left kidney -0.03 ± 0.54 Gy;
- for right kidney 0.25 ± 0.55 Gy;
- for liver 0.096 ± 0.83 Gy;
- for spleen 0.40 ± 0.84 Gy;
- for the lesions 1.33 ± 4.74 Gy.

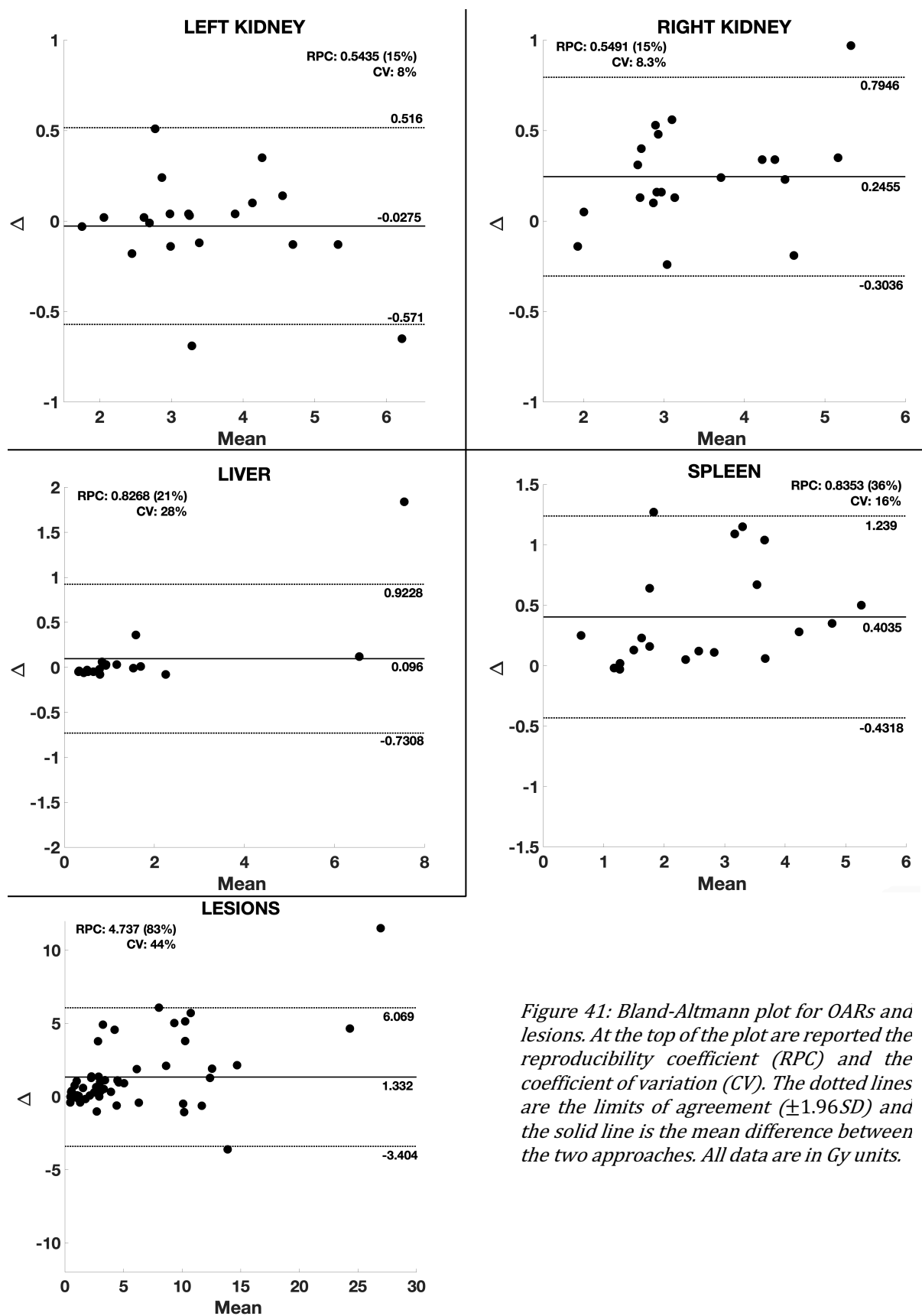


Figure 41: Bland-Altman plot for OARs and lesions. At the top of the plot are reported the reproducibility coefficient (RPC) and the coefficient of variation (CV). The dotted lines are the limits of agreement ($\pm 1.96SD$) and the solid line is the mean difference between the two approaches. All data are in Gy units.

Differences in the right kidney are higher than the ones in the left kidney because of the liver proximity. In fact, in some cases (e.g. Figure 42), the rigid registration may overlap the liver radioactivity to the kidney anatomy, resulting in a higher (and incorrect) estimation of the absorbed dose to the right kidney. On the other hand, the non-rigid registration algorithm is able to better register the anatomy, reducing the radioactivity estimation error. This does not happen with the left kidney, because there is not any significant overlap with the spleen anatomy.

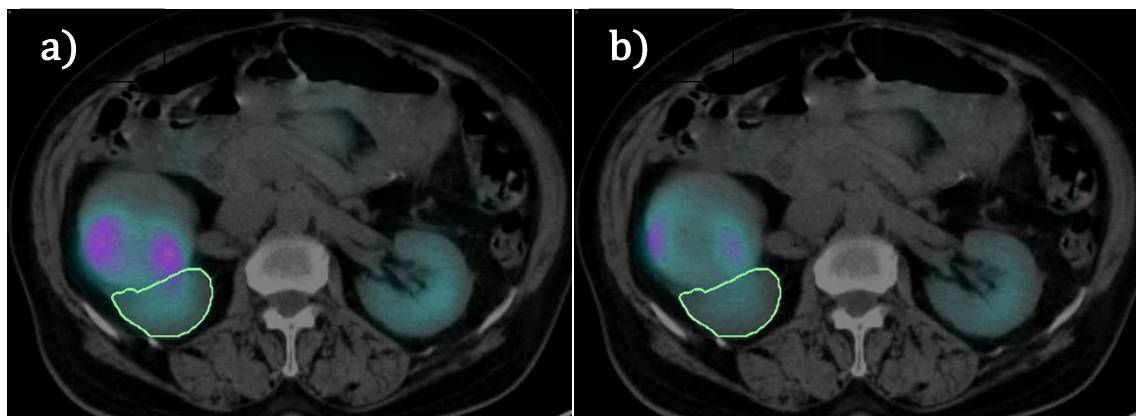


Figure 42: The picture shows the example of a SPECT number 3 (in colour scale) rigidly registered (a) and non-rigidly registered (b) to the CT1 (in greyscale). The contour of the right kidney is in light green. It can be noted that in the rigid registration case, some radioactivity from the liver overlapped the kidney anatomy, which does not happen if a non-rigid registration is used.

The outlier in the liver plot is from case 9. The high mean dose is due to two very hot lesions present in the liver; in this case the non-rigid registration algorithm changed the shape of one of the two lesions, overlapping part of the liver on the stomach anatomy (due to the similar tissue density between the two organs).

Figure 43 shows the lesion from NM1 (a) and from NM3 (b) after the application of the non-rigid registration algorithm. It can be noted that part of the lesion activity overlapped with the stomach anatomy, reducing the amount of activity inside the liver outline.

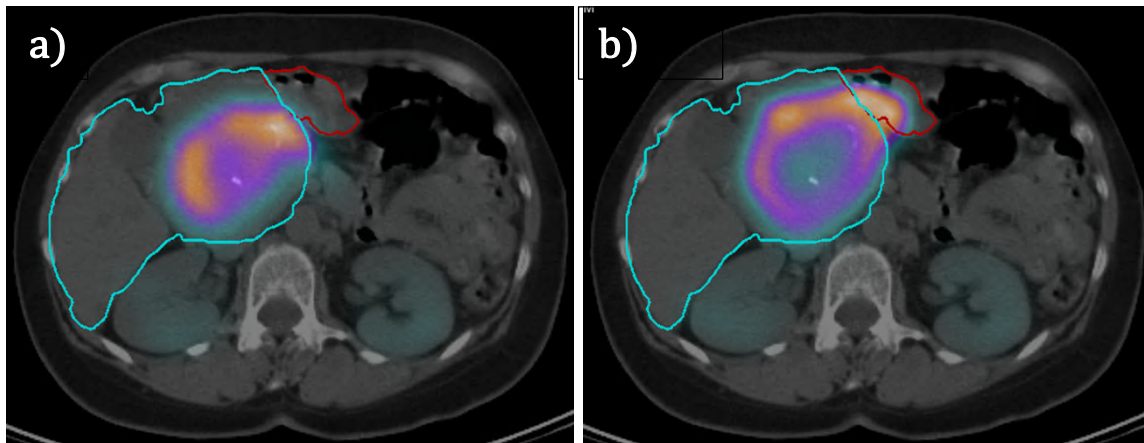


Figure 43: The picture shows a) NM1 over CT1 identically registered and b) NM3 over CT1 non-rigidly registered. This mis-registration caused the outlier in the Bland-Altman plot for the dose analysis between the rigid and the non-rigid registration algorithm. Liver outline is in cyan, while stomach is outlined in red.

The similarities between the anatomical images are translated to the SPECT scans, since the applied registration matrices are the same. Since the previous section proved the superiority of the non-rigid algorithms over the rigid ones, this demonstrates a higher degree of improvement for the absorbed dose calculated with the non-rigid registration algorithm than the one calculated using the rigid version. In EBRT, several works about non-rigid registration have been published with plenty of results (180–182), but in MRT only few papers are available (183,184). Furthermore, recent works

have demonstrated the superiority of non-rigid registration for PET/CT (105), 4-dimensional CT (185) and MRT (106).

D_{def} was found to be generally higher than D_{rig} , this result was expected since the non-rigid algorithm may vary the quantification of the activity inside VOIs during registration. These differences were very similar to the ones calculated with a small number of cases (n=10) by Grassi et al. (106); on the other hand, differences in absorbed dose from this study were found on average to be lower than the ones calculated by Ao et al. (183). As noted in the work by Grassi et al., this may be due to the fact that Ao et al. used a single CT image acquired at 24 h for the attenuation correction in the reconstruction of each sequential SPECT image. In addition, VOIs were outlined on SPECT scans that in many cases are larger than VOIs contoured on CT images. The approach taken in the present work (analogous to Grassi et al.) makes quantitative imaging more accurate and more appropriate for a PRRT trial.

As determined by the Bland-Altman analysis (Figure 41), differences in absorbed dose were statistically significant. This demonstrates that image-based dosimetry for ^{177}Lu PRRT is affected by the type of algorithm used to co-register the sequential SPECT/CT scans. For this reason, the implementation of a workflow which implements a non-rigid registration

algorithm in clinical trials such as DOTATER can bring important beneficial implications in personalised dosimetry.

4.3. Impact of the non-rigid algorithm: activity vs dose registration

The superiority of non-rigid registration compared to rigid registration has been demonstrated on recent PET and SPECT imaging studies (105,106,183,186) as well as in the previous section. Although non-rigid registration algorithms are often applied to SPECT images, an investigation of a workflow which involves dose maps has not previously been reported in the literature.

In this section, two different workflows involving deformable image registration (DIR) algorithms are described in order to evaluate how these algorithms perform when applied to SPECT scans and to the dose maps used to calculate the patient-specific 3D dose calculations.

For this part of the study, the same subset of patients from the previous section has been used. To evaluate the impact of different image registration maps on the dosimetry assessment, the following two workflows were evaluated in this study: (a) activity deformation workflow (AD), (b) dose

deformation workflow (DD). In the AD workflow, for each patient, the activity map from each sequential SPECT/CT scan was deformed on the same frame of reference as the first CT scan, as described in Section 4.1. In the DD workflow, the original activity scans were first used to calculate time-point 3D dose maps (partial DM). Since the partial DMs were created as secondary volumes with an identity registration to the primary CT scan, it was then possible to register them on the frame of reference of the first CT scan and sum them to obtain the cumulative dose map. The two workflows are detailed in Figure 44.

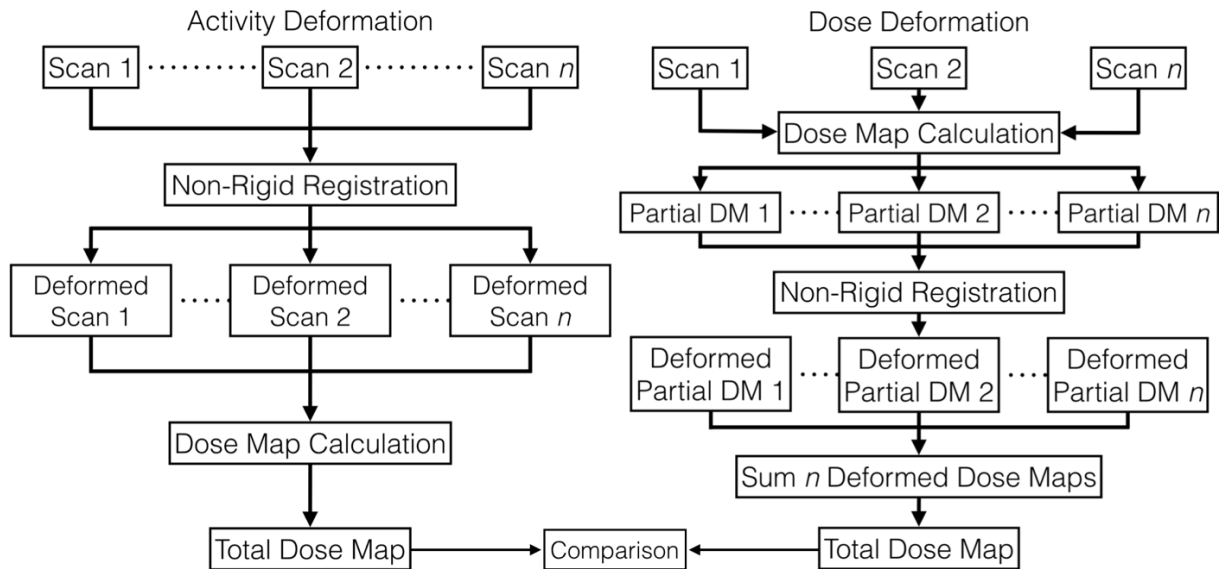


Figure 44: Details of AD workflow (left) and DD workflow (right) implemented in this study for 3D dosimetry assessment.

It is worth noting that although the two workflows used the same non-rigid registration maps, two different integration methods had to be used in order to produce the total dose map.

For the AD workflow, since 5 activity maps in the same frame of reference were supplied, the total dose was obtained using a VOI-specific Time Activity Curve (TAC) calculated with a trapezoidal method and linear fit between each scan point. For the DD workflow, since only 1 activity map was supplied for each time point, the dose was calculated using an exponential decay model with an effective decay constant from the current scan time to the next scan time. An example of TAC calculated for both AD and DD workflows is shown in Figure 45.

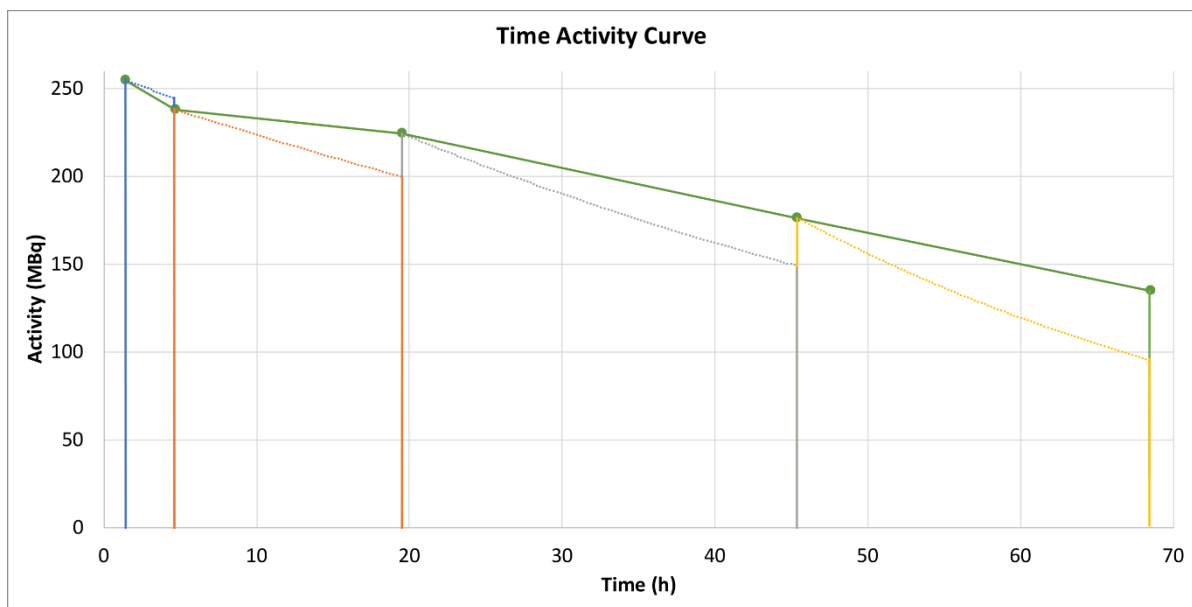


Figure 45: Time Activity Curve calculated for AD workflow (solid line) and DD workflow (dotted line).

In both workflows, an exponential tail was added after the last scan point with the effective decay constant, evaluated with a mono exponential fit from the Time Activity Curve using a spreadsheet software.

For each VOI, standard dose statistics such as mean dose and dose maximum were automatically calculated.

In order to evaluate quantitative differences between the total dose distributions obtained with the two workflows, the relative PD between mean doses were calculated analogously to equation (33):

$$PD = \frac{D_{DD} - D_{AD}}{D_{AD}} \cdot 100 \quad (56)$$

Where D_{DD} is the dose calculated using the DD workflow and D_{AD} is the dose calculated using the AD workflow. PD for OARs and lesions are reported in the boxplot of Figure 46.

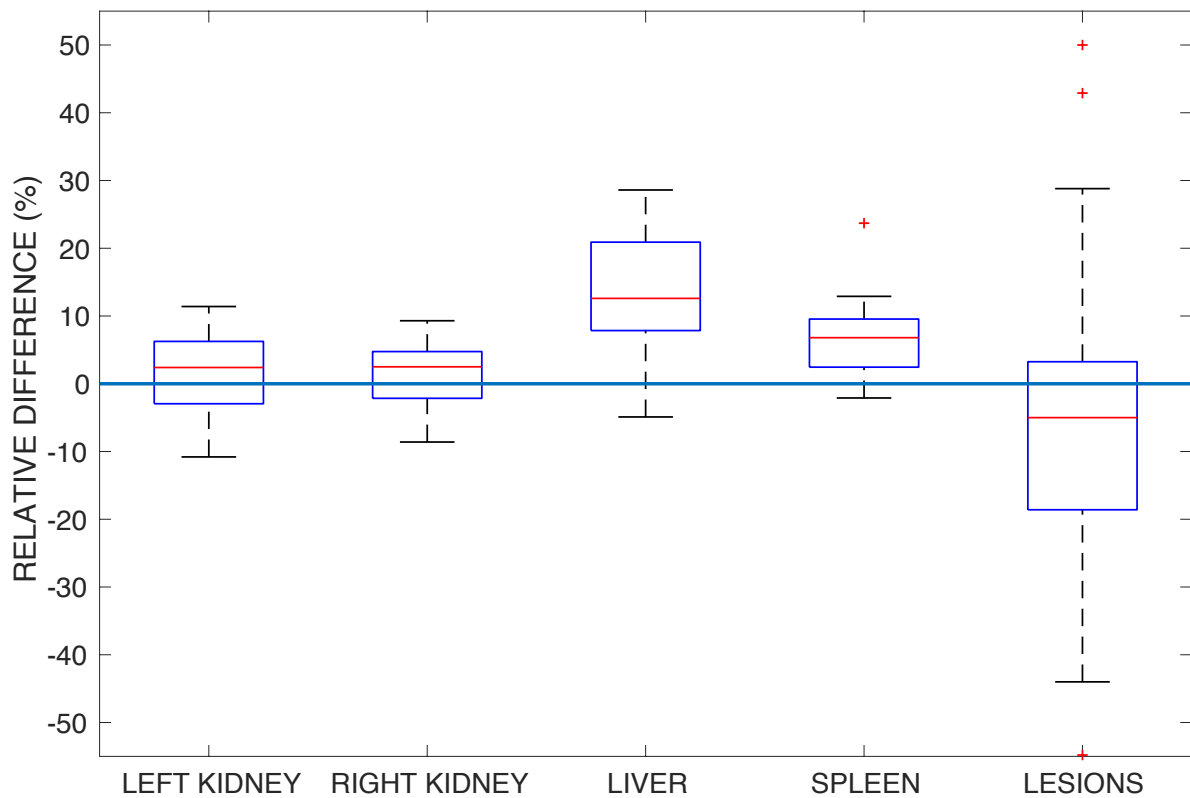


Figure 46: Boxplot with the distribution of percentage differences between AD and DD workflow for OARs and lesions.

These differences were not statistically significant according to a paired sample Wilcoxon test (two sides, significance level 0.05; p values: 0.8181 for left kidney; 0.9138 for right kidney; 0.5161 for liver; 0.9138 for spleen; 0.8341 for lesions). Furthermore, the Bland-Altman analysis is reported in Figure 47. The average difference was:

- for left kidney: 0.02 ± 0.27 Gy;
- for right kidney: 0.03 ± 0.15 Gy;
- for liver: 0.02 ± 0.17 Gy;
- for spleen: 0.07 ± 0.52 Gy;
- for lesions: -0.39 ± 3.41 Gy.

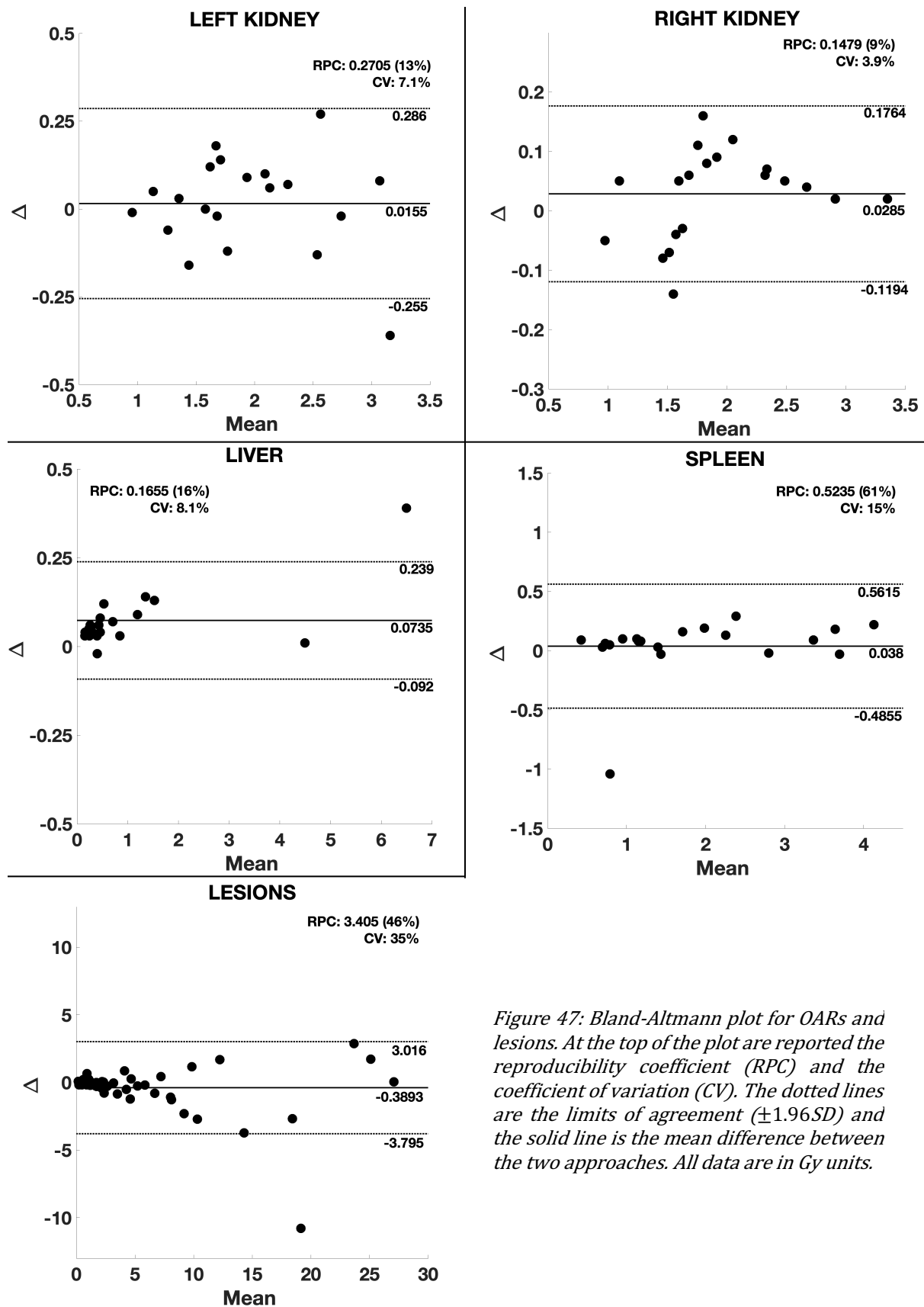


Figure 47: Bland-Altman plot for OARs and lesions. At the top of the plot are reported the reproducibility coefficient (RPC) and the coefficient of variation (CV). The dotted lines are the limits of agreement ($\pm 1.96SD$) and the solid line is the mean difference between the two approaches. All data are in Gy units.

From the Bland-Altman analysis it can be noted that only for the liver the differences in calculation were statistically significant ($p\text{-value} < 0.01$), but for the others OARs and for the lesions, this cannot be stated. The outlier on the liver plot is from the same case mentioned in the previous section. In this case, the difference in the absorbed dose is due only to the different fitting method of the TAC, since the registration map applied in both workflows is the same.

A workflow with a non-rigid registration which involves dose maps instead of activity scans has not been previously investigated in the literature. Very recently, Dewaraja et al. (187) reported initial results of fully 3D multi-SPECT/CT image-based dosimetry of lesions and kidneys. In this paper, a non-rigid registration algorithm was used to co-register dose rate maps and then they were numerically integrated to obtain 3D dose maps. However, this study was performed only to compare a multi SPECT/CT-based dosimetry with a simplified procedure with a single SPECT/CT image. This preliminary work currently does not include any comparison with a traditional workflow involving the deformation of activity scans. The study performed in this thesis demonstrates that a workflow with a non-rigid registration which involves dose maps instead of activity scans does not improve the dose calculation, since there is no significant difference between

the two approaches as demonstrated by the Bland-Altman analysis. Furthermore, the DD workflow is approximately 5 times more time consuming than the AD workflow, which makes the DD workflow disadvantageous to be implemented in a clinical trial. In fact, in clinical trials as DOTATER it is vital that the dose calculation requires the minimum possible processing time for the fastest possible planning of the MRT treatment.

5. Personalised Advanced 3D dosimetry

To increase the quality and the efficacy of clinical trials, a detailed and reliable 3D patient-specific dosimetry is required. MC techniques (cf. Chapter 2) in particular offer the most accurate approach for MRT dose calculations (188).

In the first section of this chapter, the dose calculation performed with the Raydose MC based software is compared with a computational approach based on the MIRD schema. In the second section, a new segmentation method for lesions is presented and its performance is compared against a method commonly used in routine clinical practice.

5.1. Raydose vs MIRD schema

In clinical practice, the calculation of absorbed dose is performed using the MIRD schema, as described in section 1.4.2. Following this method, dose calculation is not planned or optimised for patient-specific characteristics.

In this section, patient-specific absorbed doses for OARs and lesions evaluated with the Raydose MC code (described in section 2.2) were compared with standard dose calculations obtained with the OLINDA/EXM

software which is based on the MIRD schema at the organ level (cf. section 1.4.2.1).

For this study, the complete set of patients from the DOTATER clinical protocol was used. Sequential scans were co-registered using the non-rigid registration algorithm from the Velocity workstation described in section 4.1. OARs and lesions were manually outlined by physicians and physicists from AUSL-IRCSS. For the dosimetric calculation with Raydose, a value of 10^8 histories per scan was chosen, corresponding to an average calculation time of ~ 24 hours per patient. The dose calculation was performed with an effective decay constant that was computed for each VOI using an external spreadsheet software.

As mentioned in section 1.4.2.1, OLINDA/EXM is based on male and female anthropomorphic phantoms; for each patient, the mass of the single organs was manually changed to match the real body weight of the patient. The residence time for the calculation was evaluated using a spreadsheet software. Furthermore, a mono-exponential fit was considered for the determination of the absorbed dose to the organs. Since OLINDA/EXM considers both kidneys as a single organ, for the purpose of this analysis kidneys were treated as a single VOI. For the absorbed dose to the lesions, instead, the sphere model implemented in the software was used.

The 'boxplot' in Figure 48 shows the mean percentage error of the MC calculation carried out with Raydose for OARs and lesions. As it can be noted, the errors were well below 5% for each case in either direction.

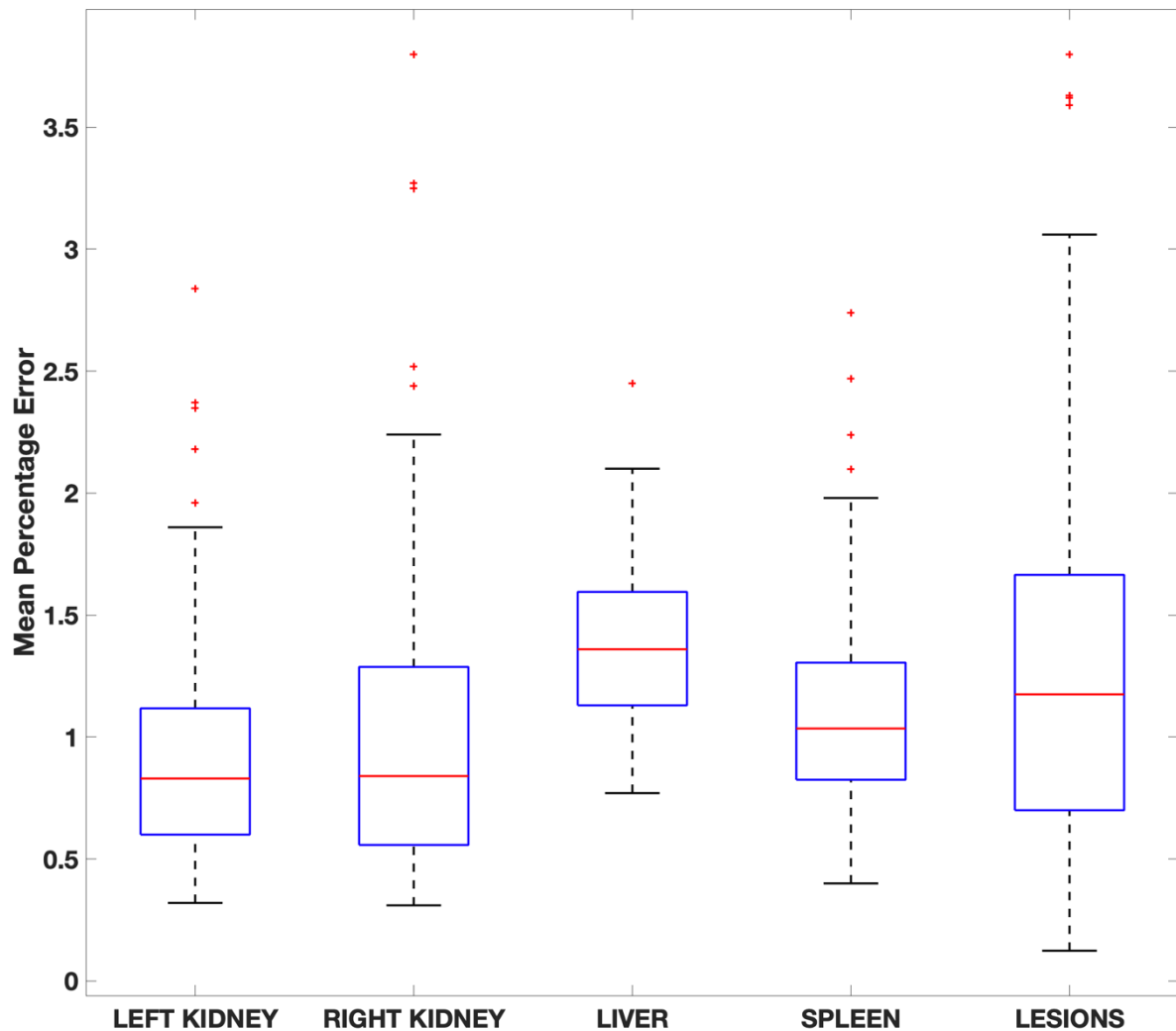


Figure 48: The boxplot reports the mean percentage errors for the MC calculation of each VOI.

Table 9 reports the mean absorbed doses calculated in Gy/GBq with Raydose and OLINDA/EXM for all the VOIs and its standard deviation error.

	Kidneys	Liver	Spleen	Lesions
Raydose	0.49 ± 0.22	0.30 ± 0.38	0.63 ± 0.85	1.17 ± 1.74
OLINDA/EXM	0.55 ± 0.28	0.32 ± 0.42	0.87 ± 2.07	2.98 ± 18.72

Table 9: The table reports the mean absorbed dose in Gy/GBq calculated with Raydose and OLINDA/EXM with its standard deviation error.

The PD between the doses calculated with the two methods was calculated as follows:

$$PD = \frac{D_R - D_O}{D_O} * 100 \quad (57)$$

where D_R is the dose calculated with Raydose and D_O the dose calculated with OLINDA/EXM.

Doses calculated with the MIRD schema were taken as reference. A boxplot of the PD is reported in Figure 49.

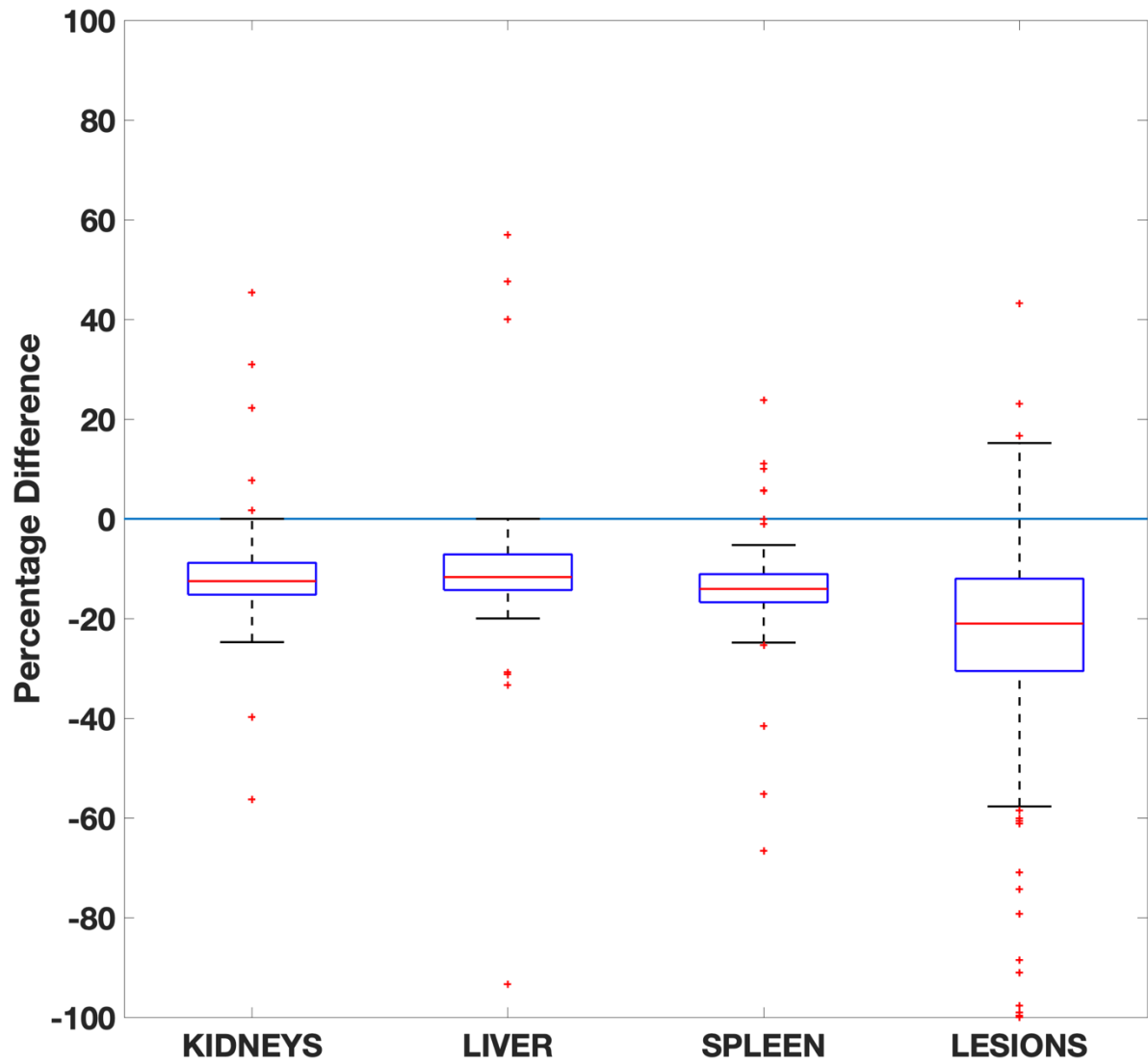


Figure 49: The boxplot reports the distribution of the differences between the two calculation methods for OARs and lesions. The plot is limited between -100% and 100% because of some whiskers $\gg 500\%$.

From Figure 49 it can be noted that PD are mainly negative for all the OARs and the lesions:

- for kidneys: range= $[-56.25, 200]$; median = -12.50 ; $Q1 = -15.22$; $Q3 = -8.84$;
- for liver: range= $[-93.33, 823.67]$; median = -11.70 ; $Q1 = -14.29$; $Q3 = -7.14$;

- for spleen: range= $[-66.55, 733.33]$; median = -14.06 ; Q1= -15.22 ; Q3= -8.84 ;
- for lesions: range= $[-99.91, 2150]$; median = -20.93 ; Q1= -15.22 ; Q3= -8.84).

These differences were statistically significant only for the kidneys and lesions (p-value<0.005). This was confirmed by the Bland-Altman analysis carried out and shown in Figure 50. The mean difference was:

- for kidneys: -0.06 ± 0.18 Gy;
- for liver: -0.02 ± 0.28 Gy;
- for spleen: -0.24 ± 2.62 Gy;
- for lesions: -0.70 ± 7.29 Gy.

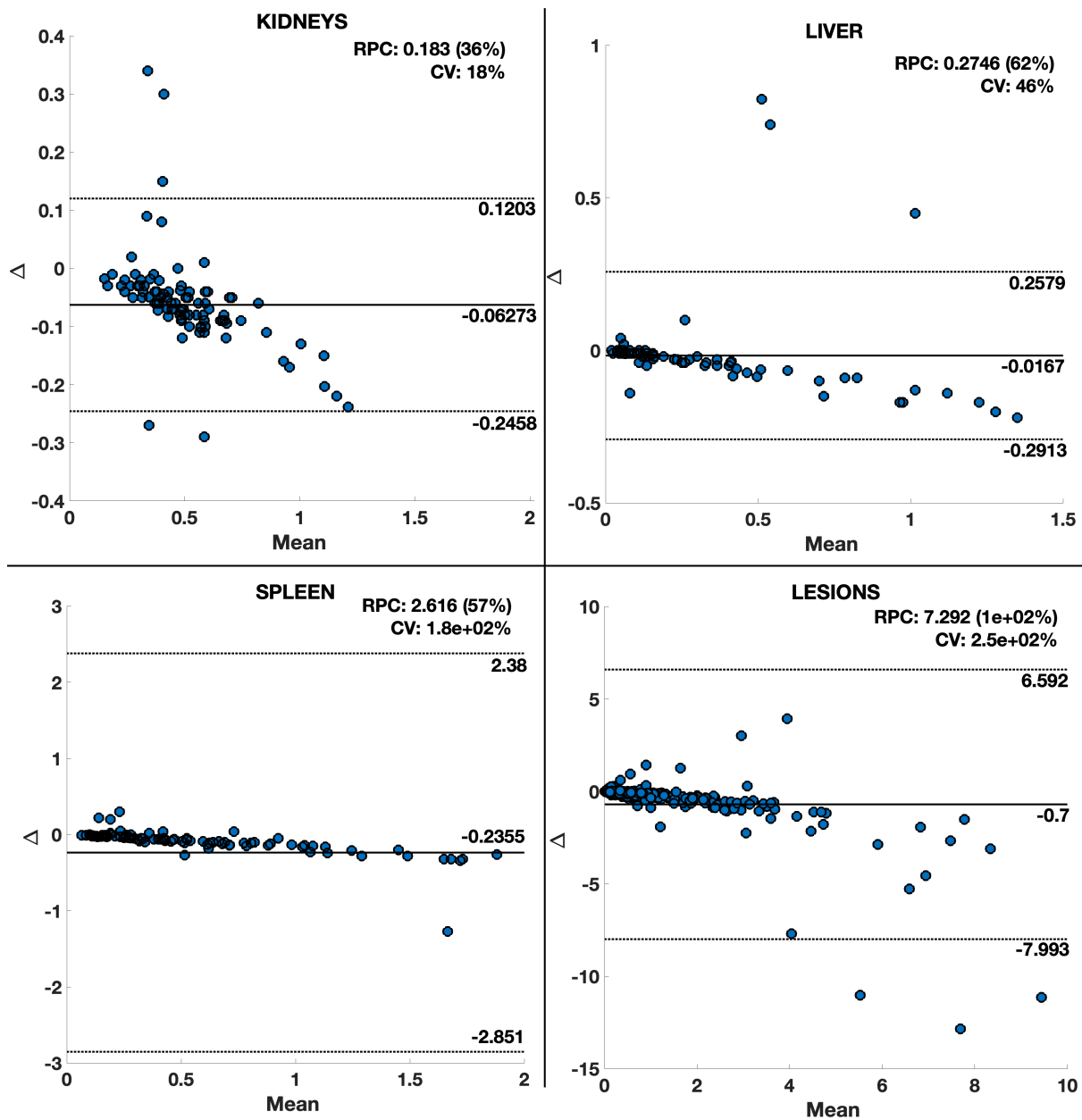


Figure 50: Bland-Altman plot for OARs and lesions. At the top of the plot are reported the reproducibility coefficient (RPC) and the coefficient of variation (CV). The dotted lines are the limits of agreement ($\pm 1.96SD$) and the solid line is the mean difference between the two approaches. All data are in Gy units.

In particular, it can be noted that for the lesions, the Spearman coefficient was very low ($R^2=0.29$) indicating that the data collected from the two software systems were not correlated.

The downward trend in the Bland Altman plots suggests that the overestimation on the absorbed dose calculated with OLINDA/EXM is higher when the mean dose absorbed by the VOI is higher.

Mean dose to the kidneys was reasonable when compared with other studies present in the literature which used OLINDA/EXM (121,129,189,190). Table 10 summarises the results obtained by these authors.

Author	Method	N of patients	Dose (Gy/MBq)
Del Prete et al. (189)	SPECT/CT images	36	0.55 ± 0.2
Marin et al. (190)	SPECT/CT images	47	[0.61;0.78;0.98]
Garkavij et al. (121)	Planar images	21	1.15 ± 0.29
Wehrmann et al. (129)	Planar images	61	0.9 ± 0.3
This study	SPECT/CT images	100	R (0.49 ± 0.22) O (0.55 ± 0.28)

Table 10: The table reports the mean dose in Gy/MBq \pm the standard deviation error for some works available in literature for the absorbed dose to the kidneys. For Marin et al. the mean does is reported as [Q1;median;Q3].

The majority of works in literature focus their attention on kidneys (and, naturally, lesions) because they are, together with the bone marrow, dose-limiting organs and thus renal function is a prescribing consideration for NET patients.

The significant difference in the absorbed dose to the kidneys between Raydose and OLINDA/EXM may be due to the paired dose approach used in the latter. The kidneys may show a patient asymmetry which is not taken into account by treating the paired organs as one mass, as is done in OLINDA/EXM. This was also noted by Wormgoor et al. in a study using ^{111}In (191). This paired organ approach was also found inaccurate by Grimes et al. (192), where dose to right and left kidneys differed by up to 73%.

The difference in the dose absorbed by the lesions may be due to the fact that OLINDA/EXM uses a spherical model for the evaluation of dose absorption by the lesions, which assumes a spherical shape and does not consider any contribution from the nearby voxels. Furthermore, this model simulates only a certain number of volumes, so to determine the dose to the right volume, a linear fit between the two closest points was assumed.

Similar differences were reported in the literature for studies comparing Monte Carlo methods with the OLINDA/EXM spherical model. Howard et al. (193) in their ^{131}I study, analysed 57 tumours (2 to 423 cc of volume) finding an average underestimation of 14% (range 2%-31%) of the OLINDA/EXM calculation against their Monte Carlo method. In another ^{131}I study, Divoli et al. (194) found a good agreement (differences <5%) between the Monte Carlo method and the OLINDA/EXM sphere model. The study was limited to

two small lesions of 7 cc of volume; the authors affirmed that for bigger volumes the spherical approach may underestimates the dose, because they have a larger probability to receive cross-irradiation from nearby tissues, which is not considered by the OLINDA/EXM model. Grimes et al. (192) analysed different radionuclides, including ^{177}Lu . For this isotope, the difference between the Monte Carlo method and the sphere model was $-6.0\% \pm 5.4\%$. In this case only 3 lesions (23 to 95 cc of volume) were taken into account.

The work presented in this thesis includes many more lesions and range of volumes compared to what currently available in the literature. A total of 273 lesions was analysed in a range between 1.5 cc and 1769.7 cc (49 cc on average); the median difference between the Monte Carlo method and the spherical approach was -20.93%. This means that in the majority of the cases, OLINDA/EXM overestimated the dose to the lesions.

Significant differences were found for kidney mean dose calculation. The paired-organ approach in the OLINDA/EXM software may be inaccurate because of the patient asymmetry that left and right kidney may have. When other organs are considered (i.e. liver and spleen) dose calculated with OLINDA/EXM were in good agreement with the Monte Carlo dose estimates. Furthermore, significant differences were found when dose absorbed by

lesions is taken into account. The Raydose Monte Carlo method provides a more accurate estimation compared to the sphere model included into OLINDA/EXM, because it can take into account cross-irradiation components from nearby tissues.

This work suggests that implementing a more accurate 3D patient specific dose calculation method based on the MC technique can significantly change the assessment of the dose absorbed to lesions. The impact of this in clinical practice should be further investigated through the preparation of clinical trials based on imaging.

5.2. Lesion segmentation: dose peak threshold

In clinical practice, an accurate delineation of the VOI is important in order to evaluate its volume and successively to calculate the absorbed dose. Contouring lesions on images provided by an anatomical imaging modality such as CT is an accurate way to define volumes but, unfortunately, this method is not always applicable since lesions may not be clearly visible on CT images (106). In particular, liver lesions are often not visible because the contrast between the tumour tissue and the liver parenchyma may be low (195). In such cases, SPECT contouring may be preferable as it provides functional information with similar performance to the CT contouring modality, especially for small volumes (196). The volume is often determined by a preselected percentage of the maximum activity within the VOI, known as threshold (196). Threshold values may vary from 25 to 70%, but values close to 40% are most often used in clinical practice (196,197). There are no specific guidelines about lesion delineation on SPECT, so different threshold methods are taken in account by different research groups. Erdi *et al.* (197) suggested a threshold of 42% of the activity when the tumour-to-non-tumour ratio (T:NT) is higher than 5:1, and a threshold of 71% when T:NT is less than 5:1, to yield fewer errors during the segmentation. Uribe *et al.* (196) compared three different methods: a fixed

40% threshold, a CT segmentation and their own iterative adaptive dual thresholding method (198). Krak *et al.* (199) outlined lesions on PET using a region growing method using a threshold of 50% and one of 75%.

Furthermore, a method based on outlining the lesions on a single scan may disregard how the total activity accumulates over time in a patient's body. This can lead to a sub-optimal definition of the target volume and, consequently, a potentially wrong assessment of the absorbed dose.

The following section describes a new segmentation method, which takes into account the total activity accumulated over time. We also compare the performance of the new segmentation method with that of the standard clinical practice.

For this study, 252 lesions have been identified and outlined with two different methods: the clinical standard (CS) and the new dose-segmentation (DS) method. For the CS method, lesions were manually outlined on the first SPECT scan, or on the scan where the uptake was demonstrated to be the highest by expert physicians and physicists from AUSL-IRCSS (200).

On the other hand, for the DS method, lesions were outlined on the dose map using a function of the threshold related to the ratio between the dose peak of the lesion and the background dose absorbed by tissue near the lesion. In

particular, background was considered as a set of 4 spheres of 1 cm in diameter placed in the four cardinal directions close to the lesion to outline, separated from the bounding box visually built around the lesion by a voxel (approximately 4.5 mm) and centred in the same axial slice of the dose peak. Dimension of the background sphere is the same as defined in the PERCIST criteria (201). Distance of the background sphere from the bounding box was taken arbitrarily, considering that the mean penetration of the β^- radiations produced by ^{177}Lu is $670\ \mu\text{m}$. Figure 51 shows an example of how the background was outlined for each lesion taken into account.

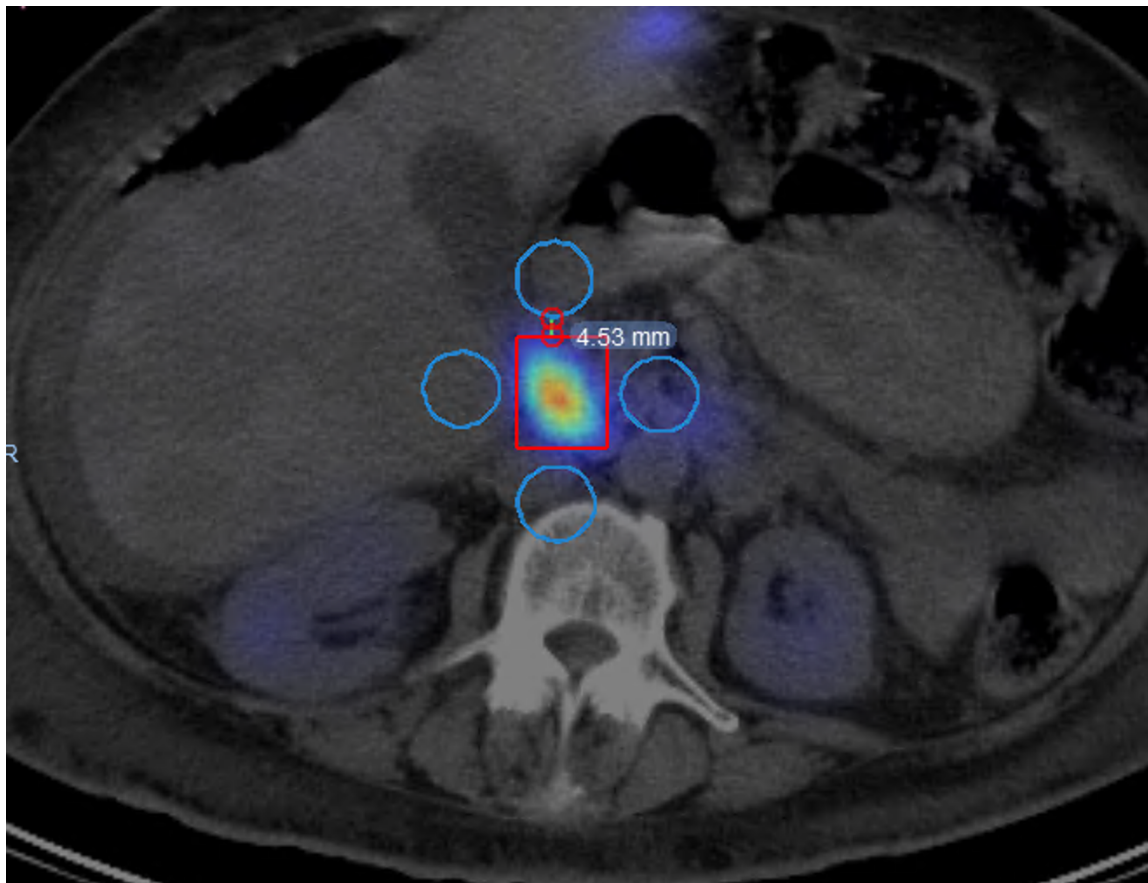


Figure 51: Example of how the background was outlined and analysed. The ruler tool shows the average distance between the sphere and the lesion uptake of 4.5mm.

To build the threshold function, an experiment was conducted using a synthetic Jaszczak phantom with dimensions 20*22*22 cm filled with water and with several spherical inserts of different size and activity concentration. SPECT scans were simulated using the Monte Carlo simulation code SIMIND (described in 1.4.3.2). Settings in SIMIND were chosen to match the SPECT scanner present in the ASMN-IRCSS.

Sizes of the inserts were chosen between the average (14 cc) and the maximum (40 cc) volume of all the lesions identified in this work (Figure 52). These two values were calculated removing the outliers using the Tukey's fences method (202,203) (all the values outside the first and the third quartile were removed).

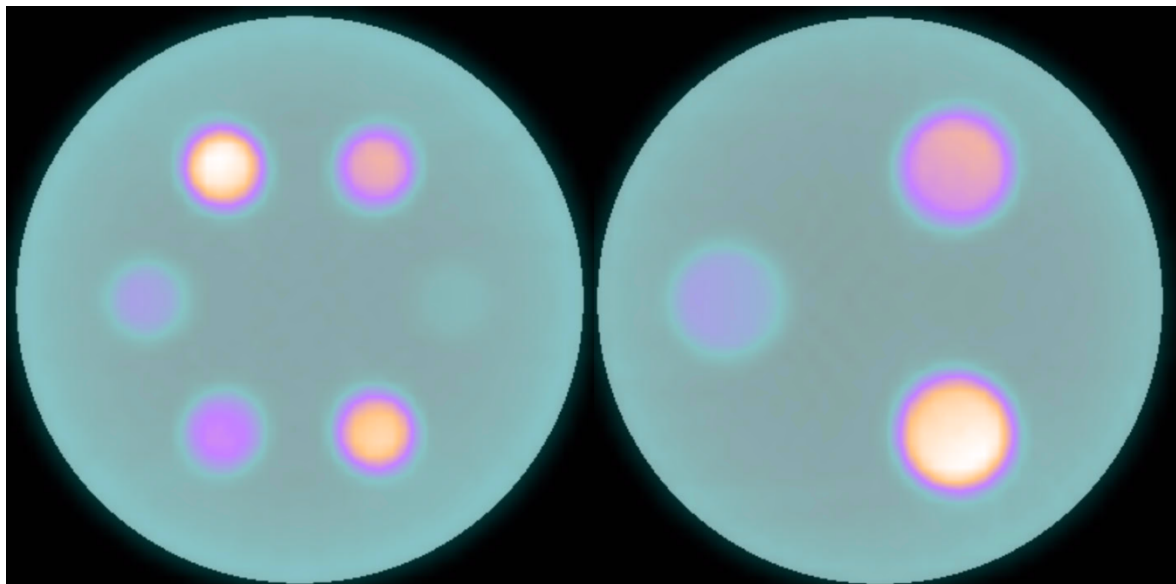


Figure 52: The picture shows the Jaszczak phantom simulated for the experiment with the average (on the left) and the maximum (on the right) volume of the lesions chosen for the inserts.

To outline the spheres, the threshold was chosen experimentally in order to match the nominal volume of the sphere and the associated dose peak-to-background ratio (DP-B ratio) was then recorded. During the experiment, the threshold value was found to be independent of the volume of the spheres.

The values obtained from the experiment are listed in Table 11.

Lesion index	Dose peak	Background	DP-B ratio	Threshold
1	35.18	16.38	2.15	69.00
2	33.27	15.05	2.21	67.70
3	49.48	16.76	2.95	60.65
4	62.62	16.94	3.70	58.00
5	60.68	15.31	3.96	57.20
6	76.97	17.07	4.51	54.50
7	91.55	16.89	5.42	52.00
8	91.48	15.88	5.76	51.00
9	54.19	4.75	11.41	47.50
10	67.07	5.13	13.07	45.70
11	79.07	5.17	15.29	44.50
12	85.23	5.04	16.91	46.00
13	32.55	1.68	19.38	45.20
14	51.08	1.84	27.76	44.70

Table 11: Experimental data obtained from the Jaszack phantoms simulations to obtain the relationship between threshold function and Dose Peak-Background Ratio.

The experimental data were modelled with a range of fitting functions and parameters including linear, exponential and power, as reported in Table 12.

Function type	Equation	R ²	SSE	Coefficients
Linear	$ax + b$	0.6451	324.71	2
Exponential (1 term)	$a * \exp(bx)$	0.6925	281.30	2
Exponential (2 terms)	$a * \exp(bx) + c * \exp(dx)$	0.9936	5.88	4
Power (1 term)	$a * x^b$	0.9187	74.35	2
Power (2 terms)	$a * x^b + c$	0.9939	5.56	3

Table 12: List of the fitting type used reporting the equation the R-squared value and the sum of squared errors (SSE).

Visual presentation of the fitting functions is provided in Figure 53.

1

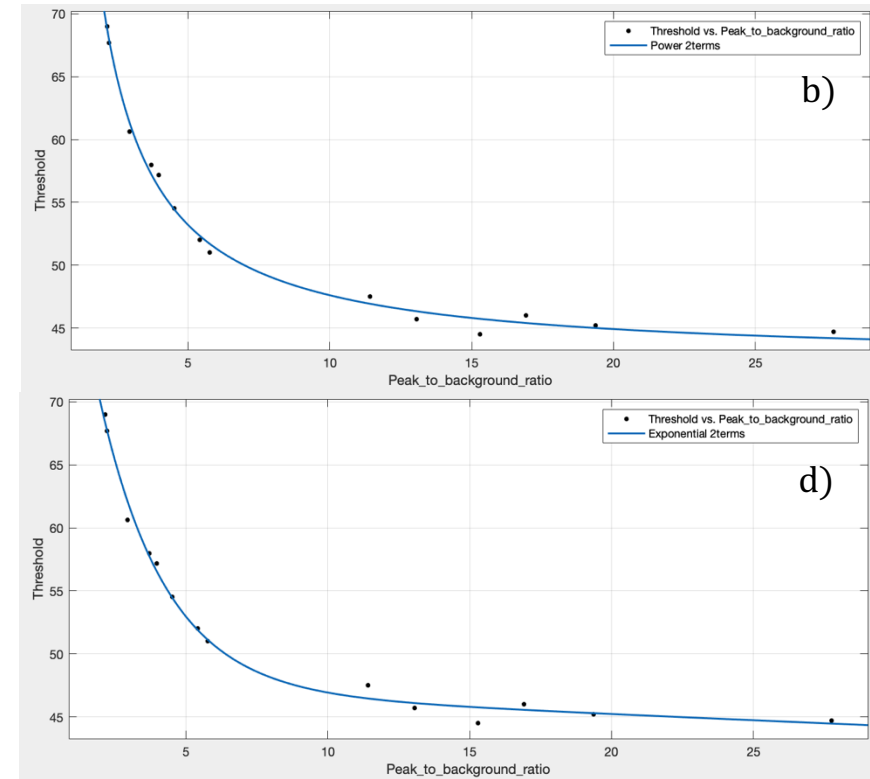
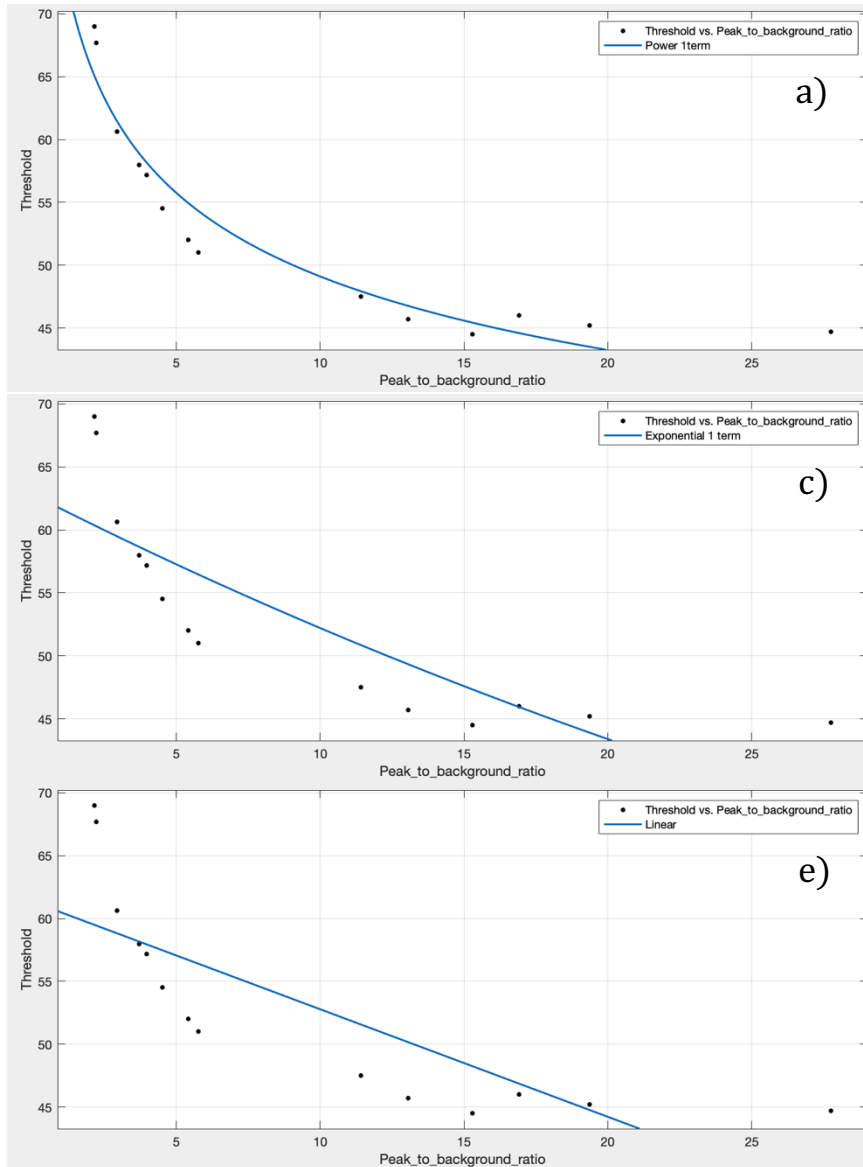


Figure 53: Fitting plot of the experimental data using the functions: a) power with 1 term; b) power with 2 terms; c) exponential with 1 term; d) exponential with 2 terms; e) linear.

As can be noted from the results, the power function with two terms and the exponential function with two terms gave the best fits, but the power function was preferred because of the smaller number of coefficients required for the analysis.

To outline the lesion, a bounding box was visually drawn around it, then the 4 spheres to calculate the background were drawn 4.5 mm apart the bounding box in the four cardinal directions. The lesion was then outlined using the threshold value obtained from the fitting function using the DP:B ratio from the lesion taken into account:

$$Threshold = a * (DP:B ratio)^b + c \quad (58)$$

From the fitting, the following constant values were obtained: $a = 59.27$; $b = -1.059$; $c = 42.44$. For the lesions outlined in this work, the range of threshold values goes from a minimum of 42.50% to a maximum of 70.65%, with an average value of 46.97%. The threshold distribution is reported in Figure 54.

For 116 lesions (46% of the total cases) a threshold between 40% and 45% was used, while for the 36% of the cases a threshold value between 45% and 50% was used. Only for the 17% of lesions a threshold up to 70.65% was obtained.

Threshold distribution

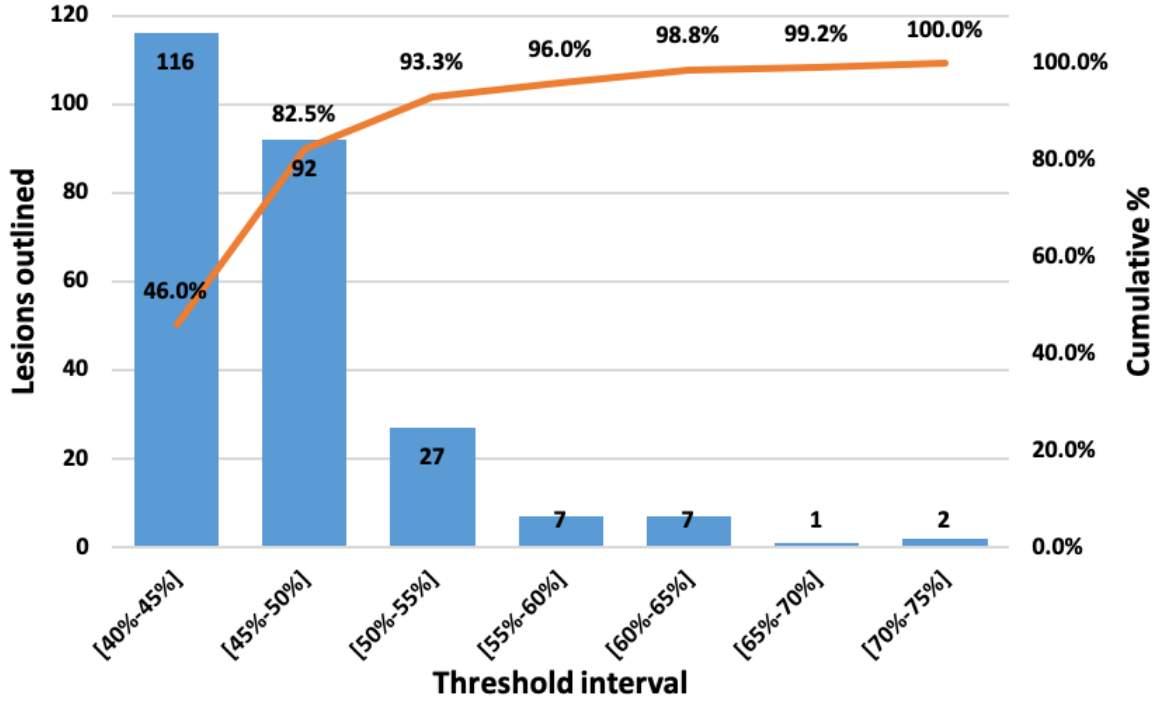


Figure 54: Threshold distribution of the lesions outlined for the purpose of this work. Orange line represents the cumulative percentage distribution to the left of the point of interest.

To evaluate similarities between the two segmentation methods, the Jaccard metric was used. This metric is defined as follows:

$$J(A, B) = \frac{|A \cap B|}{|A \cup B|} \quad (59)$$

where A and B are the two volumes taken into account. A histogram for this analysis is reported in Figure 55.

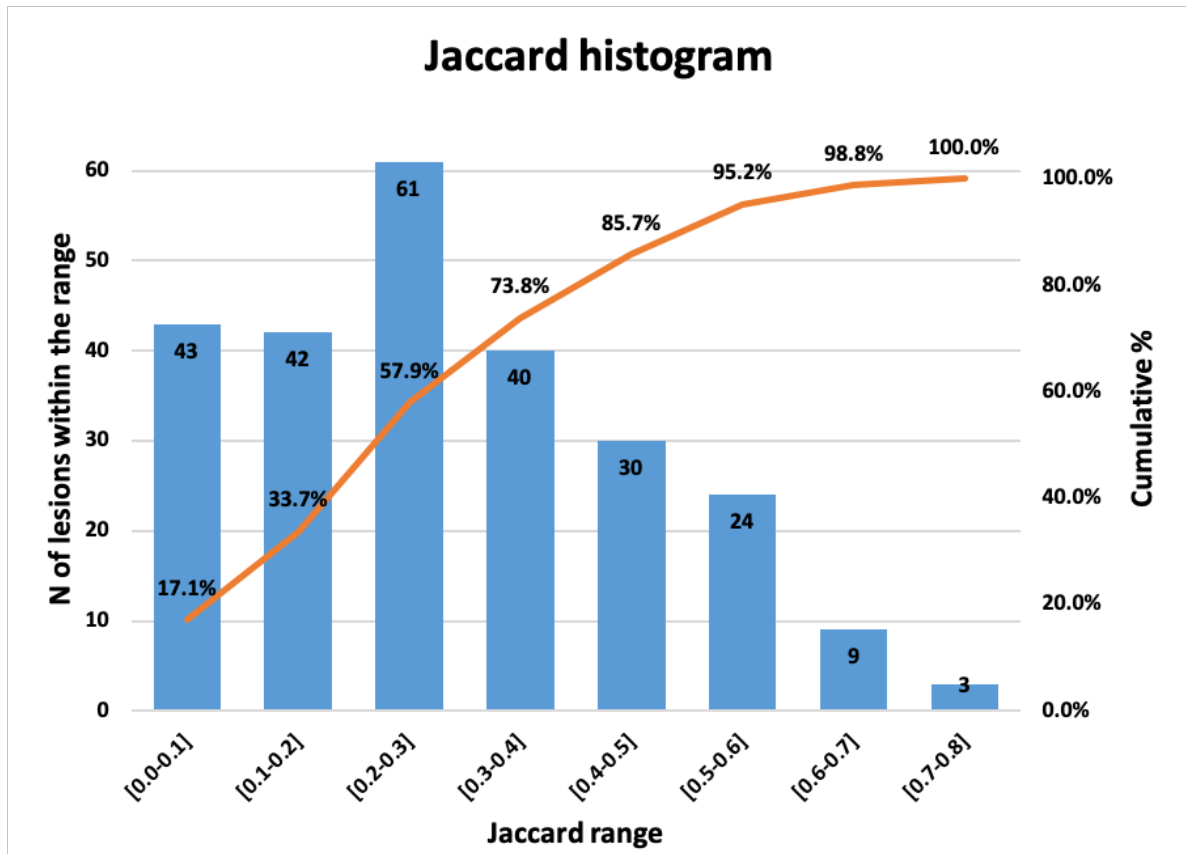


Figure 55: Histogram for the JACCARD analysis performed in this study. Orange line represents the cumulative percentage distribution to the left of the point of interest.

It can be noted that 86% of the cases had a Jaccard index lower than 0.5 and no cases had an index higher than 0.8; the mean value was 0.29. In this case, there is not a good overlap between the two volumes, because as already mentioned in section 4.1, only conformity indices higher than 0.70 show a very good overlay (179).

In addition, to evaluate differences in position of the lesions, an analysis was carried out of the shift in the Centre of Mass (COM) of the two volumes.

The distance d in cm between the two COMs in the 3D space was calculated as defined in the Euclidean geometry:

$$d = \sqrt{(x_2 - x_1)^2 + (y_2 - y_1)^2 + (z_2 - z_1)^2} \quad (60)$$

where x , y and z are the coordinates of the two centres of mass and results are reported in the histogram in Figure 56.

It can be noted that no lesions have a total shift between 0 and 0.3 cm and only the 4% between 0.3 and 0.6 cm, while in the 68% of the lesions the COM has shifted between 0.6 and 1.5 cm. Only 2 lesions (0.8%) had a shift over 3 cm. The rest of the lesions (27.4%) had a COM shift between 1.5 and 3 cm.

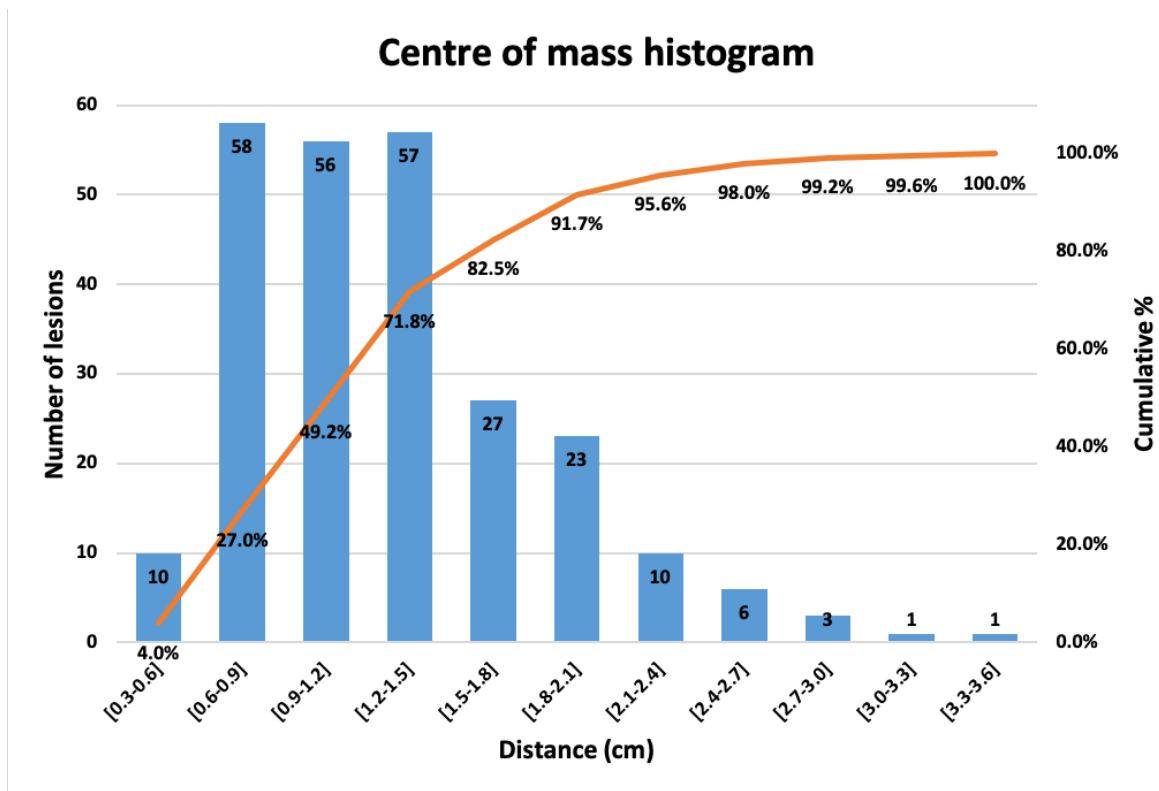


Figure 56: Histogram of the distance in cm between the two COM in the three-dimensional space. Orange line represents the cumulative percentage distribution to the left of the point of interest.

In order to visually assess the difference between the two methods, three different examples are reported in the following pages. Contours drawn by physicians are in red, while the contour taken using the DS method are in yellow.

Because of the large extent of the database, only three examples are reported for visual assessment here, since they provide a good representation of the entire dataset.

Figure 57 (patient 81, threshold 43.7%) reports the case where the two volumes have a significant shift with differences in shape and size.

Figure 58 (patient 70, threshold 43.4%) reports the case where two near lesions are outlined as a single VOI. Also, there is a significant shift and a difference in size.

Figure 59 (patient 58, threshold 44.2%) reports the case where physicians arbitrarily reduced the window level (W/L) to outline the lesion. For this reason, the VOI is very big compared to the actual size of the tumour. This example in particular shows the issue of using a non-standardised protocol for image segmentation based on W/L settings.

Patient 81

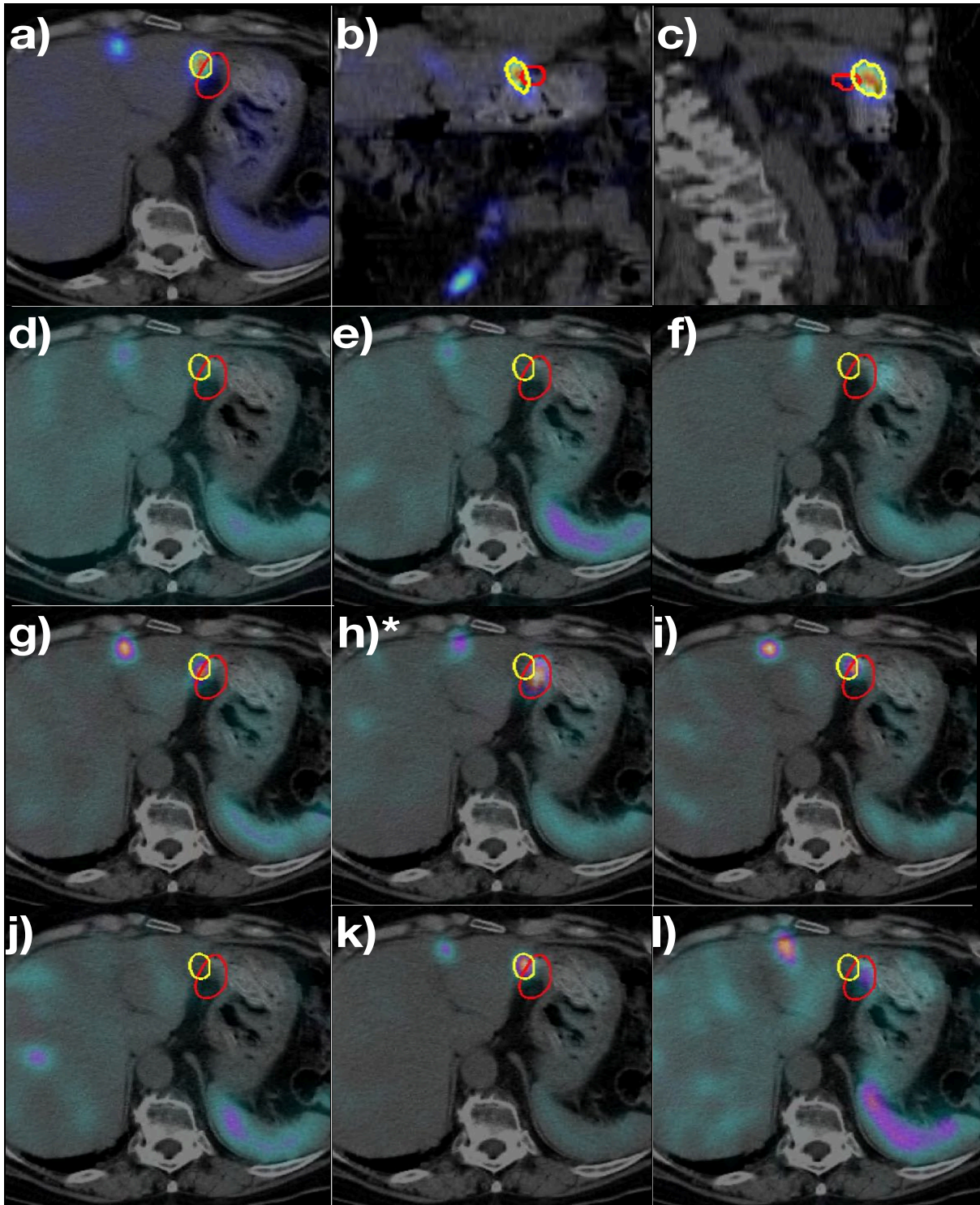


Figure 57: Collection of images showing the lesion outlined with the standard method (in red) and with the DS method (in yellow). In particular the following images are reported: a) Dose map in axial plane; b) Dose map in coronal plane; c) Dose map in sagittal plane; d) NM1 over CT1 identically registered; e) NM2 over CT1 non-rigidly registered; f) NM2 over CT1 rigidly registered; g) NM3 over CT1 non-rigidly registered; h) NM3 over CT1 rigidly registered; i) NM4 over CT1 non-rigidly registered; j) NM4 over CT1 rigidly registered; k) NM5 over CT1 non-rigidly registered; l) NM5 over CT1 rigidly registered; *)image chosen by the physician to outline the lesion.

Patient 70

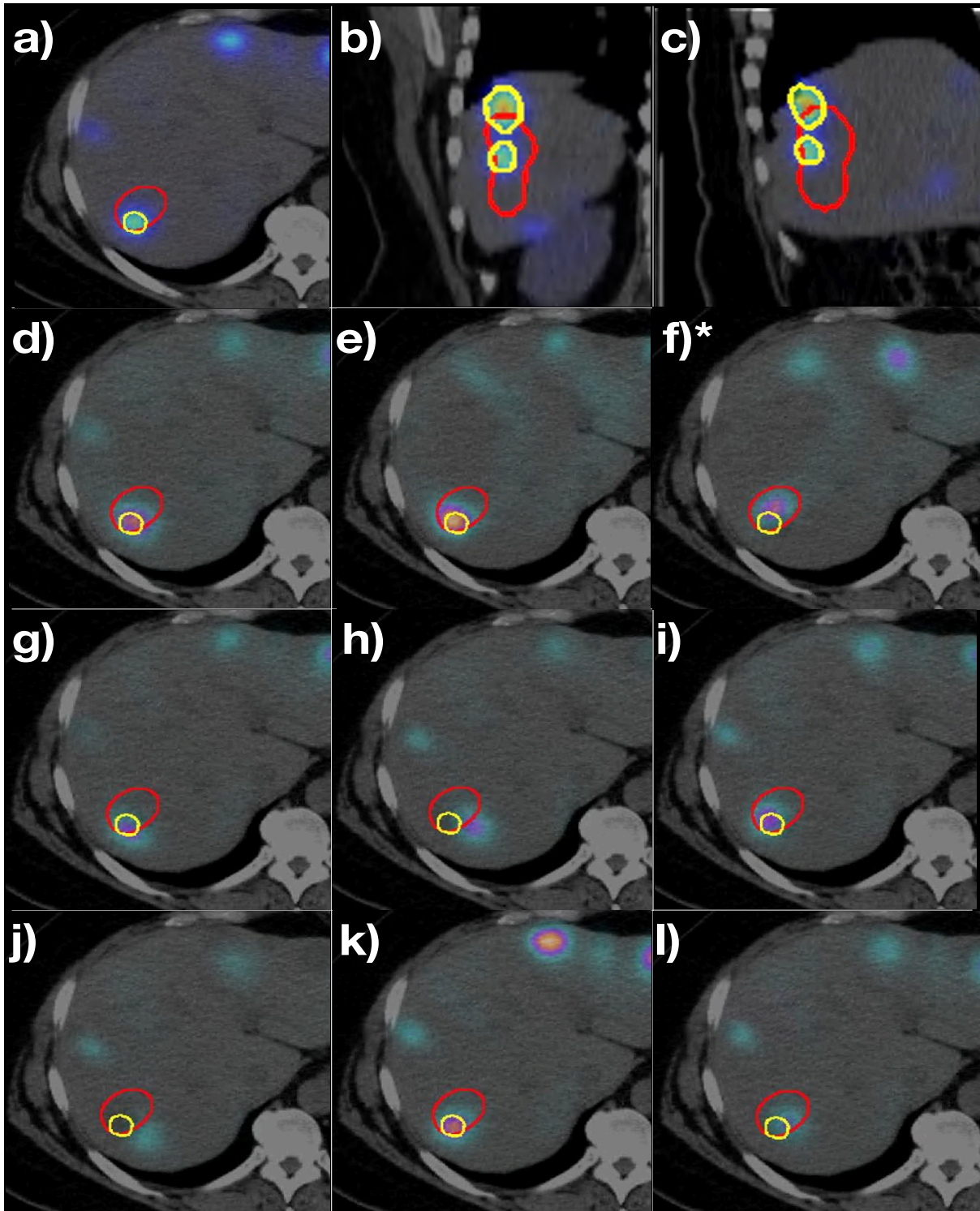


Figure 58: Collection of images showing the lesion outlined with the standard method (in red) and with the DS method (in yellow). In particular the following images are reported: a) Dose map in axial plane; b) Dose map in coronal plane; c) Dose map in sagittal plane; d) NM1 over CT1 identically registered; e) NM2 over CT1 non-rigidly registered; f) NM2 over CT1 rigidly registered; g) NM3 over CT1 non-rigidly registered; h) NM3 over CT1 rigidly registered; i) NM4 over CT1 non-rigidly registered; j) NM4 over CT1 rigidly registered; k) NM5 over CT1 non-rigidly registered; l) NM5 over CT1 rigidly registered; *)image chosen by the physician to outline the lesion.

Patient 58

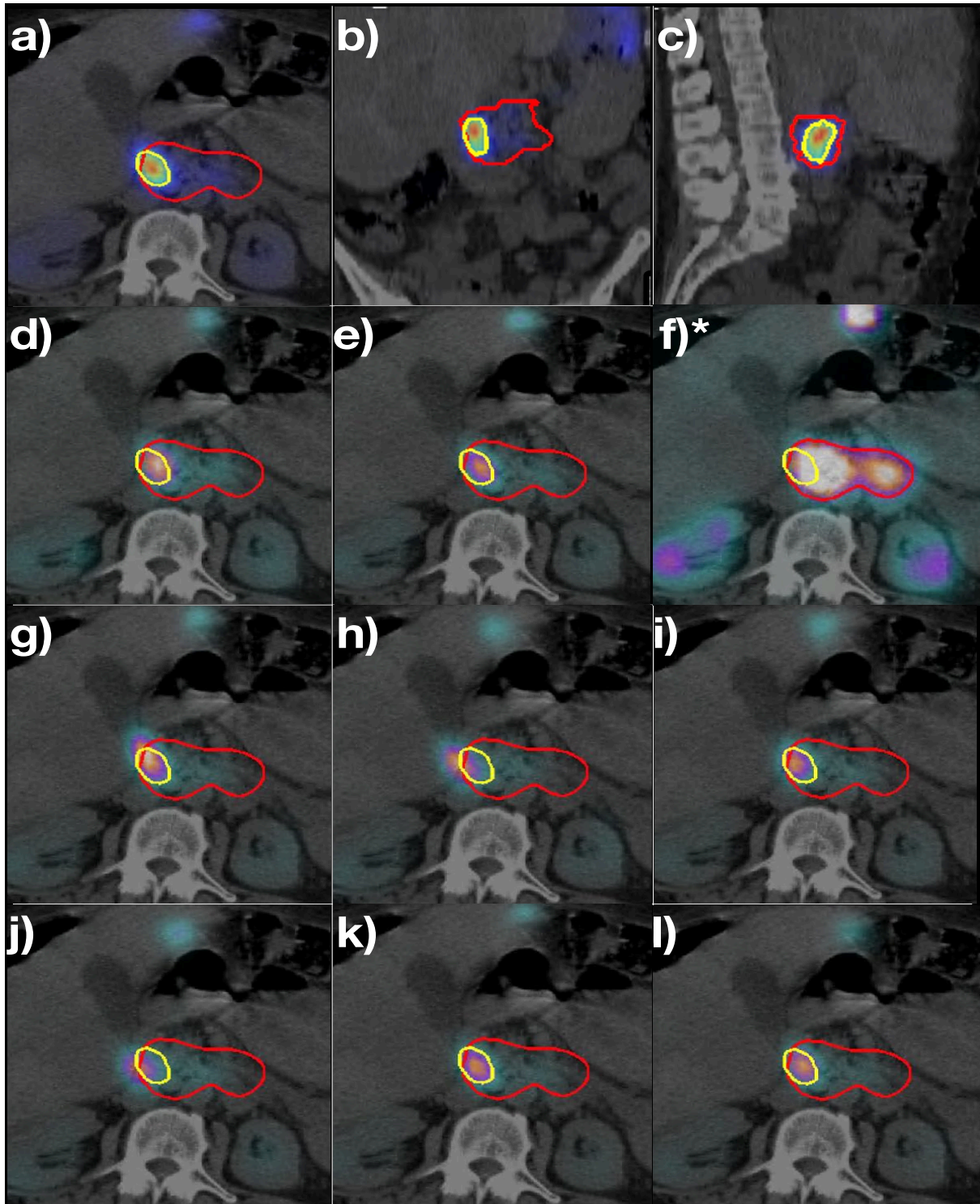


Figure 59: Collection of images showing the lesion outlined with the standard method (in red) and with the DS method (in yellow). In particular the following images are reported: a) Dose map in axial plane; b) Dose map in coronal plane; c) Dose map in sagittal plane; d) NM1 over CT1 identically registered; e) NM2 over CT1 non-rigidly registered; f) NM2 over CT1 rigidly registered; g) NM3 over CT1 non-rigidly registered; h) NM3 over CT1 rigidly registered; i) NM4 over CT1 non-rigidly registered; j) NM4 over CT1 rigidly registered; k) NM5 over CT1 non-rigidly registered; l) NM5 over CT1 rigidly registered; *)image chosen by the physician to outline the lesion.

The percentage difference (PD) between the volumes have been calculated as follows:

$$PD = \frac{volume_{CS} - volume_{DS}}{volume_{DS}} * 100 \quad (61)$$

In this case the DS method was chosen as reference, so a positive difference means an overestimation of the volume from the CS method in comparison to the DS method, while a negative PD indicates an underestimation on estimated volumes. A histogram of the PDs is reported in Figure 60.

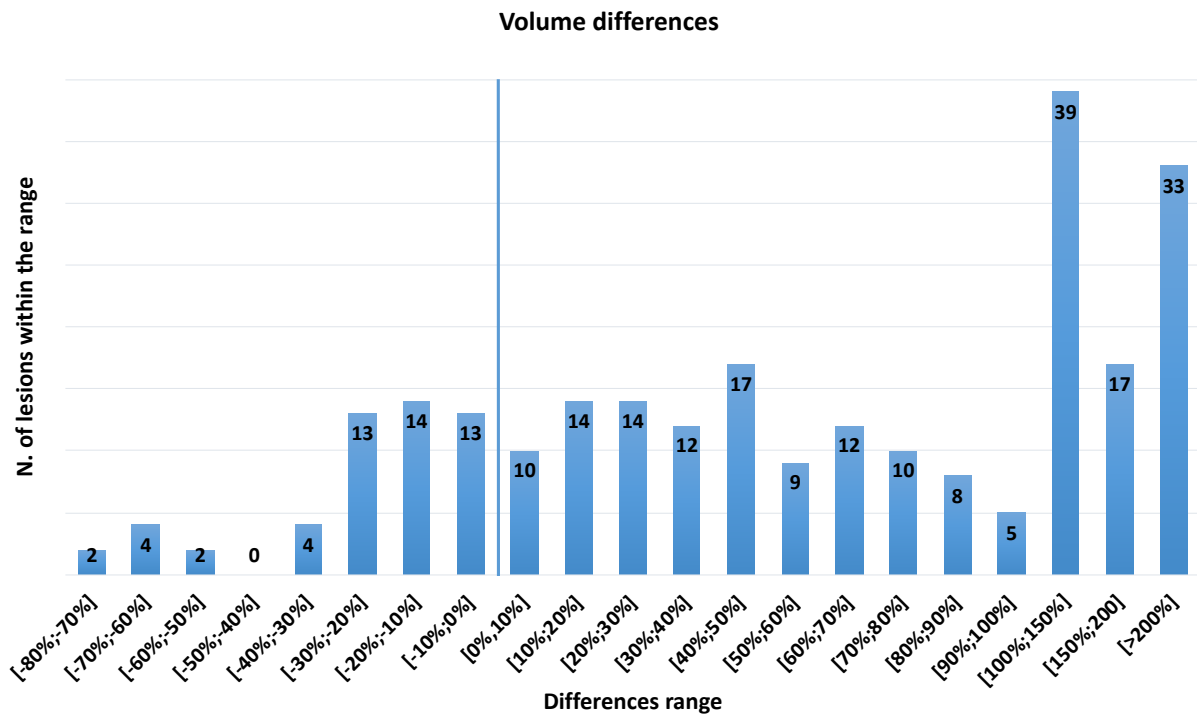


Figure 60: The histogram reports the percentage differences of the volumes of the lesions obtained with the two methods.

It can be noted that the PD is positive for 200 out of 252 lesions (79.4% of cases); this means that the volume estimated using the CS method is generally higher than the volume obtained with the DS method. In particular,

in 33 cases (13.1% of cases) the volume of the outlined lesion is doubled or more.

In addition, to evaluate the agreement (or disagreement) between the two methods, the Bland-Altman analysis is reported in Figure 61.

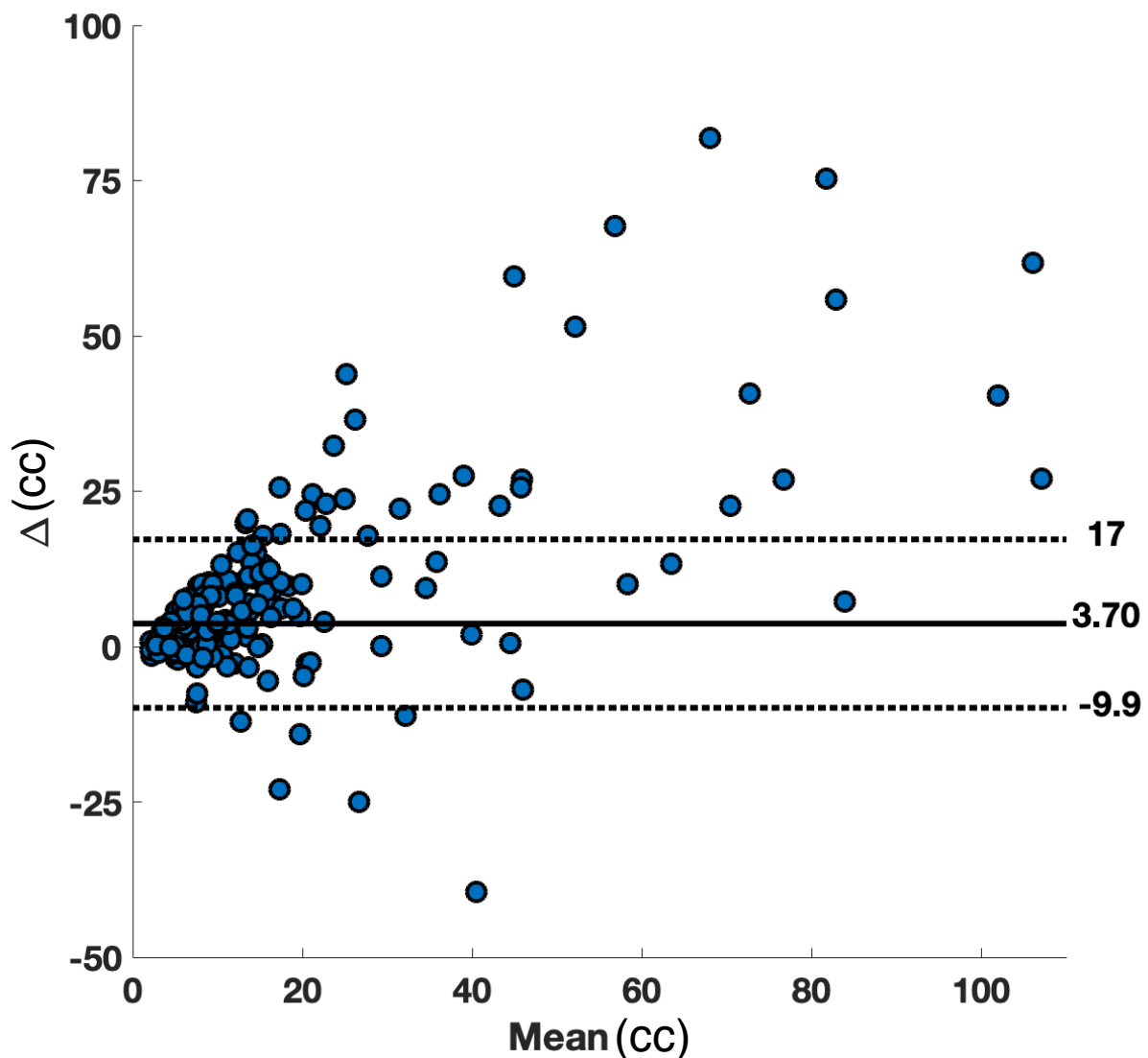


Figure 61: Bland-Altman plot for the volume analysis. It shows an average overestimation of 3.7 cc for the volumes obtained with the manual segmentation method.

The analysis showed a mean overestimation of 3.7 ± 13.3 cc in the volumes calculated with the CS method compared to the DS method.

This is an overestimation of 20% on the average volume of all the cases (which equals 14 cc). Differences in volume estimation were found to be statistically significant ($p\text{-value} < 0.05$). It can be noted a gradual upward trend in the Bland Altman analysis; this suggests that the difference between the two method is higher for bigger lesions.

The same approach was applied to the dose calculation; Figure 62 shows the histogram of the PDs between the two methods calculated with eq. (61); in this case, dose values are used.

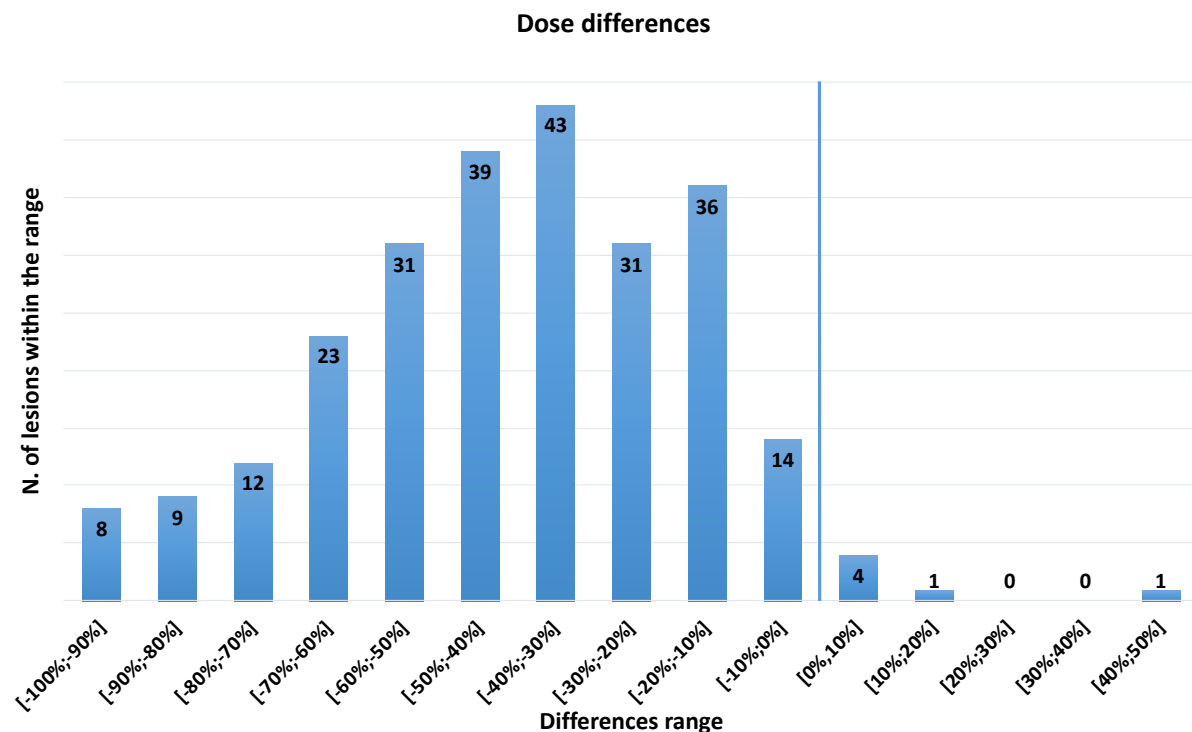


Figure 62: Histogram for the percentage differences on dose calculation.

In 245 volumes (96% of the cases), the dose calculated with the CS method was found to be lower than the dose evaluated with the DS. This means that the CS method generally underestimates the evaluation of the dose.

The corresponding Bland-Altman analysis is reported in Figure 63.

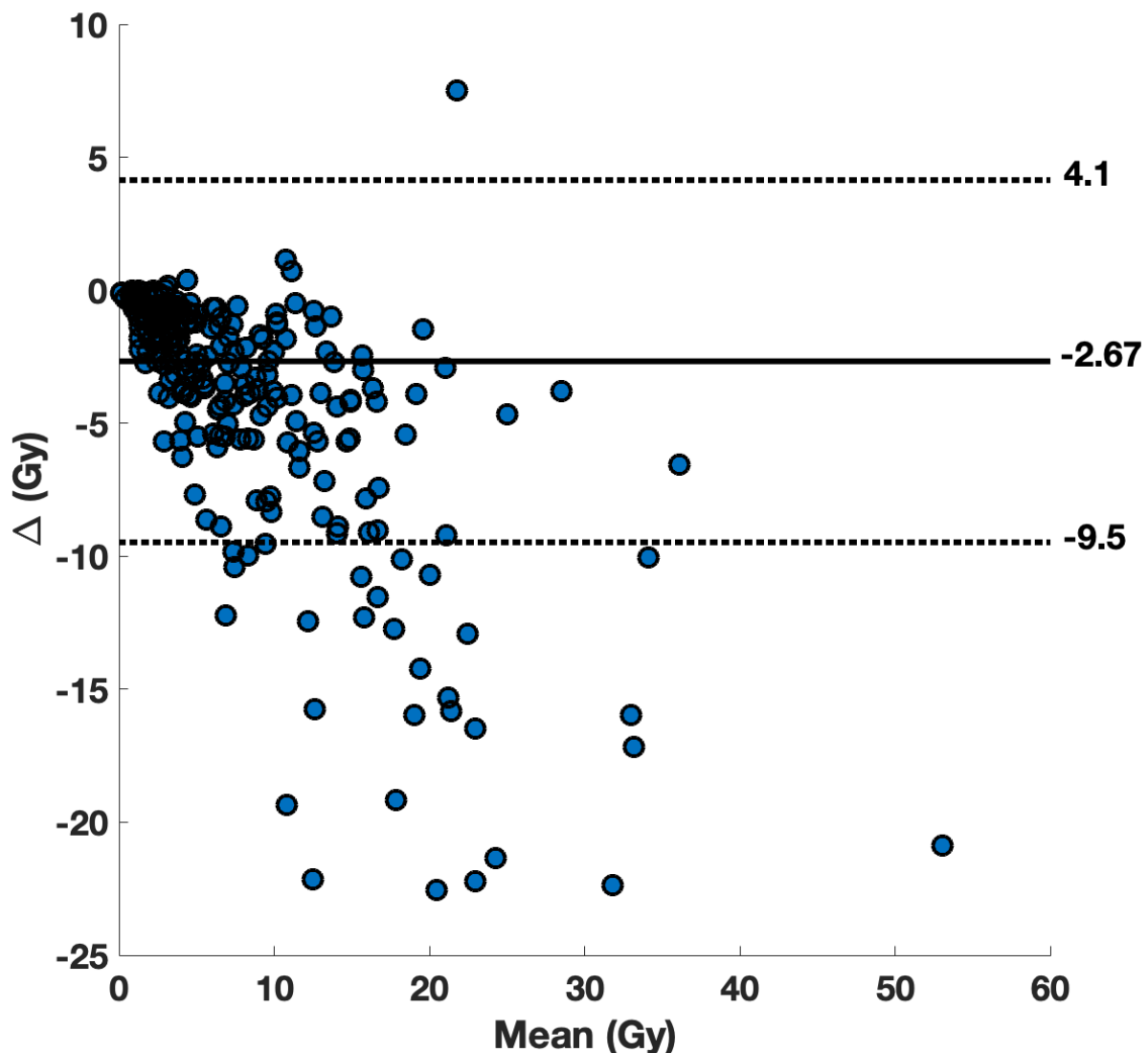


Figure 63: Bland-Altman plot for the dose analysis. Plot axes are cut to improve the readability of the graph.

The graph shows a mean underestimation of -2.67 ± 6.8 Gy. Difference between the two methods was found to be highly statistically significant (p-

value $\ll 0.05$). In this case, a downward trend in the Bland Altman analysis was found. This is expected since the dose is inversely proportional to the mass, so if the volume is overestimated, the dose is consequently underestimated.

The DS method was found to be significantly different from the CS method, as derived from the JACCARD metric analysis.

Furthermore, systematic differences in volume and dose analysis were found to be statistically significant from the Bland-Altman analysis. The examples provided as visual assessment show that the DS method represents the lesion target more accurately than the CS method; this is due to the DS method drawing the lesion directly onto the dose map and not onto the SPECT scan. For this reason, the evaluation of dose in the lesion is significantly influenced, which brings significant differences between the two methods.

The experience accumulated throughout this research work suggests that the standard clinical method is strongly user-dependent, because it is the physician who may choose the SPECT where the lesions have to be drawn and the threshold to be used. However, the proposed method removes the inter-observer variability, since the segmentation is standardised on the

same image (the dose map in this case) with a threshold determined by a calibrated function of the DP:B ratio.

Manual segmentation remains a valid solution to outline and estimate the activity in VOIs, for a non-image-based dosimetry protocol. However, it may be not accurate enough when done on a single image as part of an image-based dosimetry protocol. Furthermore, a non-standardised protocol for tumour delineation on SPECT images increases the user-dependence of the method used to segment the VOI.

The dose segmentation method proposed in this thesis obtained better results on tumour delineation. Consequently, this had a beneficial impact on the absorbed dose evaluation. Furthermore, it is based on a functional form for the determination of the threshold which is not dependent on the user.

This segmentation process has the potential to be implemented as a standardised method for image-based dosimetry which can improve the design of future trials devoted to the personalisation of MRT treatments and evaluation of their efficacy without inter- and intra-operator variability.

6. Conclusions

6.1. Final remarks

This PhD thesis has focused on the investigation of the impact of accurate 3D dosimetry on MRT treatments with an image-based dosimetry component. Four main original contributions have been presented, successfully meeting the aims set out in section 1.5.

This retrospective analysis utilised a large amount of data collected as part of a clinical trial in MRT dosimetry. Before any work could be carried out, the data needed to be manipulated and homogenised. This phase involved ensuring standardised and uniform naming convention for images, delineated volumes and calculated dose values, developing and validating a data processing pipeline to ensure that the use of calibration factors, image registration and resampling techniques used in this work were appropriate. This process of data curation and standardisation significantly improved the quality of the work, speeding up the analysis through automated scripts based on the standard naming convention adopted and has the potential of making the results of this work comparable with data coming from similar large studies in the future. Furthermore, it is in line with the recommendations of international guidelines (204) published during the

course of this thesis, and a good approach that should be replicated in future studies in order to improve data inter-operability.

Chapter 4 aimed to study the importance of image registration in image-based dosimetry. In detail, in section 4.1, registration algorithms from a commercial software used in clinical practice at our institution were compared with those developed using an open-source library. The SSIM conformity index was used as a quantitative metric for the co-registration of the sequential images. The analysis showed that despite a somewhat better performance of the open source toolkit against the commercial implementation of equivalent algorithms, differences were statistically significant only in 2 out of 5 time points. Algorithms based on B-spline functions had the best performance, demonstrating that a rigid manual registration is not sufficient to accurately register anatomical and functional information and should therefore be considered with caution when used as part of an image based dosimetry workflow. On the other hand, a significant difference was found in terms of computational time between the commercial software and the open-source library implementation of image registration. The commercial application required a processing time to co-register two images of 30 seconds and 5 seconds for a non-rigid and a rigid algorithm respectively. Much longer times were required using the open-

source library (around 346 seconds for the non-rigid registration and around 35 seconds for the rigid registration). Due to very similar performance, significant difference in processing time, and the availability of the software as part of a certified medical device used in the clinical settings, the commercial implementation was preferred for the intensive data processing tasks involved in the next phase of this investigation. The systematic approach used in this phase of the work, and the data produced can provide valuable information and guidance for future studies involving the processing of large sets of imaging and dosimetric data in MRT.

This work has shown that the use of non-rigid registration algorithms significantly improved the correspondence of the anatomical and functional locations in the relevant scans. As a consequence, a significant difference in the dose calculated for each individual patient was also obtained, as shown in section 4.2. Differences were statistically significant for lesions and organs at risk. This analysis demonstrated that image-based dosimetry is strongly affected by the nature of the algorithm used to co-register images to the same frame of reference. The better correspondence of the anatomical and functional locations in the relevant scans provided by the non-rigid algorithms improves the estimation of the absorbed dose to the volumes of interest.

In addition, this study has also shown that dose calculation is not affected by the application of a registration algorithm at different stages of a workflow in image-based dosimetry as reported in section 4.3. Here, two different workflows were compared: (a) registration of the individual activity scans in the same frame of reference followed by a calculation of the cumulative dose (AD workflow) and (b) calculation of the dose distribution at each scan time point followed by registration of the individual dose maps in the same frame of reference to calculate the cumulative dose (DD workflow). This original analysis did not find significant differences in the estimation of the absorbed dose. A shorter processing time was observed for the AD workflow, because of the lesser number of computational steps required (the DD workflow involved the calculation of 5 dose maps, compared to just 1 required for the AD workflow). In clinical practice, a shorter computational time is preferred; for this reason, the AD workflow was the preferred method of dose calculation. To the best of our knowledge this is the first work to provide a thorough investigation of the two approaches to 3D dose calculation in image-based dosimetry for MRT. We trust the results of this work will provide useful data and guidance to the wider community as dosimetry for MRT continues to evolve.

The aim of chapter 5 was to implement and use the techniques developed in the previous chapters to study the importance of a more personalised and accurate dose calculation in MRT clinical trials that included the acquisition of sequential anatomical and functional scans to monitor treatment. In section 5.1 we compared a voxel dosimetry approach using a Monte Carlo code with an organ-based dosimetry approach based on the MIRD schema. Significant differences were found for kidneys and lesions. Differences in the kidney dose were due to the paired-organ approach that the MIRD-based software employed, which was found to be inaccurate due to the left and right kidney asymmetry. Differences in the lesions dose were due to the sphere model included in the organ-level dosimetry software. This model does not take into account the cross-irradiation from nearby tissues that may be a major component, in particular for big lesions. These results are in line with, and consolidate the outcome of, similar but smaller studies carried out by other research groups. By definition, voxel-based dosimetry provides more detailed information about the absorbed dose distribution and on a much finer scale compared to an organ-level dosimetry approach. This investigation, that has been carried with a very systematic approach on a very large dataset, provides the abundance and variety of data needed to confirm the crucial importance of using workflows and tools to maximise the

accuracy of patient specific dose calculation in MRT. We anticipate that accurate 3D patient-specific dosimetry performed with the workflow and techniques developed in this investigation will lead to a better understanding of treatment outcomes in MRT clinical trials with an image-based dosimetry component.

To this end we have also improved on the analysis and interpretation of 3D dose maps by developing, in Section 5.2, a novel segmentation method for lesions. In our approach, lesions are outlined on dose maps using a threshold determined by a mathematical function that has been specifically constructed using MC simulations of SPECT images for a range of radionuclide activities. The comparison of this method with a standard manual segmentation approach showed significant variations in both shape and location of the segmented lesion. Qualitative and quantitative analysis carried out in this work demonstrated the more accurate identification of the lesions obtained with the proposed novel segmentation technique. We have shown that differences in volumes and absorbed doses of lesions were statistically significant. Currently, there is no standardised method to outline lesions on SPECT images, hence manual segmentation remains the default option in the clinic to segment the volumes of interest and estimate the activity delivered to them. Clearly, this approach is strongly affected by

intra- and inter-observer variability. In addition, volumes segmented on the basis of a single time point are unlikely to be representative of the actual lesion as the radionuclide uptake is the result of underlying individual biokinetic processes. The novel segmentation method developed in this work has the capability to resolve these crucial issues and we have indicated the workflows by which it could be implemented in clinical practice. We anticipate that after patient imaging, the dosimetry would be performed, and the team of clinicians would be able to outline the target lesion using the calculated threshold with no further manual inputs required. The proposed segmentation method with its simplicity of use and its ability to remove the operator dependency would improve both the accuracy of the segmentation and the calculation of the quantitative metrics such as volume and absorbed dose derived from it. This would in turn provide a better quantitative basis for the evaluation of treatment outcome in MRT clinical trials and the interoperability and comparative use of trial data.

The patient-specific component in image-based treatments is rapidly becoming of greater interest in MRT. A more accurate dose calculation for both OARs and lesions is key to develop personalised treatments. This aspect is of major concern in clinical practice and improved processes are needed. The techniques developed in this work show how a more accurate

representation of patient specific dosimetric data can be provided, and we have indicated how such workflows could be implemented to help obtain more accurate information to improve treatment outcomes in MRT. It has been the intention of this work to demonstrate the importance of assessing an accurate absorbed dose to lesions and OARs and to provide a worthwhile contribution to the advancement of patient-specific dosimetry in MRT.

6.2. Future work

The areas investigated in this thesis open up the possibility of further work in several aspects. For all of the analysis, particularly in sections 4.1, 4.2 and 4.3, a non-rigid registration algorithm was implemented to align the sequential images to the same frame of reference. The similarity index analysis undertaken between the non-rigid and the rigid algorithms proved the superiority of the non-rigid registration algorithms with a good correspondence between the sequential image and the image taken as reference. Both the software systems used for the analysis showed a very good correspondence but significantly different computational times were required to perform the registration. With the development of new registration algorithms and new optimisers, this study could be improved in

particular to better co-register the lesion area, in order to enhance the assessment of the absorbed dose for these VOIs.

In section 5.1 simulations were carried out using only the data from the first injection. This was mainly due to the long time needed to simulate one cycle (approximately 24 hours per patient). This analysis can be improved through simulation of all treatment cycles for both ^{177}Lu and ^{90}Y radionuclides with the data provided by the clinical centre. Subsequently, the results obtained from these simulations can be compared with the results obtained by ASMN-IRCSS and correlated with the clinical outcomes available at the end of the trial.

The work on the segmentation method in section 5.2 used a threshold function correlated to the dose peak-to-background ratio. The function was built with an experiment using a Jaszczak phantom with several spherical inserts. Further experiments with inserts of different shapes and activity concentrations may further tune the actual fitting function, improving the threshold value obtained as an outcome. Additionally, this method could be improved by building an automated function to calculate the background dose, to completely remove the user-dependence. Further studies could be performed comparing different segmentation models (applied by different users) with the proposed segmentation method. This comparison would be

helpful to analyse the influence of intra- and inter-user variability on the method choices and the differences on quantitative metrics obtained from each segmentation process.

Currently, a collaboration between Cardiff University and Varian Medical Systems (grant reference n. 518256) is investigating and developing further the technologies and solutions presented in this thesis to improve methods for personalised dosimetry.

APPENDIX A: Publications and presentations

Published papers

1. Berenato S, Amato E, Fischer A, et al. Phys Medica. 2016;32(10):1259–62;
2. Grassi E, Fioroni F, Berenato S, et al. Phys Medica. 2018 Jan 1;45:177–85;
3. Finocchiaro D, Berenato S, Grassi E, et al. Phys Medica. 2019 Jan 1;57:153–9;

Papers in preparation

4. Berenato S, Grassi E, Fioroni F, et al. *Development and impact of two non-rigid registration workflows for a clinical trial in Peptide Receptor Radionuclide Therapy using Monte Carlo code Simulation.*
5. Berenato S, Grassi E, Fioroni F, et al. *A novel segmentation method of neuroendocrine tumours for image-based dosimetry.*

Oral presentations at international conferences (indexed)

6. Berenato S, Grassi E, Fioroni F, et al. Phys Medica. 2017 Oct 1;42:34.
[International Conference on Monte Carlo Techniques for Medical Applications (*MCMA October 2017 – Naples*, oral presentation);

7. Berenato S, Grassi E, Fioroni F, et al. *Phys Medica Eur J Med Phys*. 2018 Aug 1;52:65. [European Congress of Medical Physics (*ECMP August 2018 – Copenhagen*, oral presentation)].

Oral and poster presentations at national and international conferences (non-indexed)

8. Berenato S, Grassi E, Fioroni F, et al. *Advanced Personalised 3D Dosimetry in a clinical trial for Peptide Receptor Radionuclide Therapy*. [The All Wales Medical Physics & Clinical Engineering Conference (*MPCE June 2016 – Cardiff*), oral presentation)];
9. Berenato S, Grassi E, Fioroni F, et al. *Image based Monte Carlo simulation of Peptide Receptor Radionuclide Therapy*. [The future of molecular radiotherapy dosimetry (Internal Dosimetry User group *BIR meeting June 2016 – Oxford*, poster presentation)];
10. Berenato S, Grassi E, Fioroni F, et al. *Image based Monte Carlo simulation of a clinical trial in Peptide Receptor Radionuclide Therapy*. [Medical Physics and Engineering conference (*MPEC September 2016 – Manchester*, oral presentation)];
11. Berenato S, Grassi E, Fioroni F, et al. *Impact of non-rigid registrations for a clinical trial in Peptide Receptor Radionuclide Therapy*. [UK Radiological and Radiation Oncology Congress – Multidisciplinary

- scientific congress and technical exhibition (*UKRCO June 2017 – Manchester*, oral presentation)];
12. Berenato S, Grassi E, Fioroni F, et al. *Impact of non-rigid registrations for Peptide Receptor Radionuclide Therapy*. [The All Wales Medical Physics & Clinical Engineering Conference (*MPCE June 2017 – Swansea*, poster presentation)];
 13. Berenato S, Grassi E, Fioroni F, et al. *Assessing the impact of registration methods on absorbed dose calculation in Peptide Receptor Radionuclide Therapy*. [30th Annual Congress of the European Association of Nuclear Medicine (*EANM October 2017 - Vienna*, oral presentation)];
 14. Berenato S, Grassi E, Fioroni F, et al. *Monte Carlo advanced 3D dose calculation in Peptide Receptor Radionuclide Therapy*. [The All Wales Medical Physics & Clinical Engineering Conference (*MPCE June 2018 – Cardiff*, poster presentation)];
 15. Berenato S, Grassi E, Fioroni F, et al. *A novel segmentation method for advanced personalised 3D image-based dosimetry in Peptide Receptor Radionuclide Therapy*. [MRTDosimetry scientific workshop (September 2018 - Prague, oral presentation)].

Courses attended at Cardiff University

- EndNote: An introduction to managing your references (February 2016);
- EndNote: Further Techniques for managing your references (February 2016);
- ARC: An Introduction to Linux with Command Line (March 2016);
- Statistics for Beginners (April 2016);
- MATLAB: An Introduction (June 2016);
- Be a Better Writer (Sciences) (May 2018).

APPENDIX B: Raydose manual

Raydose User Manual



Version 1.0

Contents

1. PREPARING DATA FOR RAYDOSE	3
1.1 DATA STRUCTURE	3
1.1 VIRTUAL PATIENT	4
1.2 ACTIVITY DATA (MODALITY SPECIFIC INFORMATION)	4
2. RUNNING RAYDOSE - COMMAND LINE	6
2.1 SETTING THE ENVIRONMENT	6
2.2 COMMAND LINE ARGUMENTS	6
2.3 SPECIFYING DATA INPUT AND OUTPUT DIRECTORY	7
2.4 SPECIFYING NUMBER OF SIMULATION THREADS	8
2.5 SPECIFYING THE SIMULATION ISOTOPE	8
2.6 SPECIFYING THE NUMBER OF HISTORIES	8
2.7 SPECIFYING DOWNSAMPLING OF CT OR NM/PT ACTIVITY DATA	9
2.8 SPECIFYING TO INCLUDE AN AMOUNT OF TIME BEFORE THE SCAN IN THE TOTAL DOSE CALCULATION	9
2.9 SPECIFYING ANALYSIS TYPE	10
3. RUNNING RAYDOSE-GRAPHICAL INTERFACE	11
3.1 LAUNCHING FOR THE FIRST TIME	11
3.2 SETTING UP A SINGLE SIMULATION	14
3.3 SETTING UP MULTIPLE SIMULATIONS	16
3.4 ANALYSIS TYPES	17
4. DOSE CALCULATIONS	18
4.1 OUTLINE OF A SINGLE SCAN SPECT/PET DATASET	18
4.2 OUTLINE OF MULTISCAN SPECT/PET DATASET	20
5. RAYDOSE SIMULATION OUTPUT	23
5.1 VIEWING THE CONTENTS OF THE SIMULATION FILE	24
5.2 WHAT IS STORED WITHIN THE SIMULATION FILE?	27
6. ICRP PHANTOM AND COMPARTMENTAL MODEL	29
6.1 HOW ARE TIME ACTIVITY CURVES DERIVED?	30
7 RADIOACTIVE DECAY SIMULATION	31
8. TECHNICAL DETAILS	32
8.1 SYSTEM REQUIREMENTS	32
8.2 LICENSES	32
ANNEX A	33

1. Preparing Data for Raydose

Raydose required DICOM data as input in order to perform a dose calculation. At a bare minimum the user must provide:-

- One patient CT scan
- A minimum of one NM/SP/PET scan (activity image)

Notably, you must specify a minimum of one NM/SP/PET scan, but more accurate information about the bio-distribution of the radiopharmaceutical can only be obtained with multiple scans spanning a range of times post injection. If a single activity image is provided then the only thing that can be assumed in the simulation is a static activity distribution which exponentially decays. This is a reasonable assumption for Y90, which remains static within the liver, but less true for other isotopes.

1.1 Data Structure

Assuming you wish to provide 4 PET scans along with your patient CT scan, you will first need to arrange your data into a directory structure that Raydose will be able to analyse and use in the simulation.

The first step is to create a folder, in this example we shall call this folder “Patient1”. Inside this folder you should create 5 further subfolders to hold the DICOM data for each of the scans you wish to utilize in the simulation. The names of these folders does not matter, since Raydose extracts the information from the DICOM data themselves. However, it is good to adopt a clear naming convention. Therefore, name these 5 subfolders “CT”, “PET1”, “PET2”, “PET3” and “PET4”. From here it should be clear that you will place the relevant DICOM data into their respective directories. Again, for good book-keeping, the PET images should probably be placed in the respective PET directories in time order, HOWEVER this is not a requirement. Raydose extracts the date and time of acquisition from the DICOM data directly and uses this to time order the data internally.

Path to Clinical Case:
/home/User/ClinicalData/Patient1/

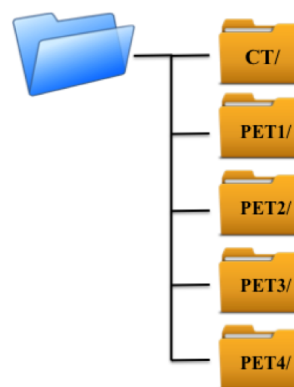


Figure 1 A schematic diagram of how a directory structure, containing your DICOM data, should be arranged before being supplied to Raydose.

After you have created your directory structure in which you will replace the DICOM data, you must be aware of the way in which the data should be treated prior to using Raydose.

It is the responsibility of the user to register their activity images to the CT scans prior to using Raydose. It may be that the user wishes to rigidly register each of their PET scans into the same frame of reference as the CT scan, or alternatively elastically (deformably) register each of their PET scans into the same frame of reference as the CT image. This choice is up to the user.

An example, using VelocityAI to perform the registrations, is outlined in Figure 2. In this example the second PET-CT scans (CT2) is registered into the same frame of reference as the first PET-CT scan (CT1). Here CT2 is elastically deformed to best match CT1. The deformation map can then be used to elastically deform the PET2 image into the same frame of reference of CT1.

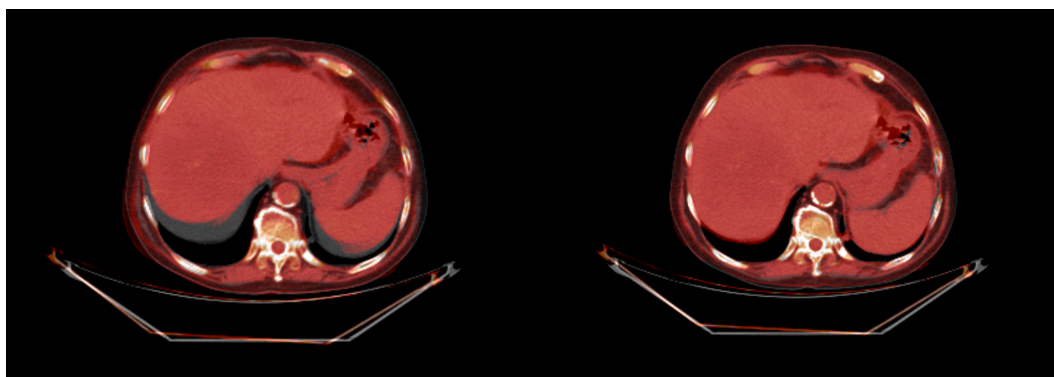


Figure 2 Elastic registration of a CT2 to CT1. The deformation map can be used to deform the PET2 map into the same frame of reference as CT1.

This process should be repeated for each of your NM/SP/PET scans using whichever registration protocol you prefer. As long as the user is aware and clear that Raydose requires the user to place the activity images into the same frame of reference as the CT image using whatever method of registration they prefer.

1.1 Virtual Patient

A patient CT image is used to create a virtual phantom within Raydose. The HU units are converted into a material and density within Raydose. Every voxel in the CT image is transformed into a full 3D virtual phantom of the patient in which photons and charged particle interactions resulting from simulated decays can be scored and a dose calculated at the voxel level.

If you are following the naming convention outlined in Figure 1, you should place the CT DICOM data inside the CT sub-folder.

1.2 Activity Data (modality specific information)

The activity data should be registered with the CT image you have chosen to act as your virtual patient and then each of the scans placed into individual sub-folders as shown in Figure 1. Remember, although it is advisable that your time ordered activity scans are placed into the directories PET1, PET2, PET3.. etc. in time order, this is not essential. The subfolders can be called anything you wish also. Raydose will scan the directories and time order them. The time between scans, which is essential in producing time-activity-curves (TAC's) to produce total dose maps, is

deduced by Raydose internally by extracting the date and time the image was acquired from the DICOM header data. This is then used to determine how far apart each scan was taken and also in which order the scans were taken.

Modality is particularly important within Raydose. You may provide your activity data in 3 modalities. These are NM, SP and PT. However their structure is also very important and you must be careful to know what your data contains.

Modality	Calibrated	Frame type
SP	No (contains no RescaleSlope tag)	Multiframe (Single DICOM file with multiple slices)
NM	No (contains no RescaleSlope tag)	Multiframe (Single DICOM file with multiple slices)
PET	YES (does contain a RescaleSlope tag)	Singleframe (Multiple single slice DICOM files to form an overall 3D volume)

Table 1 Modality parameters for SP/NM and PET DICOM Data.

Important Information (must read)

Table 1 highlights how the different activity image modalities vary. Notably SP and NM modality can not be calibrated since the DICOM standard specifies these modalities cannot contain a RescaleSlope DICOM tag. Therefore, if quantified images have been sent to you in SP or NM modality, you will likely have been given a “calibration factor” which converts the voxel values stored in the DICOM data from “raw counts” to “Bq per voxel”. When using Raydose, you must specify if your data is NM/SP modality and also supply the calibration factor to convert your data into true activity per voxel. Internally, Raydose will then converted each voxel into an activity concentration (Bq/ml).

The PET modality does allow for a RescaleSlope tag and therefore data which is supplied in this modality is usually calibrated in Bq/ml. Nothing needs to be done here and Raydose will handle these images correctly as long as the DICOM voxel data and the RescaleSlope supplied within the PET image gives units of Bq/ml.

Finally, the DICOM standard is clear that SP and NM modality data should be single file multi-frame data (i.e. a SP or NM scan should be a single DICOM file which contains the whole 3D image). PET standards are that you will have singleframe data (i.e. multiple DICOM files each containing a slice of the 3D image volume). Raydose adheres to this standard.

2. Running Raydose - Command Line

As a research tool much of the data analysis thus far has been conducted using Raydose as a command line tool. Effectively, the Raydose Monte Carlo simulation is an engine which is always launched at the command line with a list of arguments which are provided by the user and act as input parameters required by Raydose in order to run.

2.1 Setting the Environment

When running Raydose from the command line you will need to set the environment. You must open your .profile or .bashrc profile and add the following line:-

```
. ~/PATH_TO_RAYDOSE/Raydose/RaydoseEnvironment.sh
```

Save your file and restart your terminal. If you have performed this step correctly, you should be able to type "Raydose" without being in the Raydose install directory and it will execute.

2.2 Command Line Arguments

The parameters which are currently in regular use within Raydose are listed below, and individual details are given regarding each parameter.

Argument	Description	Type	Further information
-input directory	Directory containing the CT and PET/SPECT images.	Mandatory	2.3
-output directory	Directory where simulation results should be exported to.	Optional	2.4
-threads integer	Number of threads to be created when running simulation.	Optional	2.5
-A integer	Mass number of isotope to be simulated.	Mandatory	2.6
-Z integer	Atomic number of isotope to be simulated.	Mandatory	2.6
-histories integer	Number of histories to be simulated per scan.	Mandatory	2.7
-nm-resample integer	NM/PT data down sample scale factor (must be integer).	Mandatory	2.8
-ct-resample integer	CT data down sample scale factor (must be integer).	Mandatory	2.8
-includeTimeBeforeScan double	Consider X hours before the first scan in the total dose calculation.	Optional	2.9
-do-analysis <options>	Run analysis at end of simulation to obtain total dose calculation	Optional	3.0

Table 2 Arguments which can be provided to Raydose at the command line.

2.3 Specifying Data Input and Output Directory

Please read section 1 to understand how input data should be provided to Raydose.

Input

It is mandatory to specify the location of the root path to the CT and NM/PT activity data. The data which is contained within this directory must be in DICOM format. It has been determined that most medical software devices which may be used in processing or post-analysis of CT/PT/NM or RTDOSE data will be performed using the DICOM standard. Therefore it was chosen that Raydose will primarily interact with data in the DICOM format.

The directory which contains the CT and NM/PT data must take a very specific form. Lets assume we have a patient dataset, here referred to as "Patient001". Inside this directory the user must ensure that there is at least **one** CT directory and any number of NM/PT directories which will contain NM/PT DICOM data which is registered to the CT data. Inside of each directory the user must place the corresponding DICOM data which will contain NM/PT DICOM data which is registered to the CT data. Inside of each directory the user must place the corresponding DICOM data.

Command Line Usage:

```
./Raydose -threads 8 -input ~/ClinicalData/Patient001/ -output  
~/Desktop/RaydoseResults/Patient001/ -A 90 -Z 39 -nm-resample 4 -  
ct-resample 4 -histories 10000000 -do-analysis singlescan
```

Output

It is optional that the user specified the output location of the Raydose simulation data. If the user does not specify a path for the output data, a default directory named "OUTPUT DATA" is created in the Raydose root installation path. This directory will be overwritten if it already exists.

At the end of the simulation this directory will contain a subdirectory named "Simulation Files" which contains the raw simulation data (such as scan activity maps, dose rate maps, etc.) as well as the total dose map. These are stored in ROOT files. If you chose to resample your images (for example from 512x512 to 128x128) these resampled images are exported to DICOM format and are placed in the subdirectory "ResampledImages" so that they can be inspected by the user if required. Finally, if an analysis option was selected by the user, a total dose calculation will be supplied to the user in a RTDose modality DICOM file.

Command Line Usage:

```
./Raydose -threads 8 -input ~/ClinicalData/Patient001/ -output  
~/Desktop/RaydoseResults/Patient001/ -A 90 -Z 39 -nm-resample 4 -  
ct-resample 4 -histories 10000000 -do-analysis singlescan
```

2.4 Specifying Number of Simulation Threads

Geant4.10 now includes support for multithreading and allows the simulation to be spread across multiple processing cores on a given machine. The user can specify how many threads that Raydose should create in order to run the calculation. These threads will then be spread across the available processing cores.

This is an optional parameter and therefore if the number of threads is not specified then a default number of 4 threads will be created.

Command Line Usage:

```
./Raydose -threads 8 -input ~/ClinicalData/Patient001/ -output  
~/Desktop/RaydoseResults/Patient001/ -A 90 -Z 39 -nm-resample 4  
-ct-resample 4 -histories 10000000 -do-analysis singlescan
```

2.5 Specifying the Simulation Isotope

It is mandatory that the user specifies the mass and the atomic number of the decaying isotope to be simulated. Without these parameters being supplied, no simulation can be performed and Raydose will exit. Technically, Raydose will simulate any isotope that Geant4 currently holds nuclear decay data for (which is numerous). You must define the atomic mass and atomic number of the isotope you wish to simulate the decay for.

NOTE: By default Raydose will simulate the radioactive decay from parent nucleus ground state and will terminate at the ground state of the daughter nucleus.

Command Line Usage:

```
./Raydose -threads 8 -input ~/ClinicalData/Patient001/ -output  
~/Desktop/RaydoseResults/Patient001/ -A 90 -Z 39 -nm-resample 4  
-ct-resample 4 -histories 10000000 -do-analysis singlescan
```

2.6 Specifying the Number of Histories

It is mandatory to specify the number of histories to be simulated. If the user specifies that 100,000,000 histories/events are to be simulated and provides 5 SPECT scans to be simulated, a total of 500,000,000 histories/events will be simulated overall.

Command Line Usage:

```
./Raydose -threads 8 -input ~/ClinicalData/Patient001/ -output  
~/Desktop/RaydoseResults/Patient001/ -A 90 -Z 39 -nm-resample 4  
-ct-resample 4 -histories 10000000 -do-analysis singlescan
```

2.7 Specifying Downsampling of CT or NM/PT Activity Data

Typically, CT data are supplied as a 512x512 DICOM set. In order to run simulations more quickly and to utilise significantly less RAM it is possible to down sample the data in the X-Y plane (functionality may be added at a later date to down-sample in the axial direction also) to something like 128x128 by down sampling by a factor of 4.

Similarly, this down sampling can also be applied to the NM/PT images also. Sometimes this is required if the NM/PT images have been registered with the CT image and have been exported on a larger 512x512 grid than the original NM/PT images (which were more likely to have been 128x128 initially).

Command Line Usage:

```
./Raydose -threads 8 -input ~/ClinicalData/Patient001/ -output  
~/Desktop/RaydoseResults/Patient001/ -A 90 -Z 39 -nm-resample 4 -  
ct-resample 4 -histories 10000000 -do-analysis singlescan
```

2.8 Specifying to Include an Amount of Time Before the Scan in the Total Dose Calculation

You may wish to include a period of time BEFORE the time of the first supplied scan in the total dose calculation. For example, if the first scan was taken 6 hours after the injection time, by default the simulation would not include dose deposition during this 6 hour period. However, using the `-includeTimeBeforeScan` argument will include this in the simulation with the following assumption:-

- Any period of time to be included before the first scan will assume that the distribution of the activity is the same as the first scan AND that the functional form of the time activity curve (TAC) before the first scan was of the form of an exponential decay.

Other options are being implemented, such as “linear uptake”.

Command Line Usage:

```
./Raydose -threads 8 -input ~/ClinicalData/Patient001/ -output  
~/Desktop/RaydoseResults/Patient001/ -A 90 -Z 39 -nm-resample 4 -  
ct-resample 4 -histories 10000000 -includeTimeBeforeScan 6 -do-  
analysis singlescan
```

2.9 Specifying Analysis Type

At the end of the simulation the Monte-Carlo results can then be used to calculate a total dose map. You must specify the “-do-analysis” argument along with the type of analysis to be performed. The list of analysis types currently included are outlined in section 3.4 Analysis Types).

You run these from the command line in the following fashion: -

A multiscan run which includes an exponential tail (out to 500 hours after the first scan) and a linear uptake for 4 hours before the first scan.

Command Line Usage:

```
./Raydose -threads 8 -input ~/ClinicalData/Patient001/ -output  
~/Desktop/RaydoseResults/Patient001/ -A 90 -Z 39 -nm-resample 4 -  
ct-resample 4 -histories 10000000 -includeTimeBeforeScan 4 -do-  
analysis multiscan6 500.
```

Note that you must include a “-includeTimeBeforeScan” argument if you wish to run an analysis type that includes a period of time before the first scan.

A multiscan run that includes an exponential tail (out to 500 hours after the first scan) but does not consider anything before the first scan in the dose calculation.

Command Line Usage:

```
./Raydose -threads 8 -input ~/ClinicalData/Patient001/ -output  
~/Desktop/RaydoseResults/Patient001/ -A 90 -Z 39 -nm-resample 4 -  
ct-resample 4 -histories 10000000 -do-analysis multiscan2 500.
```

3. Running Raydose–Graphical Interface

The Raydose graphical user interface (UI) allows the user to more easily create and submit a simulation job. Although the command line interface may be preferable for some users, particularly for those who wish to script a number of simulations to execute in a bash script, the UI allows users to graphically select their simulation parameters and submit the job in this way.

It is also possible to create multiple simulations using the graphical interface, where the simulations run one after the other.

3.1 Launching for the first time

When launching the Raydose job submission GUI for the first time, you will be presented with a screen similar to the one shown in Figure 2.1. The information screen, located at the bottom of the window, notifies you that this is the first time you have run the GUI and you must specify where the Raydose simulation is installed.

To do this, first click on the “Select Raydose Path” button which will launch a directory browser dialog as shown in Figure 2.1. Locate the install path of Raydose (this is the directory that contains the directories for *Raydose* and *RaydoseUI*). Select *Raydose* directory and the dialog screen will reload and show the contents of the this directory, as shown in Figure 2.1. You should be able to see that this directory contains the Raydose binary. If so, click *open*.

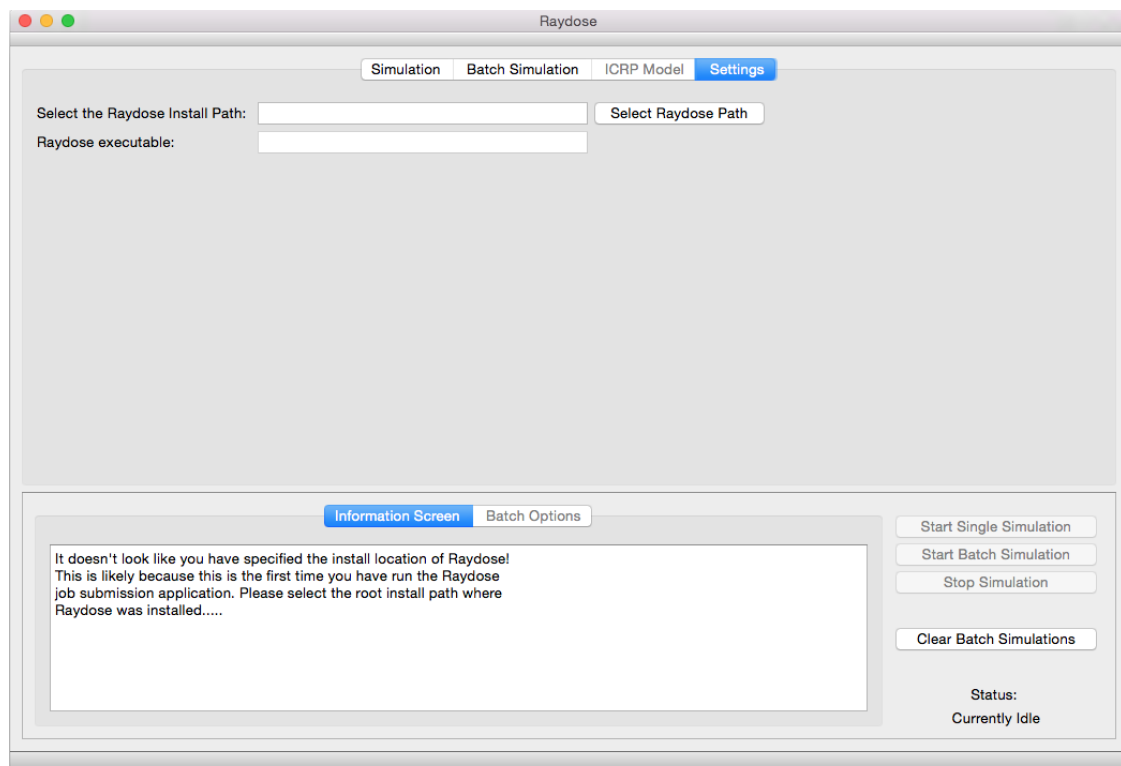


Figure 3 Raydose User Interface on first launch, requiring the user to specify the location of the Raydose simulation engine.

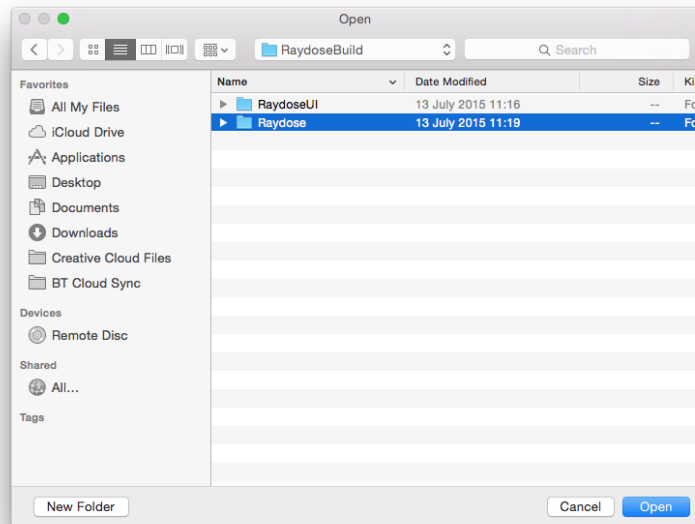


Figure 4 Dialog screen where the directory of the Raydose simulation engine is installed.

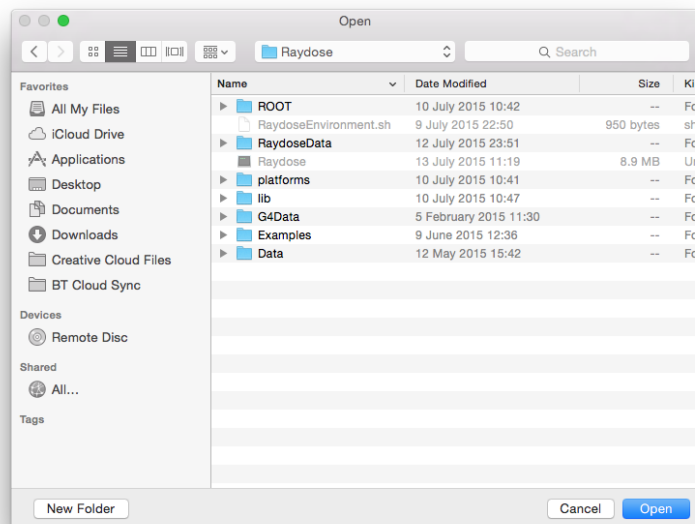


Figure 5 The Raydose executable is located within the Raydose simulation engine path. This directory should be used as the install path for Raydose.

Once done, the RaydoseUI application should correctly identify the Raydose simulation is in the directory you have specified and the main RaydoseUI screen, shown in Figure 2.1 will up- date and text in information box at the bottom of the screen will indicate that they Raydose engine has been successfully found.

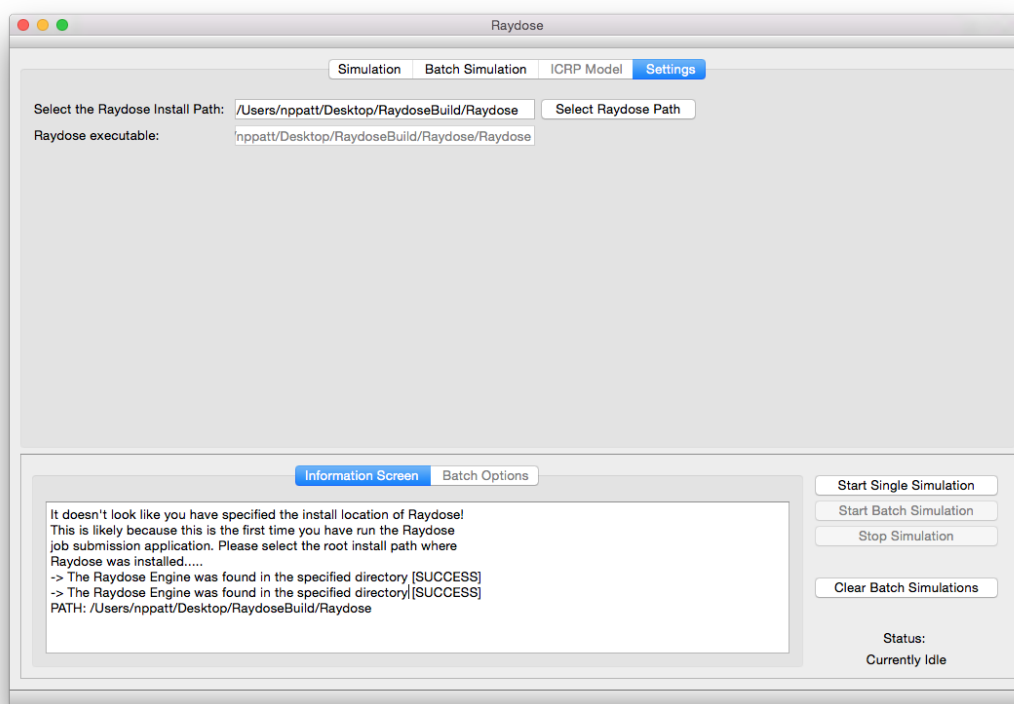


Figure 6 If the correct path to the Raydose simulation engine has been selected, the information screen will indicate that this has been successful.

You do not need to do this upon each launch of the RaydoseUI application as the configuration is stored in a file local file and will therefore be remembered for all subsequent uses of this application.

3.2 Setting up a single simulation

To setup and launch a single simulation, select the *Simulation* tab on the top screen. A form will appear, similar to that shown in Figure 2.2 with a number of input options that can be specified by the user.

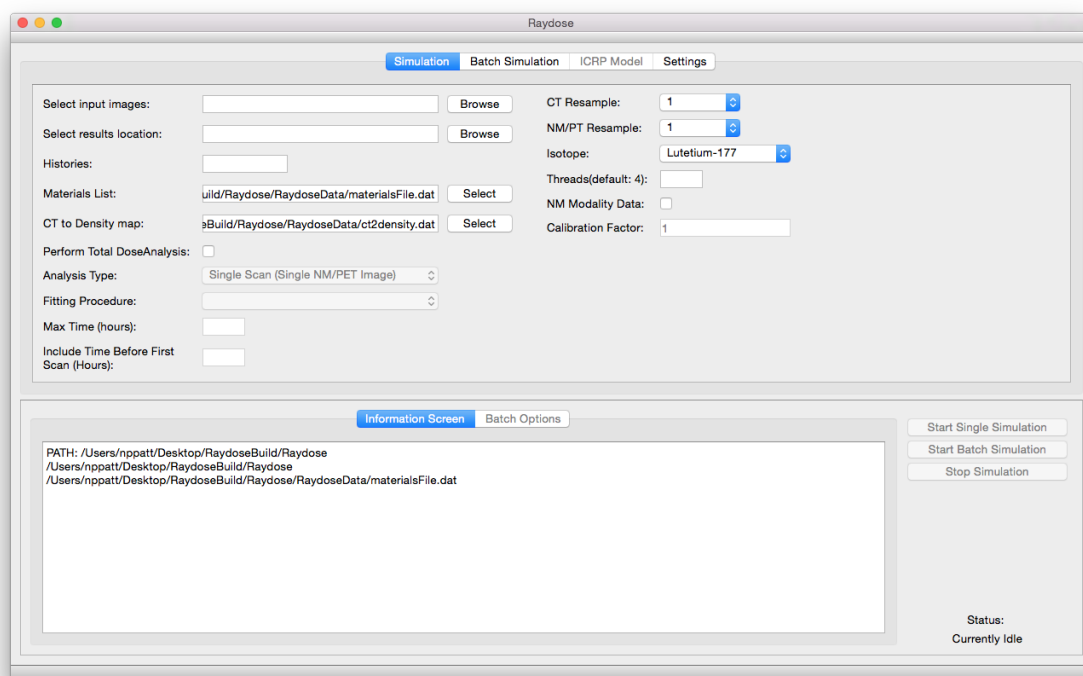


Figure 7 Single simulation configuration screen.

The options that are included in the user interface are:-

Select input images - The directory that contains the CT images subdirectory and all PT/NM/SP image subdirectories.

Select results location - The directory where all of the simulation output should be placed.

Histories - the number of events to be simulated. As an example, if you request 100,000,000 events to be simulation and supply 5 PET images, then each image would be simulated with 100,000,000 events (NOT 20,000,000 events for each PET image).

CT Resample - The factor by which the CT DICOM image should be down sampled. E.g. a factor of 4 would down sample a 512x512 image to 128x128.

NM/PT Resample - The factor by which the NM/PT DICOM image should be down sampled. E.g. a factor of 4 would down sample a 512x512 image to 128x128.

Isotope - Select the isotope that is to be simulated.

NM Modality Data - Select if the data is of the NM or SP modality. These DICOM modalities cannot include a RescaleSlope tag and therefore the data they contain will not be calibrated in terms of Bq.

Calibration Factor - If *NM Modality Data* is selected then a calibration factor must be supplied. This factor should be provided along with the DICOM data. This factor acts as the RescaleSlope tag and will convert each voxel value from *raw counts per voxel* to *Bq per voxel*.

Materials List - This file contains a list of materials and their corresponding density. A default file is supplied. A user can specify their own file if they wish.

CT to Density map - This file contains the mapping of HU to density.

Perform Total Dose Analysis - At the end of the simulation calculate a total dose map.

Analysis type - There are two types of analysis available. If you only supplied a single PET/NM image, then you should select *single scan*. Otherwise, you should select *multi scan*. Single scan analysis calculates the total number of decays assuming a simple exponential decay using the activity data in the supplied image. The multi scan analysis determines the total number of decays between each scan.

Fitting procedure - There are a number of options available, depending on the type of analysis that has been selected (see 3.4 Analysis Types).

Max Time (hours) - If the user selects an option that specifies "User defined upper time", the user can specify how long the exponential tail should extend to in hours. This time is relative to the *first scan* time.

3.3 Setting up multiple simulations

The user can set up multiple simulations that are to be run one after the other. The input options are the same as for those outlined in section 2.2. Although the user may wish to run multiple simulations at the same time, this is generally unsafe using Raydose due to the difficulty in managing memory. As an example, if 4 simulations were to be run at the same time, each having large geometries of something like 128x128x100 voxels, such geometries would quickly cause memory to run short. This is particularly true if the user creates multiple threads per simulation.

The simulation parameters are identical to those offered for a single simulation. The parameters should be entered in the same manner, with the only difference being that you must click on the “Add Simulation” button once satisfied with the selected settings. After doing this, your simulation settings will appear in the “Batch Options” tab at the bottom of the screen.

You may continue to add as many simulations to the batch as you wish. If you wish to clear the current list of batch simulations and start again, then click on the “Clear Batch Simulations” button.

When you are fully satisfied that you have added all of the simulations that are required you must then submit them to the Raydose simulation engine. Do this by simply clicking on the “Start Batch Simulation” button. The Raydose engine will be called with the arguments that you have specified in the input boxes. The simulations run one at a time, and the progress is indicated in the bottom right hand corner of the screen. Noticeably, the “Start Batch Simulation” button will blank out when running so that you cannot submit any further jobs to Raydose. This ensures memory consumption is handled as safely as possible. When Raydose is running, a stop button becomes active and you may click on this to terminate the simulation at any stage.

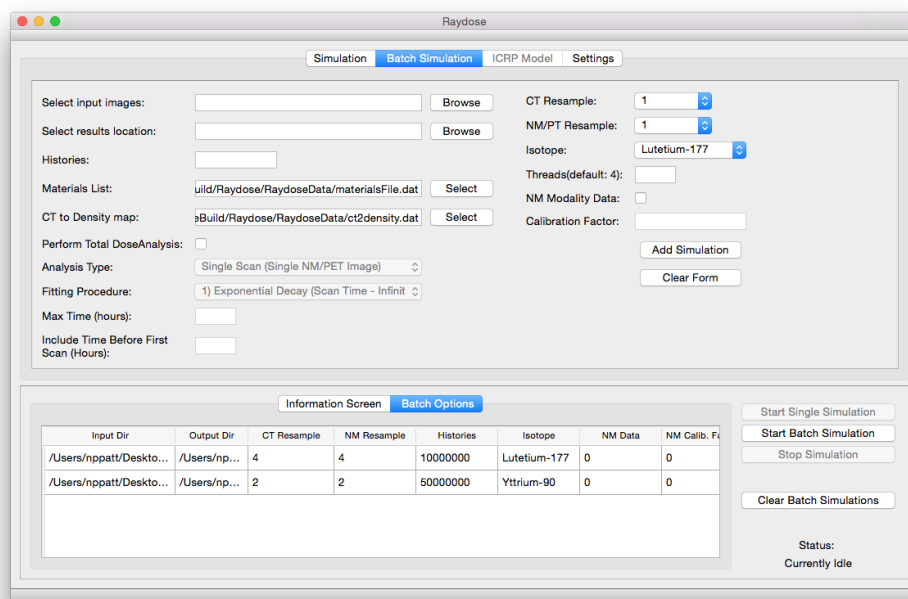


Figure 8 Creating a list of multiple simulations to be run one after the other.

3.4 Analysis Types

There are currently a number of analysis types that are built in to Raydose at present. They are outlined in Table 3. Replace <double> with a user specified time in hours.

Analysis	Command Line Argument	Description
Single Scan	-singlescan1	A single PET/NM image has been supplied. The dose is calculated assuming exponential decay from the scan time to infinity. The decay constant is that of the isotope.
Single Scan Limits	-singlescan2 <double>	A single PET/NM image has been supplied. The dose is calculated assuming exponential decay from the scan time to a user defined upper time (X hours after the first scan).
Multi Scan	-multiscan1	Multiple PET/NM images are supplied. The dose is calculated assuming a linear fit (trapezoid method) between each scan point to determine the TAC.
Multi Scan Exponential Decay After Last Scan	-multiscan2 <double>	Multiple PET/NM images are supplied. The dose is calculated assuming a linear fit (trapezoid method) between each scan point to determine the TAC. A an exponential tail is added after the last scan point with the relevant isotope decay constant.
Multi Scan Exponential Before First Scan (No exponential tail)	-multiscan3	Multiple PET/NM images are supplied. The dose is calculated assuming a linear fit (trapezoid method) between each scan point to determine the TAC. However, a period of time BEFORE the first scan is considered, assuming that exponential decay has occurred before the first scan point.
Multiscan with Linear uptake (No exponential tail)	-multiscan4	Multiple PET/NM images are supplied. The dose is calculated assuming a linear fit (trapezoid method) between each scan point to determine the TAC. Linear uptake is assumed before the first scan time point. The user specifies the number of hours before the first scan (as an example assume injection in 2 hours before the first scan was acquired).
Multiscan with exponential decay before first scan AND exponential tail	-multiscan5 <double>	As above , but with exponential tail
Multiscan with Linear uptake before first scan AND exponential tail	-multiscan6 <double>	As above, but with exponential tail

Table 3 List of analysis types currently programmed into Raydose. Also displayed are the command line arguments to run each analysis type.

4. Dose Calculations

Each patient data set consists of N SPECT scans which are all registered (either rigidly or elastically) to the same CT scan. The patient CT scan is constructed within Raydose and acts as a virtual phantom in which charged particles and photons can propagate. The dose deposition of the decay radiations are scored within the virtual CT phantom grid. The voxels which make up the virtual phantom are assigned a material and density according to the Hounsfield Unit (HU) present in the original CT image. Ten materials have been defined within the simulation with each material able to be assigned a different density. The HU of the CT voxel is looked up and translated into a material type and density. The corresponding voxel in the virtual phantom is then assigned this material.

4.1 Outline of a Single Scan SPECT/PET Dataset

The single-scan analysis can be run when only a single activity image has been supplied by the user. In this scenario, it is assumed that the radionuclide decays exponentially with a decay constant which represents the physical half-life of the isotope in question.

Figure 9 and 10 outline two common scenarios surrounding the treatment of single scan data. Let look at each scenario separately.

The assumption here is that we do not consider the dose deposition between the time of the injection and the time that the first scan was acquired (however this is possible). Therefore $t=0$ is assumed to coincide with the time of the first scan.

This data is therefore straightforward to treat. The first step is to determine the total number of decays within the entire image between $t=0$ and a user specified upper time limit t . This can be infinity if required (and is often true in treatments such as Y-90, where the microspheres remains lodged within the liver).

The first thing to do is to use the PT/NM activity data to generate a dose rate grid which has units of Gy/event. As a reminder, this grid is generated by simulating N events (say 100,000,000 events). Each event represents a decay, where the event is positioned within the patient according to the intensity of the underlying NM/PT 3D image. After the simulation of the 100,000,000 decays a 3D grid of scored dose is produced (D^1). This grid is then normalized by the number of simulated events to obtain the *dose per simulated event grid* (\dot{D}):-

$$\dot{D}^1 = \frac{D^1}{N_{events}} \quad (1)$$

The next step is to determine the total number of decays in the entire 3D volume of the patient between $t=0$ and the user specified upper limit (let's assume for this example the user specifies 72 hours).

To do this we look at the activity in each and every voxel in the 3D NM/PT image. The activity in voxel (x,y,z) for the scan is denoted $A_{(x,y,z)}$. It is assumed that the activity inside each voxel decays mono-exponentially with a decay constant based derived from the isotope half-life. The total number of decay inside voxel (x,y,z) between $t=0$ and $t=T$ hours (where T should always be expressed in seconds when placed into these equations) is given by:-

$$\tilde{A}_{(x,y,z)} = A_{(x,y,z)} \cdot [1 - \exp(-\lambda T)] \quad (2)$$

and the total number of decays in the entire patient volume is therefore given by:-

$$\tilde{A} = \sum_{x=1}^{nx} \sum_{y=1}^{ny} \sum_{z=1}^{nz} \tilde{A}_{(x,y,z)} \quad (3)$$

The final step is to scale the dose per simulated event grid (\dot{D}) by the total number of decays in the mage. Therefore the total dose map is given by:-

$$D = \dot{D}^1 \cdot \tilde{A} \quad (4)$$

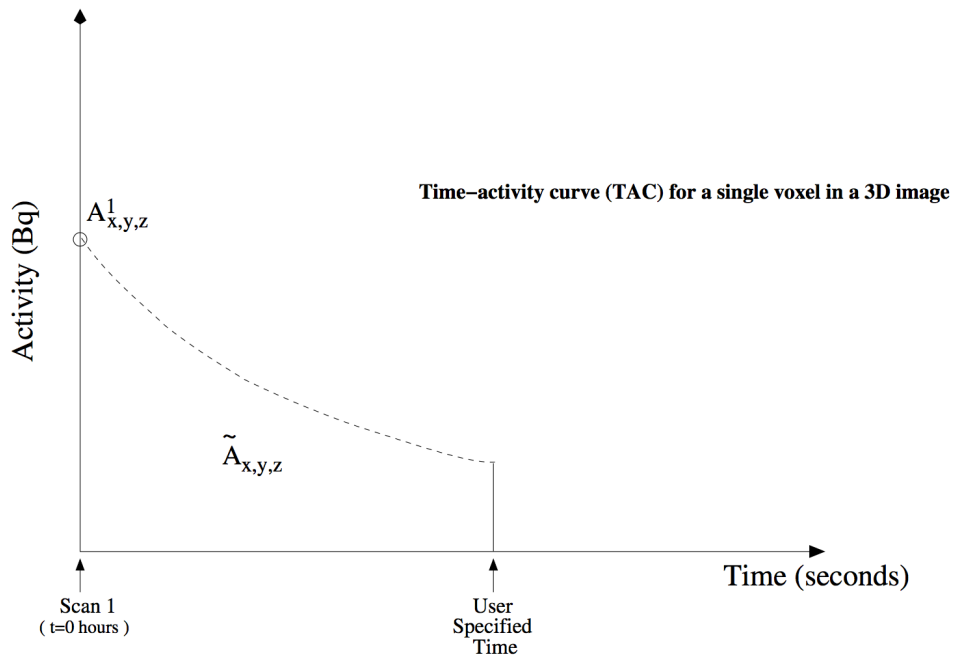


Figure 9 Single scan analysis: An example time-activity-curve for a single voxel where the total number of decays within the voxel (x,y,z) is based upon the area under an expontial curve between 0 hours and a user specified time (which can also be infinity).

4.2 Outline of Multiscan SPECT/PET Dataset

The assumption here is that we do not consider the dose deposition between the time of the injection and the time that the first scan was acquired (however this is possible). Therefore $t=0$ is assumed to coincide with the time of the first scan.

The first step that Raydose undertakes is to build the 3D virtual patient phantom and simulate the radioactive decay of a specified isotope within the patient volume based upon the distribution maps of the activity images. In this instance, assuming the user specifies to simulate 100,000,000 events, Raydose will simulate 100,000,000 decays for each scan. The dose deposition will be scored on the CT virtual patient grid and a “dose per simulated event” (\dot{D}^i) map will be generated for each of the supplied activity scans. Here, “i” indicated the i^{th} activity image.

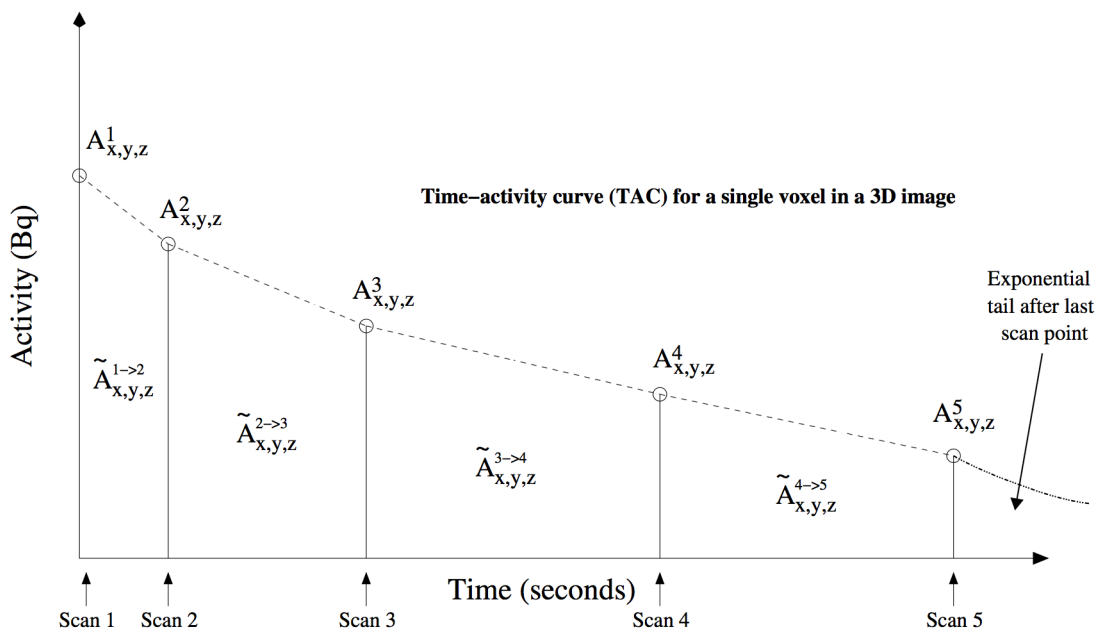


Figure 10 Overview of a 5 scan simulation showing how the individual voxel activities are used to determine the total number of decays for a given voxel at position (x,y,z) .

All of the information is now available to calculate the total dose deposition (D) within the virtual patient using all of the information gained from the Monte-Carlo “dose per simulated event” grids and the total number of decays within the patient image derived from the determination of the area under the TAC’s on a voxel-by-voxel basis.

In the simplest example, let’s assume a 5 scan data set has been supplied and also ignore any decays that may occur after the last scan point (i.e. scan 5). It is possible to determine the total number of decays between scan 1 and scan 5 by plotting a TAC for every voxel in the 3D activity image, deduce the area under TAC for each voxel, then sum over all voxels to get the total number of decays.

The total dose delivered between scan 1 and scan 2 ($D^{1 \rightarrow 2}$), according to Figure 10, is calculated

using the “dose per simulated event map” (D^1) and the total number of decays that occurred in the image between scan 1 and scan 2 ($\tilde{A}_{total}^{1 \rightarrow 2}$) in the following manner:-

$$D^{1 \rightarrow 2} = \dot{D}^1 \cdot \tilde{A}_{total}^{1 \rightarrow 2} \quad (5)$$

Similarly the other dose rate maps can be scaled in the same fashion and summed together to form the total dose map covering the time period between the first scan and the last scan, such that (assuming in this case a patient study with 5 activity image scans):-

$$D = (\dot{D}^1 \cdot \tilde{A}_{total}^{1 \rightarrow 2}) + (\dot{D}^2 \cdot \tilde{A}_{total}^{2 \rightarrow 3}) + (\dot{D}^3 \cdot \tilde{A}_{total}^{3 \rightarrow 4}) + (\dot{D}^4 \cdot \tilde{A}_{total}^{4 \rightarrow 5}) \quad (6)$$

or more generally:-

$$D = \sum_i^{N-1} (\dot{D}^i \cdot \tilde{A}_{total}^{i \rightarrow i+1}) \quad (7)$$

Where N is the number of NM/SP/PT scans. Here, Equation 7 is a resultant 3D dose grid which represents the total deposited dose between the first scan and the last scan inside the patient.

As indicated in Figure 10 it is also possible to consider that an exponential decay, representing the physical decay constant of the radionuclide (λ) can be used to determine the dose deposited out to some user specified time T. First, assume that the user specifies that the tail extends out to 500 hours after the first scan. In reality we only wish to calculate the number of decay represented by the area under the exponential between the time of the last scan and 500 hours after the first scan. Therefore if the last scan point was taken 72 hours after the first scan, then value of T becomes (500h-72h = 428h) – of course this should be converted into seconds for use in the calculations.

The total number of decays after the last scan point is given by the integral of an exponential decay. Assuming a N scan example, we use the N^{th} activity image scan to obtain the activity values of each voxel and deduce the total number of decays in the following manner:-

$$\tilde{A}_{total}^{tail} = \sum_{x=1}^{nx} \sum_{y=1}^{ny} \sum_{z=1}^{nz} \frac{A_{x,y,z}^N}{\lambda} [1 - \exp(-\lambda \cdot T)] \quad (8)$$

The more general definition of how the Monte-Carlo “dose per simulated event maps” are scaled and summed together, assuming the inclusion of an exponential tail after the last time point, is given by:-

$$D = \left[\sum_{i=1}^{N-1} (\dot{D}^i \cdot \tilde{A}_{total}^{i \rightarrow i+1}) \right] + [\dot{D}^N \cdot \tilde{A}_{total}^{tail}] \quad (9)$$

Equation 9 gives the general description for the determination of the final three-dimensional total dose grid, assuming an exponential decay of the radionuclide activity after the last time point scan.

5. Raydose Simulation Output

Whenever a simulation is performed with Raydose, all of the simulation data is written to file. The structure of the specified output directory will look similar to Figure 11. You will have 2 directories and a single DICOM file which are as follows:-

- **Resample Images** – If the user down sampled the original DICOM data this directory will appear. It contains new DICOM data for each of the supplied scans, but in the new down sampled resolution.
- **Simulation Files** – Contains the simulation data in ROOT files.
- **RTDose_Raydose.dcm** – The DICOM RTDose file which contains the simulated total dose from the Raydose simulation.

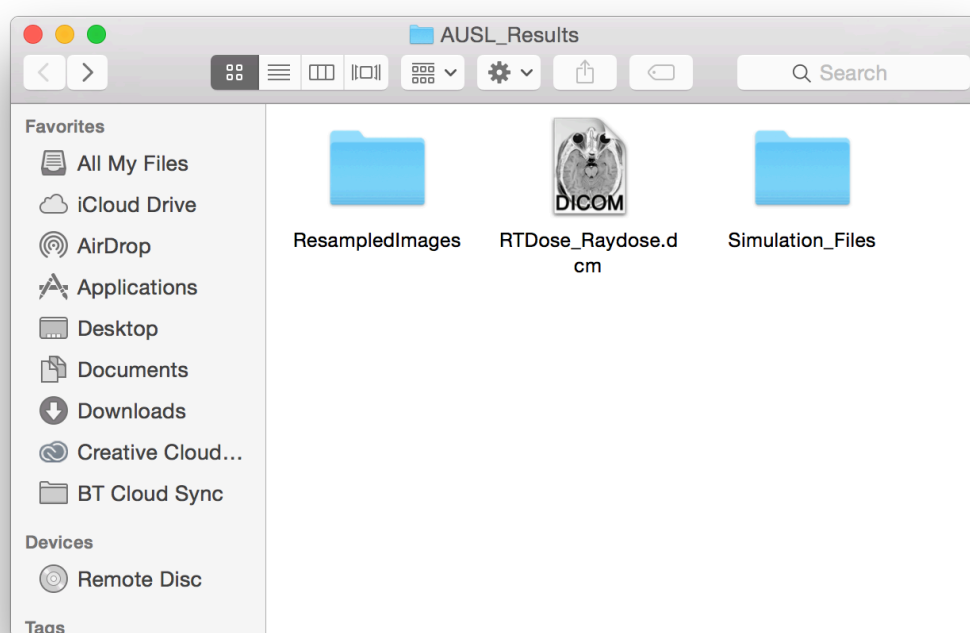


Figure 11 Structure of the output directory.

5.1 Viewing the Contents of the Simulation File

The simulation data is stored in an efficient ROOT file, with data stored in a tree hierarchy. If you wish to view the contents of the raw simulation data then you can use ROOT, which is bundled along with the Raydose application.

The first step is to ensure that you have set up your system environment to run ROOT. To do this, open a terminal and then open your ~/.profile or ~/.bashrc file depending on whether you are using a MacOS or Linux platform. Add the following line to your profile script

```
. /PathToRaydoseInstallDirectory/Raydose/ROOT/bin/thisroot.sh
```

being careful to ensure that you change the Raydose install directory. Save the profile script and then restart your terminal or source your profile script. Having done all of this you should now have configured your environment and if you issue the command “root” at the command prompt you will be presented with a ROOT splash screen similar to the one shown in Figure 12.



Figure 12 ROOT splash screen when loaded from command line

Your terminal prompt will then also become a ROOT interpreter prompt which allows you to run ROOT specific commands. If you don't see a ROOT command prompt you have likely not set your profile path to the “thisroot.sh” script correctly.

If you are still in the ROOT environment, type “.q” to exit. Now move your terminal to the directory which contains your Raydose simulation output. For example, if you specified that your simulation data should be placed in ~/home/username/RaydoseSim1 then move to this directory with your terminal.

Once inside this directory you should be able to see a further subfolder named “Simulation_Files”. Move into this directory and issue the command:-

```
root SimulationData.root
```

Which will launch root the standard simulation file “SimulationData.root” which will be brought

into scope and will be able to be interrogated by the ROOT browser. You will see a screen in your terminal which looks similar to Figure 13.



```
Simulation_Files - root.exe - 96x25
Nickys-MBP:Simulation_Files nppatt$ root SimulationData.root

Welcome to ROOT 6.04/02      http://root.cern.ch
                          (c) 1995-2014, The ROOT Team
Built for macosx64
From tag v6-04-02, 14 July 2015
Try '.help', '.demo', '.license', '.credits', '.quit'/'.'

root [0]
Attaching file SimulationData.root as _file0...
Warning in <TFile::Init>: no StreamerInfo found in SimulationData.root therefore preventing sche
ma evolution when reading this file.
(class TFile *) 0x7f8d1b74cfb0
root [1]
```

Figure 13 ROOT loaded with the SimulationData.root file in scope and ready to be interrogated.

Once you see the ROOT prompt, you can then issue a command to load a TBrowser, which allows you to graphically navigate the file structure of the Raydose Simulation file which has been stored in ROOT file format.

```
TBrowser a;
```

At this point a graphical browser will load as presented in Figure 14.

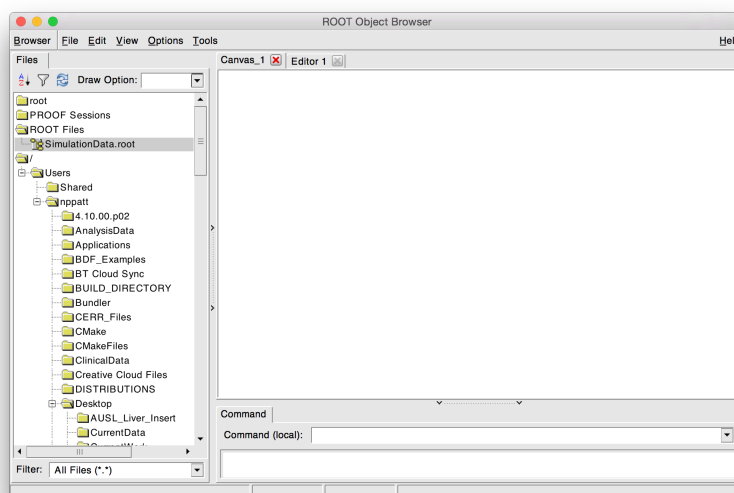


Figure 14 ROOT graphical file browser.

A drop down list of items will appear under the SimulationData.root file if you double click on it in

the graphical browser (see Figure 15). The list of parameters that are stored in the file are Activity, CT density, CT materials, Sim Data, Dose, Uncertainties, LET, Primaries and SimStats.

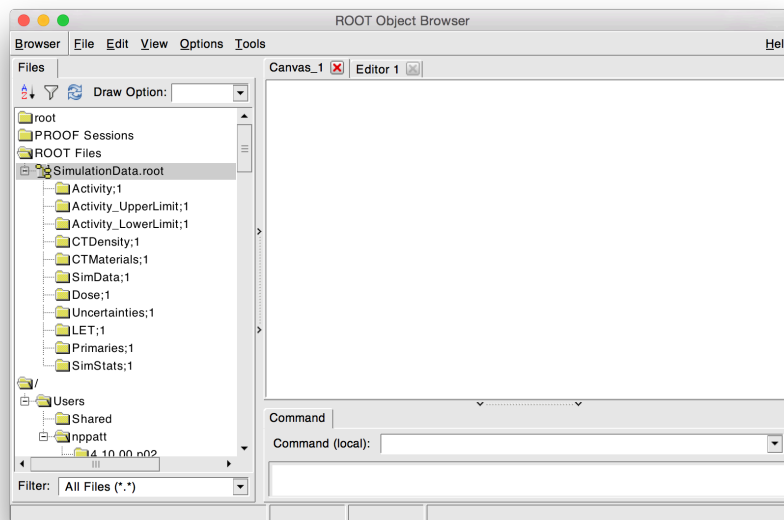


Figure 15 Available parameters, which are stored in the simulation file.

By double clicking on “Activity” for example, you will be able to look at the activity images that were used to run the Raydose simulation. To do this, double click “Activity” folder and from the drop “Draw option” down box at the top of the browser, select “colz” (see Figure 16). The image will be drawn in the canvas window (see Figure 17).

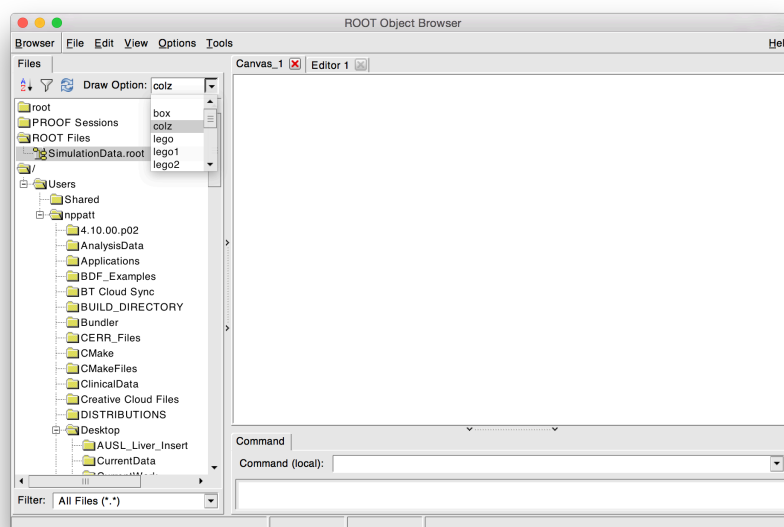


Figure 16 Enabling the “colz” option which will colour the Z axis of a 2D histogram when drawing the slice-by-slice simulation data.

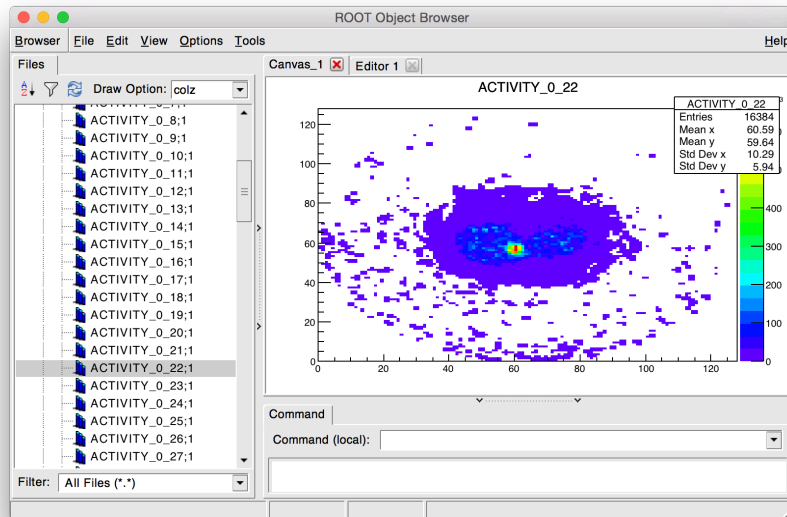


Figure 17 Selection of slice 22 of PET scan viewed in the ROOT graphical browser.

5.2 What is Stored Within the Simulation File?

The following is stored inside the simulation file:-

Activity Data

This is the slice-by-slice activity data extracted from the DICOM files (with any calibration factor applied to convert into an activity or activity concentration). The slice-by-slice data in the simulation file will be in absolute activity per voxel (Bq/voxel). The naming convention for the histograms which store this slice-by-slice information is

ACTIVITY_X_Y

Where X is the scan number (0 is by default the first scan in Raydose) and Y is the slice number.

CT Density and Material Data

Contains the material index and density of the material that was used in the virtual patient phantom.

Dose Data

This contains the output of the Raydose MC simulation. These are the “scored dose per simulated decay” maps for each of the supplied patient scans. The naming convention is:-

DOSE_X_Y

Where X is the scan number (0 is by default the first scan in Raydose) and Y is the slice number.

Uncertainty Data

This contains the Monte-Carlo uncertainty for each scan simulation.

Sim Stats

Contains stats about the simulation at run time. It contains the real time taken to run (in seconds), the number of threads used on the processing machine to run the simulation and also the number of events that were simulated.

To view these parameters, click on “SimStats” (see Figure 18) and right click on the option/parameter whose value you wish to know. Click on “Print” and the value will appear in the terminal window.

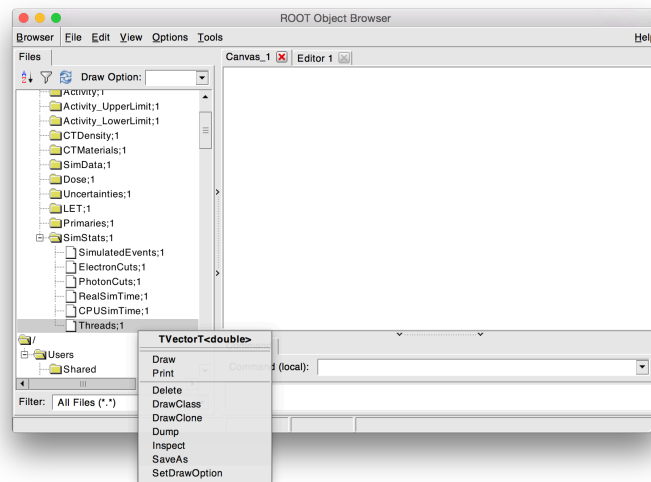
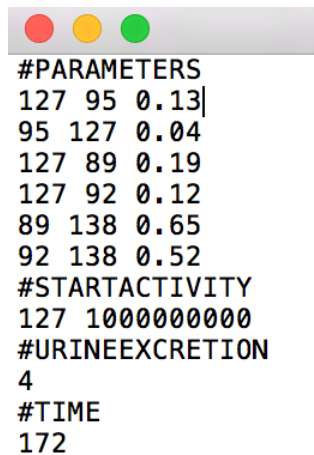


Figure 18 The SimStats option. To view the value, right click on the parameter you wish to see and click on "Print". The value will become visible in the terminal.

6. ICRP Phantom and Compartmental Model

The ICRP 110 phantom (female and male) has been implemented into Raydose with some basic compartmental modeling functionality. For the time being, the compartment model can only be executed from the command line implementation of Raydose however the compartmental model parameters will soon be able to be launched from the graphical user environment.

The ICRP phantoms have each been included as virtual patient phantoms in Raydose. These phantoms define large numbers of material compositions and organs and they have been incorporated into Raydose exactly as defined in the ICRP Publication 110¹.



```
#PARAMETERS
127 95 0.13
95 127 0.04
127 89 0.19
127 92 0.12
89 138 0.65
92 138 0.52
#STARTACTIVITY
127 1000000000
#URINEEXCRETION
4
#TIME
172
```

Figure 19 Example Compartmental Model Parameter File. A fictitious example for demonstration purposes only.

You must first of all define yourself a parameters file which defines:-

1. The transfer coefficients between organs
2. The starting activity within each organ
3. The periodic interval at which the bladder is voided
4. The time over which the simulation should be performed

An example file is outlined in Figure 19. The first block that must be defined is the parameter block. Begin by typing #PARAMETERS and then on the next line begin to specify the transfer coefficients. The transfer coefficients are defined as

From Organ ID	To Organ ID	Transfer Rate
---------------	-------------	---------------

So for example the first line in of Figure 19 it has been specified that each hour a fraction of 0.13 of the original content of organ 127 (spleen) should be transferred to organ 95 (liver). You should specify all of the exchanges both in and out of the organ in this manner.

The next block that must be defined is the #STARTACTIVITY block. This declares the activity, in Becquerel, that is homogenously spread through the organ. You may specify multiple organs, but

¹ Ann. ICRP 39 (2), 2009

in Figure 19 only organ 127 (the spleen) has been specified to have a starting activity of 100MBq.

The #URINEEXCRETION block will declare that the bladder should be voided every 4 hours. This can be changed to a user adjusted value.

The #TIME block declares that the dose calculation should be performed over a period of 172 hours.

Once you have created your file, save it. The name does not matter, however for demonstration purposes lets assume for now it has been named "icrp_model.dat". Finally, in order to run your simulation, issue the following command from the command line: -

```
Raydose -use-phantom ICRP110-F -use-compartment-model icrp_model.dat -A 90 -Z 39  
-histories 100000000 -output ~/ICPR_Results/
```

Which will use the ICRP 110 Female phantom and load the icrp_model.dat parameters to be simulated. You must also specify the isotope to be used and the number of histories to be simulated.

When the simulation is finished your results will be stored in the the output directory you have specified, where you will find an RTDose DICOM file and also a file called "ICRP110_TimeActivityCurve.dat" which contains the organ time activity curves which were derived from the supplied parameters during the simulation.

6.1 How are time activity curves derived?

The parameters that are supplied by the user form transfers coefficients between different compartments of the body. A differential equation is formed for each organ utilizing the user supplied parameters that specify the input and output coefficients that "feed" each organ. This is done for all organs and a set of N differential equations are formed for each organ in the body. The N differential equations are then solved numerically to obtain time activity curves used to deduced the number of decays occurring within each organ.

7 Radioactive Decay Simulation

Raydose makes use of the G4RadioactiveDecay² module which simulates full decay chains from a parent nucleus. However, by default the simulation is limited to simulate only the ground state decay of the chosen isotope to the ground state of the daughter nucleus. If the daughter nucleus is not stable and would further decay, this is not simulated by default.

However, this option can be turned on in Raydose if you wish to include the full decay chain. For example, there are many steps in the decay chain of the alpha emitting 223-Ra isotope. To include them all, you should include the argument “-fullddecaychain” if running Raydose from the command line or select the “Include full decay chain” box if running Raydose from the graphical submission interface.

The database from which the simulated decay schemes are modeled are taken from the respected Evaluated Nuclear Structure Data File (<http://www.nndc.bnl.gov/ensdf/>), a peer reviewed and exceptionally extensive nuclear decay database. The beta spectra are theoretically calculated beta spectra.

² Radioactive Decays in Geant4 - <http://arxiv.org/pdf/1307.0996.pdf>

8. Technical Details

8.1 System Requirements

Raydose will run on either MacOS (Yosemite, as of August 2015) and Ubuntu Linux (14.04). However, it may well work on other variants of Linux. These are however, the tested and supported platforms for the time being.

Raydose is resource intensive. It will scale to make use of the increasing CPU availability and RAM offered by your hardware. It will run on a desktop machine but will also run and make use of the resources available on a workstation server.

As an example, Raydose has been developed and run on a Dell PowerEdge Server with 20 Xeon CPU Cores and 64Gb RAM. The more processing cores that your machine has, the faster that the Raydose simulation will complete, where Raydose will run multithreaded and make use of all processing cores.

Important

You will likely find that running simulation where the CT scan has dimensions of 512x512x100 slices will not run on a standard desktop with 8Gb of RAM. This is a huge number of voxels for which the dose and other parameters need to be scored. A simulation of this size will require more RAM or you must down sample the CT image (which can be done within Raydose) so that the constructed virtual phantom is more like 128x128x100. This is much more likely to run on a machine with only 8Gb of RAM.

Also, specify multiple threads will increase the RAM that is required. For each thread that is required a unique scoring class must be created for that thread to track the dose deposition and other parameters within the virtual patient phantom. Clearly, for large voxelised volumes being tracked on multiple threads this will also increase RAM usage.

If you find that memory consumption is too high, try down sampling the input CT image and also using fewer threads.

8.2 Licenses

Raydose makes use of a number of third party libraries. Links to the license arrangements for each of these dependencies are included here for user reference.

- Geant4 (<http://geant4.web.cern.ch/geant4/license/>)
- ROOT (<https://root.cern.ch/root/License.html>)
- Insight Registration Segmentation Toolkit (<http://www.itk.org/ITK/project/licenseversion1.html>)
- Visualization Toolkit (<http://www.vtk.org/licensing/>)
- Qt5 (<http://doc.qt.io/qt-5/lgpl.html>)
- BOOST (<http://www.boost.org/users/license.html>)

Annex A

List of ICRP 110 Phantom organ ID values. Required to write a parameters file.

0	Air External	38	Ankles and foot bones, spongiosa
1	Adrenal, left	39	Mandible, cortical
2	Adrenal, right	40	Mandible, spongiosa
3	Anterior nasal passage (ET1)	41	Pelvis, cortical
4	Posterior nasal passage down to larynx (ET2)	42	Pelvis, spongiosa
5	Oral mucosa, tongue	43	Ribs, cortical
6	Oral mucosa, lips and cheeks	44	Ribs, spongiosa
7	Trachea	45	Scapulae, cortical
8	Bronchi	46	Scapulae, spongiosa
9	Blood vessels, head	47	Cervical spine, cortical
10	Blood vessels, trunk	48	Cervical spine, spongiosa
11	Blood vessels, arms	49	Thoracic spine, cortical
12	Blood vessels, legs	50	Thoracic spine, spongiosa
13	Humeri, upper half, cortical	51	Lumbar spine, cortical
14	Humeri, upper half, spongiosa	52	Lumbar spine, spongiosa
15	Humeri, upper half, medullary cavity	53	Sacrum, cortical
16	Humeri, lower half, cortical	54	Sacrum, spongiosa
17	Humeri, lower half, spongiosa	55	Sternum, cortical
18	Humeri, lower half, medullary cavity	56	Sternum, spongiosa
19	Ulnae and radii, cortical	57	Cartilage, head
20	Ulnae and radii, spongiosa	58	Cartilage, trunk
21	Ulnae and radii, medullary cavity	59	Cartilage, arms
22	Wrists and hand bones, cortical	60	Cartilage, legs
23	Wrists and hand bones, spongiosa	61	Brain
24	Clavicles, cortical	62	Breast, left, adipose tissue
25	Clavicles, spongiosa	63	Breast, left, glandular tissue
26	Cranium, cortical	64	Breast, right, adipose tissue
27	Cranium, spongiosa	65	Breast, right, glandular tissue
28	Femora, upper half, cortical	66	Eye lense, left
29	Femora, upper half, spongiosa	67	Eye bulb, left
30	Femora, upper half, medullary cavity	68	Eye lense, right
31	Femora, lower half, cortical	69	Eye bulb, right
32	Femora, lower half, spongiosa	70	Gall bladder wall
33	Femora, lower half, medullary cavity	71	Gall bladder contents
34	Tibiae, fibulae and patellae, cortical	72	Stomach wall
35	Tibiae, fibulae and patellae, spongiosa	73	Stomach contents
36	Tibiae, fibulae and patellae, medullary cavit	74	Small intestine wall

Continued...

75	Small intestine contents	113	Pancreas
76	Ascending colon wall	114	Pituitary gland
77	Ascending colon contents	115	Prostate
78	Transverse colon wall, right	116	Residual tissue, head
79	Transverse colon contents, right	117	Residual tissue, trunk
80	Transverse colon wall, left	118	Residual tissue, arms
81	Transverse colon contents, left	119	Residual tissue, legs
82	Descending colon wall	120	Salivary glands, left
83	Descending colon contents	121	Salivary glands, right
84	Sigmoid colon wall	122	Skin, head
85	Sigmoid colon contents	123	Skin, trunk
86	Rectum wall	124	Skin, arms
87	Heart wall	125	Skin, legs
88	Heart contents (blood)	126	Spinal cord
89	Kidney, left, cortex	127	Spleen
90	Kidney, left, medulla	128	Teeth
91	Kidney, left, pelvis	129	Testis, left
92	Kidney, right, cortex	130	Testis, right
93	Kidney, right, medulla	131	Thymus
94	Kidney, right, pelvis	132	Thyroid
95	Liver	133	Tongue (inner part)
96	Lung, left, blood	134	Tonsils
97	Lung, left, tissue	135	Ureter, left
98	Lung, right, blood	136	Ureter, right
99	Lung, right, tissue	137	Urinary bladder wall
100	Lymphatic nodes, extrathoracic airways	138	Urinary bladder contents
101	Lymphatic nodes, thoracic airways	139	Uterus
102	Lymphatic nodes, head	140	Air inside body
103	Lymphatic nodes, trunk		
104	Lymphatic nodes, arms		
105	Lymphatic nodes, legs		
106	Muscle, head		
107	Muscle, trunk		
108	Muscle, arms		
109	Muscle, legs		
110	Oesophagus		
111	Ovary, left		
112	Ovary, right		

APPENDIX C: MATLAB coding

- Code used to calculate the percentage error of MC simulation.

```
folder = uigetdir;
folderlist=dir(folder);
for index = 4 : (size(folderlist, 1));
    pathname = [folder, '/', folderlist(index).name];
    load(pathname);
    indexS= planC{end};
    %calculating number of error maps, structures and dose maps available
    nError=(size(planC{indexS.dose},2)-2)/2;
    nStruct=size(planC{indexS.structures},2);
    indexdose=(nError*2)+1;
    indexlast=size(planC{indexS.dose},2);
    switch nError
        case 1
            absError1 =
planC{indexS.dose}(1).doseArray.*planC{indexS.dose}(2).doseArray./100;
            absError=sqrt(absError1.^2);
            errorTot=absError./planC{indexS.dose}(indexdose).doseArray.*100;
        case 2
            absError1 =
planC{indexS.dose}(1).doseArray.*planC{indexS.dose}(3).doseArray./100;
            absError2 =
planC{indexS.dose}(2).doseArray.*planC{indexS.dose}(4).doseArray./100;
            absError=sqrt(absError1.^2+absError2.^2);
            errorTot=absError./planC{indexS.dose}(indexdose).doseArray.*100;
        case 3
            absError1 =
planC{indexS.dose}(1).doseArray.*planC{indexS.dose}(4).doseArray./100;
            absError2 =
planC{indexS.dose}(2).doseArray.*planC{indexS.dose}(5).doseArray./100;
            absError3 =
planC{indexS.dose}(3).doseArray.*planC{indexS.dose}(6).doseArray./100;
            absError=sqrt(absError1.^2+absError2.^2+absError3.^2);
            errorTot=absError./planC{indexS.dose}(indexdose).doseArray.*100;
        case 4
            absError1 =
planC{indexS.dose}(1).doseArray.*planC{indexS.dose}(5).doseArray./100;
            absError2 =
planC{indexS.dose}(2).doseArray.*planC{indexS.dose}(6).doseArray./100;
            absError3 =
planC{indexS.dose}(3).doseArray.*planC{indexS.dose}(7).doseArray./100;
            absError4 =
planC{indexS.dose}(4).doseArray.*planC{indexS.dose}(8).doseArray./100;
            absError=sqrt(absError1.^2+absError2.^2+absError3.^2+absError4.^2);
            errorTot=absError./planC{indexS.dose}(indexdose).doseArray.*100;
        case 5
            absError1 =
planC{indexS.dose}(1).doseArray.*planC{indexS.dose}(6).doseArray./100;
            absError2 =
planC{indexS.dose}(2).doseArray.*planC{indexS.dose}(7).doseArray./100;
            absError3 =
planC{indexS.dose}(3).doseArray.*planC{indexS.dose}(8).doseArray./100;
```

```

        absError4 =
planC{indexS.dose}(4).doseArray.*planC{indexS.dose}(9).doseArray./100;
        absError5 =
planC{indexS.dose}(5).doseArray.*planC{indexS.dose}(10).doseArray./100;

absError=sqrt(absError1.^2+absError2.^2+absError3.^2+absError4.^2+absError5
.^2);
    errorTot=absError./planC{indexS.dose}(indexdose).doseArray.*100;
end
    %saving the total error map in the planC
    planC{indexS.dose}(indexlast).doseArray=errorTot;

    save_planC(planC,planC{indexS.CERROptions},'passed',[pathname(1:end-4)
'\n']);

    %calculating the mean percentage error for each structure
    for i=1:nStruct
        doseStats(i) = trialCalcDoseStats(planC,i,indexlast);
    end
    save(folderlist(index).name, 'doseStats')

end
end

```

- Code used to calculate the total activity in the VOIs.

```

function [nameStruct] = ActivityVOI(planC, scanNumb, numbStruct)
%calculating the first and the last number for the cycle
totalStruct = scanNumb * numbStruct;
StartNumb = numbStruct + 1;

%calculating the total activity
for structNum = StartNumb : totalStruct
    mask = maskCERRscan(planC, structNum);
    total = sum(mask(:));
    nameStruct(structNum - StartNumb + 1) = 28.5 * total;
end
%converting the activity in MBq and stored in a list
nameStruct = nameStruct ./ 10^6;
nameStruct = num2cell(reshape(nameStruct', [numbStruct (scanNumb - 1)]));

```

References

1. Flux G, Moss L, Buscombe J, et al. *BIR REPORT 23 Molecular Radiotherapy in the UK: current status and Recommendations for further investigation*. 2011.
2. Fleming JS, Perkins AC. *Targeted Radiotherapy: IPEM Report*. Institute of Physics & Engineering in Medicine & Biology; 2000. (Ipem Report Series).
3. Wikibooks. *The Opensource Handbook of Nanoscience and Nanotechnology*. 2013. Available from: <https://en.wikibooks.org/wiki/Nanotechnology>
4. Michael G. Stabin. *Fundamentals of nuclear Medicine Dosimetry*. Springer; 2007. 237 p.
5. L'Annunziata MF. *Radiation Physics and Radionuclide Decay*. In: Handbook of Radioactivity Analysis. 2013. p. 1–162.
6. Luster M, Clarke SE, Dietlein M, et al. *Guidelines for radioiodine therapy of differentiated thyroid cancer*. Vol. 35, European Journal of Nuclear Medicine and Molecular Imaging. 2008. p. 1941–59.
7. *Cancer Research UK statistics*. [accessed 9 May 2018] Available from: <http://www.cancerresearchuk.org/health-professional/cancer-statistics/statistics-by-cancer-type/>
8. Vallis KA, Reilly RM, Scollard D, et al. *Phase I trial to evaluate the tumor and normal tissue uptake, radiation dosimetry and safety of (111)In-DTPA-human epidermal growth factor in patients with metastatic EGFR-positive breast cancer*. Am J Nucl Med Mol Imaging.

- 2014;4(2):181–92.
9. Tennvall J, Brans B. *EANM procedure guideline for ³²P phosphate treatment of myeloproliferative diseases*. Vol. 34, European Journal of Nuclear Medicine and Molecular Imaging. 2007. p. 1324–7.
 10. Cheung M, Haynes A, Stevens A, Meyer R, Imrie K. *Yttrium ⁹⁰ ibritumomab tiuxetan in lymphoma*. Vol. 47, Leukemia and Lymphoma. 2006. p. 967–77.
 11. Edelman MJ, Clamon G, Kahn D, Magram M, Lister-James J, Line BR. *Targeted radiopharmaceutical therapy for advanced lung cancer: Phase I trial of rhenium ¹⁸⁸ P2045, a somatostatin analog*. J Thorac Oncol. 2009 Dec;4(12):1550–4.
 12. Heinzer H, König F, Klutmann S. *Alpha Emitter radium-223 Dichloride: New Therapy in Castration-Resistant Prostate Cancer With Symptomatic Bone Metastases*. Urologe A. 2014;53(4).
 13. Gallicchio R, Mastrangelo PA, Nardelli A, et al. *Radium-223 for the treatment of bone metastases in castration-resistant prostate cancer: when and why*. Vol. 105, Tumori. Tumori; 2019. p. 367–77.
 14. Bilen MA, Johnson MM, Mathew P, et al. *Randomized phase 2 study of bone-targeted therapy containing strontium-89 in advanced castrate-sensitive prostate cancer*. Cancer. 2015 Jan 1;121(1):69–76.
 15. Sartor O. *Overview of samarium ¹⁵³ lexidronam in the treatment of painful metastatic bone disease*. Rev Urol. 2004;6 Suppl 10(Suppl 10):S3–12.
 16. NCRI. *CTRad: identifying opportunities to promote progress in molecular radiotherapy research in the UK*. 2016.

17. Yalcin S, Öberg K. *Neuroendocrine tumours : diagnosis and management*. Springer; 2015. 578 p.
18. Yao JC, Hassan M, Phan A, et al. *One hundred years after 'carcinoid': Epidemiology of and prognostic factors for neuroendocrine tumors in 35,825 cases in the United States*. J Clin Oncol. 2008 Jun 20;26(18):3063–72.
19. Oronsky B, Ma PC, Morgensztern D, Carter CA. *Nothing But NET: A Review of Neuroendocrine Tumors and Carcinomas*. Neoplasia. 2017 Dec 1;19(12):991–1002.
20. Taal BG, Visser O. *Epidemiology of Neuroendocrine Tumours*. Neuroendocrinology. 2004;80(1):3–7.
21. Vinik AI, Chaya C. *Clinical Presentation and Diagnosis of Neuroendocrine Tumors*. Hematol Oncol Clin North Am. 2016 Feb 1;30(1):21–48.
22. Modlin IM, Lye KD, Kidd M. *A 5-decade analysis of 13,715 carcinoid tumors*. Cancer. 2003 Feb 15;97(4):934–59.
23. Hallet J, Law CHL, Cukier M, Saskin R, Liu N, Singh S. *Exploring the rising incidence of neuroendocrine tumors: A population-based analysis of epidemiology, metastatic presentation, and outcomes*. Cancer. 2015 Feb 15;121(4):589–97.
24. Nishiyama Y, Katsura K ichiro. *The neuroendocrine system and its regulation*. In: Neuroanesthesia and Cerebrospinal Protection. Tokyo: Springer Japan; 2015. p. 31–8.
25. Fazio N, de Braud F, Delle Fave G, Oberg K. *Interferon-alpha and somatostatin analog in patients with gastroenteropancreatic*

- neuroendocrine carcinoma: single agent or combination?* Ann Oncol. 2007 Oct 3;18(1):13–9.
26. Vinik A, Moattari AR. *Use of somatostatin analog in management of carcinoid syndrome.* Dig Dis Sci. 1989 Mar;34(3 Supplement):14S-27S.
 27. Rindi G, Klöppel G, Alhman H, et al. *TNM staging of foregut (neuro)endocrine tumors: A consensus proposal including a grading system.* In: Virchows Archiv. 2006. p. 395–401.
 28. Bosman F, Carneiro F, Hruban R, Theise N. *WHO classification of tumors of digestive system.* WHO press. 2010. 417 p.
 29. Pape UF, Jann H, Müller-Nordhorn J, et al. *Prognostic relevance of a novel TNM classification system for upper gastroenteropancreatic neuroendocrine tumors.* Cancer. 2008 Jul 15;113(2):256–65.
 30. Bodei L, Cremonesi M, Grana CM, et al. *Peptide receptor radionuclide therapy with ¹⁷⁷Lu-DOTATATE: the IEO phase I-II study.* Eur J Nucl Med Mol Imaging. 2011 Dec 3;38(12):2125–35.
 31. Papamichail DG, Exadaktylou PE, Chatzipavlidou VD. *Neuroendocrine tumors: Peptide receptors radionuclide therapy (PRRT).* Hell J Nucl Med. 2016;19(1):75–82.
 32. Nicolas G, Baum R, Herrmann K, et al. *Phase 1/2 open-label trial to assess the safety and preliminary efficacy of ¹⁷⁷Lu-OPS201 as peptide receptor radionuclide therapy in patients with somatostatin receptor-positive, progressive neuroendocrine tumours.* In: 10th NANETS Annual Meeting. 2017. p. 36.
 33. Thundimadathil J. *Cancer Treatment Using Peptides: Current*

- Therapies and Future Prospects.* J Amino Acids. 2012;2012:1–13.
34. De Herder WW, Hofland LJ, Van Der Lely AJ, Lamberts SWJ.
Somatostatin receptors in gastroentero-pancreatic neuroendocrine tumours. In: Endocrine-Related Cancer. 2003. p. 451–8.
 35. Kwekkeboom DJ, De Herder WW, Kam BL, et al. *Treatment with the radiolabeled somatostatin analog [177Lu- DOTA0,Tyr3]octreotate: Toxicity, efficacy, and survival.* J Clin Oncol. 2008;26(13):2124–30.
 36. Forrer F, Uusijärvi H, Storch D, Maecke HR, Mueller-Brand J.
Treatment with 177Lu-DOTATOC of patients with relapse of neuroendocrine tumors after treatment with 90Y-DOTATOC. J Nucl Med. 2005 Aug 1;46(8):1310–6.
 37. Romer A, Seiler D, Marincek N, et al. *Somatostatin-based radiopeptide therapy with [177Lu-DOTA]-TOC versus [90Y-DOTA]-TOC in neuroendocrine tumours.* Eur J Nucl Med Mol Imaging. 2014;41(2):214–22.
 38. Reubi JC, Schär JC, Waser B, et al. *Affinity profiles for human somatostatin receptor subtypes SST1-SST5 of somatostatin radiotracers selected for scintigraphic and radiotherapeutic use.* Eur J Nucl Med. 2000;27(3):273–82.
 39. Bodei L, Cremonesi M, Grana CM, et al. *Peptide receptor radionuclide therapy with 177Lu-DOTATATE: The IEO phase I-II study.* Eur J Nucl Med Mol Imaging. 2011 Dec;38(12):2125–35.
 40. Sansovini M, Severi S, Ambrosetti A, et al. *Treatment with the radiolabelled somatostatin analog Lu-DOTATATE for advanced pancreatic neuroendocrine tumors.* Neuroendocrinology.

- 2013;97(4):347–54.
41. Baum RP, Kluge AW, Kulkarni H, et al. *[177Lu-DOTA]0-D-Phe1-Tyr3-Octreotide (177Lu-DOTA TOC) for peptide receptor radiotherapy in patients with advanced neuroendocrine tumours: A Phase-II study.* Theranostics. 2016;6(4):501–10.
 42. Kulkarni HR, Schuchardt C, Baum RP. *Peptide Receptor Radionuclide Therapy with 177Lu Labeled Somatostatin Analogs DOTATATE and DOTATOC: Contrasting Renal Dosimetry in the Same Patient.* Recent Results Cancer Res. 2013;194:551–9.
 43. Schuchardt C, Kulkarni HR, Prasad V, Zachert C, Müller D, Baum RP. *The Bad Berka Dose Protocol: Comparative Results of Dosimetry in Peptide Receptor Radionuclide Therapy Using 177Lu-DOTATATE, 177Lu-DOTANOC, and 177Lu-DOTATOC.* Recent Results Cancer Res. 2013;194:519–36.
 44. Esser JP, Krenning EP, Teunissen JJM, et al. *Comparison of [177Lu-DOTA0,Tyr3]octreotate and [177Lu-DOTA0,Tyr3]octreotide: Which peptide is preferable for PRRT?* Eur J Nucl Med Mol Imaging. 2006 Nov;33(11):1346–51.
 45. D'Arienzo M. *Emission of β^+ Particles Via Internal Pair Production in the $0^+ - 0^+$ Transition of ^{90}Zr : Historical Background and Current Applications in Nuclear Medicine Imaging.* Atoms. 2013 Mar 8;1(1):2–12.
 46. Chinol M, Zona C. *Evaluation of a method to determine ^{90}Sr contamination of ^{90}Y by extraction chromatography.* In: Therapeutic Radionuclide Generators: $^{90}\text{Sr}/^{90}\text{Y}$ and $^{188}\text{W}/^{188}\text{Re}$ Generators. 2009. p. 248.

47. Doha FJ, Rahmani S, Rikhtechi P, Rasaneh S, Sheikholislam Z, Shahhosseini S. *Development of DOTA-rituximab to be labeled with ^{90}Y for radioimmunotherapy of B-cell non-hodgkin lymphoma.* Iran J Pharm Res. 2017;16(2):619–29.
48. Metyko J, Erwin W, Poston J, Jimenez S. *^{90}Sr content in ^{90}Y -labeled SIR-Spheres and Zevalin.* Health Phys. 2014;107:S177–80.
49. Dash A, Pillai MRA, Knapp FF. *Production of ^{177}Lu for Targeted Radionuclide Therapy: Available Options.* Nucl Med Mol Imaging (2010). 2015;49(2):85–107.
50. Tristram M, Alaamer AS, Fleming JS, Lewington VJ, Zivanovic MA. *Iodine-131-metaiodobenzylguanidine dosimetry in cancer therapy: risk versus benefit.* J Nucl Med. 1996 Jun;37(6):1058–63.
51. Snyder WS, Auxier JA, Morgan KZ. *Report of ICRP Committee II on Permissible Dose for Internal Radiation.* Health Phys. 1960 Jan 1;3(1):146.
52. ICRP Publication 30. *Limits for Intakes of Radionuclides by Workers.* Ann ICRP. 1980;5/1-6:67.
53. Loevinger R, Budinger T, Watson E. *MIRD Primer for Absorbed Dose Calculations.* New York: Society of Nuclear Medicine; 1988.
54. Snyder WS, Ford MR, Warner GG, Watson SB. *MIRD Pamphlet 11.: 'S' absorbed dose per unit cumulated activity for selected radionuclides and organs.* Soc Nucl Med Reston, VA. 1975 Jan 1;1–257.
55. Cristy M, Eckerman K. *Specific absorbed fractions of energy at various ages from internal photons sources.* ORNL/TM-8381. 1987.
56. Bolch WE, Bouchet LG, Robertson JS, et al. *MIRD pamphlet No. 17: the*

- dosimetry of nonuniform activity distributions--radionuclide S values at the voxel level. Medical Internal Radiation Dose Committee. J Nucl Med. 1999 Jan;40(1):11S-36S.*
57. Moyes JS, Babich JW, Carter R, Meller ST, Agrawal M, McElwain TJ. *Quantitative study of radioiodinated metaiodobenzylguanidine uptake in children with neuroblastoma: correlation with tumor histopathology. J Nucl Med. 1989 Apr;30(4):474-80.*
 58. Stabin MG, Sparks RB, Crowe E. *OLINDA/EXM: the second-generation personal computer software for internal dose assessment in nuclear medicine. J Nucl Med. 2005 Jun;46(6):1023-7.*
 59. Stabin MG. *MIRDOS: personal computer software for internal dose assessment in nuclear medicine. J Nucl Med. 1996 Mar;37(3):538-46.*
 60. Stabin MG, Siegel JA. *Physical models and dose factors for use in internal dose assessment. Health Phys. 2003 Sep;85(3):294-310.*
 61. Howard DM, Kearfott KJ, Wilderman SJ, Dewaraja YK. *Comparison of I-131 radioimmunotherapy tumor dosimetry: unit density sphere model versus patient-specific Monte Carlo calculations. Cancer Biother Radiopharm. 2011 Oct;26(5):615-21.*
 62. Stabin MG, Konijnenberg MW. *Re-evaluation of absorbed fractions for photons and electrons in spheres of various sizes. J Nucl Med. 2000 Jan;41(1):149-60.*
 63. Grassi E, Fioroni F, Ferri V, et al. *Quantitative comparison between the commercial software STRATOS® by Philips and a homemade software for voxel-dosimetry in radiopeptide therapy. Phys Medica. 2015 Feb 1;31(1):72-9.*

64. Grimes J, Uribe C, Celler A. *JADA: A graphical user interface for comprehensive internal dose assessment in nuclear medicine*. Med Phys. 2013 Jun 19;40(7):072501.
65. Marcatili S, Pettinato C, Daniels S, et al. *Development and validation of RAYDOSE: A Geant4-based application for molecular radiotherapy*. Phys Med Biol. 2013;58(8):2491–508.
66. McKay E. *Mister Voxel: 3D internal dosimetry software for nuclear medicine*. Aust N Z J Med. 1998;28(3):376.
67. Dhawan A. *Medical Image Analysis*. 2011. 390 p.
68. Birkfellner W. *Applied Medical Image Processing*. 2011. 1–10 p.
69. Hyafil F, Gimelli A, Slart RHJA, et al. *EANM procedural guidelines for myocardial perfusion scintigraphy using cardiac-centered gamma cameras*. Eur J Hybrid Imaging. 2019;3(1).
70. Goshen E, Beilin L, Stern E, Kenig T, Goldkorn R, Ben-Haim S. *Feasibility study of a novel general purpose CZT-based digital SPECT camera: initial clinical results*. EJNMMI Phys. 2018 Mar 14;5(1):6.
71. Miyazaki Y, Kato Y, Imoto A, Fukuchi K. *Imaging of the thyroid and parathyroid using a cardiac cadmium-zinc-telluride camera: Phantom studies*. J Nucl Med Technol. 2018 Mar 1;46(1):39–44.
72. Keidar Z, Raysberg I, Lugassi R, Frenkel A, Israel O. *Novel Cadmium Zinc Telluride Based detector General Purpose Gamma Camera: Initial Evaluation and Comparison with a Standard Camera*. J Nucl Med. 2016;57(supplement 2):259.
73. Ljungberg M, Strand SE. *A Monte Carlo program for the simulation of scintillation camera characteristics*. Comput Methods Programs

- Biomed. 1989 Aug 1;29(4):257–72.
74. Ljungberg M. *SIMIND Monte Carlo based image reconstruction*. J Nucl Med. 2015 May 1;56:43.
 75. Ljungberg M. *The SIMIND Monte Carlo Program Manual*. 2012;111–28. Available from:
http://www2.msf.lu.se/simind/download/Simind_manual.pdf
 76. Smith NB, Webb A. *Introduction to Medical Imaging; Physics, Engineering and Clinical Applications*. Vol. 53, Journal of Chemical Information and Modeling. 2011. 1689–1699 p.
 77. Zitová B, Flusser J. *Image registration methods: A survey*. Image Vis Comput. 2003;21(11):977–1000.
 78. Paulino AC. *PET-CT in Radiotherapy Treatment Planning*. PET-CT in Radiotherapy Treatment Planning. Saunders/Elsevier; 2008. 1–259 p.
 79. Brock KK, Mutic S, McNutt TR, Li H, Kessler ML. *Use of image registration and fusion algorithms and techniques in radiotherapy: Report of the AAPM Radiation Therapy Committee Task Group No. 132*. Med Phys. 2017 Jul;44(7):e43–76.
 80. Bookstein FL. *Principal warps: thin-plate splines and the decomposition of deformations*. IEEE Trans Pattern Anal Mach Intell. 1989;11(6).
 81. Coselmon MM, Balter JM, McShan DL, Kessler ML. *Mutual information based CT registration of the lung at exhale and inhale breathing states using thin-plate splines*. Med Phys. 2004;31(11):2942–8.
 82. Rohr K, Fornefett M, Stiehl HS. *Spline-based elastic image registration: Integration of landmark errors and orientation attributes*. Comput Vis

- Image Underst. 2003 May 1;90(2):153–68.
83. Johnson HJ, Christensen GE. *Landmark and intensity-based, consistent thin-plate spline image registration*. In: Lecture Notes in Computer Science (including subseries Lecture Notes in Artificial Intelligence and Lecture Notes in Bioinformatics). 2001. p. 329–43.
 84. Sprengel R, Rohr K, Stiehl HS. *Thin-plate spline approximation for image registration*. In: Annual International Conference of the IEEE Engineering in Medicine and Biology - Proceedings. 1996. p. 1190–1.
 85. Wu Z, Lan T, Wang J, Ding Y, Qin Z. *Medical image registration using B-spline transform*. Int J Simul Syst Sci Technol. 2016;17(48):1.1-1.6.
 86. Yin Y, Hoffman EA, Lin CL. *Mass preserving nonrigid registration of CT lung images using cubic B-spline*. Med Phys. 2009;36(9):4213–22.
 87. Bai W, Brady M. *Regularized B-spline deformable registration for respiratory motion correction in PET images*. Phys Med Biol. 2009;54(9):2719–36.
 88. Jacobson T, Murphy M. *Optimized Knot Placement for B-Splines in Deformable Image Registration*. In: Medical Physics. 2011. p. 3761.
 89. Shusharina N, Sharp G. *Analytic regularization for landmark-based image registration*. Phys Med Biol. 2012;57(6):1477–98.
 90. Sorzano CÓS, Thévenaz P, Unser M. *Elastic registration of biological images using vector-spline regularization*. IEEE Trans Biomed Eng. 2005;52(4):652–63.
 91. Rueckert D, Hayes C, Hill DLG, Leach MO, Hawkes DJ, SLI. *Nonrigid registration using free-form deformations: application to breast MR images*. IEEE Trans Med Imaging. 1999;18(8):18:712-21.

92. Du X, Dang J, Wang Y, Wang S, Lei T. *A Parallel Nonrigid Registration Algorithm Based on B-Spline for Medical Images*. Comput Math Methods Med. 2016 Dec 7;2016:1–14.
93. Jenkinson M, Bannister P, Brady M, Smith S. *Improved Optimization for the Robust and Accurate Linear Registration and Motion Correction of Brain Images*. Neuroimage. 2002 Oct;17(2):825–41.
94. Jenkinson M, Smith S. *A global optimisation method for robust affine registration of brain images*. Med Image Anal. 2001 Jun;5(2):143–56.
95. Studholme C, Hill DLG, Hawkes DJ. *Automated 3-D registration of MR and CT images of the head*. Med Image Anal. 1996 Jun;1(2):163–75.
96. Dame A, Marchand E. *Second-order optimization of mutual information for real-time image registration*. IEEE Trans Image Process. 2012;21(9):4190–203.
97. Pluim JPW, Maintz JBAA, Viergever MA. *Mutual-information-based registration of medical images: A survey*. IEEE Trans Med Imaging. 2003;22(8):986–1004.
98. West J, Fitzpatrick JM, Wang MY, et al. *Comparison and evaluation of retrospective intermodality brain image registration techniques*. J Comput Assist Tomogr. 1997;21(4):554–66.
99. Klein S, Staring M, Pluim JPW. *Evaluation of optimization methods for nonrigid medical image registration using mutual information and B-splines*. IEEE Trans Image Process. 2007;16(12):2879–90.
100. Klein S, Pluim JPWW, Staring M, Viergever MA. *Adaptive stochastic gradient descent optimisation for image registration*. Int J Comput Vis. 2009 Mar 28;81(3):227–39.

101. Nocedal J, Wright SJ. *Numerical Optimization*. 2000.
102. Guerra L, De Ponti E, Elisei F, et al. *Respiratory gated PET/CT in a European multicentre retrospective study: Added diagnostic value in detection and characterization of lung lesions*. Eur J Nucl Med Mol Imaging. 2012 Sep 16;39(9):1381–90.
103. Verhey LJ. *Immobilizing and positioning patients for radiotherapy*. Semin Radiat Oncol. 1995 Apr 1;5(2):100–14.
104. Kutcher GJ, Coia L, Gillin M, et al. *Comprehensive QA for Radiation Oncology: Report of AAPM Radiation Therapy Committee Task Group 40*. Med Phys. 1994 Apr 1;21(4):581–618.
105. Ward G, Ramasamy S, Sykes JR, et al. *Superiority of Deformable Image Co-registration in the Integration of Diagnostic Positron Emission Tomography-Computed Tomography to the Radiotherapy Treatment Planning Pathway for Oesophageal Carcinoma*. Clin Oncol. 2016 Oct;28(10):655–62.
106. Grassi E, Fioroni F, Berenato S, et al. *Effect of image registration on 3D absorbed dose calculations in ¹⁷⁷Lu-DOTATOC peptide receptor radionuclide therapy*. Phys Medica. 2018 Jan 1;45:177–85.
107. Balter JM. *Image Processing in Radiation Therapy*. Vol. 42, Medical Physics. 2015. 1138–1139 p.
108. Berthon B, Marshall C, Evans M, Spezi E. *ATLAAS: An automatic decision tree-based learning algorithm for advanced image segmentation in positron emission tomography*. Phys Med Biol. 2016;61(13):4855–69.
109. Geets X, Lee JA, Bol A, Lonnew M, Grégoire V. *A gradient-based*

- method for segmenting FDG-PET images: Methodology and validation.* Eur J Nucl Med Mol Imaging. 2007 Sep;34(9):1427–38.
110. Halt M, Le Rest CC, Turzo A, Roux C, Visvikis D. *A fuzzy locally adaptive Bayesian segmentation approach for volume determination in PET.* IEEE Trans Med Imaging. 2009 Jun;28(6):881–93.
 111. Gustafsson J, Sundlöv A, Sjögren Gleisner K. *SPECT image segmentation for estimation of tumour volume and activity concentration in ¹⁷⁷Lu-DOTATATE radionuclide therapy.* EJNMMI Res. 2017;7(1).
 112. Filice A, Fraternali A, Frasoldati A, et al. *Radiolabeled somatostatin analogues therapy in advanced neuroendocrine tumors: A single centre experience.* J Oncol. 2012;2012:320198.
 113. Gupta SK, Singla S, Thakral P, Bal CS. *Dosimetric analyses of kidneys, liver, spleen, pituitary gland, and neuroendocrine tumors of patients treated with ¹⁷⁷Lu-DOTATATE.* Clin Nucl Med. 2013;38(3):188–94.
 114. Seregni E, Maccauro M, Chiesa C, et al. *Treatment with tandem [⁹⁰Y]DOTA-TATE and [¹⁷⁷Lu] DOTA-TATE of neuroendocrine tumours refractory to conventional therapy.* Eur J Nucl Med Mol Imaging. 2014;41(2):223–30.
 115. Balter H, Victoria T, Mariella T, et al. *¹⁷⁷Lu-Labeled Agents for Neuroendocrine Tumor Therapy and Bone Pain Palliation in Uruguay.* Curr Radiopharm. 2015;9(1):85–93.
 116. Limouris GS, Poulantzas V, Trompoukis N, et al. *Comparison of ¹¹¹In-[DTPA]octreotide versus non carrier added ¹⁷⁷Lu-[DOTA,Tyr3]-octreotate efficacy in patients with GEP-NET treated intra-arterially*

- for liver metastases. Clin Nucl Med.* 2016;41(3):194–200.
117. Said MA, Masud MA, Zaini MZ, Salleh RA, Lee BN, Zainon R. *Lu-177 DOTATATE dosimetry for neuroendocrine tumor: Single center experience.* J Phys Conf Ser. 2017;851(1):5–10.
 118. Hänscheid H, Lapa C, Buck AK, Lassmann M, Werner RA. *Dose mapping after endoradiotherapy with 177 Lu-DOTATATE/DOTATOC by a single measurement after 4 days.* J Nucl Med. 2018;59(1):75–81.
 119. Thakral P, Sen I, Pant V, et al. *Dosimetric analysis of patients with gastro entero pancreatic neuroendocrine tumors (NeTs) treated with PrCrT (peptide receptor chemo radionuclide therapy) using lu-177 DOTaTaTe and capecitabine/temozolomide (CaP/TeM).* Br J Radiol. 2018;91(1091):1–7.
 120. Kwekkeboom DJ, Bakker WH, Kam BL, et al. *Treatment of patients with gastro-entero-pancreatic (GEP) tumours with the novel radiolabelled somatostatin analogue [177Lu-DOTA0,Tyr3]octreotate.* Eur J Nucl Med Mol Imaging. 2003 Mar 9;30(3):417–22.
 121. Garkavij M, Nickel M, Sjögreen-Gleisner K, et al. *177Lu-[DOTA0,Tyr3] octreotate therapy in patients with disseminated neuroendocrine tumors: Analysis of dosimetry with impact on future therapeutic strategy.* In: Cancer. John Wiley & Sons, Ltd; 2010. p. 1084–92.
 122. Goffredo V, Paradiso A, Ranieri G, Gadaleta CD. *Yttrium-90 (90Y) in the principal radionuclide therapies: An efficacy correlation between peptide receptor radionuclide therapy, radioimmunotherapy and transarterial radioembolization therapy. Ten years of experience (1999-2009).* Vol. 80, Critical Reviews in Oncology/Hematology. Elsevier; 2011. p. 393–410.

123. Matović M. *Peptide receptor radionuclide therapy of neuroendocrine tumors: Case series*. Arch Oncol. 2012;20(3–4):143–8.
124. Beykan S, Dam JS, Eberlein U, et al. *¹⁷⁷Lu-OPS201 targeting somatostatin receptors: in vivo biodistribution and dosimetry in a pig model*. EJNMMI Res. 2016;6(1):1–9.
125. Willowson KP, Eslick E, Ryu H, Poon A, Bernard EJ, Bailey DL. *Feasibility and accuracy of single time point imaging for renal dosimetry following ¹⁷⁷Lu-DOTATATE ('Lutate') therapy*. EJNMMI Phys. 2018;5(1).
126. Del Prete M, Buteau FA, Arsenault F, et al. *Personalized ¹⁷⁷Lu-octreotate peptide receptor radionuclide therapy of neuroendocrine tumours: initial results from the P-PRRT trial*. Eur J Nucl Med Mol Imaging. 2019;46(3):728–42.
127. Del Prete M, Arsenault F, Saighi N, et al. *Accuracy and reproducibility of simplified QSPECT dosimetry for personalized ¹⁷⁷Lu-octreotate PRRT*. EJNMMI Phys. 2018;5(1).
128. Garske-Román U, Sandström M, Fröss Baron K, et al. *Prospective observational study of ¹⁷⁷Lu-DOTA-octreotate therapy in 200 patients with advanced metastasized neuroendocrine tumours (NETs): feasibility and impact of a dosimetry-guided study protocol on outcome and toxicity*. Eur J Nucl Med Mol Imaging. 2018;45(6):970–88.
129. Wehrmann C, Senftleben S, Zachert C, Müller D, Baum RP. *Results of individual patient dosimetry in peptide receptor radionuclide therapy with ¹⁷⁷Lu DOTA-TATE and ¹⁷⁷Lu DOTA-NOC*. In: Cancer Biotherapy and Radiopharmaceuticals. Mary Ann Liebert, Inc. 2 Madison Avenue

- Larchmont, NY 10538 USA; 2007. p. 406–16.
130. Mair C, Warwitz B, Fink K, et al. *Radiation exposure after ^{177}Lu -DOTATATE and ^{177}Lu -PSMA-617 therapy*. Ann Nucl Med. 2018;32(7):499–502.
 131. Chicheportiche A, Grozinsky-Glasberg S, Gross DJ, et al. *Predictive power of the post-treatment scans after the initial or first two courses of [^{177}Lu]-DOTA-TATE*. EJNMMI Phys. 2018;5(1):1–15.
 132. Chicheportiche A, Artoul F, Schwartz A, et al. *Reducing the number of CTs performed to monitor personalized dosimetry during peptide receptor radionuclide therapy (PRRT)*. EJNMMI Phys. 2018;5(1):1–15.
 133. Zaidi H, Sgouros G. *Therapeutic Applications of Monte Carlo Calculations in Nuclear Medicine*. Institute Of Physics Publishing; 2003.
 134. Seco J, Verhaegen F. *Monte Carlo Techniques in Radiation Therapy*. 2013.
 135. Vattulainen I, Kankaala K, Saarinen J, Ala-Nissila T. *A comparative study of some pseudorandom number generators*. Comput Phys Commun. 1995;86(3):209–26.
 136. Turner JE, Wright HA, Hamm RN. *A monte carlo primer for health physicists*. Vol. 48, Health Physics. 1985. p. 717–33.
 137. Harrison RL. *Introduction To Monte Carlo Simulation*. AIP Conf Proc. 2010 Jan 5;1204:17–21.
 138. Raeside DE. *Monte Carlo principles and applications*. Vol. 21, Physics in Medicine and Biology. IOP Publishing; 1976. p. 181–97.

139. Kawrakow I, Bielajew AF. *On the condensed history technique for electron transport*. Nucl Instruments Methods Phys Res Sect B Beam Interact with Mater Atoms. 1998;142(3):253–80.
140. Fernández-Varea JM, Mayol R, Baró J, Salvat F. *On the theory and simulation of multiple elastic scattering of electrons*. Nucl Instruments Methods Phys Res Sect B Beam Interact with Mater Atoms. 1993 Apr 1;73(4):447–73.
141. Agostinelli S, Allison J, Amako K, et al. *Geant4—a simulation toolkit*. Nucl Instruments Methods Phys Res Sect A Accel Spectrometers, Detect Assoc Equip. 2003 Jul 1;506(3):250–303.
142. Jenkins TM, Nelson WR, Rindi A. *Monte Carlo Transport of Electrons and Photons*. Springer US; 1988. 656 p.
143. Nelson WR, Hirayama H, Rogers DW. *The EGS4 Code System*. System. 1985;(SLAC-265):398.
144. Kawrakow I. *Accurate condensed history Monte Carlo simulation of electron transport. I. EGSnrc, the new EGS4 version*. Med Phys. 2000 Mar;27(3):485–98.
145. Kawrakow I, Rogers DWO. *The EGSnrc Code System: Monte Carlo Simulation of Electron and Photon Transport*. NRCC Rep PIRS-701. 2000 Jan 1;
146. Salvat F, Fernández-Varea J, Sempau J. *PENELOPE2008: A Code System for Monte Carlo Simulation of Electron and Photon Transport*. Workshop Proceedings, Data Bank NEA/NSC/DOC(2011)5, Barcelona. 2006.
147. Briesmeister JF. *MCNP(TM) – A General Monte Carlo N-Particle*

- Transport Code*. Los Alamos Natl Lab. 2000;(March):790.
148. *Introduction to Geant4*. 2010. Available from:
<http://geant4.web.cern.ch/geant4/UserDocumentation/UsersGuides/IntroductionToGeant4/fo/BookIntroToGeant4.pdf>
 149. Messel H, Crawford D. *Electron-photon Shower Distribution Function Tables for Lead, Copper and Air Absorbers*. 1970. 1512 p.
 150. Butcher JC, Messel H. *Electron number distribution in electron-photon showers in air and aluminium absorbers*. Nucl Phys. 1960 Oct 1;20:15–128.
 151. *Geant4, Physics Reference Manual*. 2017. Available from:
<http://geant4-userdoc.web.cern.ch/geant4-userdoc/UsersGuides/PhysicsReferenceManual/fo/PhysicsReferenceManual.pdf>
 152. Möller TR, Rosenow U, Bentley RE, et al. *ICRU - Report 42*. J Int Comm Radiat Units Meas. 1987 Dec 15;(1).
 153. Walters BRB, Kawrakow I, Rogers DWO. *History by history statistical estimators in the BEAM code system*. Med Phys. 2002 Nov 15;29(12):2745–52.
 154. Briesmeister JF, Booth TE, Collins DG, et al. *MCNP-A General Monte Carlo Code for Neutron and Photon Transport, Version 3A*. Los Alamos; 1986.
 155. Sempau J, Wilderman SJ, Bielajew AF. *DPM, a fast, accurate Monte Carlo code optimized for photon and electron radiotherapy treatment planning dose calculations*. Phys Med Biol. 2000 Aug;45(8):2263–91.
 156. Eisenhauer EA, Therasse P, Bogaerts J, et al. *New response evaluation*

- criteria in solid tumours: Revised RECIST guideline (version 1.1)*. Eur J Cancer. 2009;45(2):228–47.
157. Cancer Institute N. *Common Terminology Criteria for Adverse Events (CTCAE) Version 4.0*. In 2009. Available from: <http://www.meddramsso.com>
 158. Sollini M, Farioli D, Froio A, et al. *Brief report on the use of radiolabeled somatostatin analogs for the diagnosis and treatment of metastatic small-cell lung cancer patients*. J Thorac Oncol. 2013 Aug;8(8):1095–101.
 159. de Jong M, Breeman WA, Valkema R, Bernard BF, Krenning EP. *Combination radionuclide therapy using ¹⁷⁷Lu- and ⁹⁰Y-labeled somatostatin analogs*. J Nucl Med. 2005;46(Suppl. 1):13S-17S.
 160. Bison SM, Konijnenberg MW, Melis M, et al. *Peptide receptor radionuclide therapy using radiolabeled somatostatin analogs: Focus on future developments*. Vol. 2, Clinical and Translational Imaging. 2014. p. 55–66.
 161. Kunikowska J, Królicki L, Hubalewska-Dydejczyk A, Mikołajczak R, Sowa-Staszczak A, Pawlak D. *Clinical results of radionuclide therapy of neuroendocrine tumours with ⁹⁰Y-DOTATATE and tandem ⁹⁰Y/¹⁷⁷Lu-DOTATATE: which is a better therapy option?* Eur J Nucl Med Mol Imaging. 2011;38(10):1788–97.
 162. Zaknun JJ, Bodei L, Mueller-Brand J, et al. *The joint IAEA, EANM, and SNMMI practical guidance on peptide receptor radionuclide therapy (PRRNT) in neuroendocrine tumours*. Vol. 40, European Journal of Nuclear Medicine and Molecular Imaging. 2013. p. 800–16.

163. Bergsma H, Van Vliet EI, Teunissen JJM, et al. *Peptide receptor radionuclide therapy (PRRT) for GEP-NETs*. Vol. 26, Best Practice and Research: Clinical Gastroenterology. Best Pract Res Clin Gastroenterol; 2012. p. 867–81.
164. Ogawa K, Harata Y, Ichihara T, Kubo A, Hashimoto S. *A Practical Method for Position-Dependent Compton-Scatter Correction in Single Photon Emission CT*. IEEE Trans Med Imaging. 1991;10(3):408–12.
165. Shcherbinin S, Piwowska-Bilska H, Celler A, Birkenfeld B. *Quantitative SPECT/CT reconstruction for ^{177}Lu and $^{177}\text{Lu}/^{90}\text{Y}$ targeted radionuclide therapies*. Phys Med Biol. 2012;57(18):5733–47.
166. Siegel JA, Thomas SR, Stubbs JB, et al. *MIRD pamphlet no. 16: Techniques for quantitative radiopharmaceutical biodistribution data acquisition and analysis for use in human radiation dose estimates*. J Nucl Med. 1999 Feb;40(2):37S-61S.
167. Dewaraja YK, Frey EC, Sgouros G, et al. *MIRD Pamphlet No. 23: Quantitative SPECT for Patient-Specific 3-Dimensional Dosimetry in Internal Radionuclide Therapy*. J Nucl Med. 2012 Aug 1;53(8):1310–25.
168. Ljungberg M, Celler A, Konijnenberg MW, Eckerman KF, Dewaraja YK, Sjogreen-Gleisner K. *MIRD Pamphlet No. 26: Joint EANM/MIRD Guidelines for Quantitative ^{177}Lu SPECT Applied for Dosimetry of Radiopharmaceutical Therapy*. J Nucl Med. 2016 Jan 1;57(1):151–62.
169. Lawson JD, Schreibmann E, Jani AB, Fox T. *Quantitative evaluation of a cone-beam computed tomography-planning computed tomography deformable image registration method for adaptive radiation therapy*.

- J Appl Clin Med Phys. 2007 Nov;8(4):96–113.
170. Johnson HJ, McCormick MM, Ibanez L. *The ITK Software Guide*. Kitware, Inc.(January 2015). 2015. Available from: <https://itk.org/ItkSoftwareGuide.pdf>
 171. Avants BB, Tustison NJ, Stauffer M, Song G, Wu B, Gee JC. *The Insight ToolKit image registration framework*. Front Neuroinform. 2014 Apr 28;8(APR).
 172. Klein S, Staring M. *Elastix: The Manual*. 2019. Available from: <http://elastix.isi.uu.nl/download/elastix-5.0.0-manual.pdf>
 173. Klein S, Staring M, Murphy K, Viergever MA, Pluim JPW. *Elastix: A toolbox for intensity-based medical image registration*. IEEE Trans Med Imaging. 2010 Jan;29(1):196–205.
 174. Bland J, Altman D. *Statistical methods for assessing agreement between two methods of clinical measurement*. Lancet. 1986;1(8476):307–10.
 175. Bland JM, Altman DG. *Measuring agreement in method comparison studies*. In: Statistical Methods in Medical Research. 1999. p. 135–60.
 176. Mattsson S. *Patient dosimetry in nuclear medicine*. Radiat Prot Dosimetry. 2015 Jul;165(1–4):416–23.
 177. Balon HR, Brown TLY, Goldsmith SJ, et al. *The SNM Practice Guideline for Somatostatin Receptor Scintigraphy 2.0*. J Nucl Med Technol. 2011 Dec 1;39(4):317–24.
 178. Wang Z, Bovik AC, Sheikh HR, Simoncelli EP. *Image quality assessment: From error visibility to structural similarity*. IEEE Trans Image Process. 2004 Apr;13(4):600–12.

179. Zijdenbos AP, Dawant BM, Margolin RA, Palmer AC. *Morphometric Analysis of White Matter Lesions in MR Images: Method and Validation*. IEEE Trans Med Imaging. 1994;13(4):716–24.
180. Pukala J, Johnson PB, Shah AP, et al. *Benchmarking of five commercial deformable image registration algorithms for head and neck patients*. J Appl Clin Med Phys. 2016;17(3):25–40.
181. Oh S, Kim S. *Deformable image registration in radiation therapy*. Vol. 35, Radiation Oncology Journal. The Korean Society for Radiation Oncology; 2017. p. 101–11.
182. Nie K, Chuang C, Kirby N, Braunstein S, Pouliot J. *Site-specific deformable imaging registration algorithm selection using patient-based simulated deformations*. Med Phys. 2013 Mar 22;40(4):041911.
183. Ao ECI, Wu NY, Wang SJ, Song N, Mok GSP. *Improved dosimetry for targeted radionuclide therapy using nonrigid registration on sequential SPECT images*. Med Phys. 2015 Jan 29;42(2):1060–70.
184. Jackson PA, Beaugerard JM, Hofman MS, Kron T, Hogg A, Hicks RJ. *An automated voxelized dosimetry tool for radionuclide therapy based on serial quantitative SPECT/CT imaging*. Med Phys. 2013 Oct 10;40(11):112503.
185. Zhang A, Li J, Qiu H, Wang W, Guo Y. *Comparison of rigid and deformable registration through the respiratory phases of four-dimensional computed tomography image data sets for radiotherapy after breast-conserving surgery*. Med (United States). 2017 Dec;96(50):e9143.

186. Fortin D, Basran PS, Berrang T, Peterson D, Wai ES. *Deformable versus rigid registration of PET/CT images for radiation treatment planning of head and neck and lung cancer patients: A retrospective dosimetric comparison*. Radiat Oncol. 2014 Feb 10;9(1):50.
187. Dewaraja YK, Wilderman SJ, Niedbala J, Frey K, Wong KK. *Multi SPECT/CT-based patient specific lesion and kidney dosimetry for verification of simpler approaches for treatment planning in Lu-177 DOTATATE PRRT*. J Nucl Med. 2019;60.
188. Spezi E, Lewis G. *An overview of Monte Carlo treatment planning for radiotherapy*. In: Radiation Protection Dosimetry. 2008. p. 123–9.
189. Del Prete M, Buteau FA, Beauregard JM. *Personalized 177Lu-octreotate peptide receptor radionuclide therapy of neuroendocrine tumours: a simulation study*. Eur J Nucl Med Mol Imaging. 2017 Aug 31;44(9):1490–500.
190. Marin G, Vanderlinden B, Karfis I, et al. *A dosimetry procedure for organs-at-risk in 177Lu peptide receptor radionuclide therapy of patients with neuroendocrine tumours*. Phys Medica. 2018 Dec 1;56(October):41–9.
191. Wormgoor WD, Meeuwis APW, Sechopoulos I, Visser EP. *Experimental validation of semi Monte Carlo , voxel-based radionuclide dosimetry software using 3D printed phantoms and TLD measurements and application to patient scans using SPECT / CT*. In: European Society of Radiology. 2017.
192. Grimes J, Celler A. *Comparison of internal dose estimates obtained using organ-level, voxel S value, and Monte Carlo techniques*. Med Phys. 2014 Aug 14;41(9):092501.

193. Howard DM, Kearfott KJ, Wilderman SJ, Dewaraja YK. *Comparison of I-131 radioimmunotherapy tumor dosimetry: Unit density sphere model versus patient-specific monte carlo calculations*. Cancer Biother Radiopharm. 2011 Oct;26(5):615–21.
194. Divoli A, Chiavassa S, Ferrer L, Barbet J, Flux GD, Bardies M. *Effect of patient morphology on dosimetric calculations for internal irradiation as assessed by comparisons of Monte Carlo versus conventional methodologies*. J Nucl Med. 2009 Feb 1;50(2):316–23.
195. Dodd G, L Baron R. *Investigation of contrast enhancement in CT of the liver: The need for improved methods*. Vol. 160, AJR. American journal of roentgenology. 1993. 643–645 p.
196. Uribe CF, Esquinas PL, Tanguay J, et al. *Accuracy of ^{177}Lu activity quantification in SPECT imaging: a phantom study*. EJNMMI Phys. 2017 Dec;4(1):2.
197. Erdi YE, Wessels BW, Loew MH, Erdi AK. *Threshold estimation in single photon emission computed tomography and planar imaging for clinical radioimmunotherapy*. Cancer Res. 1995 Dec 1;55(23 SUPPL.):5823s-5826s.
198. Grimes J, Celler A, Shcherbinin S, Piwowarska-Bilska H, Birkenfeld B. *The accuracy and reproducibility of SPECT target volumes and activities estimated using an iterative adaptive thresholding technique*. Nucl Med Commun. 2012 Dec;33(12):1254–66.
199. Krak NC, Boellaard R, Hoekstra OS, Twisk JWR, Hoekstra CJ, Lammertsma AA. *Effects of ROI definition and reconstruction method on quantitative outcome and applicability in a response monitoring trial*. Eur J Nucl Med Mol Imaging. 2005 Mar 15;32(3):294–301.

200. Collamati F, Bellini F, Bocci V, et al. *Time Evolution of DOTATOC Uptake in Neuroendocrine Tumors in View of a Possible Application of Radioguided Surgery with ^{67}Ga Decay*. J Nucl Med. 2015 Oct 1;56(10):1501–6.
201. O JH, Lodge MA, Wahl RL. *Practical PERCIST: A Simplified Guide to PET Response Criteria in Solid Tumors 1.0*. Radiology. 2016 Aug 24;280(2):576–84.
202. Tukey JW. *Exploratory data analysis*. Reading, Mass.: Addison-Wesley Pub. Co.; 1977.
203. Hoaglin DC. *John W. Tukey and Data Analysis*. Stat Sci. 2003;18(3):311–8.
204. Moran JM, Molineu A, Kruse JJ, et al. *Executive summary of AAPM Report Task Group 113: Guidance for the physics aspects of clinical trials*. J Appl Clin Med Phys. 2018;19(5):335–46.